

DISS. ETH NO. 26299

Endurance of Polymeric Insulation under Mixed-Frequency Medium-Voltage Stress

A thesis submitted to attain the degree of

DOCTOR OF SCIENCES of ETH ZURICH

(Dr. sc. ETH Zurich)

presented by

RAPHAEL FÄRBER

MSc en Physique EPFL
École Polytechnique Fédérale de Lausanne

born on 15.09.1986
citizen of Berneck SG

accepted on the recommendations of:

Prof. Dr. Christian M. Franck,
Prof. Dr. Andrea Cavallini

2019

Abstract

In order to accommodate the requirements of future electrical energy transmission and distribution grids (in particular the need to integrate a large number of decentralized DC-type and variable AC-type sources), a growing usage of power electronic converters for electrical energy conversion at the medium-voltage (MV) level (1 kV to 20 kV) is expected. Thus, in recent years, research on so-called Solid-State Transformers (SSTs), which enable a controllable energy conversion between different voltage levels and/or frequencies, has gained considerable momentum. These MV converters employ high switching frequencies (so-called medium frequencies, MF, typically ranging from 1 kHz to 100 kHz) to achieve high power densities (conversion power per unit volume). The maturing of semiconductor switching technologies (most prominently silicone carbide based transistors) enlarges the design space of SSTs by enabling the use of higher switching frequencies, higher switching speeds as well as higher single switch blocking voltages. The design of SiC-based MV MF converters has received a lot of attention on the system and component level, while there is a relative lack of information on how the electrical insulation system should be designed in order to ensure its long-term reliability under the employed inverter voltage (and thermal) stress (without relying on inefficient over-dimensioning). A critical component in this respect is the MV MF transformer, which provides galvanic isolation in the SST.

This work thus aims at contributing to the understanding of (solid) insulation aging under inverter-generated medium voltages, in particular below partial discharge inception, where the available results in the scientific literature are not conclusive.

To this end, test facilities for dielectric material characterization were set up and subsequently used to lay an empirical basis from which design rules for the MV MF transformer insulation (as well as related insulation systems) could be derived. Namely, a modular, low-voltage (offline) dielectric spectrometer was designed and applied to determine the dielectric spectra of candidate potting materials for MF MV applications (which are needed for the thermal simulation of these insulation systems), as well as

to provide proof-of-concept measurements on the promising potential of using the dielectric permittivity as an aging marker for both homogeneous structural aging (e.g. thermal and uniform electrical stress) as well as localized insulation degradation (electrical treeing).

In order to investigate the influence of the voltage waveform on the voltage endurance of polymeric insulation, time-to-failure testing on PET insulation foil under a DC-biased rectangular MV MF pulse voltage is performed, both above and below partial discharge (PD) inception. The obtained results suggest that there is no “per pulse” degradation if care is taken to eliminate PD and excessive dielectric heating. The times to failure – and the underlying physical processes leading to breakdown under an applied DC voltage – are merely *modulated* by the varying voltage levels. Above PD inception, there is a clear “per pulse” degradation, which leads to a thinning of the insulation foil and an eventual breakdown induced by the applied DC electric field component.

The low-voltage dielectric spectrometer served as a stepping stone to the development of a high-voltage (online) dielectric spectrometer, which was designed to complement time-to-failure testing under inverter-type voltages in future investigations. It uses the broadband stressing voltage of the inverter test bench to measure the evolution of the dielectric spectrum over time. Its design process is detailed and its performance thoroughly assessed by means of a proof-of-concept measurement on the PET insulation foil employed for time-to-failure testing.

Finally, the insights gained from the experimental tests (as well as theoretical considerations) are used to compile design guidelines for dry-type MV MF transformer (and related) insulation systems. In particular, the selection process of a suitable potting material (with a focus on involved property tradeoffs) is explained. The selected potting compound is applied to a constructed MF MV transformer prototype in a vacuum potting process, and its electrical and thermal performance is assessed.

Kurzfassung

Um den Anforderungen zukünftiger elektrischer Energieübertragungs- und Verteilnetzen gerecht zu werden (insbesondere dem Einbezug einer grossen Anzahl dezentraler DC- und AC-Quellen variabler Frequenz), zeichnet sich ein grossflächiger Einsatz leistungselektronischer Konverter für die Energieumwandlung auf der Mittelspannungsebene (MV) (1 kV to 20 kV) ab. In den letzten Jahren hat deshalb die Forschung an sogenannten Solid-State Transformatoren (SSTs), welche eine kontrollierbare Energieumwandlung zwischen verschiedenen Spannungsebenen und Frequenzen erlauben, an Dynamik gewonnen. Diese Mittelspannungskonverter verwenden hohe Schaltfrequenzen (sogenannte Mittelfrequenzen, MF, im Bereich von ca. 1 kHz bis 100 kHz) um hohe Leistungsdichten (Konverterleistung pro Volumen) zu erreichen. Die Reifung halbleiterbasierter Schalttechnologien (allen voran Siliziumkarbid-Transistoren) vergrössern die Möglichkeiten bei der Auslegung von SSTs, indem sie höhere Schaltfrequenzen, höhere Schaltgeschwindigkeiten sowie höhere Sperrspannungen ermöglichen. Die Entwicklung von SiC-basierten MV MF Konvertern hat vor allem auf System- und Komponentenebene Beachtung erhalten, währenddem bezüglich der Auslegung eines unter der auftretenden Inverterspannungsbelastung (sowie thermischer Beanspruchung) langzeitstabilen elektrischen Isolationssystems verhältnismässig wenig Information verfügbar ist (ohne auf eine ineffiziente Überdimensionierung zurückgreifen zu müssen). Eine isolationstechnisch kritische Komponente ist der MV MF Transformator, welcher die galvanische Trennung im SST sicherstellt.

Diese Arbeit hat deshalb zum Ziel, das Verständnis von Alterungsvorgängen in (Feststoff-)Isolationsmaterialien unter Inverter-Mittelspannungsbeanspruchung zu erweitern, insbesondere unterhalb der Teilentladungseinsatzschwelle, wo die verfügbaren Resultate in der Literatur kein einheitliches Bild zeichnen.

Zu diesem Zweck wurden Testanlagen für die dielektrische Materialcharakterisierung aufgebaut and anschliessend verwendet um eine empirische Basis zu legen, welche der Formulierung von Auslegungskriterien für die

elektrische Isolation des MV MF Transformators (sowie artverwandten Isolationssystemen) zugrunde gelegt werden können. Namentlich wurde ein modulares dielektrisches Spektrometer (Niederspannung) aufgebaut und zur Bestimmung der dielektrischen Spektren von potenziell geeigneten Isolationmaterialien eingesetzt (welche für die thermische Auslegung dieser Isolationssysteme benötigt werden). Zudem wurden Machbarkeitsmessungen zur vielversprechenden Anwendung der dielektrischen Permittivität als Alterungsindikator für die homogene strukturelle Alterung von Isolationmaterialien (z.B. thermische und uniforme elektrische Feldbelastungen) sowie das Voranschreiten lokaler Schädigung der Isolation (elektrisches Treeing) ausgeführt und analysiert.

Um den Einfluss der Spannungsform auf die Lebensdauer polymerer Isolationsstoffe zu untersuchen, wurden Konstantspannungsversuche mit PET Isolationsfolien unter Mischspannungsbelastung (DC + MV MF Rechteckpuls) oberhalb und unterhalb der Teilentladungseinsatzschwelle durchgeführt. Die Ergebnisse deuten darauf hin, dass keine “pro Puls”-Schädigung des Isolationsmaterials auftritt, sofern Teilentladungen (TE) und eine übermässige dielektrische Erwärmung unterbunden werden. Die Lebensdauer, und damit die dem DC-Durchschlag zugrunde liegenden physikalischen Prozesse, werden durch die sich wechselnden Spannungsniveaus lediglich *moduliert*. Oberhalb des TE-Einsatzes lässt sich eine klare “pro Puls”-Schädigung des Isolationsmaterials beobachten, welche die Folienoberfläche erodiert und schliesslich zum Durchschlag unter der anliegenden DC-Komponente des elektrischen Feldes führt.

Das für Niederspannungsanregung ausgelegte dielektrische Spektrometer diene als Vorlage für die Auslegung eines entsprechenden dielektrischen Spektrometers zur Anwendung mit Konverter-Prüfspannungen (Mittelspannungsebene) und soll zukünftig in Alterungstests (in Konstantspannungsversuchen) zum Einsatz kommen. Eine Charakterisierung des Aufbaus wird durch Messungen an PET Folien vorgenommen.

Abschliessend werden die Erkenntnisse der experimentellen Untersuchungen (sowie theoretischer Überlegungen) zusammengeführt um einen Leitfaden für die Auslegung von Trockenisolationssystemen für MV MF Transformatoren (sowie artverwandten Isolationssystemen) zu erstellen. Insbesondere wird der Auswahlprozess eines passenden Vergussmaterials dargestellt und die nötigen Kompromisse in den Materialeigenschaften diskutiert. Das ausgewählte Vergussmaterial wird zum Vakuumverguss eines MV MF Transformator-Prototypen verwendet, welcher anschliessend erfolgreich einer elektrischen und thermischen Prüfung unterzogen wird.

List of Publications

The content of this thesis is to a large extent based on the following publications:

First-Author Journal Publications

- [1] R. Färber and C.M. Franck. *Modular High-Precision Dielectric Spectrometer for Quantifying the Aging Dynamics in (Sub-)Pico-farad Polymeric Specimens*. IEEE Transactions on Dielectrics and Electrical Insulation, Vol. 25, Nr. 3, p. 1056-1063, June 2018.
- [2] R. Färber, T. Guillod, F. Krismer, J.W. Kolar and C.M. Franck. *Endurance of Polymeric Insulation Foil Exposed to DC-Biased Repetitive Pulse Voltage Stress*. Submitted to *Energies* (MDPI / ISSN 1996-1073).

First-Author Conference Publications

- [3] R. Färber and C.M. Franck. *Modular Arbitrary Waveform Dielectric Spectrometer for Aging Diagnostics of Recessed Specimens*. IEEE Conference on Electrical Insulation and Dielectric Phenomena (CEIDP), p. 763-767, Toronto, October 2016.
- [4] R. Färber and C. M. Franck. *Impedance Spectra of a Silicone Rubber in a Needle-Plane Electrode Arrangement During Electrical Tree Growth*. VDE Conference on High Voltage Technology, Berlin, November 2018.

- [5] R. Färber, A. Nasef and C. M. Franck. *Online Dielectric Response Analysis Under Mixed-Frequency Medium-Voltage Stress*. International Symposium on High Voltage Engineering (ISH), Budapest, August, 2019.

Co-Authored Journal Publications

- [6] T. Guillod, R. Färber, D. Rothmund, F. Krismer, C.M. Franck, and J.W. Kolar. *Dielectric Losses in Dry-Type Insulation of Medium-Voltage Power Electronic Converters*. IEEE Journal of Emerging and Selected Topics in Power Electronics, 2019.

Co-Authored Conference Publications

- [7] T. Guillod, R. Färber, F. Krismer, C.M. Franck, and J.W. Kolar. *Computation and Analysis of Dielectric Losses in MV Power Electronic Converter Insulation*. IEEE Energy Conversion Congress and Exposition (ECCE), p. 1-8, Milwaukee, September 2016.

Author Contributions

- [1][3][4] R.F. designed and assembled the setups, programmed the control software, performed the measurements, data analysis and interpretation of results, created the figures and schematics and wrote the publication. The results and the structure of the paper were discussed with C.M.F., who also proof-read the paper.
- [2] R.F. designed and assembled the setup except for the repetitive pulse generator PCB and its software control, which was done by T.G. We greatly appreciated the support of the people at the Power Electronic System (PES) Laboratory (T.G., F.K. and J.W.K.) in all questions relating to their field of expertise. R.F.

performed all measurements and the data analysis, created all figures and schematics and wrote the paper. The results were discussed and the paper proof-read by all authors.

- [5] R.F. designed and manufactured the dielectric spectrometer hardware, created all figures and schematics and wrote the publication. A.N. incorporated the used USB oscilloscope into the graphical user interface of the inverter stress simulator and performed the measurements of the shown transfer functions as well as the permittivity of the Debye sample (as part of his Master's thesis). The results and the structure of the paper were discussed with C.M.F., and both C.M.F. and A.N. proof-read the paper.
- [6][7] T.G. did the major part of the work on these papers. R.F. initiated the awareness for considering the frequency and temperature dependence of the complex dielectric permittivity of polymeric insulation and derived the approximation of the dielectric loss for rectangular pulses with finite rise times for frequency-dependent material characteristics. R.F. manufactured the samples and performed the dielectric spectroscopy on the investigated epoxy and silicone materials. R.F. suggested the choice of the employed silicone material based on the property requirements, and set up a vacuum potting facility for encapsulating the MV MF transformer prototype. T.G. performed all simulations and the waveform measurements, designed the MV MF transformer, created all figures and schematics and wrote the publication (with support from his colleagues at PES). All authors provided feedback on the manuscript.

None of the setups used in these studies would have seen the light of the day without the great work of and helpful inputs by the workshop staff at the department of electrical engineering.

Citation Key

- [1]= [FF18a]
[2]= [FGK⁺19]
[3]= [FF16]
[4]= [FF18b]
[5]= [FNF19]
[6]= [GFR⁺19]
[7]= [GFK⁺16]

Student Theses

Five student theses were successfully completed within the framework of this project. The author would like to thank all students for their excellent contributions on the following topics. L. Deuschle and A. Philipp assessed the possibility of using a current transformer for broadband dielectric spectroscopy measurements, as well as the performance and influence of protective elements such as overvoltage clamping diodes [DP15]. T. Stiefel investigated the trade-offs inherent in the performance of current transformers (such as transimpedance gain $[V/A]$ vs. low-frequency cut off) and tested various high amplification voltage integrator circuits to be used for measuring the sample current under rectangular voltage excitation [Sti16]. F. Hoffmann studied the suitability of various USB oscilloscopes/digitizers for their use in dielectric spectroscopy and assessed the influence of acquisition variables (sampling frequency, vertical resolution, etc.) on the accuracy and precision of the impedance measurement [Hof17]. Les Messieurs P.-A. Pilloud and Q. Monney designed and constructed a relay box handling the de-energization of the 50 Hz transformer in case of test object breakdown, as well as a voltmeter box (up to 40 kV peak, DC to 50 Hz) incorporating an RMS-to-DC converter. They also assessed the functionality of the inverter stress simulator by performing first trial test series [PM17]. A. Nasef thoroughly characterized the final versions of the voltage amplifier and voltage integrator used for online dielectric spectroscopy by measuring their transfer functions and assessing their accuracy and precision for impedance measurements. He also assisted in implementing the online dielectric spectrometer on the inverter stress simulator and performed proof-of-concept measurements [Nas18].

- [DP15] L. Deuschle and A. Philipp. *Feasibility Study on the Use of Current Transformers in Dielectric Spectroscopy*. Semester Thesis, ETH Zürich, 2015
- [Sti16] T. Stiefel. *Current Sensing for Broad-Band High-Voltage Dielectric Spectroscopy*. Semester Thesis, ETH Zürich, 2016
- [Hof17] F. Hoffmann. *Implementation of a Signal Acquisition System for High-Voltage Dielectric Spectroscopy*. Semester Thesis, ETH Zürich, 2017
- [PM17] P.-A. Pilloud and Q. Monney. *Experimental Investigation on the Voltage Endurance of Polymeric Insulation Materials under*

Puls-Width-Modulated Medium Voltages. Bachelor Thesis, HES-SO Fribourg and ETH Zürich, 2017

[Nas18] A. Nasef. *Online Dielectric Spectroscopy under Medium-Frequency High-Voltage Stress*. Master Thesis, ETH Zürich, 2018

Abbreviations

AC	Alternating Current
ADC	Analog-to-Digital Converter
BDV	Breakdown Voltage
BNC	Bayonet Neill Concelman (RF Coaxial Connector)
CF	Crest Factor
CM	Common Mode
CT	Current Transformer
DAC	Digital-to-Analog Converter
DBD	Dielectric Barrier Discharge
DC	Direct Current
DFT	Digital Fourier Transform
DM	Differential Mode
DS	Dielectric Spectroscopy
EMI	Electromagnetic Interference
FEM	Finite Element Model
FFT	Fast Fourier Transform
GaN	Gallium Nitride
GUI	Graphical User Interface
HV	High Voltage
HN	Havriliak-Negami
IC	Integrated Circuit
IGBT	Insulated Gate Bipolar Transistor
IMRAD	Introduction Methods Results and Discussion
IS	Impedance Spectroscopy
ISS	Inverter Stress Simulator
LF	Low Frequency (50/60 Hz)
LV	Low Voltage
MF	Medium Frequency
MOSFET	Metal Oxide Semiconductor Field Effect Transistor
MV	Medium Voltage
PA	Polyamid
PD	Partial Discharge
PDIV	Partial Discharge Inception Voltage

PDEV	Partial Discharge Extinction Voltage
PDF	Probability Density Function
PE	Polyethylen
PEA	Pulsed Electro-Acoustic
PEN	Polyethylene Naphtalate
PET	Polyethylen Terephtalate
PID	Proportional Integral Derivative (Controller)
PMT	Photomultiplier Tube
PP	Polypropylen
PVC	Polyvinyl Chloride
PWM	Pulse-Width-Modulated
RF	Radio Frequency
RH	Relative Humidity
RPDIV	Repetitive Partial Discharge Inception Voltage
RMS	Root-Mean-Square
RTV	Room Temperature Vulcanized
SCLC	Space Charge Limited Current
SiR	Silicone Rubber
SiC	Silicon Carbide
SMA	SubMiniature version A (RF Coaxial Connector)
SNR	Signal-to-Noise Ratio
SST	Solid State Transformer
TSC	Thermally Stimulated Currents
TTF	Time to Failure
USB	Universal Serial Bus
UV	Ultraviolet

Constants and Variables

Symbol	Value	Unit	Name
c	299 792 458	m s^{-1}	Speed of light in vacuum
ϵ_0	$8.854 \cdot 10^{-12}$	F m^{-1}	Vacuum permittivity
μ_0	$4\pi \cdot 10^{-7}$	H m^{-1}	Vacuum permeability
e	$1.602 \cdot 10^{-19}$	C	Elementary electrical charge

Symbol	Unit	Name
C	F	Capacitance
C_0	F	Vacuum capacitance
D	–	Duty cycle
D	$\text{m}^2 \text{s}^{-1}$	Diffusion constant
d	m	Thickness
\mathbf{D}	C m^{-2}	Electrical displacement field
\mathbf{E}	V m^{-1}	Electric field
\mathbf{E}_{loc}	V m^{-1}	Local electric field
\mathbf{F}	N	Force
\mathbf{f}	N m^{-3}	Force density
f	s^{-1}	Dielectric response function
f_0	Hz	Fundamental frequency
f_s	Hz	Switching frequency
f_c and f_r	Hz	Cutoff frequency
\mathbf{H}	A m^{-1}	Magnetic field
$i(t)$	A	Time-dependent current
\mathbf{J}	A m^{-2}	Current density
L	H	Inductance
\mathbf{P}	C m^{-2}	Polarization density
$\underline{M} = M' + jM''$	–	Electric modulus

n	m^{-3}	Number density
P	W	Power
p	W m^{-3}	Power density
p	Pa	Pressure
q	C	Electrical charge
R	Ω	Electrical resistance
s_N		Standard deviation (estimator)
T	s	Fundamental period
t	s	Time
t	–	Student's t coefficient
TTF	s	Time to failure
$u(t)$ or $v(t)$	V	Time-dependent voltage
U_b	V	Breakdown voltage
U_p	V	Jump voltage (DC bus voltage)
U_{pp}	V	Peak-Peak voltage
V	m^3	Volume
\hat{U}	V	Voltage overshoot
U_{DC}	V	DC voltage component
W	J	Energy
w	J m^{-3}	Energy density
\underline{Z}	Ω	Electrical impedance
α	s	Weibull scale parameter
α	–	HN broadening parameter
α	$\text{C m}^2 \text{V}^{-1}$	Polarizability
α_{eff}	m^{-1}	Effective ionization coefficient
β	–	Weibull shape parameter
β	–	HN asymmetry parameter
$\frac{\beta}{\alpha}$	– and V A^{-1}	Complex transfer coefficients
$\overline{\delta}(t)$	$[t]^{-1}$	Dirac delta function
δ	rad	Loss angle
Δ		Instrument precision
$\theta(t)$	–	Heaviside step function
ϑ	$^{\circ}\text{C}$ or K	Temperature
$\underline{\varepsilon} = \varepsilon' - j\varepsilon''$	–	Relative dielectric permittivity
Γ	$\text{W K}^{-1} \text{m}^{-3}$	Cooling coefficient
$\underline{\chi}_e = \chi'_e - j\chi''_e$	–	Dielectric susceptibility
κ	S m^{-1}	Electrical conductivity
λ_D	m	Debye length
μ	C m	Electric dipole moment
μ		Mean value
μ_i	$\text{m}^2 \text{V}^{-1} \text{s}^{-1}$	Electrical mobility

ρ	C m^{-3}	Total space charge density
ρ_f	C m^{-3}	Free space charge density
ρ_b	C m^{-3}	Bound space charge density
ρ_m	kg m^{-3}	Mass density
σ	C m^{-2}	Surface charge density
σ		Standard deviation
τ	s	Time constant
τ	s	Pulse width
τ_r	s	Rise time
ω	rad s^{-1}	Angular frequency
Ω	m^3	Volume

Symbol	Name
\cdot	Scalar product
\times	Vector product
$\nabla \cdot$	Divergence
$\nabla \times$	Curl
∇	Gradient
$\nabla^2 = \Delta$	Laplace operator
$*$	Convolution operator
j	Unit imaginary number

Contents

Abstract	iii
Kurzfassung	v
List of Publications	vii
Nomenclature	xiii
1. Introduction	1
1.1. Context: Power Electronics Meets High-Voltage Engineering	1
1.2. The Project	4
1.3. Outline of the Thesis	6
2. Literature Review	9
2.1. Inverter Waveform Characterization	10
2.2. Impact of Voltage Waveform on Local Electric Field Stress	14
2.3. Impact of Voltage Waveform and Frequency on Degradation, Aging and Failure of Electrical Insulation Materials/Systems	15
2.3.1. Above Partial Discharge Inception	15
2.3.2. Below Partial Discharge Inception	18
2.3.3. Lifetime Testing of Insulation Exposed to Mixed-Frequency Voltages (DC+AC repetitive impulse)	24
2.3.4. Other Stress Factors Influencing Insulation Endurance	27
2.3.5. The Elektrokinetic Model of Dielectric Endurance	29
2.3.6. Literature Review: Synopsis I	31
2.4. Online Dielectric Spectroscopy under Inverter-Generated Medium-Voltage Waveforms	34
2.4.1. Dielectric Permittivity as an Insulation Aging Marker	34
2.4.2. Dielectric Permittivity: Nonlinearity	35
2.4.3. Dielectric Spectroscopy Measurement Systems Operating under Inverter-Generated Voltages	37
2.4.4. Literature Review: Synopsis II	38

3. Theoretical Background	41
3.1. Mathematical Tools	41
3.1.1. Fourier Transform	41
3.1.2. Fourier series	42
3.1.3. Fourier sum	44
3.1.4. Spectrum of a Trapezoidal Pulse Train	46
3.2. Dielectric Polarization	49
3.2.1. Dielectric Susceptibility	52
3.2.2. Charge Transport in Dielectric Solids	57
3.2.3. Capacitive Currents in the Presence of Dynamic Bound Space Charge in the Dielectric Volume	61
3.2.4. Relaxation of free space charge in conducting di- electric solids	66
3.2.5. Average Dielectric Losses Under Mixed-Frequency Excitation	68
3.2.6. Dielectric Loss under Transient Excitation	69
4. Aim of this Work	71
5. Theoretical Considerations	73
5.1. Capacitive Currents in the Presence of Free Space Charge in a Dielectric Volume	73
5.2. Electric Field Distribution in a Layered Dielectric under Mixed-Frequency Voltage Stress	80
5.3. Dielectric Losses Under Inverter-Type Voltages: A Simple Approximation	87
5.4. Instantaneous Dielectric Loss Rate?	95
6. Modular Offline Dielectric Spectrometer	97
6.1. Design and Setup	98
6.1.1. Measurement Principle	98
6.1.2. Layout and Components	102
6.1.3. Undersampling	103
6.1.4. Data Acquisition and Processing	104
6.1.5. Control and Automation Software	107
6.1.6. Benchmark Data	108
6.2. Quantifying Aging-Induced Changes of Dielectric Permit- tivity in an Epoxy Polymer	113
6.2.1. Introduction	113
6.2.2. Methods	114
6.2.3. Results	116

6.2.4.	Discussion	123
6.2.5.	Conclusion	124
6.2.6.	Limitations and Outlook	124
6.3.	Broadband Dielectric Response of a Silicone Rubber During Electrical Tree Growth	126
6.3.1.	Introduction	126
6.3.2.	Methods	127
6.3.3.	Theory	129
6.3.4.	Results	133
6.3.5.	Discussion	141
6.3.6.	Conclusion	142
6.3.7.	Limitations and Outlook	143
7.	Inverter-Stress Simulator	145
7.1.	Design and Setup	146
7.1.1.	Layout and Components	146
7.1.2.	Diagnostics	149
7.1.3.	Humidity and Temperature Control System	150
7.2.	Time-to-Failure Testing under DC-biased Repetitive Im- pulse Voltages Below PD Inception	152
7.2.1.	Introduction	153
7.2.2.	Methods	156
7.2.3.	Results	163
7.2.4.	Discussion	168
7.2.5.	Conclusion	169
7.2.6.	Limitations and Outlook	170
7.3.	Time-to-Failure Testing under DC-biased Repetitive Im- pulse Voltages Above PD Inception	172
7.3.1.	Introduction	172
7.3.2.	Methods	173
7.3.3.	Results	176
7.3.4.	Discussion	181
7.3.5.	Conclusion	184
7.3.6.	Limitations and Outlook	185
8.	Online Dielectric Spectrometer for Inverter-Type Medium Voltages	187
8.1.	Introduction	187
8.2.	Design and Setup	188
8.2.1.	Voltage Source	188
8.2.2.	Excitation Voltage and Response Current	189

8.2.3.	Signal Conditioning and Measurement	191
8.2.4.	A Definition of Instrument Precision	198
8.2.5.	Calculating the Dielectric Permittivity	200
8.3.	Results	201
8.3.1.	Instrument Accuracy – Debye Sample	201
8.3.2.	Instrument Precision and Stability	203
8.3.3.	Pre-Breakdown Evolution of Dielectric Response	204
8.4.	Discussion	204
8.5.	Summary	208
8.6.	Limitations and Outlook	208
9.	Design Process of MF MV Transformer Insulation	211
9.1.	MF MV Transformer Insulation Design Guidelines	211
9.2.	Material Properties: Requirements	212
9.3.	Material Characterization and Selection	214
9.4.	Vacuum Potting	216
9.5.	Simulation and Measurements	219
9.6.	Summary	221
9.7.	Limitations and Outlook	221
10.	Conclusion and Outlook	223
	Appendices	225
	Bibliography	235
	Acknowledgement	253
	Curriculum Vitae	257

1. Introduction

“Many electrical and mechanical devices, perhaps due to performance and/or cost issues, push their standard operating conditions (use conditions) very close to the intrinsic strength of the materials used in the design. Thus, it is not a question of whether the device will fail, but when.”

J.W. McPherson

in *Reliability Physics and Engineering* (2013)

1.1. Context: Power Electronics Meets High-Voltage Engineering

In addition to established applications of power electronics in high-voltage technology such as FACTS (Flexible AC Transmission Systems) devices or HVDC (High Voltage Direct Current) Transmission, actively controlled semiconductor switches are expected to play a key role in future “smart” electrical transmission and distribution grids [TN17]. A basic requirement for a system to be “smart” is its ability to autonomously react to monitored system variables. Controllability is thus an important aspect of (part of) the devices that constitute a smart electrical grid. This is in contrast to conventional electrical grids, which are to a large extent passive connectors between the centralized power plants (generators) and the decentralized loads, and where an important contribution to inherent system stability is obtained through the balancing role of the reservoir of kinetic energy stored in the rotating mass in asynchronous generators.

The trend in electrical energy generation clearly points away from big centralized sources (such as nuclear or coal power plants) towards a more distributed configuration of a large number of renewable sources [Tan15]. These can either be of DC-type (e.g. photovoltaics) or variable-frequency

AC-type (e.g. wind turbines). This brings about a number of new challenges, whose possible solutions (e.g. new grid topologies such as *microgrids* [MRBA19]) rely heavily on the use of power electronic devices on the MV level or at the MV–LV interface [SMC⁺18]. Firstly, there is a need for interfacing grids, sources and sinks of various voltages and frequencies (including DC). Secondly, the volatile nature of renewable sources, the reduction of system inertia by fewer asynchronous generators, and the dynamic bidirectional power flows at end-user interfaces pose a potential threat to system stability and hence reliability. In order to mitigate this threat, active power flow control at numerous grid-grid/ grid-load and grid-source interfaces is required, with the mentioned flexibility to convert between DC and variable-frequency voltages. Moreover, efficient and highly dynamic energy storage is needed to dampen the renewable source volatility.

In this respect, medium-voltage power electronic transformers (also known as *Solid-State Transformers*, SSTs) [HK16] are key technology enablers in the adaptation of the electrical energy transmission and distribution grid to meet the above-mentioned challenges. Medium-voltage (MV, ≥ 1 kV) power electronic converters based on medium-frequency (MF, ≥ 1 kHz) transformers in the isolation stage have stimulated numerous research efforts over the recent years. These converters use semiconductor switches (typically MOSFETs or IGBTs) to interface a medium-voltage power grid with a load or generator via the MF MV transformer (and other passive components). They thereby provide a galvanically isolated interface with controllable electric power flow between grids / loads / generators / storage units of different voltage levels and/or frequencies (including DC), see Figure 1.1. By employing switching frequencies of several tens of kilohertz and beyond, these converters achieve significantly higher power densities (at equal efficiency) than their low-frequency (50 Hz) counterparts because – for a specified current rating – the magnetic components scale approximately with the inverse of their operating frequency.¹ For these reasons, MV SSTs are expected to play a key role where actively controlled electric power conversion (AC–AC, AC–DC, DC–DC) is needed (e.g. for MVDC grids), and/or when space/weight constraints apply, such as in medium-voltage electric mobility and electric aircraft/spacecraft applications [ROAR07].

While a lot of research has focused on the component level (e.g. new

¹The magnetic core volume scales approximately as $f^{-\frac{3}{4}}$ [HK16]. In an SST, however, inverter components and the active cooling system add a substantial fraction of the magnetic volume.

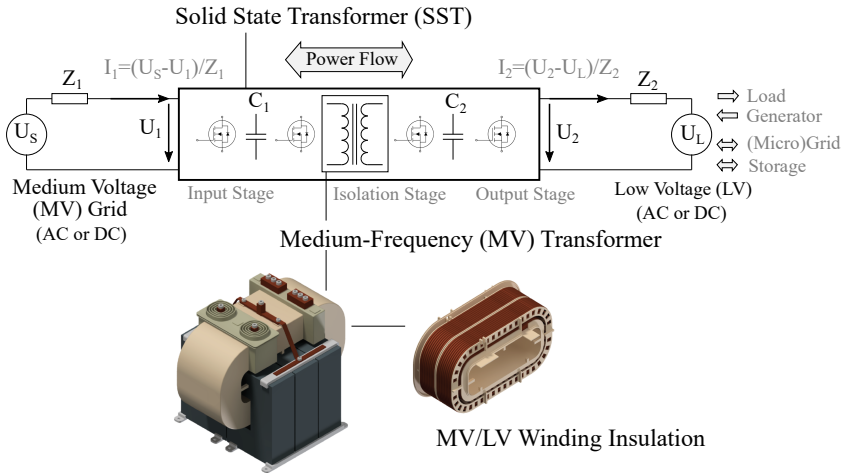


Figure 1.1.: The winding insulation of the medium-frequency transformer in a medium-voltage SST is exposed to repetitive impulse voltages (typically several ten thousand impulses per second). Moreover, in MF transformers the power (loss) densities are considerably higher than in LF transformers (see Appendix A), and the thermal stress on the insulation due to the copper, magnetic core and dielectric losses increased accordingly.

semiconductor materials [Bin18]) and system level (e.g. new converter topologies and scalable configurations [HK16]), there are comparatively few investigations that concentrate on the insulation concept of the MF transformer. Yet, there are good reasons to have a closer look at this topic, because...

- ...it sets boundary conditions on the transformer design (e.g. clearance distances) and its design is in turn influenced by the targeted operating conditions (e.g. maximal temperature rise, frequency, voltage waveform etc.)
- ...there are numerous interdependencies (insulation thickness – dielectric field stress – dielectric losses – thermal resistance to heat sink – parasitic capacitance – magnetic coupling – converter efficiency), which need to be quantified in order to be able to make well-considered tradeoffs.

- ...it is intimately linked to the reliability of the galvanic isolation between MV and LV that the SST is supposed to provide
- ...MV MF voltage stress has been observed to cause premature failure in solid insulation systems [BDM⁺09].

The long-term endurance of the transformer insulation system will be of concern especially when prototypes are to be moved towards market maturity, and considerable overdimensioning is no longer a viable option. Quoting J.W. McPherson from the beginning of this chapter: “it is not a question of whether the device will fail, but when.” [McP13] (p. vii). While oil-based insulation systems are common in medium-voltage high-power² converters, comparatively little information is available on dry-type systems, which represent an appealing alternative for achieving highly compact converter designs. This has motivated the initiation of a project assessing the use of dry-type insulation materials and systems for high-power ($\gg 1$ kW) medium-voltage (> 1 kV) power electronic converters based on medium-frequency (> 1 kHz) magnetic coupling in the isolation stage.

1.2. The Project

The present thesis grew out of a collaborative approach between the High Voltage Laboratory (HVL) and the Power Electronic Systems (PES) Laboratory at ETH Zürich within the framework of SCCER FURIES³. The motivating questions for this project revolve around the possible use of dry-type insulation materials for MV MF transformers in SSTs (and other MV converter systems):

- Are dry-type insulation systems a viable alternative to oil-impregnated systems for compact MF MV transformers?
- What are the relevant properties of the insulation material(s) in such an application?
- How can these properties be characterized?
- What are potential threats to the long-term reliability of the insulation system, in particular in relation to the unconventional voltage

²Typical values of conversion power of the targeted converters are 10 kW to a few hundred kW. Power densities are on the order of 10 kW/dm³ or more. [OLHK17]

³Swiss Competence Centers for Energy Research (SCCER) for the Future Swiss Electrical Infrastructure (FURIES).

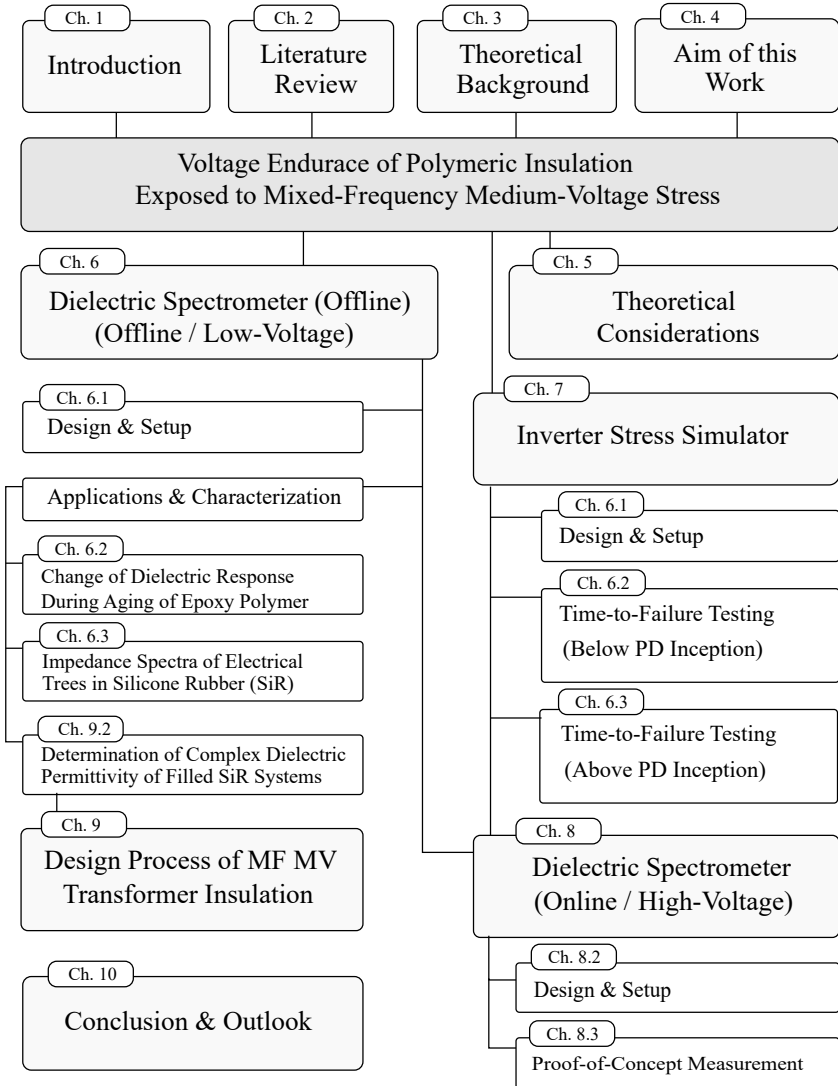
waveforms (high fundamental frequency, fast slew rates)?

- How can the aging/degradation of electrical insulation under inverter-type voltages be quantified, especially in the regime where partial discharges are absent?

The overall aim of the project was twofold. On the very practical level, one goal consisted in establishing a list of relevant material properties for the use conditions occurring in high-power MV MF converters, and to subsequently identify a suitable potting material for encapsulating a MF MV transformer prototype designed by the PES laboratory. This part included, in particular, the design and construction of a modular dielectric spectrometer, with which the dielectric properties of candidate materials could be investigated across the relevant ranges of frequency and temperature. This dielectric data served as input for accurate dielectric modelling of the transformer prototype (dielectric losses, electric field distribution, capacitive couplings).

On a more academic level, the project set out to further the understanding of insulation aging under inverter-type medium voltages, especially in the less investigated regime below PD inception. To this end, an “inverter stress simulator”, which allows to expose insulation materials to combined thermal, environmental (e.g. controlled atmospheric humidity) and electric field stresses, had to be set up. Moreover, suitable and possibly novel diagnostic techniques to quantify insulation aging under these conditions had to be identified and implemented.

1.3. Outline of the Thesis



Note: the IMRAD structure is applied *locally*, in particular in chapters 6.2, 6.3, 7.2 and 8.3, which are all closely based on scientific journal or conference articles.

Chapter 2 provides an extensive literature review on the electrical insulation challenges associated specifically with inverter-generated medium voltages, with a particular focus on the regime below PD inception and the possible role of space charge in inverter voltages with a non-vanishing DC component. The potential of using the dielectric permittivity as an insulation aging marker is presented. Research gaps are identified and unresolved questions formulated.

Chapter 3 summarizes theoretical concepts (textbook knowledge) that are used throughout this thesis. The reader may refer to this section on an as-needed basis.

Chapter 4 formulates the aim of this work.

Chapter 5 presents the results of a number of theoretical investigations motivated by questions that emerged in the context of mixed-frequency stressing of dielectric materials. In particular, the role of space charge in the presence of mixed voltages (DC + repetitive impulse voltage) is investigated.

Chapter 6 is based on the publications [1,3,4] and describes the design, characterization and application of a modular low-voltage dielectric spectrometer. Presented use cases of the setup are the determination of the complex dielectric spectra of candidate potting materials for MF MV applications (which are needed for the thermal simulation of these insulation systems, Chapter 9), proof-of-concept measurements on using the dielectric permittivity as an aging marker, and the investigation of the evolution of the dielectric response during electrical tree growth.

Chapter 7 is based on publication [2] and presents the constructed inverter stress simulator as well as an experimental investigation on the role of bulk space charge in insulation aging under DC-biased repetitive pulse voltages. No experimental evidence for a further hypothesized aging mechanism based on electromechanical stress from space charges was found (i.e. besides partial discharge and thermal aging/runaway due to enhanced dielectric losses).

Chapter 8 is based on publication [5] and outlines the development of an online dielectric spectrometer specifically designed for use with time-to-failure testing under inverter-type medium voltages. The

precision and accuracy of the setup are thoroughly characterized, and a proof-of-concept measurement on the PET insulation foil used for time-to-failure testing (Chapter 7) is given.

Chapter 9 uses the insights gained from the previous chapters to propose insulation design guidelines for MF MV transformers and related MF MV insulation systems. Moreover, this chapter provides details about the insulation material selection and the employed vacuum potting process used for the constructed MF MV transformer prototype.

Chapter 10 summarizes the main conclusions of this work. Moreover, it discusses promising topics for future investigations, based on questions that have remained unanswered or newly emerged in the course of this thesis.

2. Literature Review

“I’m a couple of books ahead – not because I write so quickly, but because I am published so slowly.”

John Steinbeck
in *A life in Letters* (1935)

This chapter provides a survey of the published literature on selected topics relating to¹

- the impact of voltage waveform and fundamental frequency on the degradation, aging and failure of electrical insulation
- the non-destructive characterization of insulation degradation and aging exposed to inverter-generated medium-voltage stress by means of dielectric spectroscopy

Specifically, it covers the characterization of the voltage waveform generated by power electronic inverters (Section 2.1) and how the waveform parameters influence the local electric field to which the constituent parts of an insulation system are exposed (Section 2.2). A synthesis of literature results on how the wave shape and fundamental frequency of the electric field stress impact the degradation, aging and failure of electrical insulation materials and systems is provided in Section 2.3. Section 2.4 covers the non-destructive characterization of insulation aging under inverter-generated medium-voltage waveforms by means of (online) dielectric spectroscopy.

¹Due to the sheer number of publications on these topics the following literature review is necessarily selective. Every effort was made to include the relevant contributions (both original and most recent) relating to the subtopics of this thesis.

The aim of this chapter is to...

- ...introduce basic **definitions and terms** (Section 2.1).
- ...provide a synthesis of **the state-of-the-art knowledge** available in the scientific literature and relevant to the topics covered in this thesis.
- ...identify **research gaps** or **inconclusively resolved questions** in this body of knowledge by analyzing and discussing it.
- ...set a frame for the formulation of the aim of this work (given in Chapter 4).

Electrical insulation degradation, aging and failure under non-conventional voltage waveforms generated by power electronic inverters is a largely investigated topic. Some 25 years ago [SCT00], the advent of the large-scale use of power-electronic inverters (variable speed drives) and the subsequent increase in induction motor insulation failures [Whe05] stimulated a growing body of research aiming at a better understanding of insulation failures associated in particular with repetitive impulse voltages².

An extensive review with an emphasis on rotating machine insulation is provided in [Cig17] as well as the international standards [IECa] and [IECb]. Another very readable, somewhat more general introduction to the electrical insulation challenges associated with medium-voltage converter operation is found in [BDM⁺09] as well as the review series [CFM10a] [CFM10b] [CFM10c].

The following sections provide a selective survey of the main findings available in the published literature for the indicated subtopics.

2.1. Inverter Waveform Characterization

Typical voltage waveforms generated by power electronic inverters are shown in Figure 2.1. The waveforms are characterized by [IECa]

- the employed pulse-width modulation scheme [Hol92], which determines the duty cycle D for each switching period.
- the number n of voltage levels.

²We follow here the terminology suggested in [IECa], 3.10, Note 1: “The term impulse is used to describe the transient stressing voltage applied to the test object and the term pulse is used to describe the partial discharge signal.”

- the fundamental frequency f_0 .
- the switching frequency f_s .
- the impulse rise time τ_r .
- the DC bus voltage U_p . This is the peak/peak value of the voltage impulses (without the overshoot).
- the voltage overshoot \hat{U} .
- the DC component U_{DC} of the impulse voltage.

An inverter voltage is said to be *unipolar* if it never changes sign with respect to system ground, and *bipolar* otherwise. The terms *mixed-frequency voltage* or *mixed voltage* are not defined unanimously in literature. In this thesis the term *mixed voltage* will be used to denote voltages with both significant DC and AC components in their frequency spectrum, whereas *mixed-frequency voltage* will be used slightly more generally to denote voltages with more than two (non-noise) Fourier components in their frequency spectrum (hence all mixed voltages are mixed-frequency voltages but not vice versa).

Unipolar voltage waveforms (that are not constant) are always mixed-frequency voltages. Bipolar voltages are mixed voltages only if they possess a DC offset, and they are mixed-frequency voltages only if they are not pure sinusoids. Finally, the term *strictly unipolar* will be used to designate unipolar voltages that are always either strictly positive or negative.

Typical ranges of some of the parameters characterizing the terminal voltage waveforms of inverter-fed medium-voltage devices are given in table 2.1 (adapted from the values for rotating machines given in [IECa] Table 1). The ranges given for f_s , U_p and τ_r indicate what is meant by “medium frequency”, “medium voltage” and “short rise times” in the present context.

Owing to continued advancements in semiconductor switching technology – namely the maturing of wide band gap semiconductor technology, such as silicon carbide (SiC) and gallium nitride (GaN) devices [Bin18] [EC02] – some of the future medium-voltage converters are expected to operate beyond the indicated limits of switching frequency, rise time and peak/peak voltage. Increasing the switching speed³ reduces switching losses and thus leads to increased converter efficiency and reduced hot

³*Switching speed* and *slew rate* are used interchangeably. They quantify the steepness of the voltage flanks occurring in inverter voltages (unit: kV/ μ s).

Symbol	Parameter	Range	Unit
U_{pp}	Peak/Peak voltage	0.5 .. >10	kV
U_p	Impulse (jump) voltage	0.5 .. 10	kV
τ_r	Rise/fall time	<0.05 .. 2	μ s
	Slew rate / switching speed	0.5 .. >50	kV/ μ s
f_s	Switching frequency	0.5 .. >50	kHz
f_0	Fundamental frequency	5 .. f_s	Hz

Table 2.1.: Typical ranges of parameter values for voltage waveforms at the terminal of inverter-fed devices (adapted from [IECa] to include medium-frequency transformer applications). Note that U_{pp} refers to the peak/peak voltage of the overall waveform, whereas U_p is the jump voltage of the individual pulses (they are equal for the 2-level voltages considered in this thesis).

spot temperatures within the semiconductor die (the latter typically limits the achievable switching frequency). An increase in the converter power density is achieved by increasing the switching frequency because it reduces the required cross-section of magnetic cores (and capacitors for charge storage) for a given current rating. Finally, the high achievable single switch blocking voltages of wide band gap power electronic switches (≥ 10 kV with SiC technology) allow to simplify converter topologies (e.g. interfacing a MV grid with a simple half-bridge topology) at the expense of higher jump voltages impinging on the electrical insulation system.

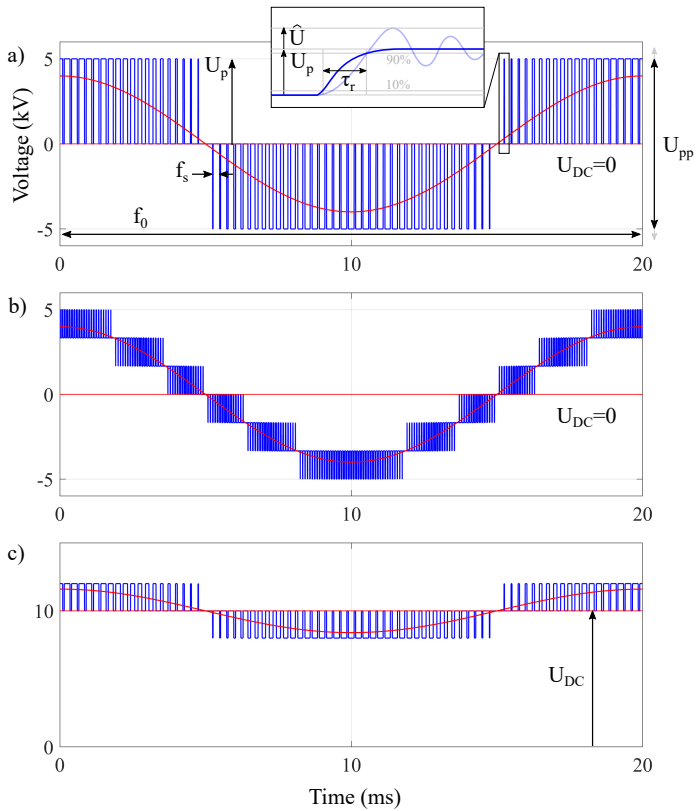


Figure 2.1.: Examples of pulse-width-modulated voltage waveforms generated by power electronic inverters: a) 3-level inverter b) 7-level inverter c) 3-level inverter with DC-bias. The red curves correspond to the the DC component and fundamental frequency in the Fourier spectrum, respectively.

2.2. Impact of Voltage Waveform on Local Electric Field Stress

It has been recognized early on that the terminal voltage waveform (and the value of the fundamental frequency) can strongly influence the electric field distribution inside an electrical insulation system [DW91] [MBL⁺97] [KAB⁺00]. The insulation system between two chosen conductor terminals is typically represented by a complex equivalent circuit consisting of resistive, inductive and capacitive elements [SSR⁺14]. The distribution of the terminal voltage along the nodes of this equivalent circuit (and hence the local electrical field stress on the insulation) is thus typically a function of the excitation frequency.⁴ A well-known example is the electric stress concentration on the first few windings of power transformers or form-wound motors when exposed to fast transient voltages (see e.g. Figure 7 in [IECa]), which is due to the capacitive coupling between windings and between windings and grounded conductors. The stress enhancement on certain parts of the insulation system is e.g. taken into account in the type and routine tests on inverter-fed systems by a prescription of allowed test waveforms (see Table 5 in [IECa]).

Mechanisms of overvoltage generation (i.e. voltages exceeding the levels of the open converter output) are described in detail in the literature, and are associated with the excitation of system resonances [WFA51] [PEH⁺03] [RPS⁺06] or the constructive interference of (wire-bound) travelling waves due to the impedance mismatch at the cable/load interface [MLVB01] [Kau95] [Cig17].

A related problem was observed to occur in certain field-grading systems (e.g. cable terminations [MSH⁺04] or end-winding corona protection of stator bars in rotating machines [SCL07]) that are usually not designed to operate reliably at converter switching frequencies. For example, resistive/refractive field grading systems suffer from a distorted electric field distribution beyond the intended operating frequency due to the reasons mentioned above, but also generate enhanced thermal losses in the field-grading layer (due to the higher capacitive currents). The associated increase of temperature affects the non-linear I–V characteristics of the field-grading material, and thus the field-grading performance (in addition the filling grease in the cable/termination interface can evaporate/dry out, paving the way for partial discharge erosion).

⁴This also highlights the importance of considering inductive and capacitive couplings in the design process of insulation systems for MF applications.

2.3. Impact of Voltage Waveform and Frequency on Degradation, Aging and Failure of Electrical Insulation Materials/Systems

Note: Sections 2.3.1 and 2.3.2 cover both bipolar and (not strictly) unipolar impulse waveforms. Strictly unipolar mixed voltages (see definition on page 11) are treated separately in Section 2.3.3.

There are numerous in-depth studies on the endurance and aging of insulation materials/systems exposed to voltage stress with non-conventional waveforms and/or higher (i.e. $\gg 50$ Hz) fundamental and harmonic frequencies. Due to the mentioned increased insulation failure rates for inverter-fed motors, many investigations focus on parts of the rotating machine insulation system [Yin97] [CMFT11], in particular the turn/turn insulation (e.g. [Kau95] [WCM14] [HJCS06]), the ground-wall insulation (e.g. [HJC05]) and the end-winding stress grading system (e.g. [SJC10]). While not researched as intensely, there are a few studies on transformer insulation, namely oil-impregnated Kraft paper [KCD⁺11] and dry-type systems [KHS98].

2.3.1. Above Partial Discharge Inception

Early systematic evidence for the important role of PD erosion in the premature failure of rotating machine insulation exposed to inverted-generated voltages was presented in the seminal paper [Kau95]. This investigation deals with Type I insulation systems (i.e. those not designed to withstand continuous PDs) consisting of two parallel wound, enamelled and impregnated wires. The repetitive impulse voltage consists of unipolar and bipolar voltage impulses with repetition rates from 10 Hz to 8 kHz and rise times⁵ from 0.02 μ s to 1 μ s. One of the general conclusions is that “Sufficient lifetime of inverter-fed low voltage motors can be achieved only if PDs in the winding insulation are avoided” (p. 257), and it is proposed that for a given electrode arrangement and a given peak/peak voltage of the pulse train, there is a certain number n_b of PD pulses required to cause insulation breakdown (independent of the impulse repetition rate). Then, if the probability of a PD occurrence (i.e. the number of

⁵The used impulse waveform is asymmetric, i.e. rise time \neq fall time.

recorded PDs divided by the number of applied impulses) is denoted by p_{PD} , this study observed that the number of voltage impulses needed to cause breakdown is approximately given by n_b/p_{PD} . This entails in particular that the lifetime is not affected by the impulses at all if they are not able to incept PDs: “High frequencies, small rise times and fast oscillating pulses shorten the lifetime, but if no PDs occur, even after two years under considerably high electrical and thermal stress, no breakdown could be observed” (p. 257).

Another important conclusion of the paper [Kau95] concerns the difference between unipolar and bipolar impulse voltages: *for a fixed waveform and PD as the primary cause of insulation failure*, it is the peak/peak voltage of the impulses that is observed to determine the lifetime (and not their peak voltage). Thus, at the same peak voltage, the lifetime under unipolar impulses is about twice as long as the lifetime under bipolar impulses. In the explanation for this observation, the paper identifies the decisive role of surface charges deposited on the dielectric surfaces by the PDs. These surface charges create an electric field which cancels⁶ the instantaneous electric field in the air gap undergoing PD, thus quenching the discharge. It is then the *variation* of the electrode field (and not its value in absolute terms) that determines the field in which subsequent gas discharge avalanches develop (which in turn deposit surface charges).⁷

The understanding of the deleterious effects of repetitive impulse voltages on organic insulation materials in the presence of PDs is refined in numerous subsequent investigations. While there is general agreement that the lifetime in the presence of PD decreases with increasing switching frequency, $TTF \propto f_s^{-k}$, there is some disagreement about the value of the exponential factor $k > 0$. [MJC15] observe the lifetime to scale inversely with frequency ($k = 1$), while from the data of other investigations, values $k < 1$ are obtained (typically between 0.6 and 0.8) [WCM14]. In the first case ($k = 1$) the “per impulse” degradation is unaffected by the repetition rate of the impulses, while in the latter case ($k < 1$) the damage per impulse decreases with increasing repetition rate. Lower values of k are obtained from lifetime data on “PD-resistant” magnet wires (i.e. containing inorganic micro/nano-fillers) [HJCS06].

⁶More precisely, the field is reduced to a certain small residual value. See [Nie95] for more details.

⁷The relaxation/recombination of the surface charges will also lead to a renewed increase of the field in the air gap even if the electrode voltage remains constant. Typically, however, the associated time constant is large compared to the period of AC line frequency, let alone converter switching frequencies. A notable exception is PD under DC voltage stress.

The influence of rise time of the voltage impulses on insulation lifetime has also been investigated by several researchers [Kau95] [WCM14] [KKB⁺11] [Yin97] [GFK99]. There is general agreement that shorter rise times reduce the lifetime in the PD regime. This observation is congruent with the observation that PD magnitudes increase with shorter rise times [WCM14] [HBBG14].

The body of research on the impact of duty cycle on the voltage endurance under repetitive impulse voltages is comparatively scarce. An early study [GFK99] on magnet wires observed a threefold increase of lifetime when decreasing the duty cycle from 50% to 15%. A more recent study on crossed enamelled wires [WXWC16] supports the trend of this finding, by reporting a roughly 30% increase in time to failure when the duty cycle is decreased from 50% to 5%. The authors in [WXWC16] also show that the results of the life tests are congruent with the provided analysis of the dependence of PD repetition frequency and magnitude on the duty cycle variations.

The general impact of the voltage waveform on PD and thus insulation lifetime is emphasized in [GCDT04]: “[T]hese results evidence that different waveforms with an equal peak-to-peak value can originate completely different (values and shape) life curves” (p.3). The authors compared sinusoidal, PWM and PWM+peak⁸ voltage stressing on twisted pairs of enamelled wire, and find lifetime at equal peak/peak voltages to decrease in the order of the mentioned waveforms (i.e. longest for sinusoidal). This contrasts, however, with the conclusion in [FM01]: “the peak-to-peak voltage is the most significant feature of the voltage waveform, which causes the acceleration of the degradation process independently of the voltage waveshape” (p. 31). The latter statement is probably meant to be read as applying only to the comparison between the sinusoidal and unipolar rectangular waveform (with a relatively slow slew rate of 0.75 kV/ μ s) investigated by these researchers.

All the above-mentioned investigations highlight the decisive role of PD and its characteristics (amplitude, rate of occurrence) under repetitive impulse voltages for the insulation aging in this regime. This has spurred numerous technical developments for the measurement of PDs under fast-rising voltage fronts and in-depth investigations on how the waveform parameters affect the PDs [OHM07] [Lin09] [WCM14] [HBBG14], espe-

⁸PWM+peak is a PWM voltage with voltage spikes (resonant ringing) after the transition. The voltage spikes are included in the calculation of the peak/peak voltage.

cially on the role of slew rate on PDIV and PD magnitude. The research agrees on the observation that shorter rise times of the voltage impulse increase the PD amplitude and thus its erosive effect on the insulation. According to [WCM14] this increase in magnitude is explained by the statistical time lag for the availability of a an avalanche-initiating electron: the shorter the rise time, the higher the average electric field in which the PD develops (also see Figure 3.18 in [Lin09]).

There is, on the other hand, no clear consensus on the impact of slew rate on the inception voltage (RPDIV). The authors in [OHM07] point out the heterogeneous character of the investigations as a possible cause for disagreement: “The variety of the results may be attributed to the difference in experimental conditions, such as the applied voltage waveform with or without overshoot, the different environmental condition (more or less controlled) and so on” (p. 1519). The authors of the recent study [LCC⁺18] also emphasize the possible dependence of the measured RPDIV on external factors such as sample conditioning during measurements, the differences in (twisted-pair) sample manufacturing and the system-dependent, often insufficiently specified waveform of the stressing voltage (e.g. voltage overshoot at the rising/falling edges of a square voltage).

2.3.2. Below Partial Discharge Inception

The impact of inverter-generated voltages on the endurance of insulation materials/systems and the identification of causes for premature failure below PD inception have not been studied as extensively as the PD regime. Most available studies observe a similar “aging acceleration” under high-frequency voltage stress (both for sinusoidal and impulse waveforms) in the absence of PD, although the impact on lifetime is typically much less drastic than in the PD regime. Figure 2.2 from publication [CMFT11] illustrates the observed drop in lifetime of enamelled wire insulation exposed to 50 Hz sinusoidal and 10 kHz rectangular voltages (same peak/peak value) for the PD and non-PD regime, respectively.

[FM01] investigated twisted pair specimens exposed to both sinusoidal and square wave voltages at low frequency (50 Hz) and high frequency (10 kHz). The specimens where either kept in air or immersed in silicone oil with the aim of singling out the impact of PD activity on aging acceleration. The authors conclude that the results “emphasize the effects of frequency increase on ageing acceleration of conventional insulation, both in the presence and in the absence of PD activity” (p. 30).

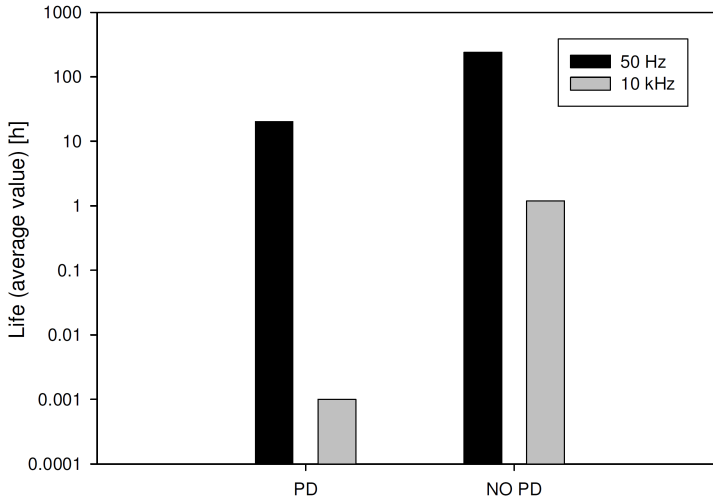


Figure 2.2.: Observed drop in lifetime of enamelled wire insulation between 50 Hz sinusoidal and 10 kHz rectangular voltages (same peak/peak value) for the PD and non-PD regime (from [CMFT11]).

[KCD⁺11] investigates the breakdown voltage of oil-impregnated Kraft paper samples exposed to square voltage waveforms of varying rise times (0.3 to 1 μ s) and fundamental frequencies (1 to 10 kHz). The peak voltage is slowly ramped up (1 kV min⁻¹) until breakdown occurs. The leading cause of failure is identified to be PD, but interestingly there are samples for which no PD inception could be measured, yet these samples did not show breakdown values which are statistically higher or lower than samples for which PD is measurably incepted. The paper concludes that “Overall, the correlation between PDIV and BDV indicates that, most probably, breakdown is due to partial discharge. The existence of missing PDIV values, however, may suggest that (a) in some cases PD are incepted, but below detection sensitivity, (b) breakdown is in some case associated with other mechanisms, likely thermal runaway” (p. 51).

The investigation [KHS98] compares the life curves between sinusoidal high voltages of different frequency (50 Hz and 50 kHz), both in the presence and absence of PD (in what they call “defective” and “healthy” samples). The sample is a dry-type layer construction consisting of plastic

foil and fleece layers, impregnated with and enclosed by an epoxy polymer. The healthy samples are measured to inception PD around a peak voltage of 20 kV, yet they already fail below 10 kV when stressed with 50 kHz. Under the 50 Hz stress, on the other hand, all samples fail exclusively above PD inception. The authors ascribe the premature failure under the 50 kHz voltage stress to dielectric heating: “Comparing the healthy samples at AC 50 Hz and 50 kHz their dielectric strength at 50 kHz is much lower. This can be explained with the dielectric losses in the insulating material which are 1000 times higher at the 50 kHz test voltage than at 50 Hz. This causes a heating of the material which leads to an earlier deterioration of the insulation” (p. 705).

The above-mentioned investigations on various insulation systems/materials show that premature failure under high-frequency sinusoidal and inverter-type waveforms are observed even in the absence of PD. The enhanced dielectric losses due to higher fundamental frequencies and the possible presence of harmonics is invoked in all discussions, and its possible role in causing (or contributing to) insulation failures below PD inception has been recognized early on [Yin97]. The review [SC14] on insulation issues in inverter-fed medium voltage motors lists the enhanced dielectric heating of the mainwall insulation as a possible cause for premature failure of the motor insulation due to accelerated thermal aging. Insulation temperature is indeed known as a key influencing variable in determining the rate at which aging processes within insulation materials occur.⁹ Moreover, the risk for thermal runaway ([O’D73] Chapter 6) increases.

An in-depth analysis of dielectric heating of dielectrics subject to waveforms with high harmonic content is presented in [SBBG09]. The authors note that “Dielectric heating is one potential aging mechanism active below partial discharge inception voltage in materials used as high voltage insulation. When exposed to voltage waveforms containing high amount of harmonics, the heat generation will be larger due to increased power losses as compared with power frequency excitation. This may result in a decreased life or even failure of insulation due to the increased operating temperature or to thermal runaway” (p. 926). They also point out the importance of considering the temperature dependence of a material’s dielectric loss factor when assessing the risk for excessive insulation temperature/thermal runaway. Indeed, the (di)electric properties of poly-

⁹See e.g. the “10 °C rule” and its subsequent ramifications. It states that the lifetime of an insulation system is halved for every increase in insulation temperature by a certain amount ΔT (e.g. 7 °C to 10 °C in the early investigation by Dakin on power transformers [Dak48]).

mers in particular are known to be strongly temperature dependent (see e.g. [MP09] Chapter 6).

The paper [NG14] proposes “an explanation for aging of insulating materials exposed to high frequency repetitive voltage pulses ... based on the thermal stimulating processes within dielectric material triggered by losses generated due to damped oscillation of dipoles within insulating material in high frequency electric fields” (p. 304). It must be inferred that the oil impregnation eliminates the presence of PD (not monitored) under the applied unipolar 3 kV rectangular impulse voltage. The authors investigate variations in the loss tangent of the samples before and after stressing and conclude that “specimens aged by application of repetitive high voltage pulses show the same behavior as those aged thermally” (p. 309). Unfortunately, no comparative data on samples aged under pure thermal stress is provided. Nonetheless, the results are interesting in that they show stronger changes (with respect to the virgin sample) in the loss tangent spectrum (most pronounced around 1 Hz) when stressing is done at shorter rise times and/or higher switching frequencies. Both conditions cause higher dielectric losses and thus higher insulation temperatures, which is compatible with the proposed degradation process of thermal aging.

The early paper [Yin97] points out that the resonance effects (overshoot ringing after switching transitions) contributes to enhanced dielectric heating, because the ringing adds a resonance peak to the spectrum of the ideal trapezoidal pulse train (see Figure 3.2) far above the fundamental frequency (see e.g. Figure 2.19 in [Lus18]). The author hypothesizes that the shorter lifetime observed at shorter rise times of the applied stressing voltage may be explained by the associated increase in dielectric losses.

The study [SvB92] is somewhat different in that it investigates the aging of (unfilled) epoxy insulation in an inhomogeneous needle-plane configuration (needle tip radius: 5 μm , gap distance: 100 μm , degree of inhomogeneity: 5%) under repetitive, unipolar voltage surges of 1 μs duration. The voltage peak value is varied from 7 to 13 kV, and the surge repetition frequency from 5 Hz to 5 kHz. Electroluminescence and PD were monitored by means of a PMT. Although the samples fail due to electrical tree growth (internal PD) in the final stage of breakdown, this phase is observed to last only a few tens of seconds (due to the small gap distance) and is thus negligible compared to the aging during the initiation stage, which occurs in the absence of PD. The authors conclude that “The results of the statistical aging experiment demonstrate with statistical significance that

epoxy does age under the influence of positive and negative voltage surges, even in the absence of partial discharges.” Moreover, they find the time to failure to decrease on the surge frequency and, interestingly, to depend on the polarity of the applied surges (in general shorter failure times with positive sphere potential). Concerning the aging mechanism, the authors thus consider the possible influence of space charge: “Although our understanding of how repetitive surges cause electrical aging is not complete, we believe that it does involve the injection of electrons into the epoxy, which form a negative space charge region” (p. 760). They expect an even faster aging under bipolar surges: “If electrons have been injected into the insulation by an initially negative surge, and the electrode voltage becomes positive due to oscillation, then the electric field near the electrode will be higher than would occur in the absence of a polarity reversal. This higher field is expected to increase the aging rate, resulting in more rapid failure” (p. 760).

The role of space charge¹⁰ in the failure of electrical insulation under inverter-type voltages is also investigated in [Fab03]. It is reported that under unipolar rectangular voltage (1 kV peak, 50 % duty cycle) space charge build-up is measurable, and its magnitude at a switching frequency of 0.1 Hz is roughly half the value measured for pure DC stress (i.e. showing the expected scaling with the average applied field). Interestingly the space charge magnitude drops to about a quarter of the DC value as the switching frequency is increased to 10 kHz, although the average electric field remains unchanged. The measured space charge magnitude under a bipolar rectangular voltage (1 kV peak, 50 % duty cycle) is observed to be strongly dependent on the switching frequency, and falls below the detection threshold of the system in the kHz range. Concerning the possible effects of the injected space charges on voltage endurance, the author mentions the effect of the distortion of the electrode field by the accumulated space charges, which is well-known to play a key role in DC insulation systems [HBFB03].

[GWHL07] uses TSC measurements and observes that more space charge is accumulated within the insulation bulk under a bipolar square voltage (3.5 kV peak/peak, 10 kHz, $U_{DC} = 0$) as compared to a sinusoidal voltage (4.24 kV peak/peak, 50 Hz, $U_{DC} = 0$), and the authors thus hypothesize that space charge may be responsible for the observed shortening of insulation lifetime under high-frequency impulse stress, even below

¹⁰Here the focus is on space charge within the insulator volume, i.e. not the deposited charge on the insulator surface by PD.

PD inception. No clear information is however provided on the actual mechanism by which space charge would promote insulation aging under these conditions.

The study [KJ17] compares insulation aging under bipolar ($U_{DC} = 0$) and unipolar rectangular voltage stress (300 Hz, 1.5 kV peak-peak) on oil-impregnated 127 μm thick Kraft paper by means of dielectric spectroscopy. There is no significant difference in the observed changes for the unipolar and bipolar waveform, which implies that either space charge did not evolve under the DC component of the unipolar waveform, or that it did not play a major role in the aging process quantified in this study.

The study [HAL⁺00] uses lifetime tests in combination with TSC and surface charge measurements on polymeric insulation foils to find that “At lower voltages, PD is unlikely to play a major role in the degradation of the insulation. Nevertheless, many specimens have failed even at voltages as low as 900 V peak to peak (450 V peak), which is lower than the [P]DIV. In this case, another process, referred to as intrinsic, could lead to the insulation failure. Charge injection, charge displacement and/or permanent dipole group motion could be responsible for intrinsic aging” (p. 786). The mechanism of this aging process due to space charge in the absence of PD is not specified further, except that “this charge injection can cause local electric field enhancement which could lead to a direct breakdown” (p. 788).

An interesting investigation on recessed PE specimens on the interaction between the space charge established under DC voltage stress and the subsequent interaction with a single superimposed voltage impulse (rise time: 1 μs , fall time: 8 ms) is presented in [BCV71]. It is observed that after a 4 min DC prestressing (at levels ranging up to 75 % of the DC breakdown voltage $U_{b,DC}$) does not appreciably alter the impulse breakdown strength when the impulse has the same polarity as the prestressing voltage (it is even slightly increased). When the impulse is of opposite polarity, however, the subsequent electric strength under the impulse voltage decreases approximately linearly with the applied level of the prestressing DC voltage, and is only about 20 % of its value without prestressing when the prestressing is done at $0.75 \cdot U_{b,DC}$. In addition it was observed that the electric strength recovered when the opposing voltage impulse was applied after the prestressing voltage had been removed for about 10 ms. In a very meticulous analysis, the authors substantiate their conclusion that “[t]he observed effects are attributed to space-charge injection from the electrodes” (p. 247).

In a much more recent study [CZLZ16] the role of space charge in the intrinsic electric breakdown of insulators under both DC and AC stress is reexamined by means of a bipolar charge injection/transport model. While space charge has long ago been recognized to play a critical role in DC insulation systems (see e.g. [HBFB03] and references therein), this paper suggests rather convincingly that the role of space charge in AC breakdown might have been underestimated. “We demonstrate the differences in charge accumulations under both dc and ac stresses and estimate the breakdown strength, which is modulated by the electric field distortion induced by space charge. It is concluded that dc breakdown initializes in the bulk whereas ac breakdown initializes in the vicinity of the sample-electrode interface. Compared with dc breakdown, the lower breakdown strength under ac stress and the decreasing breakdown strength with an increase in applied frequency, are both attributed to the electric field distortion induced by space charges located in the vicinity of the electrodes” (p. 1). These results are interesting in the context of the present investigation in that they predict a decrease of breakdown strength with increasing frequency (see Figure 2a in [CZLZ16]) in the intrinsic aging regime (i.e. in the absence of extrinsic aging due to PD).

2.3.3. Lifetime Testing of Insulation Exposed to Mixed-Frequency Voltages (DC+AC repetitive impulse)

Since a particular type of unipolar mixed voltage consisting of a DC offset with a superimposed repetitive rectangular impulse voltage will be the object of investigation in chapters 7.2, a selected review on lifetime testing under these voltages is provided here. The focus here is on *strictly* unipolar mixed voltages, that is, mixed voltages which are always strictly positive (or negative).¹¹ Not strictly unipolar rectangular voltages (i.e. DC-biased rectangular impulse voltage with the lower voltage being zero) are included in Sections 2.3.2 and 2.3.2.

The literature on lifetime testing under this type of voltage stress in the absence of repetitive PD is relatively scarce. The study [KHS98] (already discussed above) adds DC voltages up to 20 kV to a 50 kHz sinusoidal voltage. The samples are observed to break down (no PD) when the

¹¹The transition from one to the other type is of course gradual, and measured parameters (e.g. voltage endurance) are expected to behave continuously in these limits.

AC voltage is around 8 to 9 kV (RMS) irrespective of the value of the underlying DC voltage. This suggests that in the studied insulation system and for the investigated stress levels, the DC voltage plays a negligible role in insulation failure. In the investigated parameter range, no “synergistic” effect is observed, which would reduce the lifetime under AC stress when a DC stress is added.

This behavior can qualitatively be understood within an empirical theory about (short-term) breakdown under mixed voltages suggested in [GK86] [GF97]. It was developed in order to allow the determination of breakdown strengths of transformer insulation systems exposed to combined DC and sinusoidal AC 50 Hz voltages (see Figure 2.3) as a function of the breakdown voltages under pure DC stress ($U_{b,DC}$) and pure sinusoidal AC stress ($U_{b,AC}$, peak value) as well as the magnitude ratio of the applied DC and AC voltage components ($p = U_{AC}/U_{DC}$). It simply states that the breakdown voltage under a mixed voltage lies between the breakdown voltages measured for pure DC and pure AC voltage stress, and provides the appropriate weighing coefficients to match the empirically observed shape of the transition. Its validity has been verified for a number of insulation systems, including paper-oil and polypropylene film-oil systems, for 50 Hz sinusoidal AC voltages. The work was motivated by the need for quantitative data on the electrical strength of insulation exposed to this type of stress in HVDC converter station equipment.

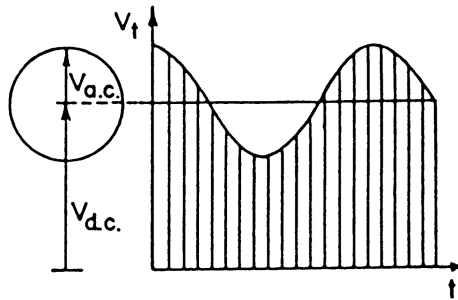


Figure 2.3.: Mixed voltages (DC + AC sinusoidal) investigated in [GK86] (Figure 2 in that publication).

The theory states that the breakdown strength (peak value) under a

combined voltage $U_{\text{DC}} + U_{\text{AC}}$ is given by

$$U_{\text{b,DC+AC}} = U_{\text{b,DC}} \frac{2}{\pi} \cot^{-1} \left(\frac{p}{\alpha} \right) + U_{\text{b,AC}} \frac{2}{\pi} \tan^{-1} \left(\frac{p}{\beta} \right), \quad (2.1)$$

where the parameters α and β are obtained from

$$\beta = \left(\frac{U_{\text{b,AC}}}{U_{\text{b,DC}}} \right)^2 \alpha^{-1} \quad (2.2)$$

$$\alpha = \tan \left(\frac{U_{\text{b,AC}}}{U_{\text{b,DC}}} \tan^{-1} [\beta^{-1}] \right). \quad (2.3)$$

By way of example, let us calculate the expected breakdown strength under a mixed voltage stress for the data provided in [KHS98]:¹²

$U_{\text{b,AC} 50\text{kHz}} = \sqrt{2} \cdot 9 \text{ kV} \approx 12.5 \text{ kV}$ and $U_{\text{b,DC}} = 90 \text{ kV}$.¹³ Then $\alpha = 0.21$ and $\beta = 0.09$. The associated breakdown voltages for a range of ratios $p = U_{\text{AC}}/U_{\text{DC}}$ are shown in Figure 2.4.

This graph first shows that the common-sense result that a voltage will always lead to breakdown irrespective of its composition if the applied peak voltage $\hat{U} = U_{\text{AC}} + U_{\text{DC}}$ is greater than $\max(U_{\text{b,DC}}, U_{\text{b,AC}})$, and that (short-term) breakdown will not occur if $\hat{U} < \min(U_{\text{b,DC}}, U_{\text{b,AC}})$. For voltages with $U_{\text{b,AC}} < \hat{U} < U_{\text{b,DC}}$ breakdown occurs only if the AC component exceeds the indicated threshold value (red broken line). For example, with an AC amplitude of 9 kV peak, a DC component of 46 kV needs to be added for sample breakdown to occur. Thus, according to this theory, only when the AC voltage is already set to $0.9 \cdot U_{\text{b,DC}} = 11.2 \text{ kV}$ would the available 20 kV DC source used in [KHS98] have been able to cause breakdown.

A few lifetime test results with strictly unipolar mixed voltages have been reported in more recent studies (e.g. [WLZ⁺12]), yet these use 50 Hz sinusoidal voltages for the AC component, a case which had already been covered in detail in the work [GK86] [GF97] discussed in the previous paragraph. Breakdown testing with strictly unipolar mixed voltages at higher frequencies (DC + 8 kHz sinusoid) is presented in [BL13]. The

¹²Although the empirical relationship (2.1) was derived with breakdown tests using 50 Hz voltage, there is no *a priori* theoretical reason invalidating its applicability at higher frequency.

¹³The short-time electric strength for 50 kHz is obtained by extrapolation of the life curve. The short-time electric strength under pure DC stress is measured by the authors and indicated to lie between 80 and 100 kV.

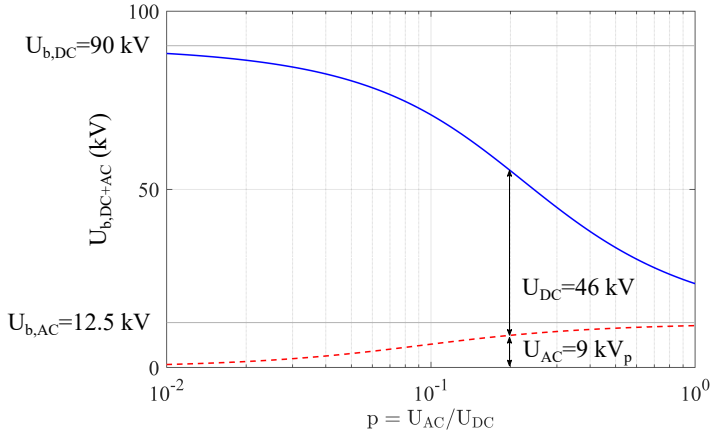


Figure 2.4.: Example of breakdown voltages (continuous line) for mixed voltages (DC+AC sinusoidal) for a range of magnitude ratios, calculated according to the theory of [GK86] [GF97].

experimental results are congruent with [KHS98], in that the value of the preset DC offset does not significantly affect the value of the AC voltage at which breakdown occurs. This investigation is moreover interesting because it investigates different polymeric materials and observes that breakdown under DC+HF AC electric stress leads to breakdown in polyvinyl chloride (PVC) but not in polypropylen (PP). PVC features significantly higher dielectric losses than PP [BL13]. This, together with the negligible influence of the DC component, is a strong indicator that in this case the samples failed due to a thermal runaway initiated by the dielectric losses associated with the MF AC component. In addition, the samples used in this study were relatively thick (0.5 mm), which increases the risk for thermal runaway (see Section 7.2).

2.3.4. Other Stress Factors Influencing Insulation Endurance

The above review is concerned with insulation aging and degradation specific to inverter-type waveforms (as well as high-frequency harmonic stress). It is understood that other stress factors that are not specific to the investigated stress profile (electrical and thermal) must be properly

addressed in the insulation design process. For example, mechanical stress can arise due to vibrations (e.g. from rotating parts), forces on conductors during fault currents, electrostriction/magnetostriction and differential thermal expansion. These can either mechanically degrade the insulation, or make it vulnerable to other means of attack, such as PD. Under a high temperature rise of the insulation system during operation, the different thermal expansion coefficients of the constituting materials may entail the loss of bonding between an insulator and its substrate (delamination) or the emergence of cracks in rigid and brittle parts. The created gas-filled voids then pave the way for partial discharge erosion.

Another important aspect of insulation aging in general are environmental influences, such as irradiation (e.g. by UV light) or the chemical interactions between absorbed gases and the polymer chains (e.g. catalyzed chain scission/depolymerization in the presence of oxygen [Fla18]). Unlike gas-insulated designs, solid insulation systems are typically “open”, in the sense that they are permeated by small molecules (e.g. molecular oxygen and water) from the surrounding atmosphere, and in turn expel low-molecular weight byproducts (e.g. of depolymerization reactions).

For a more detailed review of aging under general electrical, thermal, mechanical and environmental stresses (or a combination of these) the reader is referred to [IECc]. It is emphasized therein that multifactor aging (i.e. aging in the presence of more than one stressor) is the norm rather than the exception, and that (positive or negative) synergistic effects between aging processes are possible.

In the specific context of inverter-generated voltages it is interesting to note that electromechanical effects have been observed that are specifically related to insulation stressing with steep voltage wavefronts. [BCL99] report the removal of the thin metal coating (“demetallization”) used as electrodes on polymer films (PET, PEN) when the samples are exposed to repetitive rectangular impulse voltages. The effect is more pronounced at higher switching speeds ($> 1 \text{ kV}/\mu\text{s}$). The authors explain the phenomenon as a consequence of the electrostatic force between electrode charges and a subset of bound charges at the insulator-electrode interface: bound charges that are polarized in between switching transitions but depolarize on time scales that are long compared to the switching transition generate a transient homopolar (bound) space charge layer in front of the electrodes. The repulsive force between the homocharges and electrode charges is hypothesized to cause the observed demetallization. The authors support their theory by the observation that the phenomenon

is more pronounced with materials having a larger relaxation strength on the relevant time scales (e.g. no demetallization is observed with PE).

2.3.5. The Elektrokinetic Model of Dielectric Endurance

See [BB05] Chapter 6.6 for a more extensive summary.

This model was developed by T.J. Lewis and coworkers to describe the microphysical dynamics of dielectric aging in semi-crystalline polymers (e.g. PE or PET) [JLL05]. It bears resemblance to other models of dielectric aging that consider electro-mechanical stress and space charge as fundamental ingredients. See e.g. Zeller and Schneider's electrofracture mechanics [ZS84], Crine's Thermodynamic Model [CPL89] or the aging model by Dissado, Mazzanti and Montanari [DMM97]. All these theories incorporate elements of the early Griffith theory of crack propagation and brittle fracture [Gri21].

In a nutshell, the theory assumes that the (macroscopic) electro-mechanical force density¹⁴,

$$\mathbf{f} = \underbrace{\rho_f \mathbf{E}}_{\text{free charge}} + \underbrace{\frac{\varepsilon_0}{2} E^2 \nabla \varepsilon}_{\text{bound charge}} + \underbrace{\frac{\varepsilon_0}{2} \nabla \left(E^2 \frac{\partial \varepsilon}{\partial \rho_m} \rho_m \right)}_{\text{electrostriction}}, \quad (2.4)$$

plays a fundamental role in the long-term aging of dielectric, in that it induces microscopic morphological changes (opening of microvoids and crack propagation, see Figure 2.5) in the polymer that, thus paving the way for the ultimately fatal *electrical* degradation processes (such as internal PD) to set in. In this sense, the action of the electro-mechanical force is seen as an *initiator* of insulation failure, operating via a deterioration of its morphological structure (generation of low-density regions favoring charge multiplication processes).

In alternating electric fields, the microscopic deformation of the polymer structure (e.g. straining of polymer ties in the amorphous regions) will be modulated by the dynamics of the electrode field. The cyclic stress causes the polymer chains to occupy conformational states that are more varied relative to the quasi-equilibrium states occupied under a constant

¹⁴The electrostriction term depends on the variation of the dielectric permittivity magnitude ε with mass density ρ_m . See e.g. [Str41] (p. 137-151) for a detailed treatment of electro-mechanical forces in dielectrics.

stress. Furthermore, an additional dissipation of energy (proportional to the product of excitation frequency and the imaginary part of the elastic compliance [BB05] Equation (6.26)) facilitates molecular motion. [BB05] concludes that “We can thus appreciate that an alternating field will therefore accelerate the formation of voids in the amorphous region” (p. 208). Moreover, “the energy dissipation depends on the [fourth power of the electric field] and so will be particularly strong where the field is locally enhanced, e.g. at electrodes and where space charges are present” (p. 208).

For these reasons, the above-mentioned aging mechanism is susceptible to contribute to dielectric aging under the highly dynamic electric fields occurring under MF rectangular voltages, in particular in the presence of a space-charge-generating DC-bias field. This hypothesized degradation mechanism will be further discussed in the following section, and lays the foundation for the experimental study presented in Chapter 7.2.

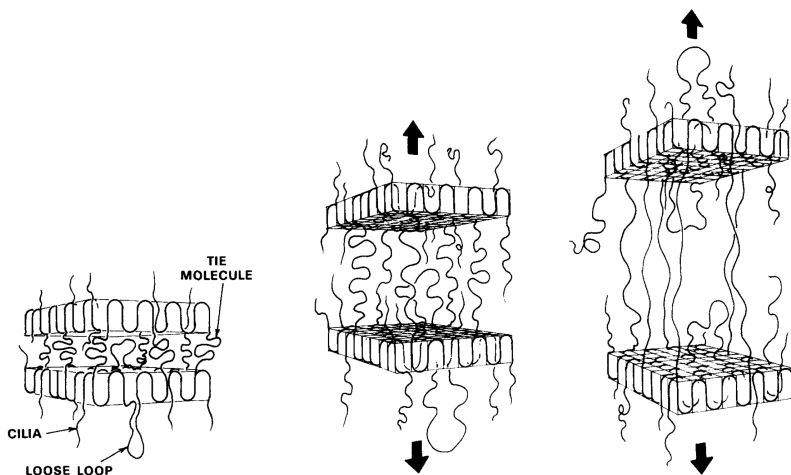


Figure 2.5.: Opening of microvoids in amorphous regions of a semicrystalline polymer by the action of electromechanical stress (illustration from [LM83]).

2.3.6. Literature Review: Synopsis I

Based on the analysis of the above-cited literature¹⁵, three risk factors are identified that are linked specifically to the risk of premature failure of insulation systems exposed to inverter-generated (medium) voltages:

- a. **Enhanced partial discharge (PD) intensity.** The number of PDs per unit time is proportional to the switching frequency. In addition, PD amplitudes are observed to increase with switching speed. Thus, if PD is incepted, the total PD charge is greatly enhanced when switching frequency and speed are increased.
- b. **Systemic overvoltages.** The broad spectral content of the terminal voltage can excite system resonances, generate standing wave phenomena on electrically long conductors (cable/load impedance mismatch), and lead to strongly nonlinear voltage drops along windings or field-grading layers due to parasitic capacitive couplings. As a result, the local electric field stress on certain parts of the insulation can be increased significantly.
- c. **Excessive insulation temperature.**¹⁶ An increased conversion power density at constant efficiency leads to a corresponding increase in power loss density¹⁷, and hence higher insulation temperatures. Moreover, increased capacitive currents at higher frequencies can lead to enhanced conduction losses, e.g. in semiconducting field-grading layers. An increased insulation temperature enhances thermally activated degradation processes (thermal aging) and – especially for organic materials – leads to compromised (di)electric properties. Moreover, the problem of stress cracking and delamination is accentuated when the operating temperature is increased. Moreover, due to the high fundamental frequencies and large harmonic content of inverter-generated waveforms, dielectric losses favor thermal runaway, especially in bulky insulation where the thermal resistance to the heat bath is more susceptible to exceed the tolerable threshold.

¹⁵The references to the statements given in this synopsis are found in Sections 2.3.1 to 2.3.4 and are not repeated here.

¹⁶What constitutes an “excessive temperature” is of course strongly material and/or system-dependent and quantified by, e.g., the thermal class of the insulation [IECc].

¹⁷Mainly winding and core losses, but dielectric losses can contribute a non-negligible share [GFR⁺19].

Type II [IECb] insulation systems can tolerate a certain degree of continuous PD during operation (e.g. the stator insulation in medium-voltage motors) by employing PD resistant inorganic materials such as mica at critical locations inside the insulation system. The literature offers a relatively complete picture of how the voltage waveform (including its fundamental frequency) impact the PD characteristics and hence the physico-chemical attack of the insulation materials by the PDs. However, some practically relevant points (such as the influence of voltage rise time on the PDIV) still lack a unanimous answer in the scientific literature.

The time delay in the provision of a start electron for initiating the partial discharge is on the same order of magnitude as the rise time of the voltage impulse. Consequently the electron avalanche develops in a higher average electric field when the impulse rise time is decreased (resulting in higher PD amplitudes). The dynamics of the deposition of surface space charge by a PD event (as well as its subsequent relaxation/recombination) affects the dynamics of the resultant electric field in the discharging air gap and thus is an important ingredient in many explanations concerning the behavior of PDs under inverter-type waveforms (as it is for other waveforms).

For **Type I** [IECa] electrical insulation systems (e.g. the winding insulation of a medium-voltage medium-frequency transformer) the inception of PD is typically an end of life criterion [IECa] and thus no PD is tolerated within these systems. Accelerated aging under inverter-type waveforms (as compared with 50 Hz sinusoidal waveforms) below PD inception is reported in the literature, although the life-shortening impact is not as pronounced as in the presence of PD.

Although the calculations may be computationally involved, there are numerical tools/procedures that allow the calculation of the local electrical field stress acting on the insulation (the stress distribution is generally strongly dependent on excitation waveform).

Increased dielectric losses and the associated increase in insulation temperature are often mentioned as a likely cause of premature insulation failure (thermal aging/thermal runaway) in the non-PD regime. The basic theory of dielectric loss calculations under inverter-type waveforms is well documented and the loss density can be calculated numerically if the dielectric spectra of the materials are available in the relevant frequency and temperature ranges.

The presence of injected space charge under inverter-type voltages has

been corroborated experimentally and is – as expected – found to be most pronounced for mixed voltages. Several investigators invoke the possible role of (volume) space charge in the accelerated aging in the presence of repetitive impulse voltage stress, but the specific aging mechanism by which this accelerated aging could occur is often left in the dark (except for the Poissonian distortion of the electrode field, which is however an effect not specific to (mixed) inverter-type voltage). Thus, at present, there is no clear answer to the question whether space charge is of concern when it occurs concurrently to a stressing by voltage waveforms featuring high slew rates.

Yet, besides the anecdotal evidence on space charge effects in insulation aging under repetitive impulse stressing reported above, there is a sound theoretical basis – the *electrokinetic model of dielectric endurance* outlined in 2.3.5 – to grant this topic special consideration in the context of inverter-generated mixed voltages.

Based on its described mechanism of action (opening of microvoids and crack initiation/propagation by electro-mechanical forces on space charge evolving in the dielectric volume), we hypothesize that this mode of dielectric aging – if active at all – should be particularly pronounced when, instead of a low-frequency AC voltage stress, a highly dynamic medium-frequency voltage with steep slew rates is applied, and a DC bias is present which promotes the creation of space charges. The proposed aging mechanism would then be the Coulombic interaction between the bulk space charges (both free and bound) with the highly dynamic electrode field, and the initiation of insulation aging by the associated force density (as described by the electrokinetic model). This hypothesis is one of the motivations for the experimental tests presented in Chapter 7.2. At present, there is no lifetime data available in the literature on strictly unipolar repetitive impulse voltages that could help decide whether or not such an effect should be added to the list of risk factors when dealing with mixed voltages:

- (d.) Coulombic interaction of (bulk) **space charge** with highly dynamic electrode fields?

2.4. Online Dielectric Spectroscopy under Inverter-Generated Medium-Voltage Waveforms

2.4.1. Dielectric Permittivity as an Insulation Aging Marker

The dielectric spectrum of a dielectric material – that is, the magnitude and phase of the complex dielectric permittivity as a function of frequency (and temperature) – provides a rich source of information about the dynamics of its constituent (bound and mobile) charge carriers [KS03] [MP09]. Thus, it is potentially susceptible to changes in the molecular structure of a dielectric, provided that these changes occur in a sizable fraction of the probed volume in order to make a measurable contribution to the (integral) electrode current.

As a consequence, dielectric spectroscopy has found widespread application as a valuable tool in non-destructive material characterization, ranging from the “observation” of chemical reactions (e.g. cure kinetics of epoxy polymers [DP11]), fundamental studies on structural (physical) aging in glassy polymers [OB11], the detection of cancerous/irradiated tissue in mammals [SKF⁺17] and, last but not least, the condition assessment of high-voltage insulation systems [Zae03b] [Zae03a].

A few literature studies are available that highlight the potential usefulness of assessing insulation aging in the specific context of inverter-type voltages by means of dielectric spectroscopy, in particular below PD inception where the powerful apparatus of PD diagnostics is not available.¹⁸ [NG14] observe changes in the dielectric spectrum ($\tan \delta$ at room temperature) of oil-impregnated Kraft paper samples after aging them under rectangular pulse voltage stress. They show that the waveform parameters (switching frequency, rise time) and the number of applied pulses influence the magnitude of the observed changes. A similar impact of inverter voltage rise time on the loss tangent of oil-impregnated Kraft paper is reported in [KKB⁺11]. The investigation [KJ17] studies the dielectric response (frequency range 1 mHz to 100 Hz, room temperature) of oil-insulated Kraft paper aged under rectangular voltage impulses. The spectra are recorded with a commercial DS system at five specific

¹⁸Of course PD diagnostics can still (and should) be used to confirm the absence of PD or determine inception levels.

times during the aging process. An increase of the imaginary part of the dielectric permittivity is reported with increasing aging time. These findings illustrate that the impact of various waveform parameters on the aging dynamics can in principle be differentiated and quantified by means of dielectric spectroscopy. It would thus be an interesting tool for complementing lifetime testing under these conditions, desirably in the form of an online dielectric spectrometer that records a full spectrum (fundamental frequency plus available/measurable harmonics) of the complex permittivity at regular intervals in time right up to sample breakdown.

2.4.2. Dielectric Permittivity: Nonlinearity

While the nonlinear dielectric response can constitute an interesting diagnostic tool in itself [WTE⁺01] or be used deliberately for electric field control [WCR⁺10], it represents a source of uncertainty in insulation design when values of low-voltage dielectric spectroscopy are used without further ado for operating field strengths which are typically higher by a factor of 1000 or more. Although it is generally accepted that the polarization response for typical solid insulation materials used in high voltage engineering (e.g. epoxy polymers and polyesters) is sufficiently linear under AC stress¹⁹ in the range of operating field strengths (< 20 kV/mm) [Pop15], it has been observed that nonlinear effects can be significant in certain composite systems. The early investigation [Rap72] reports a marked decrease of the $\tan \delta$ value of an oil-impregnated paper insulation (cable) at 50 Hz and 96 °C when a DC bias voltage is applied (see Figure 2.6). The proposed explanation assumes that the dielectric loss is – at least partially – due to mobile ionic charge carriers: “[t]he decrease in the loss tangent can be explained by immobilization of part of the free ions due to the dc component of the applied voltage and the localization of these ions on the interfacial surfaces” (p. 101).

It is interesting to see opposing effects of the AC and DC voltage component, and thus the strong dependence of $\tan \delta$ on the ratio $p^{-1} = U_{AC}/U_{DC}$. For example, for a given peak voltage of 25 kV the $\tan \delta$ value is about 1.8% for $p^{-1} = 0$ (pure AC voltage 18 kV RMS), while it equals about 0.8% when $p^{-1} = U_{AC}/U_{DC} = 1.3$ (8 kV RMS AC + 14 kV DC). Similarly strong effects are described in the recent study [SL19] on

¹⁹At 50 Hz and higher frequencies, where free space charge buildup is typically not yet a dominant contribution to the loss tangent.

non-impregnated Transformerboard.

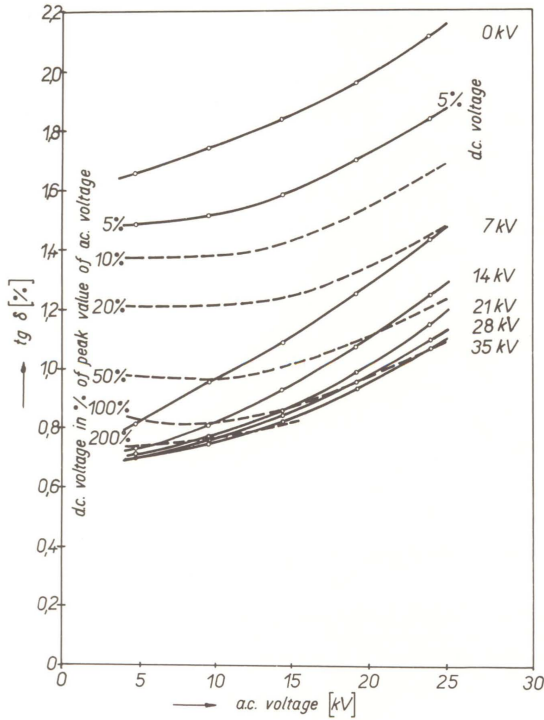


Figure 2.6.: Variation of the loss tangent $\tan \delta$ of an oil-insulated cable insulation for mixed voltages (50 Hz sinusoidal + DC). The RMS value of the AC component is given on the x-axis. From [Rap72].

Reference data on polymeric insulation materials for dry-type applications (epoxy polymers, silicone elastomers, polyester foils) could not be found in the available literature. This means that based on the current knowledge it is difficult to estimate the accuracy of, e.g., dielectric loss calculations for high-amplitude/mixed voltages. This is unsatisfying because an accurate thermal design is crucial especially for voltages containing significant medium-frequency components (see Section 2.3.6).

2.4.3. Dielectric Spectroscopy Measurement Systems Operating under Inverter-Generated Voltages

The use of non-harmonic excitations for dielectric response analysis is not new. For example, broadband voltage step excitations are typically used in the lower (< 1 MHz) and upper (> 100 MHz) range of the excitation frequencies covered by dielectric spectroscopy [KS03]. The measured time-domain data (phase-resolved voltage and current measurement) is converted into frequency-domain parameters (e.g. the complex dielectric permittivity) by means of simple approximations²⁰ or with numerical Fourier analysis. With the advent of ever more powerful analog-to-digital converters and numerical processing units, the direct digitization of the excitation voltage and the dielectric response current through the sample, with a subsequent Fourier correlation analysis ([KS03], Chapter 2.2.1) has become widely established. This also relaxed the requirements on the excitation waveform, since the analysis no longer assumed a sinusoidal input (creating a sinusoidal output in a linear system). Instead, each frequency present in the excitation frequency is correlated one by one with the corresponding response current at this same frequency.

Researchers have used this measurement/data processing principle as a flexible tool for dielectric material characterization (e.g. [HB05] [SBBG09] [PCC15]). The study [SBBG08] on “Arbitrary Waveform Impedance Spectroscopy (AWIS)” is particularly interesting in that it demonstrates the possibility to use semi-square wave excitations, which in principle opens the door for a simultaneous monitoring of the dielectric properties under inverter-type voltage stresses. For time-to-failure testing, however, the measurement setup must be able to withstand sample breakdowns on a regular basis, which is not easily achieved with the used shunt configuration for the sample current measurement – especially when the voltage is further increased above the 200 V peak level used in this study. Furthermore, the system requires “[e]xtensive circuit modeling and calibrations ... in order to perform accurate measurements” [SBBG08] (p. 920). This sacrifices some of the advantages of the system’s flexibility and modularity, since any change of hardware requires another round of circuit modelling and calibration. Moreover, the presented system is susceptible to systematic errors due to aliasing, which requires a trade-off between the number of measurable harmonics in the test waveform and the acceptable aliasing error [SBBG11]. Anti-aliasing filters are not easily incorporated into the system because it “introduces a frequency-dependent behavior,

²⁰E.g. the *Hamon approximation*, see [Kao04] Chapter 2.7.1.

which can be difficult to model and affects measurement results at higher frequencies.” [SBBG11] (p. 3880). This requires to limit the spectral content (i.e. the rise time) of the applied impulses to levels that would no longer be representative of the stresses occurring in actual applications. All these issues are addressed within Chapter 8 of this thesis.

The experience and findings published in the papers [HB05] [SBBG08] [SBBG09] [SBBG11] have been a very valuable resource for the development of the dielectric spectrometer for pulse-width-modulated medium voltages presented in this thesis (see Chapter 8). In this sense, the presented work on this topic can be seen as a continuation of this line of research.

2.4.4. Literature Review: Synopsis II

The research reviewed in Section 2.4.1 demonstrates that the complex dielectric permittivity $\underline{\varepsilon}$ (or any of its alternative representations $f(\underline{\varepsilon})$ ²¹) is a promising aging marker for quantifying the impact of various parameters of inverter-type medium voltages on the pre-breakdown dynamics occurring in the stressed insulation volume. The available investigations focus on insulation materials for oil-impregnated insulation systems. If these measurements would be combined with time-to-failure testing, it may become possible to establish a quantitative aging criterion which allows to assess a material’s resilience to inverter-type voltages by simply observing the change of $f(\underline{\varepsilon})$ when it is exposed to a certain inverter voltage.

In order to have an online dielectric spectrometer reliably working under medium-voltage inverter-type waveforms, several challenges must be overcome:

- Immunity to (regular) sample breakdown.
- Minimizing noise (EMI) and aliasing without modifying the excitation waveform.
- If possible, remove the need for extensive circuit modelling and calibration.
- Accurate digitization of the sample current, which features a high crest factor²² especially at high switching speeds.

²¹E.g. $f(\underline{\varepsilon}) = \underline{\varepsilon}^{-1}$ yields the electric modulus [TO14] and so on.

²²Ratio of the peak value to the RMS value of a signal.

Moreover, a software tool for a systematic assessment of the accuracy and precision of the impedance measurement as a function of the excitation waveform, noise, the vertical/horizontal resolution of the DAC, sampling frequency etc. would be desirable in order to optimize the acquisition system for a specific application.

Last but not least, it was shown that there is a certain degree of uncertainty associated with the variation of dielectric parameters when values from low-voltage measurements are used (and/or if a significant DC bias is present). An online dielectric spectrometer would allow to measure the relevant dielectric parameters directly under the respective use conditions and could thus put the low-voltage approach to dielectric loss calculation on a more solid foundation. This would be desirable since low-voltage setups are more easily available and feature a bigger frequency range and higher measurement accuracy/precision.

3. Theoretical Background

“And thus the principle became established, that facts have to be accepted, irrespective of the human desire to make nature conform to preconceived rationalizations.”

Arthur von Hippel
in *Molecular Science and Molecular Engineering* (1959)

This chapter describes a number of basic concepts that will be used in later parts of the thesis. It covers textbook knowledge and is intended to establish a coherent notation and serve as a compilation of short introductions (with references for further reading) to selected topics.

3.1. Mathematical Tools

3.1.1. Fourier Transform

Given a function $f : \mathbb{R} \rightarrow \mathbb{C}$, the *Fourier transform* is defined as (if it exists)

$$\mathcal{F}[f](\omega) \equiv \tilde{f}(\omega) \equiv \frac{1}{2\pi} \int_{-\infty}^{+\infty} f(t)e^{-j\omega t} dt \quad (3.1)$$

The original function can be recovered via

$$f(t) = \int_{-\infty}^{+\infty} \tilde{f}(\omega)e^{j\omega t} d\omega \quad (3.2)$$

\tilde{f} is in general complex-valued even if f is not.

The *convolution* of f with g is given

$$(f * g)(t) \equiv \int_{-\infty}^{+\infty} f(\tau)g(t - \tau) d\tau = (g * f)(t). \quad (3.3)$$

Direct calculation leads to the *convolution theorem*:

$$\mathcal{F}[f * g](\omega) = 2\pi \tilde{f}(\omega) \tilde{g}(\omega). \quad (3.4)$$

Often *real-valued* harmonic fields are manipulated in terms of their *complex representation*, bearing in mind that only operations are used that commute with the operator Re (returning the real part of a complex number). For the field $f(t) = f_0 \cos(\omega t + \delta)$, with $f_0 \in \mathbb{R}$, the complex representation $f_c(t) = \underline{f} e^{j\omega t}$ is used, with $\underline{f} = f_0 e^{j\delta}$ and $f(t) = \text{Re}[f_c(t)]$. Similarly, for arbitrary real-valued functions $f : \mathbb{R} \rightarrow \mathbb{R}$ (whose Fourier transform exists) one can write

$$f(t) = \text{Re}[f_c(t)] \quad \text{with} \quad f_c(t) = \int_0^\infty \underline{f}(\omega) e^{j\omega t} d\omega, \quad (3.5)$$

where

$$\underline{f}(\omega) = 2\tilde{f}(\omega) \quad \omega \geq 0. \quad (3.6)$$

The complex representation of arbitrary real-valued functions by means of the continuous set of complex amplitudes $\{\underline{f}(\omega) | \omega \in [0, \infty)\}$ will be referred to as the *complex Fourier representation*.

3.1.2. Fourier series

Let $f(t) : \mathbb{R} \rightarrow \mathbb{C}$ be a periodic function, $f(t+T) = f(t)$ for all $t \in \mathbb{R}$. Its Fourier series reads (if it exists)

$$f(t) = \sum_{n=-\infty}^{\infty} \tilde{f}_n e^{j\omega_n t} \quad \text{with} \quad \omega_n = n \frac{2\pi}{T}, \quad (3.7)$$

and

$$\tilde{f}_n = \frac{1}{T} \int_{-T/2}^{T/2} f(t) e^{-j\omega_n t} dt. \quad (3.8)$$

The domain of integration can be shifted arbitrarily due to the periodicity of the integrand.

Real-valued functions $f(t) \in \mathbb{R}$ whose Fourier transform exists can be represented as a positive-frequency Fourier series:

$$f(t) = \operatorname{Re} \left[\sum_{n=0}^{\infty} \underline{f}_n e^{j\omega_n t} \right] \quad (3.9)$$

with

$$\underline{f}_0 = \tilde{f}_0 = \frac{1}{T} \int_{-T/2}^{T/2} f(t) dt \in \mathbb{R} \quad (3.10)$$

$$\underline{f}_n = 2\tilde{f}_n = \frac{2}{T} \int_{-T/2}^{T/2} f(t) e^{-j\omega_n t} dt, \quad n > 0. \quad (3.11)$$

Using the notation

$$\underline{f}_n = \hat{f}_n e^{j\delta_n} = f'_n - j f''_n \quad (3.12)$$

the familiar harmonic expansions of real functions are obtained:

$$f(t) = f'_0 + \sum_{n=1}^{\infty} [f'_n \cos(\omega_n t) + f''_n \sin(\omega_n t)] = f'_0 + \sum_{n=1}^{\infty} \hat{f}_n \cos(\omega_n t + \delta_n). \quad (3.13)$$

The RMS value of the signal can be calculated by summation of the squared Fourier amplitudes:

$$f_{\text{eff}} \equiv \sqrt{\frac{1}{T} \int_0^T f(t)^2 dt} = \sqrt{\sum_{n=0}^{\infty} f_{\text{eff},n}^2} \quad (3.14)$$

where

$$f_{\text{eff},n} \equiv \sqrt{\frac{1}{T} \int_0^T \left(\operatorname{Re} \left[\underline{f}_n e^{j\omega_n t} \right] \right)^2 dt} = \begin{cases} f'_0 & \text{if } n = 0 \\ \frac{|f_n|}{\sqrt{2}} & \text{if } n > 0 \end{cases} \quad (3.15)$$

is the effective value of the n^{th} harmonic.

3.1.3. Fourier sum

Measured data exists invariably as a *finite* set $\{f_m \in \mathbb{R} | m = 0, 1, \dots, N - 1\}$ of real numbers. Let us assume that they represent samples of the physical quantity $f(t)$ at times

$$t_m = m\Delta t \quad , m = 0, 1, \dots, N - 1 \quad (3.16)$$

such that

$$f_m = f(t_m). \quad (3.17)$$

The signal values can be written as a superposition of a *finite* number of harmonically oscillating Fourier components:

$$f_m = \sum_{n=0}^{N-1} \tilde{f}_n e^{j\omega_n t_m} \quad (3.18)$$

where

$$\omega_n = n \frac{2\pi}{T} \quad (n = 0, 1, \dots, N - 1). \quad (3.19)$$

The Fourier amplitudes are obtained by¹

$$\tilde{f}_n = \frac{1}{N} \sum_{m=0}^{N-1} f_m e^{-j\omega_n t_m}. \quad (3.20)$$

Note that $\tilde{f}_n e^{j\omega_n t_m}$ is invariant under the transformation $n \rightarrow n + k \cdot N$ for all $k \in \mathbb{N}$. This means that the chosen set of frequencies ω_n with $n = 0, 1, \dots, N - 1$ is not the only possible choice. Any frequency component can be replaced by one of its infinitely many equivalents. This observation is closely related to the problem of *aliasing*, where a signal Fourier component beyond the bandwidth of the measuring system is erroneously identified as belonging to the highest equivalent frequency within the sampling system bandwidth.

¹Referenced to the notation used here, the function `fft` in MATLAB[®] returns $\tilde{f}_n^{\text{ML}} = N \cdot \tilde{f}_n$.

If $f_m \in \mathbb{R}$ for all $m = 0, 1, \dots, N - 1$ then

$$\tilde{f}_n^* = f_{-n} = f_{N-n} \quad (n = 0, 1, \dots, N - 1). \quad (3.21)$$

Define

$$M \equiv \begin{cases} \frac{N}{2} & \text{if } N \text{ even} \\ \frac{N-1}{2} & \text{if } N \text{ odd} \end{cases} \quad (3.22)$$

The complex Fourier representation is obtained by defining²

$$\underline{f}_0 \equiv \tilde{f}_0 \in \mathbb{R} \quad (\text{“DC component”}) \quad (3.23)$$

$$\underline{f}_n \equiv 2\tilde{f}_n \quad , n = 1, 2, \dots, M(-1) \quad (3.24)$$

$$(\underline{f}_M \equiv \tilde{f}_M \in \mathbb{R}). \quad (3.25)$$

Thus:

Fourier representation of digitized signals

$$f_m = \operatorname{Re} \left[\sum_{n=0}^M \underline{f}_n e^{j\omega_n t_m} \right]. \quad (3.26)$$

The highest frequency needed for representing a real signal consisting of N values sampled on an equidistant mesh of step size $\Delta t = T/N$ is seen to be equal to half the sampling frequency:

$$f_{\max} = \frac{\omega_{\max}}{2\pi} = (2\Delta t)^{-1} = \frac{f_s}{2}. \quad (3.27)$$

It is also known as the Nyquist frequency (after the electronic engineer Harry Nyquist, 1889-1976) associated with the employed sampling rate. Frequency components of the original signal that lie above f_{\max} are *aliased* into the range $[0, f_{\text{ind}}]$.

Writing out the real/complex parts,

$$\underline{f}_n = \hat{f}_n e^{j\delta_n} = f'_n - j f''_n, \quad (3.28)$$

²Contributions written in parentheses are to be ignored if N is odd.

leads to the sine/cosine representation:

$$f_m = f'_0 + \sum_{n=1}^M [f'_n \cos(\omega_n t_m) + f''_n \sin(\omega_n t_m)] \quad (3.29)$$

$$= f'_0 + \sum_{n=1}^M \hat{f}_n \cos(\omega_n t_m + \delta_n). \quad (3.30)$$

$$(3.31)$$

The Fourier series and the Fourier transform pairs can be derived from the discrete Fourier sum pair by first taking the limit $N \rightarrow \infty$ at finite T and then letting $T \rightarrow \infty$.

3.1.4. Spectrum of a Trapezoidal Pulse Train

Consider the mixed-frequency voltage shown in Figure 3.1. Direct calculation of Equations (3.10) and (3.11) leads to the Fourier representation

$$u(t) = \operatorname{Re} \left[\sum_{n=0}^{\infty} \underline{U}_n e^{j\omega_n t} \right] \quad (3.32)$$

with

$$\underline{U}_0 = U_{\text{DC}} \quad (3.33)$$

$$\underline{U}_n = 2U_p \frac{\tau}{T} \operatorname{sinc} \left(\frac{\omega_n \tau_r}{2} \right) \operatorname{sinc} \left(\frac{\omega_n T}{2} \right) \quad \text{for } n \geq 1. \quad (3.34)$$

$D = \frac{\tau}{T}$ is called the *duty cycle* of the pulse train. The envelope of the spectrum is obtained by observing that

$$|\operatorname{sinc}(x)| \leq \begin{cases} 1 & \text{for } x \lesssim 1 \\ \frac{1}{|x|} & \text{for } x \gtrsim 1 \end{cases} \quad (3.35)$$

Hence the transition frequencies related to pulse duration and rise time are given by

$$f_D = \frac{1}{\pi\tau} \quad (3.36)$$

$$f_r = \frac{1}{\pi\tau_r} \quad (3.37)$$

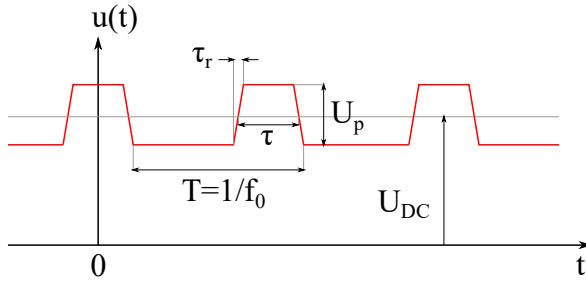


Figure 3.1.: Mixed-frequency voltage consisting of a DC-biased trapezoidal pulse train.

Typically, $\tau_r \ll \tau$ and thus $f_r \gg f_D$. Note that the constant plateau $f < f_D$ (see Figure 3.2) only exists for $n \lesssim T/(\pi\tau)$, i.e. for low duty cycle pulse trains. Between f_D and f_r the Fourier amplitudes decrease as f_n^{-1} , while above f_r the amplitude decay is proportional to f_n^{-2} . This means that on a plot of $\log(\underline{U}_n/\underline{U}_1)$ vs $\log(f_n/f_1) = \log(n)$ the envelope is displayed as straight lines of slopes 0, -1 and -2 , respectively.

Summary

The Fourier magnitudes $|\underline{U}_n|$ of a trapezoidal pulse train are proportional to...

$$\begin{aligned} n^0 & \quad \text{for } n \lesssim (\pi D)^{-1} \\ n^{-1} & \quad \text{for } (\pi D)^{-1} \lesssim n \lesssim T/(\pi\tau_r) \\ n^{-2} & \quad \text{for } n \gtrsim T/(\pi\tau_r) \end{aligned}$$

where $D = \tau/T$ is the duty cycle of the pulse and τ_r its rise and fall time.

Figure 3.2 shows the magnitude spectrum and the discussed envelope of an exemplary pulse train.

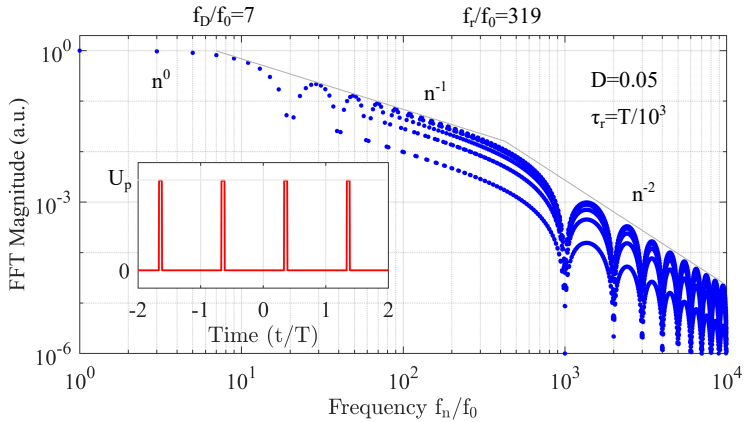


Figure 3.2.: Fourier magnitudes of a pulse train having duty cycle $D = 0.05$ and a rise time $\tau_r = T/10^3$. The cutoff frequencies are given by Equations (3.36) and (3.37).

3.2. Dielectric Polarization

Dielectric materials are by definition *polarizable* by an external electric field, that is, electric dipoles are induced by a separation of mutually neutralizing opposite charges, or preexisting permanent dipoles are (at least partially) oriented in the direction of the external field. As such, *all* matter composed of atoms is dielectric, albeit to varying degrees.³ Showing how a material's dielectric response can be characterized mathematically is the main aim of the present section. Particular emphasis is put on the frequency-domain description of linear materials, and their relation to the corresponding time-domain quantities.

If a piece of material consisting exclusively of uncharged and non-polarizable building blocks⁴ was inserted into an external electric field (i.e. one generated by charges not belonging to the block of matter), the material would not respond to and interact with the external electric field.

Typical insulation materials, however, do not behave this way because they consist of protons (charge $+e$), electrons (charge $-e$) and neutrons (zero charge), aggregated and interacting according to the laws of quantum physics. Thus, the *microscopic* charge density ρ_μ is a strongly fluctuating function of both the space and time variables, even if the *macroscopic* charge density (obtained by averaging the microscopic charge density over a “small” volume $V(\mathbf{r})$),

$$\rho(t, \mathbf{r}) = \frac{1}{V(\mathbf{r})} \int_{V(\mathbf{r})} \rho_\mu(t, \mathbf{r}') d^3 \mathbf{r}', \quad (3.38)$$

is different from zero. The physical parameters in macroscopic electromagnetism are always spatio-temporal averages on the corresponding microscopic entities. The molecular degrees of freedom are hidden within macroscopic parameters such as the dielectric permittivity. For more details on this point see [Rob73].

³And it may be overshadowed by other processes. In metals for example, the rapid rearrangement of electrons prevents the occurrence of an electric field in the material's volume under static conditions. The theory of dielectrics is thus typically concerned with dielectric *insulators*, for which the electrical conductivity is smaller than, say, $\kappa \approx 10^{-10} \text{ S m}^{-1}$. Such materials have charge relaxation time constants (see Section 3.2.4) of the order of $\tau \approx \varepsilon_0/\kappa$ ranging from seconds to dozens of hours or more (as compared to sub-femtosecond relaxation in good conductors such as metals).

⁴What constitutes a “building block” of matter depends on the involved energies; an N_2 molecule may be regarded as an irreducible unit in one case but not another.

When inserted into an external electric field, the field exerts forces on the oppositely charged atomic constituents. At this point it is the structure of matter and the corresponding equations of motion (drift, diffusion, dissociation, ionization, recombination etc.) for the constituent particles (electrons, ions, atoms, molecules) that decide how the material reacts to the external field. In general, a separation of charges (which previously neutralized each other in a macroscopic sense) ensues, producing a corresponding nonzero macroscopic space charge density. Additionally, charge carriers may *drift* in the direction of the electric field and lead to the build-up of so-called free space charge in the dielectric volume.⁵ The electric field created by this space charge (bound and free) is the most prominent macroscopic manifestation of the induced polarization of matter.

Origin of polarization: matter is composed of charged building blocks which mutually balance themselves to yield a vanishing macroscopic space charge density. In an external electric field, charge separation takes place, and non-vanishing space charge and corresponding electric fields are induced.

It can be shown (see [CL63] chapters 3.2 and 3.3) that the electric field due to bound (ρ_b) and free (ρ_f) charge densities reads

$$\mathbf{E}(t, \mathbf{r}) = \frac{1}{4\pi\epsilon_0} \int \frac{\rho_f(t, \mathbf{r}') + \rho_b(t, \mathbf{r}')}{|\mathbf{r} - \mathbf{r}'|^2} \mathbf{e}_r d^3\mathbf{r}', \quad (3.39)$$

with

$$\rho_b(t, \mathbf{r}) = -\nabla \cdot \mathbf{P}(t, \mathbf{r}) \quad (3.40)$$

$$\rho_f(t, \mathbf{r}) = \rho(t, \mathbf{r}) - \rho_b(t, \mathbf{r}) \quad (3.41)$$

$$(3.42)$$

⁵If electrodes contact the dielectric, charge carriers can also be injected into it /extracted from it.

where

$$\mathbf{P}(t, \mathbf{r}) = \frac{1}{V(\mathbf{r})} \int_{V(\mathbf{r})} \mathbf{r}' \rho(t, \mathbf{r}') d^3 \mathbf{r}' = \sum_i N_i \langle \boldsymbol{\mu}_i \rangle. \quad (3.43)$$

is the macroscopic *polarization density*,⁶ and ρ is the total space charge density (bound and free). The distinction between free and bound charge may seem somewhat vague on closer inspection – because it is. The defining characteristic of “free” is the lack of an energetically paired, neutralizing counter-charge within atomic length scales, which *can*⁷ lead to a non-zero value of $\rho_f(t, \mathbf{r})$. Since all pairings have a dissociation energy, the distinction of charge carriers into “free” and “bound” is not immutable: bound charge pairs can be freed under the impact of sufficiently energetic particle bombardment, and free charge carriers may pair up (recombine) to form bound charges. Considering a charge as free or bound is a *choice one has to make* when modelling a system. When this choice is not “good enough”, problems will arise because too many free charges are modelled as bound (i.e. within the dielectric permittivity framework) and vice versa.

The resulting electric field in the presence of a dielectric material is the linear superposition of the fields generated by the electrode charges and the induced (bound and free) charge densities in the dielectric.

From Equation (3.40) it follows that the bound space charge density is zero inside a piece-wise homogeneous dielectric, and that the bound space

⁶The coordinate origin is taken to be the geometric center of the averaging volume. Note that the integral formulation with the volume average may produce ambiguous results in some cases, e.g. when using a cube aligned with the axes of symmetry in a cubic crystal (the polarization density becomes dependent on the exact location of the volume boundaries). These “problems” are rather artificial and can be eliminated by using non-uniform averaging (e.g. Gaussian). The undesired contribution of free charge in the integral formulation of the polarization density is more problematic (this occurs if the free space charge density is not uniform inside $V(\mathbf{r})$). Overall it seems better to stick with the definition of polarization density in terms of the number densities N_i and average dipole moments $\langle \boldsymbol{\mu}_i \rangle$ of all types of *microscopic* dipoles present in the investigated dielectric. All charges that are not paired up in this process are – by definition – treated as free.

⁷It is perfectly possible that $\rho_f = 0$ in the presence of free charge, e.g. when free charge carriers have equal number densities but opposite charge.

charge is located in layers of atomic/molecular dimensions at the interfaces between the homogeneous parts or close to the electrode surfaces. The net bound surface charge density is given by

$$\sigma_b = \mathbf{P}_1 \cdot \mathbf{n}_1 + \mathbf{P}_2 \cdot \mathbf{n}_2 \quad (3.44)$$

where \mathbf{n}_i is the unit outward normal vector at the surface of dielectric i ($\mathbf{n}_1 = -\mathbf{n}_2$).

Finally, the total electric field is obtained by superimposing the electrode field onto the “response”-field calculated in Equation (3.39) (formally, this corresponds to the inclusion of the electrode charges in the free charge density ρ_f).

3.2.1. Dielectric Susceptibility

One might say that “the dielectric susceptibility is the proportionality factor between the polarization density and the electric field.” While this is not wrong, there is certainly more to it. Calculating the resulting electric field in the presence of a dielectric material is a conundrum: the induced charge density at a specific point inside the dielectric is dependent on the external field (the electrode charges) *and* the field generated by all other induced charges inside the dielectric. A way out of this complex many-body problem is the use of an approximating mean-field approach.

The *polarizability* α of a polarizable microscopic entity (atom, molecule) relates the induced electric dipole $\boldsymbol{\mu}$ to the *local* electric field \mathbf{E}_{loc} ,

$$\boldsymbol{\mu} = \alpha \mathbf{E}_{\text{loc}}. \quad (3.45)$$

In anisotropic media the polarizability is a tensor. Moreover, all dielectrics are nonlinear to *some* degree, i.e. the simple linear relationship becomes inaccurate above a certain magnitude of the electric field. For so-called linear materials (most of the materials used in electrical insulation systems), this threshold value is higher than the material’s dielectric strength.

The local electric field \mathbf{E}_{loc} is the field acting upon the considered dipole. It is different from the total electrical field at the location of the dipole because the induced dipole itself will add a non-negligible contribution to the total electric field. The latter, however, must be excluded in the calculation of the dipole’s response in order to avoid that the field generated by the dipole is allowed to act on the dipole itself. The local field \mathbf{E}_{loc} is bigger than the resulting field \mathbf{E} , because the dipole field *opposes*

the external field. Various models have been suggested to calculate the local field. They all relate the microscopic quantity $\boldsymbol{\mu}$ to the macroscopic polarization density in the form

$$\boldsymbol{\mu} = \alpha \mathbf{E}_{\text{loc}} = \alpha \left(\mathbf{E} + \gamma \frac{\mathbf{P}}{\varepsilon_0} \right), \quad (3.46)$$

where γ is on the order of unity and known as the *depolarization factor* [Coe79]. The simplest model (due to Lorentz [Lor52]) considers the polarizable entity to be placed at the center of a small spherical cavity inside an otherwise homogeneous dielectric (without interaction between the induced dipole and the dielectric). The electric field inside the cavity generated by the surrounding bound charges is given by $\mathbf{P}/3\varepsilon_0$ and thus $\gamma = 1/3$. More complicated models include the interaction between the cavity dipole and the surrounding continuum [Ons36] as well as correlation between neighboring dipoles [Kir39] [Fro49]. As long as one is only interested in macroscopic quantities (e.g. the electric susceptibility introduced below), the actual value of depolarization factor and its possible dependence on molecular quantities is not important.

The circular conundrum mentioned at the beginning of this section can now be solved by using Equation (3.46) in a self-consistent way. The polarization density is the average dipole moment per unit volume. Thus it can be written as

$$\mathbf{P} = N \boldsymbol{\mu} = N \alpha \left(\mathbf{E} + \gamma \frac{\mathbf{P}}{\varepsilon_0} \right), \quad (3.47)$$

where N is the number of polarizable entities per unit volume. In general, there is more than one type of polarizable entities, in which case $N\alpha$ is replaced with $\sum_i N_i \alpha_i$.

From Equation (3.47) a relation between the polarization density \mathbf{P} and the *total* electric field \mathbf{E} is obtained:

$$\mathbf{P} = \frac{N\alpha}{1 - N\alpha\gamma/\varepsilon_0} \mathbf{E} = \varepsilon_0 \chi_e \mathbf{E} \quad (3.48)$$

where the (static) *electric susceptibility* χ_e has been introduced.

Until now the dynamical aspect of the interaction between the external electrical field and the response of induced or permanent dipoles has not

been considered. The simple static relation 3.48 remains valid for the steady-state under quasi-electrostatic *harmonic* excitations (because of the assumed linear response in Equation (3.45)),

$$\underline{\mathbf{P}}(\omega, \mathbf{r}) = \varepsilon_0 \underline{\chi}_e(\omega, \mathbf{r}) \underline{\mathbf{E}}(\omega, \mathbf{r}), \quad (3.49)$$

where the *complex electric susceptibility*

$$\underline{\chi}_e(\omega, \mathbf{r}) = \chi'_e(\omega, \mathbf{r}) - j\chi''_e(\omega, \mathbf{r}) \quad (3.50)$$

accounts for both the response *magnitude* and the *delay* (phase lag) of the induced bound-charge dipoles. The static susceptibility is obtained in the limit $\chi_e(\mathbf{r}) = \lim_{\omega \rightarrow 0} \underline{\chi}_e(\omega, \mathbf{r})$.

The proper time-domain relation is consequently given by the convolution

$$\mathbf{P}(t, \mathbf{r}) = \varepsilon_0 (f * \mathbf{E})(t, \mathbf{r}) = \varepsilon_0 \int_0^t f(\tau, \mathbf{r}) \mathbf{E}(t - \tau, \mathbf{r}) d\tau, \quad (3.51)$$

where the dielectric *response function* f is linked to the real / imaginary part of the electric susceptibility:

$$f(t, \mathbf{r}) = \frac{2}{\pi} \int_0^\infty \chi'_e(\omega, \mathbf{r}) \cos(\omega t) d\omega = \frac{2}{\pi} \int_0^\infty \chi''_e(\omega, \mathbf{r}) \sin(\omega t) d\omega. \quad (3.52)$$

$\chi'_e(\omega)$ and $\chi''_e(\omega)$ are not independent, because $f(t)$ is subject to a number of restrictions based on physical grounds. The polarization density is a real-valued vector field, hence $f \in \mathbb{R}$ requires $\chi_e(\omega)^* = \chi_e(-\omega)$. In particular,

$$\chi''_e(0) = 0 \quad (3.53)$$

$$\chi'_e(0) = \int_0^\infty f(t) dt. \quad (3.54)$$

Furthermore, “the system cannot squeal before it is hurt” [BH83] (causality), which requires $f(t) = 0$ for $t < 0$. This translates into an interdependence of the real and imaginary part of the electric susceptibility, as expressed by the *Kramers-Kronig relations*.

Kramers-Kronig relations

$$\chi_e'(\omega) = \frac{2}{\pi} \mathcal{P} \int_0^\infty \frac{s \chi_e''(s)}{s^2 - \omega^2} ds \quad (3.55)$$

$$\chi_e''(\omega) = -\frac{2\omega}{\pi} \mathcal{P} \int_0^\infty \frac{\chi_e'(s)}{s^2 - \omega^2} ds \quad (3.56)$$

\mathcal{P} denotes the Cauchy principal value of the integral (taking care of the singularity in the integrand at $s = \omega$). See e.g. [BH83] Chapter 2.3.2 for a derivation of these relations.

For “flat” curves of $\varepsilon''(\omega)$ the following approximation to the Kramers-Kronig version can be derived:⁸

$$\chi_e'(\omega) \approx \chi_e'(\infty) + \frac{2}{\pi} \int_{\ln(\omega)}^\infty \chi_e''(\omega) d \ln(\omega). \quad (3.57)$$

Its local version reads⁹

$$\chi_e''(\omega) \approx -\frac{\pi}{2} \frac{\partial \chi_e'(\omega)}{\partial \ln(\omega)}. \quad (3.58)$$

A finite polarizability is seen to be inextricably linked to dielectric losses: the dipoles which contribute a loss-free polarization current at a certain frequency ω will fail to follow the external field at *some* frequency $\omega_0 > \omega$, and hence generate dielectric losses in this frequency range.

Since $\int_0^\infty f(t) dt = \chi_e'(0)$ is finite, the response function decays to zero as $t \rightarrow \infty$. It proves useful to quantify this decay by a time constant τ_e ,

⁸See Equation (9.45) and its derivation in [BB78]. The invoked approximations also quantify the meaning of “flat curves of $\varepsilon''(\omega)$ ”. An example of use of this approximation will be given in Chapter 5.3.

⁹In this expression, the real and imaginary part of the dielectric susceptibility χ_e can be replaced by the real and imaginary part of the dielectric permittivity $\underline{\varepsilon} = \underline{1} + \underline{\chi}_e$ (introduced below).

implicitly defined by

$$\frac{\int_{\tau_\epsilon}^{\infty} f(t)dt}{\int_0^{\infty} f(t)dt} \stackrel{!}{=} \epsilon, \quad (3.59)$$

where $0 < \epsilon < 1$ is a chosen threshold value (“the fraction of the response which happens after τ_ϵ ”). Consider e.g. the polarization response to an electric field \mathbf{E}_0 switched on at $t = 0$:

$$\mathbf{P}(t) = \epsilon_0 \mathbf{E}_0 \int_0^t f(\tau) d\tau. \quad (3.60)$$

The relaxation to the external constraint \mathbf{E}_0 has reached $1 - \epsilon$ of its equilibrium value after τ_ϵ :

$$\mathbf{P}(\tau_\epsilon) = \epsilon_0 \mathbf{E}_0 \int_0^{\tau_\epsilon} f(\tau) d\tau \quad (3.61)$$

$$= \epsilon_0 \mathbf{E}_0 (1 - \epsilon) \int_0^{\infty} f(\tau) d\tau \quad (3.62)$$

$$= (1 - \epsilon) \mathbf{P}(\infty). \quad (3.63)$$

The prototypical dielectric response function emerged from studies of P. Debye (1884-1966) on the rotational diffusion dynamics of polar molecules subject to an external electric field (see [EG99] Chapter 1.4). It reads¹⁰

$$f(t) = \frac{\chi'_e(0)}{\tau} e^{-\frac{t}{\tau}} \quad (3.64)$$

where $\tau = \tau_{1/e}$ is the *relaxation time*. The Debye polarization response to a step excitation, $E(t) = E_0 \theta(t)$, is given by

$$\mathbf{P}(t) = \epsilon_0 \chi'_e(0) \mathbf{E}_0 [1 - e^{-\frac{t}{\tau}}]. \quad (3.65)$$

The associated complex dielectric susceptibility is calculated to be

$$\underline{\chi}_e(\omega) = \frac{\chi'_e(0)}{1 + j\omega\tau} \quad (\text{Debye relaxation}). \quad (3.66)$$

¹⁰Debye related the parameters τ and $\chi'_e(0)$ to the dipole moment of the molecules, the temperature and the rotational friction coefficient.

If the frequency range is restricted to an interval $[\omega_1, \omega_2]$ wherein other relaxation processes are negligibly dispersive (i.e. their associated dipoles follow the external field with negligible delay, or cannot follow at all), one can write

$$\underline{\chi}_e(\omega) = \chi_e(\omega_2) + \frac{\chi_e(\omega_1) - \chi_e(\omega_2)}{1 + j\omega\tau}, \quad (3.67)$$

where $\chi_e(\omega_1)$ and $\chi_e(\omega_2)$ are the fully *relaxed* and *unrelaxed* susceptibilities, respectively, of the considered relaxation, whereas $\Delta\chi_e = \chi_e(\omega_2) - \chi_e(\omega_1)$ is known as the associated *relaxation strength*. Oftentimes this formula is seen in the contracted notation

$$\chi_e(\omega) = \chi_\infty + \frac{\chi_s - \chi_\infty}{1 + j\omega\tau} = \chi_\infty + \frac{\Delta\chi_e}{1 + j\omega\tau}, \quad (3.68)$$

for which it should be remembered that the subscript “infinity” refers to a finite frequency, and that the “static” value χ_s may not correspond to the actual static value $\chi'_e(0)$.

3.2.2. Charge Transport in Dielectric Solids

The total charge current density in a non-magnetic material consists of the vacuum *displacement current* \mathbf{J}_d , the *conduction current* \mathbf{J}_c and the *polarization current* \mathbf{J}_p :

$$\mathbf{J}_{\text{tot}}(t, \mathbf{r}) = \mathbf{J}_d(t, \mathbf{r}) + \mathbf{J}_c(t, \mathbf{r}) + \mathbf{J}_p(t, \mathbf{r}). \quad (3.69)$$

with

$$\mathbf{J}_d(t, \mathbf{r}) = \varepsilon_0 \dot{\mathbf{E}}(t, \mathbf{r}) \quad (\text{displacement current}) \quad (3.70)$$

$$\mathbf{J}_c(t, \mathbf{r}) = \kappa \mathbf{E}(t, \mathbf{r}) \quad (\text{conduction current}) \quad (3.71)$$

$$\mathbf{J}_p(t, \mathbf{r}) = \dot{\mathbf{P}}(t, \mathbf{r}) \quad (\text{polarization current}) \quad (3.72)$$

Only \mathbf{J}_c and \mathbf{J}_p are associated with the passage of charge carriers (free and bound, respectively) at the considered point in space. Modelling the transport of free charge in insulators is very challenging, predominantly due to the lack of long-range symmetry in most (especially polymeric)

insulation materials, which is used extensively in the study of metals and semiconductors. The *electrical conductivity*

$$\kappa = \sum_i q_i n_i \mu_i \quad (3.73)$$

is parametrized in terms of the charge carrier number densities n_i , their electrical charge q_i and their mobilities μ_i (the index i denotes the various types of carriers, e.g. electrons and different types of ions). Charge carriers can be both *intrinsic* (i.e. originating from within the insulator)¹¹ or *extrinsic* (i.e. injected into the insulator)¹² [Coe79]. The behavior of the charge carriers at the electrode-insulator interface (e.g. neutralization rates of ions, field-assisted injection/extraction of electrons) with the associated build-up of space charges inside the dielectric often dominates the measured current-voltage relationship (see e.g. SCLC model, [Coe79] Chapter 10), and thus care should be taken when interpreting the *system response* in terms of *material parameters* (e.g. determining the electrical conductivity from integral current measurements). A practical example of this situation arises in the interpretation of the response of the silicone rubber material studied in Chapter 6.3.

Most organic insulation materials (e.g. polymers) are *molecular solids* with very limited long-range order [HS16]. Various low-molecular weight constituents are typically present within the *free volume* [Art96] of the polymer, such as chemical additives (e.g. antioxidants), polymerization catalysts, degradation and dissociation products of the polymer itself, “impurity” molecules, absorbed gases (e.g. water) etc. These diffuse and (if charged) drift through the macro-molecular matrix under the influence of an external electric field, thus contributing to the measured conductivity (see [BB05] Chapter 8). This mode of transport is greatly enhanced above the glass transition temperature of the polymer because of the onset of segmental motion of the polymer chains.

While a certain degree of disorder can be accommodated in the band theory of the electronic states in crystals (resulting in *localized electronic states* near the band edges [MD79]), the consideration of polymeric insulators as wide-band-gap semiconducting crystals has certainly its practical limitations.¹³ A prominent mode of charge transport in polymeric insulators is phonon-assisted (i.e. thermally activated) hopping over (ions)

¹¹Their generation can be assisted by external energy input from the applied electric field or electromagnetic and particulate radiation.

¹²A typical example is the field-controlled injection/extraction of electrons at the insulator-electrode interface.

¹³In contrast to the abundance of band-theory related terminology (“conduction band”,

/ tunnelling through (electrons) potential barriers between (spatially) localized states [HS16]. The external electric field acts as a bias on the potential barriers, favoring charge transport in the direction of the field. The relative contribution of electronic vs. ionic transport is certainly strongly dependent on the material structure and purity as well as the electrical field strength, and it often proves difficult to separate the two experimentally. Studying the temperature, voltage (and time) dependence of the measured current often gives valuable information in this respect (see e.g. Table 1 in [CNP⁺12]).

In the quasi-electrostatic regime, the electric field in the presence of dielectric matter is determined by Gauss' law (+ boundary conditions):

$$\nabla \cdot \mathbf{E}(t, \mathbf{r}) = \frac{\rho(t, \mathbf{r})}{\varepsilon_0}, \quad (3.74)$$

where ρ is the *total* charge density. As described in Section 3.2.1, the dielectric material reacts to an external field by the orientation or induction of *local* dipoles (the associated space charge ρ_b being called *bound*) and the migration of charge carriers over distances that are large compared to the inter-atomic distance (the associated space charge ρ_f being called *free*).¹⁴

The bound space charge can be related to the electric field by using Equations (3.40) and (3.49):¹⁵

$$\nabla \cdot \varepsilon_0 \underline{\mathbf{E}}(\omega, \mathbf{r}) = \rho_f(\omega, \mathbf{r}) + \rho_b(\omega, \mathbf{r}) \quad (3.75)$$

$$= \rho_f(\omega, \mathbf{r}) - \nabla \cdot \underline{\mathbf{P}}(\omega, \mathbf{r}) \quad (3.76)$$

$$= \rho_f(\omega, \mathbf{r}) - \nabla \cdot (\varepsilon_0 \underline{\chi}_e(\omega, \mathbf{r}) \underline{\mathbf{E}}(\omega, \mathbf{r})). \quad (3.77)$$

from which it follows that

$$\nabla \cdot [\varepsilon_0 (1 + \underline{\chi}_e(\omega, \mathbf{r})) \underline{\mathbf{E}}(\omega, \mathbf{r})] = \rho_f(\omega, \mathbf{r}). \quad (3.78)$$

¹⁴“hole”) in literature discussing charge transport in insulating polymers.

¹⁴It is theoretically possible (though not typical) that ρ_f stays zero throughout the dielectric material because free charges can – as opposed to bound charges – leave and enter the material via the electrodes.

¹⁵The frequency-domain representation is used because it is simpler than the time-domain representation containing the convolution integral.

The electric field is thus determined by the free charges and the *dielectric permittivity* of the material:

$$\underline{\varepsilon}(\omega, \mathbf{r}) = 1 + \underline{\chi}_e(\omega, \mathbf{r}) = \varepsilon'(\omega, \mathbf{r}) - j\varepsilon''(\omega, \mathbf{r}). \quad (3.79)$$

Apparently, the *displacement field*

$$\underline{\mathbf{D}}(\omega, \mathbf{r}) = \varepsilon_0 \underline{\mathbf{E}}(\omega, \mathbf{r}) + \underline{\mathbf{P}}(\omega, \mathbf{r}) = \varepsilon_0 \underline{\varepsilon}(\omega, \mathbf{r}) \underline{\mathbf{E}}(\omega, \mathbf{r}) \quad (3.80)$$

is the field whose sources are the *free* charges only:

$$\nabla \cdot [\varepsilon_0 \underline{\varepsilon}(\omega, \mathbf{r}) \underline{\mathbf{E}}(\omega, \mathbf{r})] = \nabla \cdot \underline{\mathbf{D}}(\omega, \mathbf{r}) = \underline{\rho}_f(\omega, \mathbf{r}). \quad (3.81)$$

The total current (Equation (3.69)) can thus simply be written as

$$\underline{\mathbf{J}}_{\text{tot}}(\omega, \mathbf{r}) = j\omega \underline{\mathbf{D}}(\omega, \mathbf{r}) + \kappa \underline{\mathbf{E}}(\omega, \mathbf{r}) \quad (3.82)$$

$$= j\omega \varepsilon_0 \left[\underline{\varepsilon}(\omega, \mathbf{r}) - j \frac{\kappa}{\varepsilon_0 \omega} \right] \underline{\mathbf{E}}(\omega, \mathbf{r}), \quad (3.83)$$

where the quantity in square brackets is called the *effective* dielectric permittivity. This is the quantity determined in dielectric spectroscopy, because the measured response current includes contributions from both bound (polarization current) and free (conduction current) charges.

3.2.3. Capacitive Currents in the Presence of Dynamic Bound Space Charge in the Dielectric Volume

This section determines the influence of bound charge dynamics on the electrode charging currents in an arbitrary conductor arrangement as shown in Figure 3.3. A vanishing free charge density is assumed here (a generalization including free charge dynamics is given in Section 5.1). The following development is based on the derivation of the capacitance matrix given in [HM89] (pp. 147-149). A minor generalization is added by introducing the bound charge dynamics with the definition of an *effective dielectric permittivity matrix*.

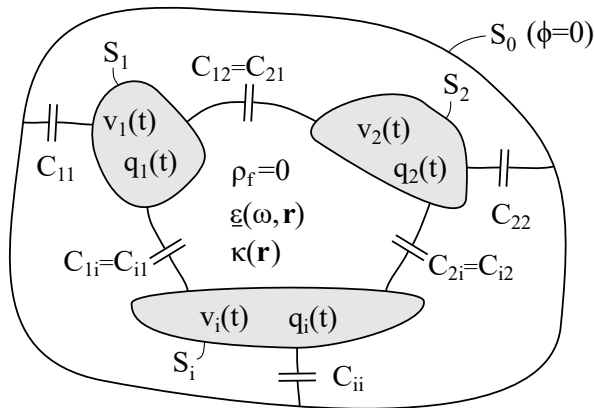


Figure 3.3.: N electrodes are excited with voltages $v_i(t)$, $i = 1, \dots, N$, in the presence of dynamic bound charge in the dielectric volume (described by the complex permittivity $\underline{\epsilon}(\omega, \mathbf{r})$). What are the associated free charge supply currents $i_i(t) = \dot{q}_i(t)$ to the electrodes?

The electrode potentials $v_i(t)$, $i = 1, \dots, N$, are assumed to be given and referenced to the surface S_0 . The voltage spectra $|\underline{v}_i(\omega)|$ are assumed to be limited to frequencies $\omega \ll L/c$, where L is the largest dimension of the region of interest and c is the speed of light in the dielectric. The electric field is then quasi-electrostatic and can be described as the gradient of a potential function:

$$\mathbf{E}(t, \mathbf{r}) = -\nabla\phi(t, \mathbf{r}). \quad (3.84)$$

Let u_i be the solutions of the Laplace equation

$$\nabla^2 u_i(\mathbf{r}) = 0 \quad (3.85)$$

with the boundary conditions

$$u_i(S_j) = \delta_{ij} \quad \text{for } i, j = 1, \dots, N, \quad (3.86)$$

where δ_{ij} is equal to one if $i = j$ and equal to zero otherwise. Note that the scalar functions u_i are only dependent on the *geometry* of the electrode configuration. By linearity of the Laplace equation, it follows that

$$\phi(t, \mathbf{r}) = \sum_{i=1}^N v_i(t) u_i(\mathbf{r}) \quad (3.87)$$

satisfies the Laplace equation with the boundary conditions

$$\phi(t, S_i) = v_i(t) \quad \text{for } i = 1, \dots, N. \quad (3.88)$$

The net charge on electrode i is thus given by

$$\begin{aligned} q_i(\omega) &= \oint_{S_i} \varepsilon_0 \underline{\varepsilon}(\omega, \mathbf{r}) \underline{\mathbf{E}}(\omega, \mathbf{r}) \cdot d\mathbf{S} \\ &= \sum_{j=1}^N v_j(\omega) \oint_{S_i} -\varepsilon_0 \underline{\varepsilon}(\omega, \mathbf{r}) \nabla u_j(\mathbf{r}) \cdot d\mathbf{S} \\ &= \sum_{j=1}^N \underline{\varepsilon}_{ij}(\omega, \mathbf{r}) C_{ij} v_j(\omega), \end{aligned} \quad (3.89)$$

where

$$C_{ij} = - \oint_{S_i} \varepsilon_0 \nabla u_j(\mathbf{r}) \cdot d\mathbf{S} \quad (3.90)$$

is the standard definition of the (vacuum) *capacitance coefficients* C_{ij} (see [HM89] p. 149) and

$$\underline{\varepsilon}_{ij} = \frac{\oint_{S_i} \underline{\varepsilon}(\omega, \mathbf{r}) \nabla u_j(\mathbf{r}) \cdot d\mathbf{S}}{\oint_{S_i} \nabla u_j(\mathbf{r}) \cdot d\mathbf{S}} \quad (3.91)$$

are the *dielectric permittivity coefficients*.

In the following it is assumed that the dielectric permittivity is not dependent on the space variable (thus $\underline{\varepsilon}_{ij} \equiv \underline{\varepsilon}$), and that the material possesses a spatially homogeneous conductivity κ .¹⁶ The supply current to electrode i is then given by

$$\underline{i}_i(\omega) = j\omega \underline{q}_i(\omega) + \oint_{S_i} \kappa \underline{E}(\omega, \mathbf{r}) \cdot d\mathbf{S}, \quad (3.92)$$

which can be written as

$$\underline{i}_i(\omega) = j\omega \underbrace{\left[\underline{\varepsilon}(\omega) + \frac{\kappa}{\varepsilon_0 j\omega} \right]}_{\underline{\varepsilon}_{\text{eff}}(\omega)} \sum_{j=1}^N C_{ij} \underline{v}_j(\omega) \quad (3.93)$$

$$= j\omega \underline{\varepsilon}_{\text{eff}}(\omega) \sum_{j=1}^N C_{ij} \underline{v}_j(\omega). \quad (3.94)$$

The *effective* dielectric permittivity $\underline{\varepsilon}_{\text{eff}}(\omega) = \varepsilon'_{\text{eff}}(\omega) - j\varepsilon''_{\text{eff}}(\omega)$ has been introduced [Jon83]:

$$\varepsilon'_{\text{eff}}(\omega) = \varepsilon'(\omega) \quad (3.95)$$

$$\varepsilon''_{\text{eff}}(\omega) = \varepsilon''(\omega) + \frac{\kappa}{\varepsilon_0 \omega}. \quad (3.96)$$

In the following, consider two electrodes ($N = 2$) with $\underline{v}_1(\omega) = \underline{u}(\omega)/2$ and $\underline{v}_2(\omega) = -\underline{u}(\omega)/2$. The *vacuum* or *geometric* capacitance between the two electrodes is given by¹⁷

$$C_0 \equiv -C_{12} = -C_{21} > 0. \quad (3.97)$$

The electrodes are assumed to be more strongly coupled to each other than to the environment, i.e. $C_{11} \ll C_0$ and $C_{22} \ll C_0$. The charging

¹⁶This eliminates the formation of a non-zero free space charge density. The most general condition for avoiding the formation of free space charge is that $\frac{\underline{\varepsilon}(\omega, \mathbf{r})}{\kappa(\mathbf{r})}$ be independent of \mathbf{r} .

¹⁷The off-axis elements of the capacitance matrix are symmetric and negative: $C_{ij} = C_{ji} < 0$ for $i \neq j$. See [HM89] pp. 147.

currents $\underline{i}(\omega) = \underline{i}_1(\omega) = -\underline{i}_2(\omega)$ of the electrodes are then related to the potential difference $\underline{u}(\omega)$ between the electrodes by¹⁸

$$\underline{i}(\omega) = j\omega \underline{\varepsilon}_{\text{eff}}(\omega) C_0 \underline{u}(\omega). \quad (3.98)$$

This means that under harmonic voltage excitation $u_0 \cos(\omega t)$ (hence $\underline{u}(\omega) = u_0 \in \mathbb{R}$), the corresponding current response will also be harmonic, but affected by a phase shift with respect to the driving voltage (also see Figure 3.4):

$$i_{\sim}(t) = C_0 \sqrt{\underline{\varepsilon}'_{\text{eff}}(\omega)^2 + \underline{\varepsilon}''_{\text{eff}}(\omega)^2} u_0 \cos(\omega t + \pi/2 - \delta(\omega)) \quad (3.99)$$

with

$$\delta(\omega) = \tan^{-1} \left[\frac{\underline{\varepsilon}''_{\text{eff}}(\omega)}{\underline{\varepsilon}'_{\text{eff}}(\omega)} \right] = \tan^{-1} \left[\frac{\underline{\varepsilon}''(\omega)}{\underline{\varepsilon}'(\omega)} + \frac{\kappa}{\underline{\varepsilon}'(\omega)\omega} \right]. \quad (3.100)$$

The charging current of the vacuum capacitance leads the voltage by $\pi/2$. All electrical energy that flows into the vacuum capacitance during the charging half-cycle will leave it again during the discharging half-cycle – there is no loss of electrical energy. The effect of a lossy polarizable material ($\varepsilon''(\omega) > 0$) between the plates is the occurrence of a current component *in phase* with the applied voltage (the same holds true for the DC conductivity). As will be discussed more closely in Section 3.2.5, more electrical energy then flows into the capacitor than out of it during one period of oscillation – electrical energy is dissipated as heat. This is why δ is known as the *loss angle*.

From the expression of the effective dielectric permittivity, it follows that the contribution of the DC conductivity to the imaginary part becomes

¹⁸Note that $i_1(t) = -i_2(t)$ does not hold when asymmetric free charge injection/extraction takes place. This is however excluded here because it is assumed that there is no free space charge dynamics inside the dielectric.

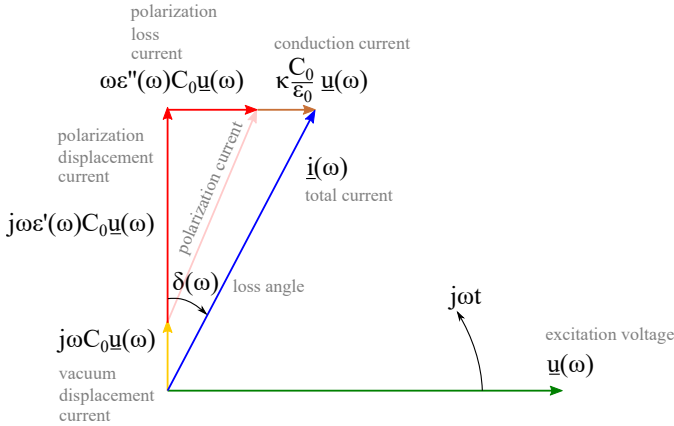


Figure 3.4.: Phasor diagram for a lossy dielectric of complex permittivity $\underline{\epsilon}(\omega) = \underline{\epsilon}'(\omega) - j\underline{\epsilon}''(\omega)$ and electric conductivity κ inside a capacitor of geometric (vacuum) capacitance C_0 excited by a harmonic voltage $\underline{u}(\omega)$.

dominant for $\omega < \frac{\kappa}{\epsilon_0 \underline{\epsilon}''(\omega)}$. A ω^{-1} dispersion in $\underline{\epsilon}''(\omega)$ while $\underline{\epsilon}'(\omega) = \text{const}$ as $\omega \rightarrow 0$ is a clear indication that the current response is dominated by DC conduction mechanisms [Jon83]. More often, however, the real part is not constant at low frequencies, but increases due to the build-up of macroscopic free charge dipoles as $\omega \rightarrow 0$ (see example of strong low-frequency dispersion due to space charge in Chapter 6.3).

In addition to harmonic excitations, it is instructive to calculate the current response to a voltage step $u_{\mathcal{F}}(t) = u_0 \theta(t)$. By using 3.51 and 3.70 to 3.72 it follows that

$$i_{\mathcal{F}}(t) = C_0 u_0 \left[\frac{\kappa}{\epsilon_0} \theta(t) + \delta(t) + f(t) \right] \quad (\text{“polarization current”}). \quad (3.101)$$

This is why step excitations are useful: they directly give access to the dielectric response function $f(t)$ via a measurement of the current response. There is however a caveat: the response function only includes the dynamics of *bound* space charge. Yet, in most practical situations, *free* space charge will evolve inside the dielectric under a step voltage stress, which is not taken into account in Equation (3.101). It is not surprising then that the charging current and the discharging current,

$$i_{\perp}(t) = -C_0 u_0 [\delta(t) + f(t)] \quad (\text{“depolarization current”}), \quad (3.102)$$

are rarely measured to obey the predicted relationship

$$i_{\perp}(t) + i_{\perp}(t) = C_0 u_0 \frac{\kappa}{\varepsilon_0}. \quad (3.103)$$

“It is a measure of nonlinearity of most dielectric systems that this expression is hardly ever satisfied and instead the difference between the charging and discharging currents depends on time and may even become negative” [Jon83] (p. 269).

This observation suggests that the use of (low-frequency) non-linear dielectric spectroscopy for studying the space charge dynamics in insulators might prove useful. And indeed, there has been some research activity in this direction (see e.g. [Alm15]).

3.2.4. Relaxation of free space charge in conducting dielectric solids

In a solid with DC conductivity κ and a dielectric response function $f(t)$ the continuity equation for free charge reads¹⁹

$$\nabla \cdot \mathbf{J}_f(t) = \nabla \cdot [\kappa \mathbf{E}(t)] = \mathbf{E}(t) \cdot \nabla \kappa + \kappa \nabla \cdot \mathbf{E}(t) = -\frac{\partial \rho_f(t)}{\partial t}. \quad (3.104)$$

Free space charge and electric field are related by

$$\rho_f(t) = \nabla \cdot [\varepsilon_0 \mathbf{E}(t) + \mathbf{P}(t)] = \varepsilon_0 \nabla \cdot \mathbf{E}(t) + \varepsilon_0 \nabla \cdot \left(\int_0^\infty f(\tau) \mathbf{E}(t - \tau) d\tau \right). \quad (3.105)$$

For position-independent material parameters, free space charge dynamics is thus governed by

$$\rho_f(t) = -\frac{\varepsilon_0}{\kappa} \left[\dot{\rho}_f(t) + \int_0^\infty f(\tau) \dot{\rho}_f(t - \tau) d\tau \right]. \quad (3.106)$$

An approximate solution can be obtained when free charge relaxation is slow as compared to bound charge (polarization) relaxation (then $\dot{\rho}_f(t - \tau)$

¹⁹Space coordinates are implicit.

is almost constant where $f(\tau)$ is significantly non-zero over the domain of integration):²⁰

$$\rho_f(t) \approx -\frac{\varepsilon_0[1 + \chi'_e(0)]}{\kappa} \dot{\rho}_f(t), \quad (3.107)$$

which is solved by

$$\rho_f(t) = \rho_f(0)e^{-t/\tau_D} \quad \text{with} \quad \tau_D = \frac{\varepsilon_0\varepsilon'(0)}{\kappa}. \quad (3.108)$$

τ_D is the *free space charge relaxation time*. Quantitatively, neglecting the *dynamics* of polarization is justified when the time scale of free charge dynamics, τ_D , is much greater than the time scale of dielectric relaxation (which is typically the case in insulators due to the low values of the conductivity κ).

The physical picture behind the decay: like charges repel and spread inside the host material, hence their density at any point inside the considered *homogeneous* domain decreases according to the above dynamics. The relaxation time is proportional to $\varepsilon'(0)$ because the free charges are *screened* by the bound charges and the repulsion force between free charges is lowered by the factor $\varepsilon'(0)$.²¹ The relaxation time is inversely proportional to the conductivity κ , because the drift velocity of the charges is proportional to the conductivity.²²

Where do the free charges go? In an infinite medium their mutual distance would increase forever. In real systems material boundaries are present which, at least partially, block the diffusing charges and lead to the formation of layers of free charge at these boundaries.

²⁰ $\int_0^\infty f(\tau)d\tau = \chi'_e(0)$ is used. See Equation (3.54).

²¹ This follows from $\nabla \cdot \mathbf{E} = \frac{\rho_f}{\varepsilon_0\varepsilon'(0)}$.

²² When considering a single carrier type of constant carrier density.

3.2.5. Average Dielectric Losses Under Mixed-Frequency Excitation

Consider two electrodes of mutual vacuum capacitance C_0 ,²³ embedded in a dielectric material of effective dielectric permittivity $\underline{\varepsilon}_{\text{eff}}(\omega)$. A periodic voltage

$$u(t) = \text{Re} \left[\sum_{n=0}^{\infty} \underline{u}_n e^{j\omega_n t} \right] \quad \text{where} \quad \omega_n = n \frac{2\pi}{T} \quad (3.109)$$

is imposed between them. From Equation (3.98) the electrode charging currents are calculated to be $\pm i(t)$ with

$$i(t) = \text{Re} \left[\sum_{n=0}^{\infty} j\omega_n \underline{\varepsilon}_{\text{eff},n} C_0 \underline{u}_n e^{j\omega_n t} \right], \quad (3.110)$$

where $\underline{\varepsilon}_{\text{eff},n} = \underline{\varepsilon}_{\text{eff}}(\omega_n)$. The *instantaneous* electrical power supplied to the system is given by

$$\dot{W}(t) = u(t) \cdot i(t). \quad (3.111)$$

The *average* electrical power absorbed by the dielectric volume – i.e. the dielectric loss power – is given by

$$P_d \equiv \langle \dot{W} \rangle_T = \frac{1}{T} \int_0^T u(t) i(t) dt. \quad (3.112)$$

Inserting 3.109 and 3.110 into 3.112 leads to²⁴

$$P_d = \frac{C_0}{\varepsilon_0} \kappa \underline{u}_0^2 + \frac{C_0}{2} \sum_{n=1}^{\infty} \omega_n \underbrace{\left[\varepsilon_n'' + \frac{\kappa}{\varepsilon_0 \omega_n} \right]}_{\varepsilon_{\text{eff},n}''} |\underline{u}_n|^2. \quad (3.113)$$

²³The following analysis also holds for a volume delineated by field lines (and the electrode surfaces), representing a partial capacitance between two electrodes.

²⁴All terms containing different frequencies vanish due to time averaging.

3.2.6. Dielectric Loss under Transient Excitation²⁵

Consider an unpolarized medium subject to a continuous electric field evolution $E(t)$ with $E(t < 0) = 0$, but otherwise arbitrary. The net energy (density) that has flown into polarization degrees of freedom up to time $t \geq 0$ (now either stored as electrical energy or dissipated²⁶) is calculated by

$$\begin{aligned} w_p(t) &= \int_0^t \dot{w}_p(t') dt' = \int_0^t E(t') \partial_{t'} P(t') dt \\ &= \int_0^t dt' E(t') \int_0^\infty \varepsilon_0 f(\tau) \partial_{t'} E(t' - \tau) d\tau. \end{aligned} \quad (3.114)$$

If the electric field is varied “slowly” (i.e. such that variations of $E(t)$ on a time scale τ_ϵ , see Equation (3.59), are insignificant, and thus the “memory effect” is negligible), Equation (3.114) evaluates to

$$w_{p,\text{slow}}(t) = \frac{1}{2} \varepsilon_0 \chi'_e(0) E(t)^2 \quad . \quad (3.115)$$

The polarization is at all times described by

$$P(t) \approx \varepsilon_0 \chi'_e(0) E(t) \quad (\text{“adiabatic relaxation”}) \quad (3.116)$$

(also called quasi-static relaxation²⁷). No energy is dissipated during this “infinitely slow” process, because at any time t one could reduce the field adiabatically to zero again and obtain $w_p(t \rightarrow \infty) = -w_{p,\text{ad}}(t)$. The energy density stored in a polarization density $P_s = \varepsilon_0 \chi'_e(0) E_0$ induced by a *static* electric field E_0 is thus

$$w_s = \frac{1}{2} E_0 P_s = \frac{\varepsilon_0}{2} \chi'_e(0) E_0^2 \quad (\text{energy stored in static polarization}). \quad (3.117)$$

Under a step excitation $E(t) = E_0 \theta(t)$ one finds that the energy supplied to the polarization degrees of freedom is

$$w_{p,\mathcal{L}}(t \gtrsim \tau_\epsilon) = \varepsilon_0 \chi'_e(0) E_0^2. \quad (3.118)$$

²⁵This section is based on [Jon78].

²⁶What fraction of this energy has been dissipated up to time t ? This question is considered in Section 5.4.

²⁷Compare to quasi-static processes in thermodynamics.

Yet, the polarization after relaxation ($t \gtrsim \tau_\epsilon$) is $P_s = \epsilon_0 \chi_e'(0) E_0$ and the stored (recoverable) energy thus given by (3.117). Hence, the energy (density) dissipated under a perfect square step excitation is equal to

$$w_{\text{diss}\mathcal{L}} = w_{\text{p}\mathcal{L}}(t \gtrsim \tau_\epsilon) - w_s = \frac{\epsilon_0}{2} \chi_e'(0) E_0^2 = w_s. \quad (3.119)$$

This rather surprising result [Jon78] has its origin in the fact that Fourier amplitudes of all frequencies are present in the step function, and thus all loss peaks are probed by the excitation. The result can be verified by a corresponding frequency-domain calculation.

Since all practical pulse excitations have finite rise times, formula (3.119) is of limited practical applicability. Thus, a more general formula taking into account the finite rise time will be derived in Section 5.3.

4. Aim of this Work

In the literature review (Chapter 2.3.1) it was shown that there is indeed ample information available on the accelerated aging due to enhanced PD activity under inverter-type voltages, and also the PD phenomenon itself under steep voltage flanks is relatively well characterized. In contrast, while there also is experimental evidence on the life-shortening impact of inverter-type voltages below PD inception, the associated investigations are less numerous and the conclusions more diverse (Chapter 2.3.2). Thus:

The aim of this work is to contribute to a better understanding of the aging of solid insulation materials under inverter-type medium voltages, with a particular focus on the aging regime where repetitive PD is absent. To this end, the following specific goals are addressed:

- Set up test facilities for (di)electric material characterization (time-to-failure testing under inverter-type voltages, online/offline dielectric spectrometers).
- Use the constructed test facilities to answer specific questions (see Sections 2.3.6 and 2.4.4) on dielectric (complex dielectric permittivity) and electric (voltage endurance) material properties.
- Formulate requirements for insulation materials exposed to the stresses encountered in medium-voltage converters.
- Identify a suitable dry-type insulation material for a MF MV transformer and apply it to a transformer prototype in a vacuum potting process.

The ultimate goal would be to establish a complete list of risk factors associated with the use of dry-type insulation systems for all relevant

types inverter-type medium voltages and environmental conditions. It is clear that within a single PhD thesis that includes the setup of various test facilities, only a contribution towards this goal can be achieved, for a specific subset of inverter voltages, environmental conditions and insulation materials (**Chapters 7.2** and **7.3**).

A major sub-task of the work presented in this thesis included setting up a test facility (“Inverter Stress Simulator”) for electrical endurance testing of solid insulation materials under specified electrical (variable square wave voltage stress with DC/AC 50 Hz bias) and environmental conditions (e.g. air relative humidity and temperature) (**Chapter 7.1**) as well as a broadband dielectric spectrometer for a thorough dielectric characterization of potentially suitable insulation materials (effective complex dielectric permittivity in the frequency range 10 mHz to 100 kHz and temperatures from 20 °C to 125 °C) (**Chapter 6.1**). The performance of the dielectric spectrometer and its ability to quantify insulation deterioration has been assessed by measurements on insulation specimens aged/degraded under various high-intensity stressors consisting of thermal, hygrothermal and UV radiation on an unfilled epoxy polymer (**Chapter 6.2**) as well as electrical treeing in a silicone elastomer (**Chapter 6.3**).

With its main focus on the PD-free regime, another sub-task of this work was to provide an experimental framework for the further assessment of the potential of the complex dielectric permittivity as an aging marker under inverter-type voltages. Thus, a dielectric spectrometer operating directly under the medium voltage of the inverter stress simulator has been designed for this purpose (**Chapter 8.2**), and its performance verified and characterized (**Chapter 8.3**).

Details about the selection process of a suitable potting material for the MF MV transformer prototype [GFR⁺19] as well as its application in a vacuum potting process are given in **Chapter 9**.

Where useful, own theoretical considerations were developed and applied to assist the interpretation of results (e.g. “Is dielectric spectroscopy sensitive to static space charge in the insulation bulk?”) or explore possible adverse effects arising under (mixed) inverter-type voltages (“Are dielectric losses influenced by the presence (static) of space charge in the insulation bulk?” or “How does the space-charge distorted electric field distribution look like in the presence of mixed voltages (DC+AC)?”). These considerations are detailed in the following **Chapter 5**.

5. Theoretical Considerations

This chapter summarizes a number of theoretical considerations aiming at answering the following questions:

- Chapter 5.1: How does free space charge in the insulation bulk influence the electrode charging currents (and hence dielectric losses) under an arbitrary voltage excitation?
- Chapter 5.2: Does the formation of space charge in the insulation bulk under mixed voltages (DC+AC) lead to a more critical electric field distribution than under pure DC or AC stress alone?
- Chapter 5.3: Is there a simplified approximate expression for dielectric losses under inverter-type voltages with finite rise time?
- Chapter 5.4: Is it possible to write down an expression of the instantaneous dielectric loss rate in terms of the dielectric response function (complex dielectric permittivity)?

5.1. Capacitive Currents in the Presence of Free Space Charge in a Dielectric Volume

Motivating question: *How does free space charge in the insulation bulk influence the electrode charging currents (and hence dielectric losses) under an arbitrary voltage excitation?*

Consider an arbitrary configuration of N conductors embedded in a dielectric volume of relative dielectric permittivity ϵ_r . The electrode voltages $v_i(t)$, $i = 1, \dots, N$, are assumed to be given and referenced to the surface S_0 . The question of how free space charge ρ_f in the dielectric volume between conductors influences the supply currents $i_i(t) = \dot{q}_i(t)$ to the electrodes is of particular interest for online dielectric spectroscopy,

yet no answer could be found in the relevant literature on this topic. The following treatment is a generalization of the presentation of the capacitance matrix given in [HM89] (pp. 147-149).

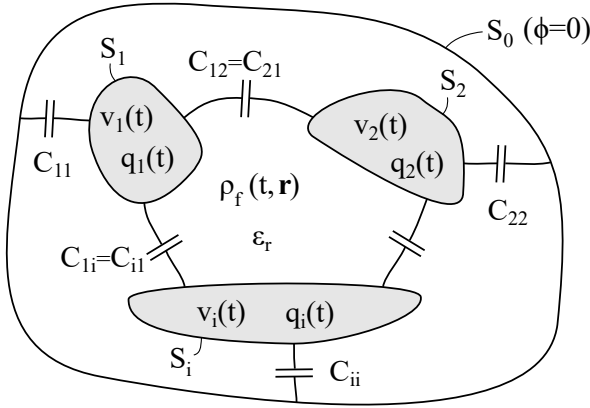


Figure 5.1.: N electrodes are excited with voltages $v_i(t)$, $i = 1, \dots, N$, in the presence of free space charge ρ_f in the dielectric volume of permittivity ϵ_r . What are the associated free charge supply currents $i_i(t) = \dot{q}_i(t)$ to the electrodes?

The voltage spectra $|v_i(\omega)|$ are assumed to be limited to frequencies $\omega \ll L/c$, where L is the largest dimension of the region of interest and c is the speed of light in the dielectric. The electric field is then quasi-electrostatic and can be described as the gradient of a potential function:

$$\mathbf{E}(t, \mathbf{r}) = -\nabla\phi(t, \mathbf{r}) \quad (5.1)$$

The potential function is the solution of Poisson's equation

$$\nabla^2 \phi(t, \mathbf{r}) = -\frac{\rho_f(t, \mathbf{r})}{\varepsilon_0 \varepsilon_r} \quad (5.2)$$

with the boundary conditions

$$\phi(t, S_i) = v_i(t) \quad \text{for } i = 1, \dots, N. \quad (5.3)$$

A solution to equations (5.2) and (5.3) can formally be written in the following way.

1. Let ϕ_ρ be the solution of Poisson's equation 5.2 under the condition of zero *net* electrode charge, $q_i(t) = 0$. The conductor voltages $v_{i,\rho}(t) = \phi_\rho(S_i, t)$ will be induced by the presence of the space charge $\rho_f(t, \mathbf{r})$.
2. Let u_i be the solutions of the Laplace equation

$$\nabla^2 u_i(\mathbf{r}) = 0 \quad (5.4)$$

with the boundary conditions

$$u_i(S_j) = \delta_{ij} \quad \text{for } i, j = 1, \dots, N, \quad (5.5)$$

where δ_{ij} is equal to one if $i = j$ and equal to zero otherwise.

Note that the scalar functions u_i are only dependent on the *geometry* of the electrode configuration. By linearity of the Laplace equation, it follows that

$$\phi(t, \mathbf{r}) = \phi_\rho(t, \mathbf{r}) + \sum_{i=1}^N [v_i(t) - v_{i,\rho}(t)] u_i(\mathbf{r}) \quad (5.6)$$

satisfies Equations (5.2) and (5.3). The net charge on electrode i is thus

given by

$$\begin{aligned}
 q_i(t) &= \oint_{S_i} \varepsilon_0 \varepsilon_r \mathbf{E}(t, \mathbf{r}) \cdot d\mathbf{S} \\
 &= \sum_{j=1}^N [v_j(t) - v_{j,\rho}(t)] \underbrace{\oint_{S_i} -\varepsilon_0 \varepsilon_r \nabla u_j(\mathbf{r}) \cdot d\mathbf{S}}_{\equiv \varepsilon_r C_{ij}} \\
 &\quad + \underbrace{\oint_{S_i} -\varepsilon_0 \varepsilon_r \nabla \phi_\rho(t, \mathbf{r}) \cdot d\mathbf{S}}_{=0} \\
 &= \sum_{j=1}^N \varepsilon_r C_{ij} [v_j(t) - v_{j,\rho}(t)].
 \end{aligned} \tag{5.7}$$

The standard definition of the *capacitance coefficients* C_{ij} (see [HM89] p. 149) has been used.

The net electrode charging currents are given by

$$i_i(t) = \dot{q}_i(t) = \sum_{j=1}^N \varepsilon_r C_{ij} [\dot{v}_j(t) - \dot{v}_{j,\rho}(t)] \tag{5.8}$$

It can be seen that if $|\dot{v}_{j,\rho}(t)| \ll |\dot{v}_j(t)|$ (which is true in particular for a static space charge distribution) the electrode charging currents are not influenced by the space charge in the dielectric volume (although the *absolute* amount of charge is).

If, in the other extreme, the electrode voltages are held constant, the measurable electrode charging currents are determined by the evolving space charge in the dielectric volume (provided they are above the noise level). In the special case of two electrodes with $v_1(t) = U_{\text{DC}}$ and $v_2(t) = 0$ this corresponds to the well-known polarization current measurement (or depolarization current measurement in the case $v_1(t) = v_2(t) = 0$).

When applying a sinusoidal voltage $\underline{v}_1(\omega)$ to a conductive solid containing carrier drift barriers (e.g. structural interfaces or the metal-insulator contacts), the two regimes described by Equation (5.8) can be observed. Typically, the lower the excitation frequency, the larger the peak of the induced voltages $\underline{v}_{i,\rho}$, because the space charge dipoles continue to grow

as long as the electric field does not change sign. Thus, at a certain frequency the electrode charging current will no longer be dominated by the response of bound charges (and the vacuum displacement current), but rather by the voltage-induced build-up of space charge (changing sign every period of the excitation voltage). This behavior has been observed in the silicone rubber material investigated in Chapter 6.3.

If desired, the bound space charge dynamics can be included by using the *complex* dielectric permittivity and, consequently, complex capacitance coefficients

$$\underline{C}_{ij}(\omega) = \underline{\varepsilon}(\omega)C_{ij}. \quad (5.9)$$

The charging currents in the *stationary regime*¹ are then given by the convolution

$$i_i(t) = \text{Re} \left[\int_0^\infty j\omega \sum_{j=1}^N \underline{C}_{ij}(\omega) [\underline{v}_j(\omega) - \underline{v}_{j,\rho}(\omega)] e^{j\omega t} d\omega \right]. \quad (5.10)$$

Summary

- Although a static space charge distribution inside the dielectric of a capacitor changes the absolute value of the electrode charges for a given electrode voltage, it does *not* change the stationary supply currents to the electrodes under AC excitation.
- Static space charge inside the insulation bulk does not change the dielectric losses under AC excitation.
- When the space charge is not static, it contributes to the electrode charging currents (and dielectric losses).

Addendum: from electrode voltages to space charge? The determination electrode voltages $v_{i,\rho}$ induced by a certain free space charge

¹Because the Fourier representation is used. For studying the transition from imposed initial conditions (e.g. an arbitrary initial free space charge density) to the stationary regime, the Laplace representation (or a full time-domain analysis) is needed.

distribution ρ_f must, in general, be determined by numerical FEM analysis. For practical purposes, one may proceed as follows. Divide the dielectric volume of interest Ω_0 (i.e. where space charge is expected) into a number N_ρ of partial volumes $\{\Omega_i, i = 1, \dots, N_\rho\}$ (voxels). For each voxel Ω_j , calculate the induced electrode voltages $v_{ij,\rho}$ by setting the free charge density to

$$\rho_{f,j}(\mathbf{r}) = \begin{cases} q_0/\Omega_j, & \text{if } \mathbf{r} \in \Omega_j \\ 0, & \text{otherwise} \end{cases} \quad (5.11)$$

where q_0 is a chosen normalization unit of charge. The functions $\rho_{f,j}$ constitute an orthogonal basis of Ω_0 (with a spacial resolution determined by the chosen partition). Indeed, let ρ_f be an arbitrary space charge distribution in Ω_0 . In terms of the basis functions $\rho_{f,j}$ it reads

$$\rho_f(\mathbf{r}) = \sum_{j=1}^{N_\rho} c_j \rho_{f,j}(\mathbf{r}) + R(\mathbf{r}) \quad (5.12)$$

where R is the error due to the finite voxel size. The expansion coefficients are given by

$$c_j = \bar{\rho}_j \Omega_j / q_0, \quad (5.13)$$

where $\bar{\rho}_j$ is the average space charge density in the volume Ω_j . The electrode voltages induced by ρ_f are then given by

$$v_i = \sum_{j=1}^{N_\rho} v_{ij,\rho} c_j. \quad (5.14)$$

From a practical perspective it would be interesting to solve the inverse problem, i.e. finding the coefficients c_i for given (measurable) voltages v_i . This would give access to the average space charge values $\bar{\rho}_j$. From linear algebra it is known that a necessary condition for the invertibility of $v_{ij,\rho}$ is that the number of electrodes (measured voltages) is equal to or greater than the chosen number of voxels (in the latter case the problem is usually over-constrained but can be solved in a least-square sense). The *condition number* of the matrix $v_{ij,\rho}$ (and hence its numerical invertibility) is expected to be strongly dependent on the location and shape of the electrodes.

Maybe such a space charge measurement using electrode arrays could be an interesting alternative to the established techniques (e.g. PEA)

in certain applications. In some cases it may be more practical to use a moving electrode instead of a large number of discrete electrodes. Note that this measurement principle is different from the well-known Kelvin probe for surface charge measurements [YFT87], which uses an imposed time-modulated capacitive coupling to the space charge to generate the electrode current.

5.2. Electric Field Distribution in a Layered Dielectric under Mixed-Frequency Voltage Stress

Motivating question: *Does the formation of space charge in the insulation bulk under mixed voltages (DC+AC) lead to a more critical electric field distribution than under pure DC or AC stress alone?*

This section aims at answering the question of whether or not the formation of free space charge inside the dielectric volume (or at a dielectric/structural interface) is of particular concern under mixed-frequency voltage stress. A simple model for such a system is the two-layer dielectric² shown in Figure 5.2. Indeed, it is well-known that a layer of net free charge evolves at the interface of the dielectric materials if their relaxation times $\tau_{D,i} = \varepsilon_0 \varepsilon_i / \kappa_i$ differ. The electric field generated by the evolving free charge at the interface increases the electric field stress in the layer of lower conductivity (on a time scale quantified below), until the free current densities at the interface are equal.

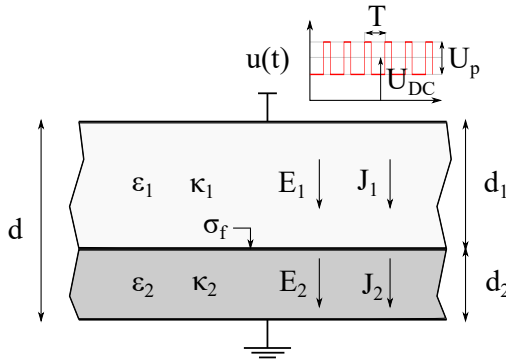


Figure 5.2.: Layered dielectric modelled with dielectric permittivities $\varepsilon_i \in \mathbb{R}$ (intrinsic dispersion not considered) and conductivities κ_i .

From Equation (3.81) it follows that the free charge at the interface can

²The n-layer dielectric has been used by J.C. Maxwell to show, among other things, that “a dielectric composed of strata of different kinds may exhibit the phenomena known as electric absorption and residual discharge, although none of the substances of which it is made exhibit these phenomena when alone.” See [Max54] pp. 453.

be written in terms of the displacement field:

$$\sigma_f(t) = -D_1(t) + D_2(t) = -\varepsilon_1 E_1(t) + \varepsilon_2 E_2(t). \quad (5.15)$$

The conservation of free charge, $\nabla \cdot \mathbf{J}_c = \dot{\rho}_f$, yields

$$\dot{\sigma}_f(t) = J_1(t) - J_2(t) = \kappa_1 E_1(t) - \kappa_2 E_2(t), \quad (5.16)$$

where J_1 and J_2 are the conduction currents in the respective layers. Thus,³

$$[\varepsilon_1 \partial_t + \kappa_1] E_1(t) = [\varepsilon_2 \partial_t + \kappa_2] E_2(t). \quad (5.17)$$

By using

$$E_1(t)d_1 + E_2(t)d_2 = u(t) \quad (5.18)$$

it is found that the electric fields in the layers are governed by an ordinary inhomogeneous differential equation of the form

$$\dot{x} + p(t)x = q(t), \quad (5.19)$$

which is solved by [MIT]

$$x(t) = e^{-\int_0^t p(t')dt'} \left[\int_0^t q(t') e^{-\int_0^{t'} p(t'')dt''} dt' + x_0 \right]. \quad (5.20)$$

In the present case, $p = \tau^{-1}$ with

$$\tau = \frac{d_2 \varepsilon_1 + d_1 \varepsilon_2}{d_2 \kappa_1 + d_1 \kappa_2} \quad (5.21)$$

and

$$q(t) = \frac{\varepsilon_2 \partial_t + \kappa_2}{d_2 \varepsilon_1 + d_1 \varepsilon_2} u(t). \quad (5.22)$$

An analytical solution for the DC-biased rectangular pulse train (switched on at $t = 0$)⁴

$$u(t) = U_{\text{DC}} \theta(t) + U_p \sum_{k=0}^{\infty} [-D \theta(t - kT) + (1 - D) \theta(t - (k + D)T)], \quad (5.23)$$

³ $\partial_t = \frac{\partial}{\partial t}$. Thus e.g. $(\varepsilon_1 \partial_t + \kappa_1) E_1(t) = \varepsilon_1 \frac{\partial E_1(t)}{\partial t} + \kappa_1 E_1(t)$.

⁴ $\theta(t)$ is equal to 1 for $t \geq 0$ and 0 otherwise.

can be found by superposition of solutions to the single step response

$$u_{\mathcal{J}}(t) = u_0\theta(t). \quad (5.24)$$

The step response is obtained by direct calculation from 5.20:⁵

$$E_1(t) = \frac{u_0}{d_1 + d_2 \frac{\kappa_1}{\kappa_2}} \left[1 - e^{-\frac{t}{\tau}} \right] + \frac{u_0}{d_1 + d_2 \frac{\varepsilon_1}{\varepsilon_2}} e^{-\frac{t}{\tau}} \quad (5.25)$$

$$+ \frac{\sigma_f(0)}{\varepsilon_1 + \varepsilon_2 \frac{d_1}{d_2}} e^{-\frac{t}{\tau}}. \quad (5.26)$$

$E_2(t)$ is obtained by exchanging the indices $1 \leftrightarrow 2$.

The time evolution of the free charge density (unit: C m^{-2}) at the dielectric interface is obtained from Equation (5.15):⁶

$$\sigma_f(t) = \sigma_f(0)e^{-\frac{t}{\tau}} + u_0 \frac{\kappa_2\varepsilon_1 - \kappa_1\varepsilon_2}{\kappa_1d_2 + \kappa_2d_1} [1 - e^{-\frac{t}{\tau}}]. \quad (5.27)$$

Thus, the parameter τ is seen to correspond to the time constant associated with the build-up or decay of free charge at the dielectric interface.

From the above solutions (5.25 to 5.27) it follows that the evolution of the electric field for a pulse of duration $D \cdot T$,

$$u_{\mathcal{J}}(t) = u_0[\theta(t) - \theta(t - DT)], \quad (5.28)$$

is given by equation 5.25 for $t < DT$ and by

$$E_1(t) = \frac{u_0}{d_1 + d_2 \frac{\kappa_1}{\kappa_2}} e^{-\frac{t}{\tau}} \left[e^{\frac{DT}{\tau}} - 1 \right] + \frac{u_0}{d_1 + d_2 \frac{\varepsilon_1}{\varepsilon_2}} e^{-\frac{t}{\tau}} \left[1 - e^{\frac{DT}{\tau}} \right] \quad (5.29)$$

$$+ \frac{1}{\varepsilon_1 + \varepsilon_2 \frac{d_1}{d_2}} e^{-\frac{t}{\tau}} \left[\sigma_f(0) - \sigma_f(DT)e^{\frac{DT}{\tau}} \right]. \quad (5.30)$$

⁵ $\partial_t\theta(t) = \delta(t)$ (Dirac delta function). Or use $u(t) = u_0(1 - e^{-t/\tau_r})$ and take the limit $\tau_r \rightarrow 0$.

⁶Note that σ_f changes sign under permutation of indices $1 \leftrightarrow 2$, as expected on physical grounds.

for $t \geq DT$. Thus, if the pulse duration is much shorter than the time constant for the evolution of (free) space charge in the system (i.e. $DT \ll \tau$), the local electric field stress due to the AC component of a repetitive pulse voltage stress is determined by the spatial variation of the dielectric permittivity. The total electrical stress is obtained by adding the (space-charge distorted) electric field caused by the DC component of the pulse train 5.23, and is given by:⁷

$$DT \ll \tau$$

$$E_1(t) = \frac{U_{\text{DC}}}{d_1 + d_2 \frac{\kappa_1}{\kappa_2}} \left[1 - e^{-\frac{t}{\tau}} \right] + \frac{U_{\text{DC}}}{d_1 + d_2 \frac{\varepsilon_1}{\varepsilon_2}} e^{-\frac{t}{\tau}} \quad (5.31)$$

$$+ U_{\pm} \frac{1}{d_1 + d_2 \frac{\varepsilon_1}{\varepsilon_2}}, \quad (5.32)$$

with the zero-mean pulse voltage levels

$$U_{\pm} = \begin{cases} U_{\text{p}}(1 - D) \\ -U_{\text{p}}D \end{cases} \quad (5.33)$$

$E_2(t)$ is again obtained by permutation of the indices $1 \leftrightarrow 2$. For medium-frequency pulses ($T \lesssim 1$ ms) the condition $DT \ll \tau$ is fulfilled except for insulators on the extreme of the conductivity scale ($\kappa \geq 10^{-8} \text{ Sm}^{-1}$).

The electric field after the build-up of space charge due to U_{DC} is given by

$$E_1(t \gg \tau) = \frac{U_{\text{DC}}}{d_1 + d_2 \frac{\kappa_1}{\kappa_2}} + U_{\pm} \frac{1}{d_1 + d_2 \frac{\varepsilon_1}{\varepsilon_2}}. \quad (5.34)$$

This case is illustrated in Figure 5.3a.

⁷It is assumed here that no free space charge is at the interface at $t = 0$, i.e. $\sigma_{\text{f}}(0) = 0$.

DC-biased pulse train with $DT \ll \tau$

The electric field stress magnitude at any point inside the insulation is given by the vector sum of the the DC field stress evolving under the DC component of the pulse train and the AC electric field associated with the AC pulse voltage (distributed according to the dielectric permittivity).

On the other hand, for systems containing semi-conductive parts ($\kappa \gg 10^{-8} \text{ Sm}^{-1}$), such that $DT \gg \tau$, the system reaches a new space charge equilibrium corresponding to the plateau levels of the total voltage:

$$\sigma_{f,\pm} = (U_{\text{DC}} + U_{\pm}) \frac{\kappa_1 \varepsilon_2 - \kappa_2 \varepsilon_1}{\kappa_1 d_2 + \kappa_2 d_1}. \quad (5.35)$$

By using equations 5.15 and 5.18, the electric field can be split into an “instantaneous” contribution from the electrode voltage $u(t)$ (free charge on electrodes and bound charge in insulator) and a delayed response (time constant τ) due to the field generated by the free interface charge $\sigma_f(t)$ in the insulator:

$$E_1(t) = \frac{u(t)}{d_1 + \frac{\varepsilon_1}{\varepsilon_2} d_2} - \frac{\sigma_f(t)}{\varepsilon_1 + \varepsilon_2 \frac{d_1}{d_2}} \quad (5.36)$$

$$E_2(t) = \frac{u(t)}{d_2 + \frac{\varepsilon_2}{\varepsilon_1} d_1} + \frac{\sigma_f(t)}{\varepsilon_2 + \varepsilon_1 \frac{d_2}{d_1}}. \quad (5.37)$$

The highest electric field stress occurs in the limit of a highly conductive layer,

$$\frac{\kappa_1}{\kappa_2} \gg \max \left(\frac{\varepsilon_1}{\varepsilon_2}, \frac{d_1}{d_2} \right). \quad (5.38)$$

In this case, the field is expelled from layer 1 in the quasi-stationary case, i.e. $\gg \tau$ after a switching transient (this is found by evaluating 5.36 with $u(t) = U_{\pm}$ and $\sigma_f(t) = \sigma_{f,\pm}$). The conductive layer will however be exposed to a transient field⁸ of magnitude

$$\frac{U_p}{\frac{\varepsilon_2}{\varepsilon_1} d_2 + d_1}, \quad (5.39)$$

⁸Of rise time τ_r and fall time τ .

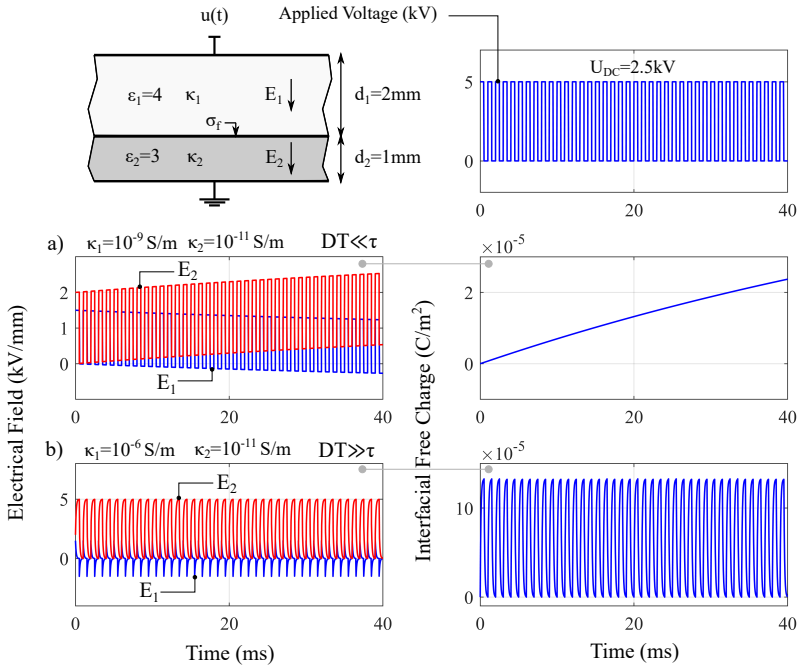


Figure 5.3.: Electrical fields in a 2-layer dielectric under a mixed voltage inverter-type stress. The two regimes a) and b) are described in the main text. DT equals 0.5 ms in this example, and the time constants τ have been chosen above ($\tau_a = 87\text{ ms}$) and below ($\tau_b = 89\text{ }\mu\text{s}$) this value.

during the switching transition, provided that the switching time τ_r is smaller than the time constant for the evolution of free charge τ (see Figure 5.3b).⁹ Note that this case (pulse duration $\gg \tau$) is well-known from the problem of polarity reversal $U_+ \rightarrow U_-$ in DC insulation systems (e.g. cables), where the local field stress can reach values (worst case) that would occur under an AC stress (no free space charge) of amplitude $U_+ + |U_-|$.

⁹If $\tau_r > \tau$, the shielding effect of the free charges will be set up fast enough to permanently exclude the electric field from the conductive layer. The layer can then be considered as part of the electrode.

DC-biased pulse train with $DT \gg \tau$

The electric field magnitude at any point inside the insulation is given by the DC field stress evolving under the plateau voltage values of the pulse train, except for a transient phase of duration τ after switching. During this time interval the step voltage of the pulse appears as a transient contribution to the electric field (distributed according to the dielectric permittivity).

In conclusion, the above considerations on a simple model system suggest that there is no critical interaction between the space charge field (driven by the DC component of the pulse train) and the electric field due to the AC component of the pulse train. It has been shown that the AC component generates a field that is distributed according to the variation of the dielectric permittivity (in the case $\tau \ll DT$ this contribution is of transient duration τ , after which it is cancelled by the rearrangement of free space charge). This is not to say that designing an insulation system for mixed-voltage stress is straightforward. Rather, the above simple analysis suggests that there does not seem to be a complicating interaction between the DC and AC components, and thus the main challenge is the design of a *single* insulation system which endures *both* DC and repetitive pulse voltage stress.

5.3. Dielectric Losses Under Inverter-Type Voltages: A Simple Approximation

Motivating question: *Is there a simplified approximate expression for dielectric losses under inverter-type voltages with finite rise time?*

The average dielectric loss for an arbitrary periodic excitation (period T) is given by equation (3.113),

$$p_d = \underbrace{\frac{C_0}{\varepsilon_0} \kappa \underline{u}_0^2}_{p_{d,DC}} + \frac{C_0}{2} \underbrace{\sum_{n=1}^{\infty} n \omega_0 \varepsilon''_{\text{eff},n} |\underline{u}_n|^2}_{p_{d,AC}}. \quad (5.40)$$

For the DC-biased (U_{DC}) trapezoidal pulse train of amplitude U_p (peak-peak), duty cycle $D = \tau/T = 0.5$ and rise time τ_r (Section 3.1.4), the Fourier coefficients are given by $\underline{u}_0 = U_{DC}$ and

$$\underline{u}_n = U_p \operatorname{sinc}\left(n\pi \frac{\tau_r}{2}\right) \operatorname{sinc}\left(n \frac{\pi}{2}\right) \quad \text{for } n \geq 1. \quad (5.41)$$

Since

$$\operatorname{sinc}^2\left(n \frac{\pi}{2}\right) = \begin{cases} \left(\frac{2}{\pi n}\right)^2 & \text{for } n \text{ odd} \\ 0 & \text{for } n \text{ even} \end{cases} \quad (5.42)$$

and

$$\operatorname{sinc}\left(n\pi \frac{\tau_r}{T}\right) = \begin{cases} 1 & \text{for } n \lesssim N_{\max} \equiv \left\lfloor \frac{T}{\pi\tau_r} \right\rfloor \\ \left(\frac{T}{n\pi\tau_r}\right)^2 & \text{for } n \gtrsim N_{\max} \end{cases} \quad (5.43)$$

the AC dielectric loss can be written as

$$p_{d,AC} = \frac{4}{\pi} C_0 U_p^2 f_0 \left[\sum_{n=1 \text{ (odd)}}^{N_{\max}} \frac{\varepsilon''_{\text{eff},n}}{n} + \underbrace{\sum_{n=N_{\max}+1 \text{ (odd)}}^{\infty} \frac{\varepsilon''_{\text{eff},n}}{n(n-N_{\max})^2}}_{\text{negligible}} \right] \\ \approx \frac{4}{\pi} C_0 U_p^2 f_0 \sum_{n=1 \text{ (odd)}}^{N_{\max}} \frac{\varepsilon''_{\text{eff},n}}{n} \quad (5.44)$$

Due to the additional factor n^{-2} from (5.43), the cumulative sum converges quickly above N_{\max} , which is why these terms can be neglected.

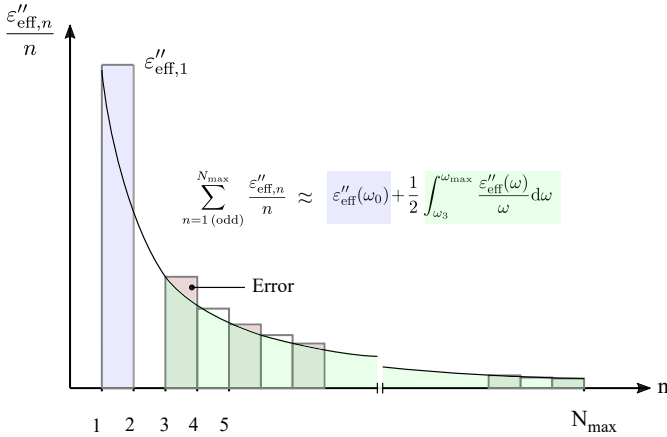


Figure 5.4.: Approximation of the discrete summation in equation 5.45 by an integral. Keeping the first term separate significantly reduces the error without introducing a substantial complication.

If the average AC dielectric loss is normalized with $f_0 \frac{1}{2} C_0 U_p^2$ it takes the dimensionless form

$$p'_{d,AC} \equiv \frac{p_{d,AC}}{f_0 \frac{1}{2} C_0 U_p^2} = \frac{8}{\pi} \sum_{n=1 \text{ (odd)}}^{N_{\max}} \frac{\varepsilon''_{\text{eff},n}}{n} \quad (5.45)$$

Since N_{\max} is in general large¹⁰, it seems that an efficient evaluation of $p'_{d,AC}$ can only be done numerically. Surprisingly, however, its value can be calculated approximately by using the three values $\varepsilon''_{\text{eff}}(\omega_0)$, $\varepsilon'_{\text{eff}}(\omega_0)$ and $\varepsilon'_{\text{eff}}(\omega_{\max})$ only.

To achieve this simplification, the summation from $n = 3$ to $n = N_{\max}$ is approximated by an integration (see Figure 5.4):

$$\sum_{n=1 \text{ (odd)}}^{N_{\max}} \frac{\varepsilon''_{\text{eff},n}}{n} = \varepsilon''_{\text{eff},1} + \sum_{n=3 \text{ (odd)}}^{N_{\max}} \frac{\varepsilon''_{\text{eff},n}}{n} \approx \varepsilon''_{\text{eff}}(\omega_0) + \frac{1}{2} \int_{\omega_3}^{\omega_{\max}} \frac{\varepsilon''_{\text{eff}}(\omega)}{\omega} d\omega, \quad (5.46)$$

¹⁰E.g. $N_{\max} = 3184$ for $\tau_r = 100$ ns and $T = 1$ ms.

where the factor $\frac{1}{2}$ is introduced because only odd terms are to be considered.

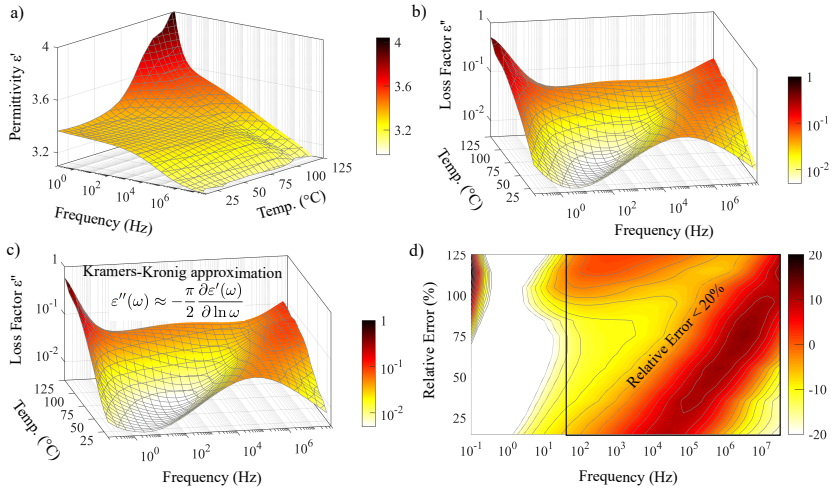


Figure 5.5.: Local Kramers-Kronig approximation applied to the dielectric spectrum of PET (Melinex® S). Measured a) real and b) imaginary part of the complex dielectric permittivity (used setup described in Chapter 8.2). Figure c) is calculated exclusively from the data in a) by using the shown formula. d) Above about 50 Hz the relative error of the approximation is within $\pm 20\%$ across the whole measured temperature range.

The integral can in turn be rewritten by making use of the local Kramers-Kronig relation, see equation (3.58). The approximation and its accuracy are illustrated in Figure 5.5 for the PET insulation foil used in the time-to-failure testing described in Chapter 7.2.

$$\int_{\omega_3}^{\omega_{\max}} \frac{\epsilon''_{\text{eff}}(\omega)}{\omega} d\omega = \int_{\ln(\omega_3)}^{\ln(\omega_{\max})} \epsilon''_{\text{eff}}(\omega) d \ln(\omega) \approx -\frac{\pi}{2} [\epsilon'_{\text{eff}}(\omega_{\max}) - \epsilon'_{\text{eff}}(\omega_3)] \quad (5.47)$$

Thus,

$$p'_{\text{d,AC}} = \frac{8}{\pi} \sum_{n=1}^{N_{\max}} \approx 2[\epsilon'_{\text{eff}}(\omega_3) - \epsilon'_{\text{eff}}(\omega_{\max})] + \frac{8}{\pi} \epsilon''_{\text{eff}}(\omega_0) \quad (5.48)$$

and

$$\begin{aligned}
 p_{d,AC} &= f_0 \frac{1}{2} C_0 U_p^2 p'_{d,AC} \\
 &\approx f_0 C_0 U_p^2 \left[\frac{4}{\pi} \varepsilon''_{\text{eff}}(\omega_0) + [\varepsilon'_{\text{eff}}(\omega_3) - \varepsilon'_{\text{eff}}(\omega_{\text{max}})] \right]. \\
 &= \frac{1}{2} \omega_0 C_0 \varepsilon''_{\text{eff}}(\omega_0) \left[\frac{2}{\pi} U_p \right]^2 \tag{5.49}
 \end{aligned}$$

$$+ f_0 [\varepsilon'_{\text{eff}}(\omega_3) - \varepsilon'_{\text{eff}}(\omega_{\text{max}})] C_0 U_p^2. \tag{5.50}$$

Typically, $\varepsilon'_{\text{eff}}(\omega_0) - \varepsilon'_{\text{eff}}(\omega_3)$ will be small compared to $\varepsilon'_{\text{eff}}(\omega_3) - \varepsilon'_{\text{eff}}(\omega_{\text{max}})$ so that ω_3 can be replaced by ω_0 in the expression 5.50. In addition, $\frac{2}{\pi} U_p$ is the amplitude $|U_1|$ of the fundamental sinusoid.¹¹ Thus:

The approximate AC dielectric loss under a trapezoidal pulse train (peak-peak voltage U_p , rise time τ_r , fundamental frequency f_0) excitation is thus given by the loss of the fundamental sinusoid of the pulse train (of peak voltage $|U_1| = \frac{2}{\pi} U_p$), plus the energy stored in a capacitance $C = [\varepsilon'_{\text{eff}}(\omega_0) - \varepsilon'_{\text{eff}}(2/\tau_r)] C_0$ at voltage U_p *at every switching transition*:

$$\begin{aligned}
 p_{d,AC} &\approx \pi f_0 C_0 \varepsilon''_{\text{eff}}(\omega_0) |U_1|^2 \\
 &\quad + 2f_0 \left[\varepsilon'_{\text{eff}}(\omega_0) - \varepsilon'_{\text{eff}} \left(\omega = \frac{2}{\tau_r} \right) \right] \frac{1}{2} C_0 U_p^2. \tag{5.51}
 \end{aligned}$$

Physical picture: the first term approximates the losses due to the low-frequency content in the power spectrum (i.e. changes occurring on the time scale $T = f_0^{-1}$), while the second term accounts for the losses during switching transitions (occurring on the time scale $\tau_r \ll T$). The latter

¹¹One could add a further refinement by estimating the “Error” in Figure 5.4. In dielectric relaxations the variation of $\varepsilon''_{\text{eff},n}$ with n is never more than an order of magnitude per decade in frequency (which is the asymptotic case of the Debye relaxation – the sharpest possible relaxation peak [MP09]). An upper bound for the error (the triangular-shaped areas above the continuous line in Figure 5.6) is thus approximately given by $\frac{1}{4} \left(\frac{\varepsilon''_{\text{eff}}(\omega_3)}{3} - \frac{\varepsilon''_{\text{eff}}(\omega_{\text{max}})}{N_{\text{max}}} \right) > 0$. This will add at most $\frac{1}{12} \approx 8\%$ to the term (5.49).

loss equals the energy stored in the polarization degrees of freedom that are able to reach a quasi-static value within the fundamental period (this excludes dipoles whose relaxation time is longer than $\sim T$) and are unable to follow the external field during the transition (this excludes dipoles whose relaxation time is smaller than $\sim \tau_r$).

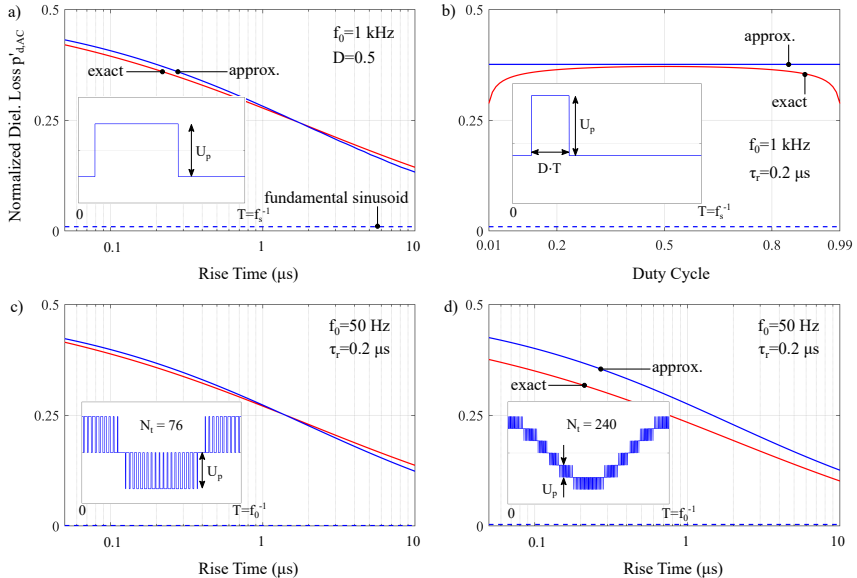


Figure 5.6.: Comparison of exact (5.45) and approximate (5.52) formulas for the dielectric loss of PET foil (see figure 5.5) under inverter-type voltages. The loss is normalized with $\frac{N_t}{2} \frac{1}{2} C_0 U_p^2$, where N_t is the number of transitions occurring within one fundamental period.

Formula 5.52 can be regarded as an approximate generalization of the result which states that under an ideal voltage step $U(t) = U_p \theta(t)$ the dielectric loss in units of $\frac{1}{2} C_0 U_p^2$ exactly equals the static electric susceptibility [Jon78], that is $\varepsilon'(0) - 1$ (see Section 3.2.6, equation (3.119)). This particular result is contained in equation (5.48) as the limit $\omega_0 \rightarrow 0$ and $\tau_r \rightarrow 0$, since $\lim_{\omega \rightarrow \infty} \varepsilon'_{\text{eff}}(\omega) = 1$ and (for $\kappa = 0$) $\lim_{\omega \rightarrow 0} \varepsilon''_{\text{eff}}(\omega) = 0$ (the factor 2 results from the fact that there are two voltage steps per period in the pulse train).

Figure 5.6a shows the comparison between the exact formula 5.45 of

the (normalized) dielectric loss and the derived approximation 5.52 as a function of pulse rise time. Although the approximation has been derived for a pulse train of duty cycle $D = 0.5$ (and hence does not appear as a variable in the derived expression), Figure 5.6b shows that the dielectric loss varies relatively little as a function of the pulse duty cycle the practical range from 1% to 99%. This allows to extend the approximation to pulse-width-modulated – even multilevel – waveforms, as illustrated in Figures 5.6c and 5.6d. In this general case, the approximation formula reads

$$p_{d,AC} \approx \pi f_0 C_0 \varepsilon''_{\text{eff}}(\omega_0) |U_1|^2 + N_t f_0 \left[\varepsilon'_{\text{eff}}(2\pi f_s) - \varepsilon'_{\text{eff}}\left(\omega = \frac{2}{\tau_r}\right) \right] \frac{1}{2} C_0 U_p^2, \quad (5.52)$$

where now U_p is the *jump voltage*, and N_t the number of switching transitions within one fundamental period $T = f_0^{-1}$.

It can be seen that the contribution of the fundamental 50 Hz sinusoid is generally negligible, except for rectangular pulse trains with slow rise times ($\tau_r/T \gtrsim 1\%$). Therefore, in most practical situations, the dielectric loss under an arbitrary multilevel inverter waveform can be estimated by the following simple formula:

Inverter Voltage Stress: Approximate Dielectric Losses

$$p_{d,AC} \approx 2f_s [\varepsilon'_{\text{eff}}(\omega_s = 2\pi f_s) - \varepsilon'_{\text{eff}}(\omega_c = 2/\tau_r)] \frac{1}{2} C_0 U_p^2, \quad (5.53)$$

where $f_s = \frac{N_t}{2T}$ is the (average) switching frequency and U_p the jump voltage. This illustrates that in applications using inverter-type voltages the quantity

$$\varepsilon'_{\text{eff}}(\omega_s = 2\pi f_s) - \varepsilon'_{\text{eff}}(\omega_c = 2/\tau_r) \quad (5.54)$$

is *the* figure of merit of insulation materials with respect to dielectric losses. It allows a quick evaluation of an insulation material's suitability for use in inverter applications with respect to the important design parameter “dielectric losses” (its role in causing premature insulation failure under inverter-type voltages is discussed in Section 2.3.2). Figure

5.7 provides an example for three different silicone potting materials. Both the amplitude and the real part of the complex dielectric permittivity are plotted (superimposed). The approximation $|\underline{\varepsilon}| \approx \varepsilon''$ is very good (relative error $< 0.12\%$) for all “low-loss” dielectric materials ($\tan \delta < 5\%$ in the relevant frequency range). This is interesting because the magnitude of the dielectric permittivity is more easily accessible experimentally, as no phase-sensitive measurement is required.¹² $|\underline{\varepsilon}(\omega)|$ is related to the magnitudes of the applied harmonic excitation voltage $\hat{u}(\omega)$ and the magnitude of the resulting sample current $\hat{i}(\omega)$ by

$$|\underline{\varepsilon}(\omega)| = \frac{\hat{i}(\omega)}{\omega C_0 \hat{u}(\omega)}, \quad (5.55)$$

where C_0 is the vacuum capacitance of the electrode arrangement.¹³

¹²One could for example use an analog peak detection circuit (these are available as monolithic ICs, e.g. PKD01 from Analog Devices). This eliminates the need for a high-speed ADC and FFT processing and could thus provide a low-cost broadband dielectric characterization.

¹³Linear transfer coefficients of the measurement system can be eliminated by a reference measurement (R) on the empty (air-filled) sample cell of capacitance $C_{0,R}$ (also see Chapter 8.2). The permittivity magnitude is then given by

$$|\underline{\varepsilon}(\omega)| = \frac{C_{0,R} \hat{i}_S(\omega) \hat{u}_R(\omega)}{C_{0,S} \hat{i}_R(\omega) \hat{u}_S(\omega)}. \quad (5.56)$$

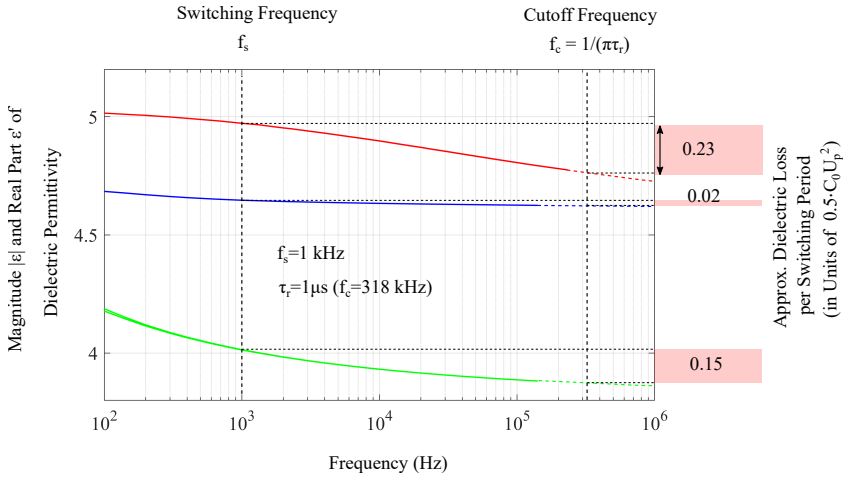


Figure 5.7.: Real part and magnitude (coinciding) of the complex dielectric permittivity of three commercial silicone potting compounds (measured with the setup described in Chapter 6). By using the approximation formulas derived in this chapter, a classification according to the dielectric loss rate under inverter voltages is easily obtained.

5.4. Instantaneous Dielectric Loss Rate?

Motivating question: *Is it possible to write down an expression of the instantaneous dielectric loss rate in terms of the dielectric response function (complex dielectric permittivity)?*

An expression of the *time-averaged* dielectric loss under arbitrary periodic excitations has been derived in Section 3.2.5. Is it possible to write an expression of the *instantaneous* dielectric loss rate in terms of the complex dielectric permittivity?¹⁴

Electrical energy flowing into a certain volume is either stored in there as recoverable (macroscopic¹⁵) electromagnetic energy (represented by an energy density w with units J m^{-3}) or irreversibly transformed (“dissipated”) into other forms of energy (e.g. thermal energy) at a rate p_d (units: W m^{-3}).

Consider an electromagnetic field described by the electric and magnetic field vectors¹⁶ $\mathbf{E}(t, \mathbf{r})$ and $\mathbf{H}(t, \mathbf{r}) = \mathbf{B}(t, \mathbf{r})/\mu_0$ inside a dielectric but nonmagnetic ($\chi_m = 0$) and nonconducting ($\kappa = 0$) material. The polarization response shall be modelled by

$$\mathbf{P}(t, \mathbf{r}) = \varepsilon_0 \int_0^\infty f(\tau) \mathbf{E}(t - \tau, \mathbf{r}) d\tau. \quad (5.57)$$

As follows from Maxwell’s equations [HM89], the electromagnetic energy flux density is given by the Poynting vector $\mathbf{S} = \mathbf{E} \times \mathbf{H}$. The general local energy balance can be written as

$$-\nabla \cdot \mathbf{S}(t, \mathbf{r}) = \frac{\partial w(t, \mathbf{r})}{\partial t} + p_d(t, \mathbf{r}). \quad (5.58)$$

For the considered case:

$$\begin{aligned} -\nabla \cdot (\mathbf{E}(t, \mathbf{r}) \times \mathbf{H}(t, \mathbf{r})) &= \frac{\partial}{\partial t} \left[\frac{\varepsilon_0}{2} \mathbf{E}(t, \mathbf{r})^2 + \frac{\mu_0}{2} \mathbf{H}(t, \mathbf{r})^2 \right] \\ &\quad + \mathbf{E}(t, \mathbf{r}) \cdot \frac{\partial \mathbf{P}(t, \mathbf{r})}{\partial t} \end{aligned} \quad (5.59)$$

¹⁴The question is admittedly of a rather academic nature, at least for three-dimensional systems, where the heat diffusion length within a fundamental period of the excitation voltage is generally negligible.

¹⁵Forms of energy related to microscopic electromagnetic fields – e.g. chemical binding energies, or elastic energy – are not included herein.

¹⁶Solutions of Maxwell’s equations for boundary conditions not specified here.

How to divide the right-hand side into $\frac{\partial w(t, \mathbf{r})}{\partial t}$ and $p_d(t, \mathbf{r})$?¹⁷

Conversion of electromagnetic to thermal energy can only occur through the term

$$\dot{w}_p(t, \mathbf{r}) = \mathbf{E}(t, \mathbf{r}) \cdot \frac{\partial \mathbf{P}(t, \mathbf{r})}{\partial t}. \quad (5.60)$$

It describes the rate in units of W m^{-3} at which energy is supplied to (> 0) or extracted from (< 0) the polarization degrees of freedom.

It seems that only time-average statements about the dielectric loss are possible within macroscopic electromagnetism, i.e. it seems impossible to formulate $p_d(t, \mathbf{r})$ in terms of purely macroscopic quantities (electric field and dielectric response function). In the macroscopic description, the actual mechanisms through which energy is transferred from the polarization degrees of freedom to the heat bath are not sufficiently characterized to allow the formulation of a corresponding expression. This would also imply that there is no expression for the recoverable energy $w_{\text{pol}}(t, \mathbf{r})$ stored in the polarization degrees of freedom at a certain instant of time for a given arbitrary excitation $E(t)$ (one might guess at something like $\frac{1}{2}E(t)P(t)$, but this only approaches the answer for “smooth enough” excitations, i.e. in the adiabatic limit). If it existed, then $p_d(t, \mathbf{r}) = \dot{w}_p(t, \mathbf{r}) - \dot{w}_{\text{pol}}(t, \mathbf{r})$, which was hypothesized not to exist.

This does not mean, of course, that one cannot make quantitative statements about dielectric loss, but rather that they are restricted to *integral* statements (and not local rates). For example, knowing the energy stored under static conditions (Equation (3.117)),

$$w_s = \frac{1}{2}E_0P_s = \frac{\varepsilon_0}{2}\chi'_e(0)E_0^2, \quad (5.61)$$

and the (net) amount of energy absorbed by the polarization (Equation (3.114)), one can calculate the dissipated energy from one to another static polarization state. Furthermore, the *average* dielectric loss can be calculated for *periodic* driving fields (not necessarily harmonic; see Section 3.2.5). Here, one can make use of the fact that all physical processes (including those not captured in detail by the model) are periodic in time and thus conclude that the *net* electromagnetic energy absorbed by the dielectric over one period must be dissipated during one period.

¹⁷I appreciated the supportive discussion with Prof. em. Len Dissado on this question. His timely conclusion: “I wish you luck with your question. It is good that we still have to think in science.”

6. Modular Offline Dielectric Spectrometer

“The most important aspect of any phenomenon from a mathematical point of view is that of a measurable quantity.”

James Clark Maxwell
in *A Treatise on Electricity and Magnetism*
(1873)

This chapter describes the design, setup and performance assessment of a modular low-voltage¹ (< 150 V peak) dielectric spectrometer, covering a frequency range from about 10^{-3} Hz to 10^5 Hz and a temperature range from about 15 °C to 125 °C. It is optimized for sample capacitances in the range ~ 0.1 pF to ~ 1 nF, thus allowing high-precision measurements ($\tan \delta \lesssim 10^{-4}$) on a large array of sample geometries, including low-capacitance specimens such as needle-plane configurations (example given in Chapter 6.3). Its intended areas of application include the characterization of the dielectric properties of candidate potting materials for MV MF applications (Chapter 9) as well as the quantification of aging-induced changes in insulation specimens exposed to electrical, thermal and environmental stressors (examples given in Chapter 6.2). Moreover, with its ability to use multitone excitation voltages, it served as a blueprint for an online dielectric spectrometer (Chapter 8) operating under medium-voltage inverter stress.

¹In this document, “offline” (as opposed to “online”) is meant to designate a measurement method that does not operate under an excitation voltage that significantly stresses the sample material. In other words, no aging of the material is expected to occur under offline testing.

6.1. Design and Setup

This chapter is based on the publications [FF18a] and [FF16].

6.1.1. Measurement Principle

Dielectric spectroscopy is based on a phase-sensitive impedance measurement of the specimen under study [KS03],

$$\underline{Z}(\omega) = \frac{\underline{U}(\omega)}{\underline{I}(\omega)}, \quad (6.1)$$

where \underline{U} and \underline{I} are the Fourier components of the applied voltage and the response current, respectively (see Figure 6.1). The (effective) dielectric permittivity $\underline{\varepsilon}(\omega)$ of the sample is then determined by²

$$\underline{\varepsilon}(\omega) = \varepsilon'(\omega) - j\varepsilon''(\omega) = \frac{1}{j\omega C_0 \underline{Z}(\omega)}, \quad (6.2)$$

where C_0 is the vacuum capacitance of the used electrode arrangement (e.g. $C_0 = \varepsilon_0 \left(\frac{D}{2}\right)^2 \pi/d$ for the shown parallel-plate geometry).

A voltage $U(t)$ of period $T = 2\pi/\omega$ is applied to the electrode configuration containing the dielectric material to be investigated. Guard electrodes are often used to create a well-defined probed insulation volume (e.g. parallel plate dielectric in uniform electric field).³ The supply current in the wire connected to the measurement electrode equals the sum of the vacuum displacement current (Equation (3.70)), the polarization current (Equation (3.72)) and the conduction current (Equation 3.71) from the probed sample volume.

The main challenge hinges on the required precision (resolution) and accuracy on the phase measurement. Indeed, insulation materials – especially those suitable for MF applications – feature loss angles δ on the order of 10^{-4} rad to 10^{-2} rad. Measuring 10^{-4} rad requires a system resolution on the order of $10^{-4}/2\pi$. It is thus important to take into

²The subscript “eff” is omitted here.

³At lower frequencies (typically sub-Hz), the guard electrode is in addition responsible for preventing surface currents from reaching the measurement electrode.

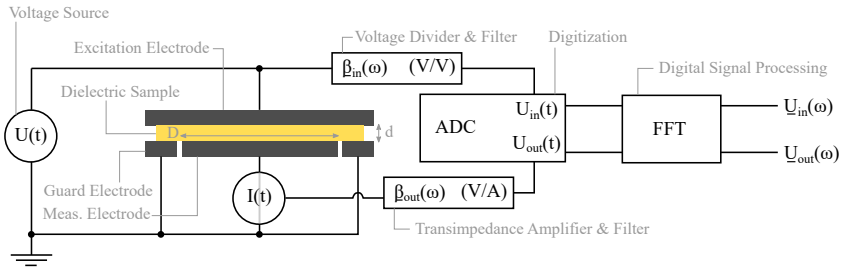


Figure 6.1.: Functional diagram the dielectric spectroscopy setup.

account the system transfer functions⁴: the Fourier components of the digitized voltages, $\underline{U}_{\text{in}}(\omega)$ and $\underline{U}_{\text{out}}(\omega)$, are related to the Fourier components of the excitation voltage, $\underline{U}(\omega)$, and the sample current, $\underline{I}(\omega)$, by complex transfer coefficients $\underline{\beta}_{\text{in}}(\omega)$ and $\underline{\beta}_{\text{out}}(\omega)$ that depend on the system configuration (voltage divider, filters, amplifiers, ADC cabling, etc.):

$$\underline{U}(\omega) = \underline{\beta}_{\text{in}}(\omega)\underline{U}_{\text{in}}(\omega) \quad (6.3)$$

$$\underline{I}(\omega) = \underline{\beta}_{\text{out}}(\omega)\underline{U}_{\text{out}}(\omega). \quad (6.4)$$

The unknown transfer functions may be determined by simulations and measurements (see discussion in Section 2.4.3), but for simplicity and increased accuracy, a reference measurement principle is applied here. It consists in first measuring the applied voltage and response current of the sample (S) of vacuum capacitance $C_0^{(S)}$:

$$\underline{U}_S(\omega) = \underline{\beta}_{\text{in}}^{(S)}(\omega)\underline{U}_{\text{in}}^{(S)}(\omega) \quad (6.5)$$

$$\underline{I}_S(\omega) = \underline{\beta}_{\text{out}}^{(S)}(\omega)\underline{U}_{\text{out}}^{(S)}(\omega). \quad (6.6)$$

The associated sample impedance thus reads

$$\underline{Z}_S = \frac{1}{j\omega C_0^{(S)}\underline{\varepsilon}(\omega)} = \frac{\underline{U}_S(\omega)}{\underline{I}_S(\omega)} = \frac{\underline{\beta}_{\text{in}}^{(S)}(\omega)\underline{U}_{\text{in}}^{(S)}(\omega)}{\underline{\beta}_{\text{out}}^{(S)}(\omega)\underline{U}_{\text{out}}^{(S)}(\omega)}. \quad (6.7)$$

⁴Measurement system linearity is assumed.

Subsequently, with the same data acquisition parameters, a reference measurement (R) is performed on an air capacitor of capacitance $C_0^{(R)}$ featuring $\underline{\varepsilon}^{(R)}(\omega) = 1$:

$$\underline{U}_R(\omega) = \underline{\beta}_{\text{in}}^{(R)}(\omega)\underline{U}_{\text{in}}^{(R)}(\omega) \quad (6.8)$$

$$\underline{I}_R(\omega) = \underline{\beta}_{\text{out}}^{(R)}(\omega)\underline{U}_{\text{out}}^{(R)}(\omega), \quad (6.9)$$

with the associated impedance

$$\underline{Z}_R = \frac{1}{j\omega C_0^{(R)}} = \frac{\underline{U}_R(\omega)}{\underline{I}_R(\omega)} = \frac{\underline{\beta}_{\text{in}}^{(R)}(\omega)\underline{U}_{\text{in}}^{(R)}(\omega)}{\underline{\beta}_{\text{out}}^{(R)}(\omega)\underline{U}_{\text{out}}^{(R)}(\omega)}. \quad (6.10)$$

An expression for $\underline{\varepsilon}(\omega)$ is found by dividing Equation (6.10) by Equation (6.7):

$$\underline{\varepsilon}(\omega) = \frac{C_0^{(R)}}{C_0^{(S)}} \cdot \underbrace{\frac{\underline{\beta}_{\text{in}}^{(R)}(\omega)}{\underline{\beta}_{\text{in}}^{(S)}(\omega)}}_{\approx 1} \cdot \underbrace{\frac{\underline{\beta}_{\text{out}}^{(S)}(\omega)}{\underline{\beta}_{\text{out}}^{(R)}(\omega)}}_{\approx 1} \cdot \frac{\underline{U}_{\text{out}}^{(S)}(\omega)}{\underline{U}_{\text{out}}^{(R)}(\omega)} \cdot \frac{\underline{U}_{\text{in}}^{(R)}(\omega)}{\underline{U}_{\text{in}}^{(S)}(\omega)}. \quad (6.11)$$

The major simplifying step is obtained by using the same data acquisition parameters on the sample and reference measurement, and hence to assume that $\underline{\beta}_{\text{in}}^{(S)}(\omega) \approx \underline{\beta}_{\text{in}}^{(R)}(\omega)$ and $\underline{\beta}_{\text{out}}^{(S)}(\omega) \approx \underline{\beta}_{\text{out}}^{(R)}(\omega)$. The complex dielectric permittivity of the sample is then directly linked to the ratio of vacuum capacitances and the measured voltages:

$$\underline{\varepsilon}(\omega) = \frac{C_0^{(R)}}{C_0^{(S)}} \cdot \frac{\underline{U}_{\text{out}}^{(S)}(\omega)}{\underline{U}_{\text{out}}^{(R)}(\omega)} \cdot \frac{\underline{U}_{\text{in}}^{(R)}(\omega)}{\underline{U}_{\text{in}}^{(S)}(\omega)}. \quad (6.12)$$

The ratio of the vacuum capacitances of the sample cell and the reference capacitor only influences the magnitude (but not the phase) of the dielectric permittivity. The vacuum capacitances can be determined by

- **Calculation:** if the electrode geometry is known, the vacuum capacitance can be determined by analytical formulas or FEM simulations.

- **Measurement:** if the electrode geometry is not known (sufficiently well), one can impose the permittivity magnitude $|\underline{\varepsilon}(\omega_r)|$ at a certain reference frequency (e.g. $\omega_r = 2\pi$ kHz). The vacuum capacitance is then obtained from an impedance magnitude measurement:

$$C_0 = \frac{1}{\omega_r |\underline{\varepsilon}(\omega_r)| |\underline{Z}(\omega_r)|}. \quad (6.13)$$

The system gain at ω_r (magnitude ratio $|\beta_{\text{out}}(\omega_r)/\beta_{\text{in}}(\omega_r)|$) can be calibrated once with an impedance standard (air capacitor GenRad 1404-B/100 pF used here).

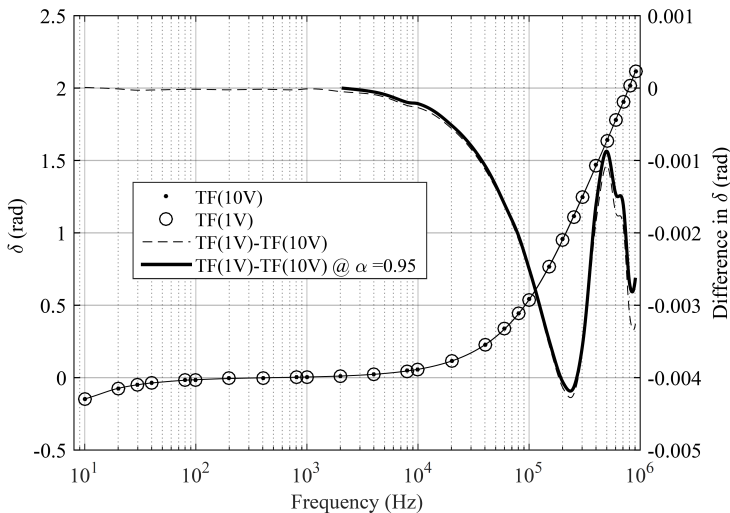


Figure 6.2.: Nonlinear phase transfer in the analog signal chain of the current measurement. In a "perfectly" linear system the two sample currents (whose amplitude differs by a factor of 10) would not generate a systematic difference in the phase value. The thick black line indicates the phase difference that is statistically significant at a confidence level of $\alpha = 0.95$.

Measurements revealed a statistically significant nonlinear phase transfer through the transimpedance amplifier, see Figure 6.2. The shown phase transfer was obtained by applying a sinusoidal signal of 1 V and 10 V (peak/peak), respectively, to a 1 M Ω through-hole resistor (metal film, 0.25 W) mounted into a coaxial housing and feeding the resulting current

to the transimpedance amplifier (with the gain set to 10^6 V A^{-1}). In this scenario, significant nonlinear behavior is observed above $f_c/10$, where $f_c = 200 \text{ kHz}$ is the -3 dB cutoff frequency of the chosen gain stage. The gain difference (locally) peaks at about f_c . Hence, the phase of the transfer coefficient $\beta_{\text{out}}(\omega)$ actually depends on the value of the sample current. In order to mitigate this influence for maximal precision, an automatically variable air capacitor has been designed. If high-precision measurements ($\tan \delta \leq 10^{-4}$) are required, its value is adjusted at every measurement frequency to ensure that the RMS value of the sample current and the current through the reference capacitor are equal to within a prescribed tolerance:⁵

$$I_{\text{RMS}}^{(R)} \approx I_{\text{RMS}}^{(S)}. \quad (6.14)$$

A more detailed description of the various components constituting the full setup is provided in the next section.

6.1.2. Layout and Components

Figure 6.3 shows a schematic of the full setup.

The periodic voltage excitation $U(t) = U(t+T)$ is applied by the arbitrary waveform generator ① (Keysight 33210A). A linear amplifier ② (Falco Systems WMA-300) is used in order to extend the excitation voltage range from $\pm 10 \text{ V}$ to $\pm 150 \text{ V}$. The excitation voltage is then either routed to the test cell ④ (sample measurement) or the variable air capacitor ⑦ (reference measurement) by a RF relay ③ (Keysight 8762A). The sample cell accommodates various sample geometries, such as parallel-plate ⑤a or recessed ⑤b specimens. The supply current to the measurement electrode is converted into a voltage U_{out} by a low-noise transimpedance amplifier ⑧. Two models are used in parallel (automatically switched) (FEMTO® DDPCA-300 and DLPCA-200) to cover an overall range of transimpedance gains from 10^3 V A^{-1} to 10^{13} V A^{-1} . The excitation voltage is stepped down by a 29:1 voltage divider⁶ to yield U_{in} . Both U_{in} and U_{out} are band-pass filtered ⑧ in order increase the SNR as well as to

⁵Unless low-capacitance samples ($\lesssim 0.5 \text{ pF}$) are measured, it is not necessary to adjust the reference capacitor at every excitation frequency. In practice, the reference capacitance is readjusted when a certain user-specified relative difference to the sample capacitance is detected.

⁶Custom-made coaxial design with a parallel R-C high- and low-voltage impedance. Its -3 dB cutoff frequency is above 1 MHz . Its phase transfer is taken into account by the referencing procedure explained in Section 6.1.1.

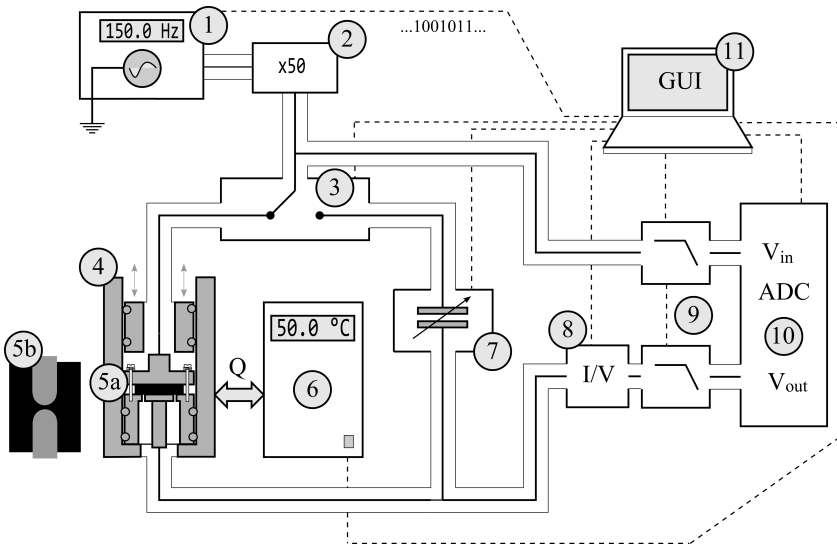


Figure 6.3.: Detailed schematic of the dielectric spectroscopy setup. The signal lines are coaxially shielded throughout the analog stage. The broken lines represent digital or analog control signals. The numbered components are mentioned in the main text.

avoid aliasing in the subsequent digitization stage (10). An NI9223 USB ADC (1MSa/s simultaneous sampling rate, 1MHz analog bandwidth, 16-bit vertical resolution) is used. A graphical user interface (11) written in MATLAB® allows to control and automate the setup (see Section 6.1.5). The thermostat (5) allows to vary the test cell temperature from 15°C (non-condensing) to 125°C.

6.1.3. Undersampling

An undersampling technique is employed to increase the apparent sampling frequency above the available 1MSa/s on periodic waveforms. To this end, the fundamental frequency f_0 is fine-tuned such that with the exactly available sampling frequencies f_s of the ADC one has $m/f_0 = n/f_s$, where n and m are positive integers (*coherent* sampling). This allows using rectangular windowing for the Discrete Fourier Transform (DFT)

without spectral leakage. In the undersampling mode one chooses in addition $n = 2^q$ with integer q and $m > 2$ prime such that m signal periods are sampled at 2^q non-equivalent phase positions. The sampled points are then reduced to a single period virtually sampled at $m \cdot f_s$. In practice, a maximal value of about $m = 19$ (corresponding to a virtual sampling frequency of 19 MHz) was determined as a reasonable upper bound for the used ADC (NI 9293), beyond which the precision/accuracy of the phase measurement was noticeably affected by timing errors.

In a later version of the setup, a USB oscilloscope (TiePie HS6 DIFF) featuring 14-bit resolution up to 100 MSa/s on two channels was used, rendering the undersampling technique unnecessary. The referencing technique takes care of the intrinsic phase shift resulting from the non-simultaneous sampling of the ADC channels.

6.1.4. Data Acquisition and Processing

Due to the use of coherent sampling (see previous section), a rectangular window was used for the FFT. First, the excitation is routed to the sample (S) cell and a number N of single fundamental periods (of duration $T = f_0^{-1}$) are digitized (n data points) and their Fourier components determined⁷

$$\underline{U}_{\text{in},k}^{(S)} = \underline{U}_{\text{out}}^{(S)}(\omega_k) \quad (6.15)$$

$$\underline{U}_{\text{out},k}^{(S)} = \underline{U}_{\text{out}}^{(S)}(\omega_k), \quad (6.16)$$

where $\omega_k = k \frac{2\pi}{T}$ with $k = 1, 2, \dots, \frac{n}{2}$. An equivalent measurement is performed on the reference (R) capacitor, yielding the Fourier components

$$\underline{U}_{\text{in},k}^{(R)} = \underline{U}_{\text{out}}^{(R)}(\omega_k) \quad (6.17)$$

$$\underline{U}_{\text{out},k}^{(R)} = \underline{U}_{\text{out}}^{(R)}(\omega_k). \quad (6.18)$$

The mean complex dielectric permittivity is then calculated according to Equation (6.12):

⁷The number of acquired fundamental periods ranges typically from $N=5$ to $N=50$, depending on the required precision.

$$\underline{\varepsilon}_k = \frac{C_0^{(R)}}{C_0^{(S)}} \frac{1}{N} \sum_{i=1}^N \frac{U_{\text{out},k}^{(S)}}{U_{\text{out},k}^{(R)}} \cdot \frac{U_{\text{in},k}^{(R)}}{U_{\text{in},k}^{(S)}}. \quad (6.19)$$

In principle, information about the dielectric permittivity can be obtained at all frequencies whose SNR is sufficiently high to generate meaningful results. Measuring several frequencies simultaneously reduces the measurement time (which can be especially relevant at sub-Hz frequencies), but also claims some compromises in precision because the SNR is highest for a single sinusoid. Multitone signals⁸ represent a good trade-off, and are used in the study presented in Chapter 6.2.

Confidence Interval

In order to assess the “robustness” of a measured value, confidence intervals (confidence level $\alpha = 0.95$) on the calculated mean value of the dielectric permittivity (Equation (6.19)) are calculated. The confidence interval associated with the mean value \bar{x} of a measured quantity (random variable) X is given by⁹

$$\left[\bar{x} - \frac{t_{\alpha/2, N-1}}{\sqrt{N}} s_N, \bar{x} + \frac{t_{\alpha/2, N-1}}{\sqrt{N}} s_N \right], \quad (6.20)$$

where s_N is the measured standard deviation, and $t_{\alpha/2, N-1}$ is Student’s t coefficient¹⁰.

⁸E.g. adding up the harmonics $f_n/f_0 = (1, 2, 3, 4, 6, 8, 14)$ with random phases and amplitudes $\propto n^{-\frac{1}{2}}$.

⁹Note that it is *not* necessary for the random variable X to be normally distributed, because for calculating the confidence interval *on the mean value*, the required assumption is that $\bar{X}_N = N^{-1} \sum_{i=1}^N X_i$ (where the X_i are distributed according to the same PDF as X) be distributed normally. This, however, is approximately the case as shown by the *Central Limit Theorem* []. A number $N \gtrsim 10$ is sufficient to obtain a degree of normality of \bar{X}_N that ensures the practical validity of the constructed confidence interval on the mean value, even if the probability distribution of X is far from normal.

¹⁰Given in MATLAB® by `tinv`($\alpha/2, N - 1$).

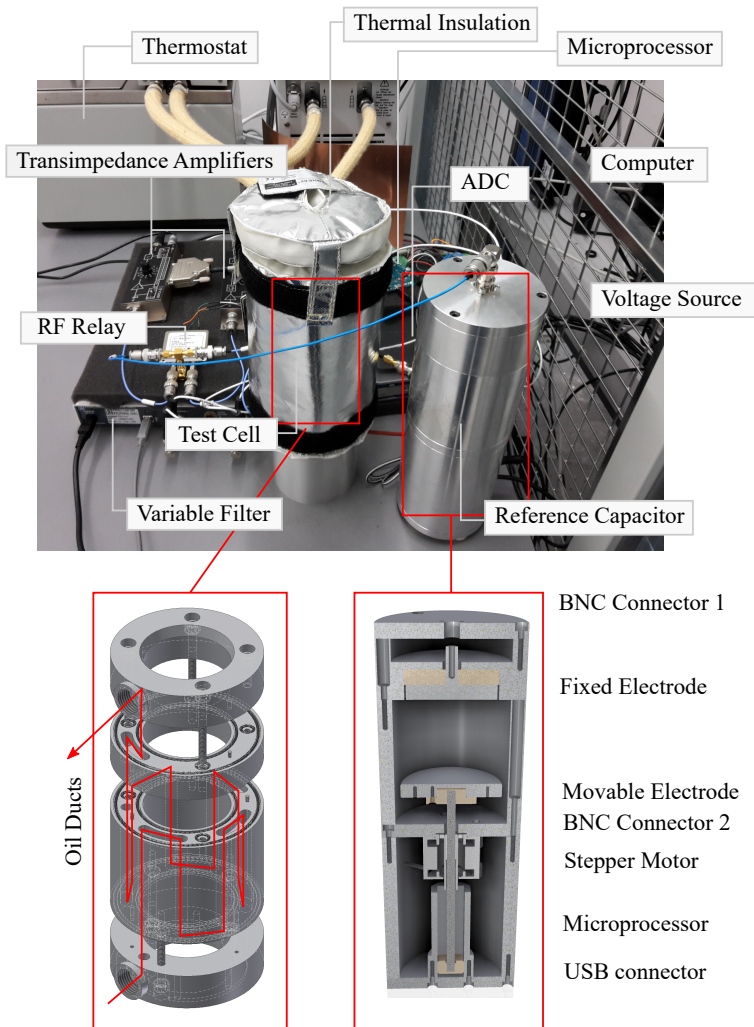


Figure 6.4.: Assembled dielectric spectroscopy setup.

6.1.5. Control and Automation Software

A graphical user interface (Figure 6.5) was implemented in MATLAB[®], interfacing all instruments (ADC, transimpedance amplifiers, variable filter, RF relays, thermostat, microprocessors, function generator) and thus allowing to control and monitor all operations of the dielectric spectrometer. In addition, text file instructions can be uploaded for automated temperature and frequency scans. Each line corresponds to one measurement and all variables on the GUI are accessible through keyword/value pairs:

```
% T=25C
f0=100000 Vac=100 T=25 Np=1000 Nphase=25 AdjustC0=1
f0=100000 Vac=200
f0=80000 Vac=100
f0=80000 Vac=200
...
f0=0.1 Vac=200 Nphase=5
% T=45C
f0=100000 Vac=100 T=45 Np=1000 Nphase=25 AdjustC0=1
...
f0=0.1 Vac=200 Nphase=5
...
% T=65C
...
```

Moreover, the acquired raw data can be inspected and processed (FFT, averaging, confidence interval), and the extracted measurement results (complex diel. permittivity, impedance,...) are automatically displayed as a function of the desired parameter (e.g. $\tan \delta$ as a function of fundamental frequency f_0 , temperature T or excitation voltage amplitude V_{ac} in the above example). The displayed parameter dependencies can then be exported as `.mat` or `.txt` files.

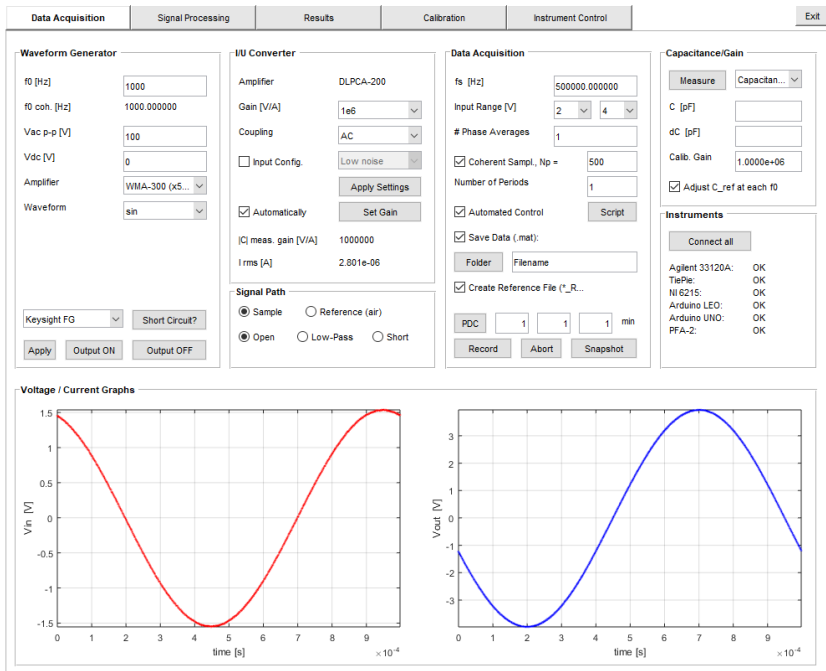


Figure 6.5.: GUI for control and automation of the dielectric spectrometer.

6.1.6. Benchmark Data

Noise and Interference

Noise and interference showing up in the measured values representing the excitation voltage and response current (i.e. U_{in} and U_{out}) limit the achievable resolution and accuracy in the derived values of the dielectric permittivity. These unwanted contributions can be intrinsic to the components in the analog signal processing devices such as the transimpedance amplifier(s), filter, ADC, etc. (in which case it is called *noise*), or be induced by a source of electromagnetic energy outside these components, such as switched power supplies, vibrating cables, etc. (in which case it is called *interference*).

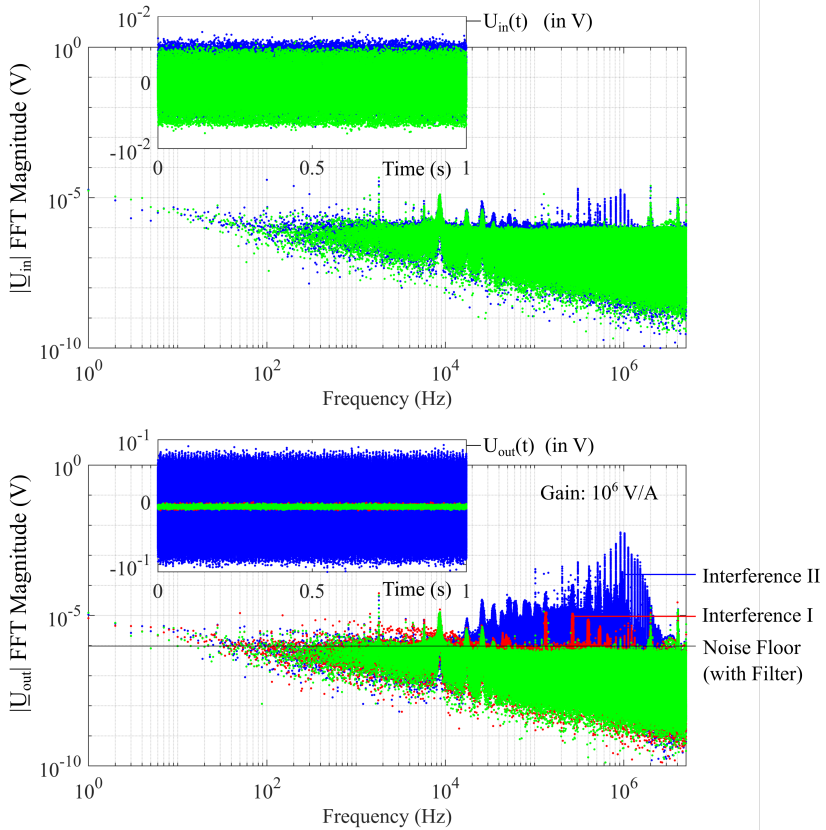


Figure 6.6.: Example of noise/interference spectra at a transimpedance gain of 10^6 V A^{-1} with no excitation voltage applied (i.e. nominal 0 V). a) Measured input voltage b) Measured output voltage. See main text for an explanation of the different curves.

Figure 6.6 shows the recorded voltages on both channels (U_{in} and U_{out}) in time and frequency domain, when no voltage is applied to the electrodes by means of the function generator/linear amplifier (i.e. nominal 0 V). The noise floor obtained by employing the filter unit is at 1 μV , which thus represents the minimum achievable (white) noise level in this configuration. The transimpedance amplification for the shown example is 10^6 V A^{-1} . The minimal achievable noise floor is limited by the amplification stage, and depends on the chosen amplification value, as specified in the data sheets of the amplifiers (FEMTO[®] DDPKA-300 and DLPCA-200). Without dedicated filtering, relatively large interference peaks are present, especially in the range from 10 kHz to 2 MHz (see “Interference II” curve in Figure 6.6). Most of these are coupled into the system upstream of the transimpedance amplifier input.¹¹ Indeed, when the input of the transimpedance amplifier is shielded with a BNC termination cap, the significantly reduced “Interference I” signal is measured.

The achievable precision (and accuracy) on the value of the (complex) dielectric permittivity is observed to be very sensitive to the magnitude of the (uncorrelated) noise/interference present in the digitized¹² excitation and response voltages. Simulations results obtained by contaminating the input voltages of the ADC (U_{in} and U_{out}) with uncorrelated white noise have shown that the achievable precision (of both the magnitude and phase of the permittivity) scales linearly with the noise floor level. The phase measurement in noisy environments is especially challenging for low-loss materials ($\delta \leq 10^{-4}$), because of the inherently high resolution and accuracy ($\delta/2\pi \leq 10^{-4}/2\pi$) required to obtain meaningful results.

Precision and Stability

Measurement precision and instrument stability are the two relevant figures of merit in aging studies. The measured time evolution of the di-

¹¹Most likely due to inductively induced circular currents in the BNC shields of the loop comprising the sample cell and the reference capacitor and the connecting cables (because the interference is strongly reduced when only the measurement cell alone is connected). These currents generate associated voltage drops along the shield and thus a contaminated “ground” node potential used by the transimpedance amplifier as a signal reference. In the frequency range covered by this setup (up to a few 100 kHz), the use of shielded twisted pairs (STP) instead of coaxial cables would be a good alternative to circumvent this type of interference (there the current return conductor is separate and thus the interfering shield currents cannot induce a potential drop in it).

¹²Digitization itself adds the so-called *quantization noise*, whose noise floor level depends on the vertical resolution of the ADC.

electric response of a 3 mm thick disc of PTFE for a sinusoidal excitation frequency of 1 kHz at a regulated test cell temperature of $22(\pm 0.1)^\circ\text{C}$ is shown in Figure 6.7. The measured capacitance is $1.9(\pm 0.02)\text{pF}$. While there is no significant drift in the value of $\tan\delta$ over the examined time interval, the magnitude of the complex permittivity changes significantly. However, relatively speaking, this magnitude drift is less than 0.05 %, and thus does not noticeably compromise the practically usable precision for long-term magnitude measurements. While phase resolution is typically of the order of 5×10^{-5} rad for $N=25$ averaged periods and multitone excitation, it can be decreased down to 10^{-6} rad with pure sinusoidal excitation and $N=100$ averages, as used for the high-precision measurements on PTFE displayed in Figure 6.7. The scatter increases somewhat at the low (< 1 Hz) and high (> 10 kHz) range of the frequency spectrum, but it can in principle be decreased by increasing the number of acquired periods N (at the expense of an increased data volume/measurement time).

In conclusion, the usable (i.e. stability-limited) precision is about 10^{-3} for the relative permittivity magnitude and $5 \cdot 10^{-5}$ for its phase.

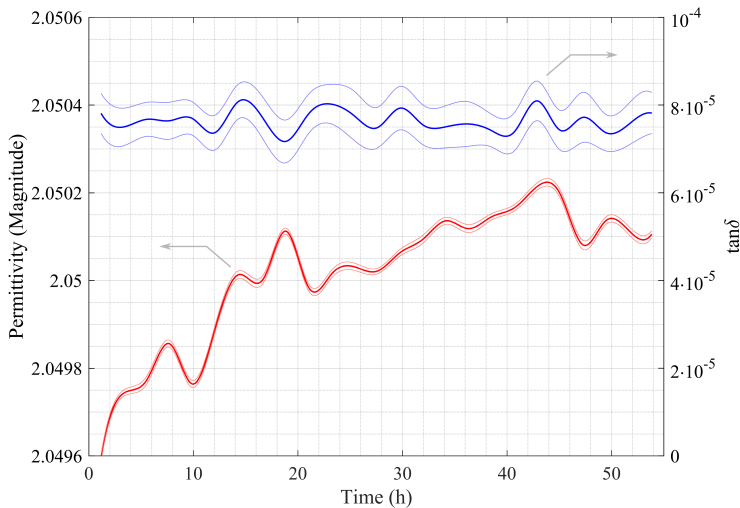


Figure 6.7.: Time evolution of the complex dielectric permittivity of a 3 mm thick PTFE disc inside the test cell at $f=1$ kHz and 22°C . The semitransparent lines demarcate the 95 % confidence interval.

Accuracy

In practice, the achievable accuracy on the permittivity magnitude is often limited by the uncertainty about the exact sample geometry rather than the inherent system accuracy. Nonetheless, the system was calibrated by means of an air capacitor standard (GenRad 1404-B/100 pF), which is expected to provide a basic relative system accuracy on the order of $\pm 1\%$. The phase accuracy is mostly determined by the impact of the non-linear signal transfer (strongly reduced by the use of a continuously variable reference capacitance) as well as the effect of parasitic line elements that are not fully “cancelled” by the employed referencing procedure (e.g. series inductance of the cabling). Measurements on PTFE disks lead to an estimated overall phase accuracy of about 10^{-4} rad in the range from 10 mHz to 100 kHz. The measured values of the magnitude (2.05) and phase (8×10^{-5}) of the dielectric permittivity of PTFE (see Figure 6.7) agree well with those reported in literature [EAB53].

Table 6.1.: Dielectric spectrometer: technical specifications.

Parameter	Value	Unit
Frequency	$10^{-3} \dots 2 \times 10^5$	Hz
Peak Excitation Voltage	150	V
DC Bias Voltage	up to 150	V
Sample Capacitance	$\leq 0.1 \dots > 100$	pF
$\tan \delta$ Resolution	5×10^{-5}	–
$\tan \delta$ Accuracy	10^{-4}	–
Abs. Magnitude Precision	0.1	%
Rel. Magnitude Accuracy	1	%
Temperature	15 .. 125	°C

6.2. Quantifying Aging-Induced Changes of Dielectric Permittivity in an Epoxy Polymer

“The process of ageing in a material like a polymer is highly complex and involves constant changes on a molecular level. This results in bond rupture and reformation. If the polymer also experiences a stress such as an applied electric field, the processes of bond rupture and reformation are altered. Eventually, there will come a time when the material has changed to such an extent that it is no longer able to perform its designed task and in the case of an electrical insulation, this will result in electrical breakdown.”

C.L. Griffiths, J. Freestone and R.N. Hampton
in *Thermoelectric Aging of Cable Grade
XLPE [GFH98]* (1998)

This chapter is based on the publication [FF18a].

Abstract

A custom-made modular high-precision dielectric spectrometer is used for quantifying aging-induced molecular changes in (sub-)picofarad polymeric samples. Validation and characterization of the setup's performance is obtained by quantifying the change in the dielectric response of an epoxy polymer following the exposure to thermal, hygrothermal and ultraviolet radiation stress. It is shown that the observed changes in the dielectric spectra can be resolved with a relative precision better than 5×10^{-5} and are in line with previous studies employing commercial instruments on samples of higher capacitance. This setup is intended to serve as a blueprint for a sensitive and extensible (because modular) measurement tool for studying the pre-breakdown dynamics in low-capacitance recessed or disc-shaped specimens as used, e.g., in high-voltage insulation testing.

6.2.1. Introduction

The goal of this chapter is to characterize the modular dielectric spectroscopy setup presented in Chapter 6.1 with respect to its ability in detecting and tracking changes in a dielectric material occurring at a

microscopic level as a consequence of intentionally exposing it to specific environmental stresses. The which are expected to lead to changes in their molecular structure and therefore, potentially, to an altered dielectric response.

6.2.2. Methods

Instrumentation & Measurement

The dielectric spectrometer described in Chapter 6.1 is used to record the dielectric response of the pristine and aged epoxy polymer disc samples. The used excitation voltage amplitude is 75 V peak.

Especially at low frequencies (< 1 Hz), a tradeoff between measurement time and precision is required. In this study, N was therefore decreased from 50 to 9 as the fundamental frequency approached the lower end of the recorded spectrum. A further reduction in measurement time can be obtained by using multisine excitation waveforms. The multisine waveform with harmonic frequencies $f_n/f_0 = 1, 2, 3, 4, 6, 8, 14$ and amplitudes $\propto f_n^{-\frac{1}{2}}$ have been used here (random phases). Thus, only six fundamental frequencies (0.1 Hz, 1 Hz, 10 Hz, 100 Hz, 1 kHz, 10 kHz) are needed to sweep the frequency range from 0.1 Hz to 140 kHz with 42 logarithmically spaced data points. A comparative validation measurement showed very good agreement between multisine and pure sinusoidal excitations (as would be expected for a linear dielectric response).

The continuous lines in the results plot are obtained by spline interpolation between the 42 measured data points.

Samples

The unfilled epoxy system CR 76.05 / CH 76.05 from bto epoxy GmbH was chosen for these investigations. It is a slow-curing, low-viscosity resin consisting of Bisphenol-A-Epichlorhydrin (BPA-ECH) monomers (>70 %w) and the reactive diluents Oxirane (<15 %w) and Glycidylether (<10 %w). The latter reduce the cross-link density of the cured polymer, thus allowing the manufacturing of crack-free recessed specimens with embedded electrodes, which may be used in later studies focusing on electrical degradation under PWM medium-voltage stress. This property, rather than a specific stress-resistance profile, was the main reason for

choosing this epoxy system. The cross-linking into a network polymer is obtained by reaction with a diamine hardener (Polyoxipropylenediamine). The glass transition temperature (T_g) of the cured pristine polymer was determined by Differential Scanning Calorimetry (DSC) on a 10 mg sample (Mettler Toledo DSC1 Star^e) and found to be $T_{g,DSC}=39(\pm 1)^\circ\text{C}$.

Table 6.2.: Characteristics of the investigated sample.

Property	Value	Unit
Material	Unfilled Epoxy Polymer	–
$T_{g,DSC}$	$39(\pm 1)$	$^\circ\text{C}$
Thickness	4 ± 0.02	mm
Probed Diameter	20 ± 0.02	mm
Vacuum Capacitance	~ 0.7	pF

For the aging studies presented in this chapter, disc-shaped ④a rather than recessed ④b specimens were used, because the diffusion of water into the probed polymer volume of the recessed specimen would take an inordinate amount of time. Additionally, its probed volume would be protected from UV radiation by the surrounding polymer volume. A (4 ± 0.02) mm thick plate was cast and heat-cured ($T_{\max}=60^\circ\text{C}$, 48 hours overall curing time). All discs used in this study were subsequently cut from the same epoxy plate in order to ensure equal initial properties. They were stored under dry vacuum (<1 mbar, 40°C) for at least two weeks prior to exposing them to the stresses described in the following subsection. The unaged spectra shown for comparison have been recorded for each pristine sample immediately before stress exposure. Electrode contact was realized by slightly pressing the polished aluminum electrodes onto the sample with a spring-controlled force (~ 5 N). The measurement electrode is 20 mm in diameter (0.2 mm guard gap), resulting in a vacuum capacitance of about 0.7 pF. No surface treatment (e.g. conductive paint) was applied in order to avoid diffusive contamination of the sample during the prolonged stress exposures. The main characteristics of the investigated sample are summarized in table 6.2.

Imposed Stresses

Elevated temperatures, oxidation, ultraviolet radiation and water ingress are known to have significant adverse effects on many of the useful properties which characterize polymers [KMN14] (Chapter 15). These stressors were thus expected to lead to significant molecular changes in the polymer structure and thus to a potentially measurable change in its dielectric response. Thermal stress was applied by placing the sample in an air-filled oven (natural convection) at atmospheric pressure for a total of 48 hours. The temperature was regulated to $125 \pm 2^\circ\text{C}$. and the relative humidity kept below 0.5 %. Hygrothermal stressing consisted of placing the sample into deionized water at $70 \pm 2^\circ\text{C}$ for 72 hours. The sample was surface-dried for subsequent dielectric analysis. Finally, a mercury arc lamp (HBO 200 W/2 L1) was used to irradiate the sample disc with ultraviolet light (each side for 4.5 hours). The sample was convectively cooled during irradiation to keep the surface temperature at $55 \pm 2^\circ\text{C}$. The relative humidity at room temperature was $40 \pm 5\%$. An overview of the applied stress conditions is given in table 6.3.

Table 6.3.: Summary of the applied stress conditions.

Type	Duration (h)	Temp. ($^\circ\text{C}$)	Amb. medium
Thermal	48	125 ± 2	Air
Hygrothermal	72	70 ± 2	Water
UV	9	55 ± 2	Air

6.2.3. Results

This section presents the observed change in the dielectric response of the samples as a result of the stress conditions described in the previous section. The results obtained from the pristine sample are used to illustrate the microphysical origin of the typical polarization dynamics of amorphous polymers.

Pristine Sample

The measured dielectric response of the unaged sample is shown in Figure 6.8 for several temperatures around the glass transition ($T_{g,DSC}=39^\circ\text{C}$). The distinguishable relaxations in the measured frequency band are characteristic for glass-forming materials [MP09] (Chapter 6). At temperatures below the glass transition the polymer segments between crosslinks are locked in place and only local, sterically hindered orientation of permanent dipoles associated with side groups and small parts of the main chain are possible. This so-called β -relaxation is thermally activated and the corresponding loss peak thus moves to higher frequencies when the temperature increases. It thus moves out of the measured frequency window and is well distinguishable only at low temperatures between 10 kHz and 150 kHz. At the lower end of the recorded spectrum, the right wing of the loss peak of the segmental α -relaxation process enters the frequency window. It originates in movements of large segments of the polymer backbone. Its maximum enters the observed frequency range some 10°C above $T_{g,DSC}$ and merges with the β -relaxation peak at higher temperatures. For the investigated polymer, loss due to long-range charge migration is negligible in the glassy state but dominantly emerges in the viscoelastic state with its characteristic ω^{-1} contribution (see Equation (3.96)).

Thermally Aged Sample

The thermally aged sample displayed a spectrally uniform relative decrease of the loss factor in the order of 10 to 20% for temperatures up to the glass transition temperature of the unaged sample (see Figure 6.9). Higher temperatures reveal that the position of the loss peak associated with segmental motion is shifted horizontally to lower frequencies while its peak value remains unaffected. A horizontal shift of equal magnitude is also observed in the loss associated with long-range charge migration. The sample mass loss during the aging interval was found to be about 0.5%. The optical appearance of the sample turned from clear to a yellow-brownish color (still fully translucent). Another 48 hour thermal stress period lead to further changes which showed the same overall trend, but were much less pronounced as compared to the first 48 hours of thermal aging.

Hygrothermally Aged Sample

In contrast to thermal aging, the hygrothermal stressing lead to a strong relative increase in the dielectric loss factor of the order of 50 to 100 % below the glass transition (see Figure 6.10). The α -relaxation loss peak is shifted horizontally to higher frequencies while its peak value remains unaffected. An additional low-frequency relaxation process is discernable above the glass transition. It is superimposed to the strongly enhanced loss from DC conductivity and eventually becomes buried underneath the latter as the temperature is further increased.

The sample's weight gain during water immersion amounted to 1.3 %w. An additional stress period of 72 hours was observed to lead to further sample mass increase (2.3 %w) and a correspondingly even more pronounced manifestation of the changes described above. Regarding its optical appearance, a slight yellowing of the sample could be discerned. Upon drying the sample for one week at 50 °C in vacuum (1 mbar), the observed spectral changes could be largely reversed, except for the DC conduction loss, which could be reduced to some extent but remained significantly higher in comparison to the pristine sample.

UV-Irradiated Sample

As can be seen on Figure 6.11, the relative changes in the sample's dielectric response were relatively small except for the lowest measured temperature(s). The magnitude and position of the α -relaxation loss peak remained virtually unchanged.

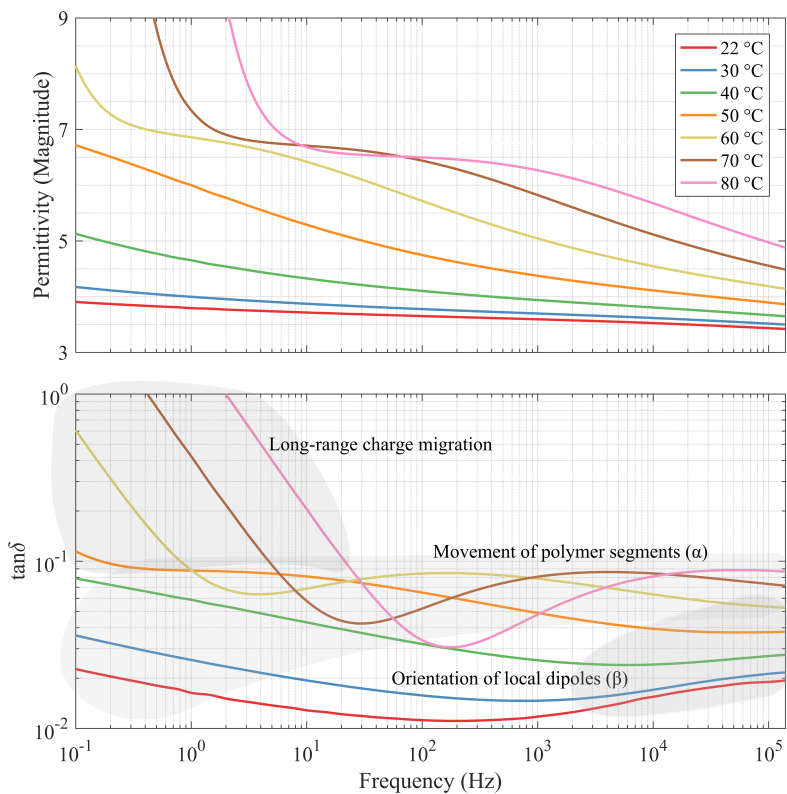


Figure 6.8.: Dielectric response of an unaged sample of the epoxy polymer as a function of excitation frequency and temperature.

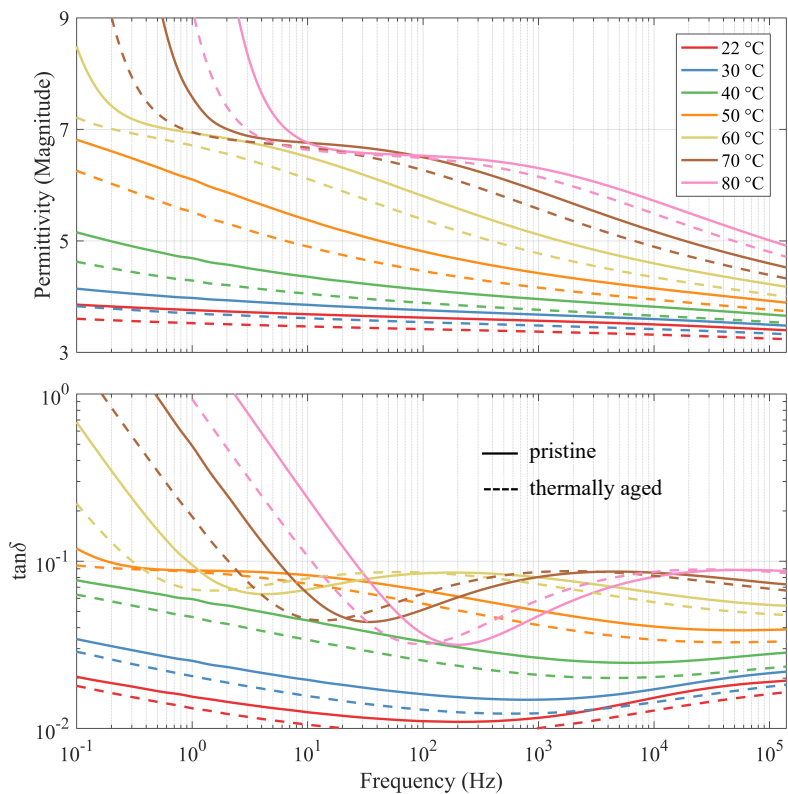


Figure 6.9.: Dielectric response of the unaged sample (continuous line) and the thermally aged sample (broken line).

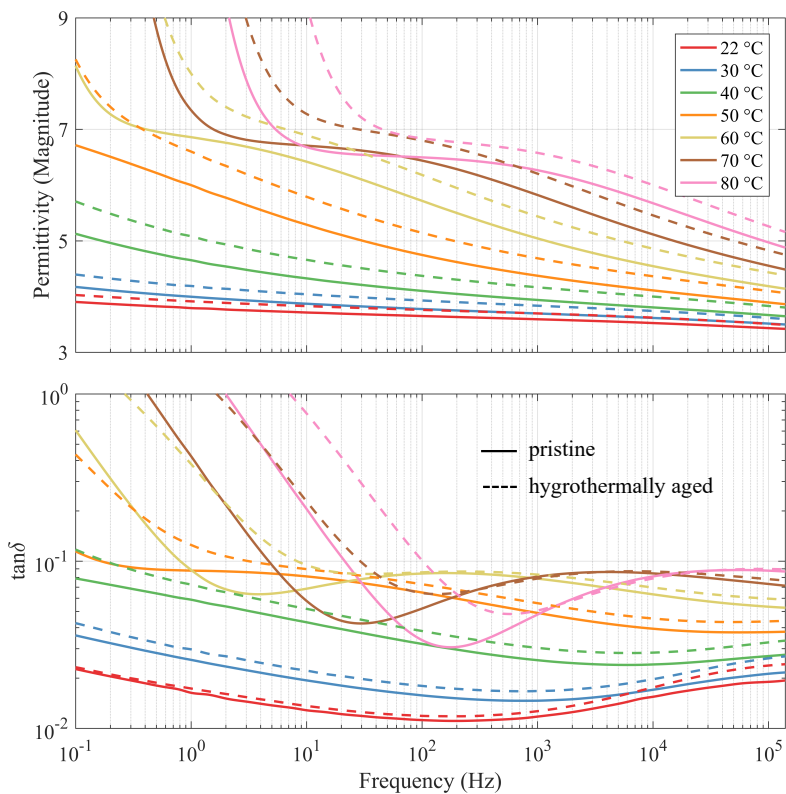


Figure 6.10.: Dielectric response of the unaged (continuous line) and the hydrothermally aged sample (broken line).

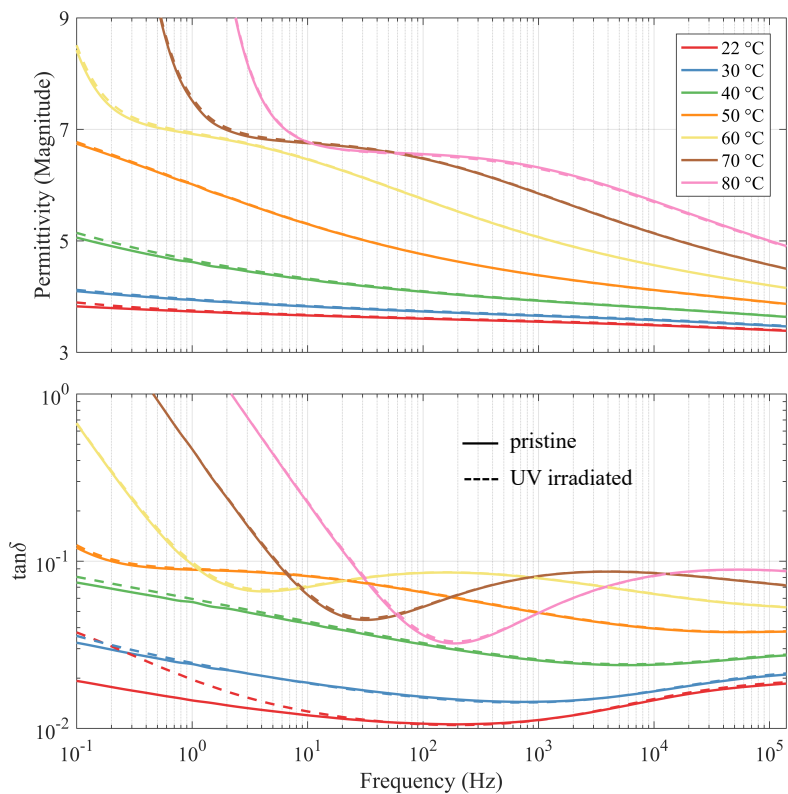


Figure 6.11.: Dielectric response of the unaged sample (continuous line) and after aging by UV radiation (broken line).

6.2.4. Discussion

The goal of this study was not to expand the body of knowledge explaining the aging of polymers on a molecular level, but rather to show that a broadband dielectric spectrometer can be tailored to non-standard requirements for specific research purposes by employing a modular approach. This modular approach allows reaching the specification of a desired application by a suitable choice of the individual modules. The setup presented in this study, for example, is designed to allow sensitive (offline) aging studies on (sub-) picofarad samples (various geometries including discs and recessed type). It employs a low-noise transimpedance amplifiers and analog filtering in combination with a tailor-made, remote-controllable variable air reference capacitor as well as a tailor-made test cell to reach this goal.

With the developed setup the typical relaxation processes present in glass-forming materials (segmental motion, orientation of local dipoles, charge migration) could be identified in the chosen epoxy polymer. Three non-electric stresses were chosen to assess the setup's ability to quantify the polymer's response to environmental stresses which are known to induce significant structural degradation in polymers.

The observed increase in the glass transition temperature during thermal aging is in line with previous literature studies [BCL⁺95] and attributed to continued cross-linking reactions. Aging times beyond 1000 hours, after which severe degradation accompanied by a loss factor increase is expected to occur [BCL⁺95], have not been investigated in this study.

Similarly, the plasticizing effect of water absorbed into the polymer matrix, characterized by a decrease of the glass transition temperature and a marked increase of dielectric loss (and relaxation strength) across large parts of the frequency spectrum, is a well-documented phenomenon [MP09]. The additional low-frequency dispersion observed here is most likely attributable to a Maxwell-Wagner-Sillars type relaxation of the additional ionic/protonic charge carriers generated as a result of water sorption.

The small measurable change of the dielectric response following UV radiation exposure was astonishing at first, because the sample showed a similar yellowing as could be observed for the other stresses. An inspection of the aged sample's cross section revealed, however, that the yellowing occurred on a tiny fraction (<0.1 mm) of its overall thickness (4 mm). Noticeable UV degradation was thus limited to the thin, strongly

absorbing surface layers of the sample. These layers constitute a negligible fraction of the probed polymer volume and thus did not noticeably change the volume-averaged dielectric response.

The obtained usable (i.e. stability-limited) precision of about $<10^{-3}$ for the relative permittivity magnitude and $<5 \times 10^{-5}$ for its phase allow for very sensitive gradual tracking of insulation deterioration. Under these circumstances, the limiting factor resides more in the difficulty to provide stable and reproducible measurement conditions (e.g. temperature, ambient gas atmosphere, electrode contact) than in the intrinsic resolution of the system.

6.2.5. Conclusion

A modular dielectric spectroscopy setup for high-precision broadband measurements of the complex dielectric permittivity of samples of various practically relevant geometries with capacitance values down to a fraction of a picofarad has been developed. In this study its performance was successfully validated and characterized by measuring the change of the dielectric response of epoxy polymer discs exposed to short-term, high-intensity environmental stresses (thermal, hygrothermal, UV radiation).

The setup represents a promising tool for future investigations on the aging dynamics in polymeric high-voltage test samples, which typically have capacitance values in the picofarad range or below (e.g. needle-plane electrodes). More specifically, using the frequency and temperature dependence of the complex dielectric permittivity as an aging marker on samples exposed to pulse-width-modulated medium-voltage stress is expected to provide a richer empirical basis and therefore a more reliable quantification of the aging dynamics (and prediction of insulation lifetime) than could be obtained from voltage endurance tests alone. In this line of research, the setup also represents a stepping stone towards an online monitoring tool using pulse-width modulated medium voltages as a multi-frequency excitation for dielectric analysis.

6.2.6. Limitations and Outlook

One limitation of the presented study is the short duration of the applied stresses, which implies that the results are of limited practical significance (in actual use cases, stress “amplitudes” are smaller, but act over much

longer periods of time). The characterization of the dielectric spectrometer thus constitutes the main result of the study. In hindsight, it would have been more representative to use standardized stressing scenarios (e.g. according to IEC-60216-1 for thermal endurance testing or DIN ISO-62 for exposure to water).

In future studies it would be interesting to apply low-voltage dielectric spectroscopy as a complement to the high-voltage setup (see Chapter 8.2) to assess the difference in aging rates (as quantified by an aging marker based on the dielectric spectrum) under different voltage waveforms and environmental conditions. While the low-voltage (offline) setup does not provide real-time measurements of the dielectric spectrum, it offers the advantage of higher precision and a larger frequency range as compared to the high-voltage setup (in particular covering the low-frequency region 10 mHz to 100 Hz, which is particularly sensitive to aging-induced, large-scale structural changes of the polymer).

6.3. Broadband Dielectric Response of a Silicone Rubber During Electrical Tree Growth

“Most engineering problems succumb to the application of software models. The days of the inventive experimenter struggling against nature and the disbelief of his colleagues are long passed in most areas, but not in the case of [electrical] insulation. Here, attempts to model degradation mechanisms using even the latest software and mathematical concepts have failed despite the claims of those involved. Heated debate involving engineers, physicists and chemists surrounds the subject, which moves slowly forward as each new conflicting set of results, interpretations and hypotheses yields new truths.”

D.W. Auckland and B.R. Varlow
in *Electrical Treeing in Solid Polymeric Insulation* [AV95]
(1995)

This chapter is based on the publication [FF18b].

Abstract

In order to assess the potential of dielectric/impedance spectroscopy as a diagnostic tool for quantifying cumulative damage due to electrical treeing in silicone rubbers, broadband impedance spectra in a needle-plane configuration at progressive stages of electrical tree degradation are presented and discussed (the tree is grown under a conventional 50 Hz sinusoidal voltage). It is shown that the grown electrical tree is invisible to frequencies in the kilohertz range, but that tree inception (formation of first microvoids in the high-field region) strongly influences the low-frequency space charge relaxation associated with electrode polarization. In such systems, the dynamics of the electrical double layer may thus be a valuable source of information to detect/probe void formation at the electrode-insulator interface.

6.3.1. Introduction

Composite electrical insulation materials using a silicone rubber (SiR) matrix possess property profiles that achieve good trade-offs between the requirements identified for applications in high power density medium-

voltage insulation systems (see Chapter 9.1), e.g. the encapsulation of medium-frequency transformers of medium-voltage converters [GFR⁺19]. At these voltage levels, the insulation's resilience to internal partial discharges (PD) originating from process-related defects and/or impurities (e.g. electrode protrusions, delamination and voids) is decisive for its long-term endurance [AV95]. As PD intensity is enhanced under repetitive pulse-shaped voltages (see Chapter 2.3.1), this aspect is even more critical in the mentioned applications.

The available studies on tree growth in SiR use optical microscopy to quantify the accumulated damage, which limits the investigations to unfilled SiR systems (e.g. [HFV⁺17]). The latter are however not suitable as bulk encapsulation materials in the above-mentioned applications, primarily because of their relatively low thermal conductivity. At this stage, the influence of the filler particles on tree growth in SiR can only be extrapolated from the vast literature available on other matrix materials (e.g. epoxy). A non-optical diagnostic method is thus needed to characterize tree growth in composite SiR materials.

Dielectric/Impedance Spectroscopy (DS/IS) is a possible candidate, as it has been used successively for characterizing cumulative damage due to pre-breakdown phenomena such as water and electrical treeing in (cross-linked) polyethylene and epoxy polymers [WTE⁺01] [SBG⁺10]. As of yet, however, it is not known if and how the growth of an electrical tree alters the (broad-band) dielectric response of SiR. This is the knowledge gap we want fill with the present investigation. It will allow to assess the potential of DS/IS as a diagnostic tool for quantifying electrical tree degradation in SiR (filled and unfilled), as well as provide a contribution to the understanding of the mechanisms of electrical treeing in SiR. To this end, broad-band impedance spectra (20 mHz to 10 kHz) of a needle-plane electrode arrangement ($C_0=20$ fF) during progressive growth stages of a single tree are presented and discussed. In order to be able to correlate cumulative damage with the established optical method, an unfilled SiR is used for the presented investigations.

6.3.2. Methods

Specimen

The SiR system Sylgard 182 from Dow Corning[®] was used as supplied to produce the cylindrical specimens shown in Figure 6.12. A needle

with a tip radius of $1\ \mu\text{m}$ (Ogura X-253-16, 30° tip cone, $\varnothing 1\ \text{mm}$) is placed in one of the aluminum electrodes to provide a well-defined site for tree inception. Since electrode adhesion is a key influencing factor in the inception process of an electrical tree a thin uniform film of the primer 1200 OS from Dow Corning[®] was applied to the electrode surfaces. The resin/hardener mixture was degassed at room temperature under dynamic vacuum (minimum pressure 25 mbar) before filling of the mold. Another 15 minutes vacuum degassing of the filled mold, followed by curing at 125°C for 2 hours completed the process. No special post-cure conditioning (e.g. degassing, tempering) was applied and the specimens were stored at ambient temperature and atmospheric pressure in air with $(50 \pm 5)\%$ relative humidity for a few days before testing.

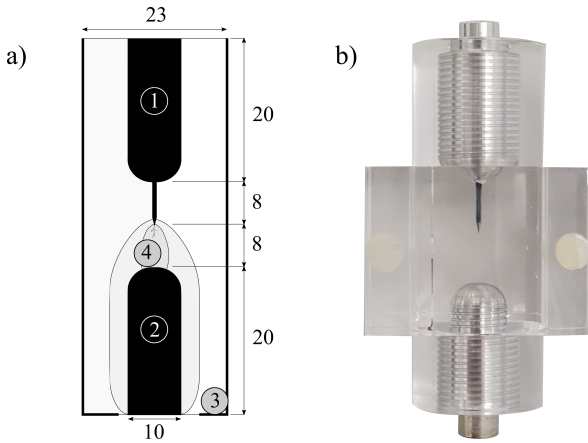


Figure 6.12.: a) Geometry of the specimen inserted into the dielectric measurement cell (dimensions in mm) b) Actual sample with mounted viewing window for better optical inspection. Vacuum capacitance $C_0=20\ \text{fF}$.

During voltage stressing and optical microscopy a plexiglass window was mounted onto the specimen to enhance image quality and eliminate the lens effect of the cylindrical specimen which is disturbing in the used backlight illumination.

High-Voltage Stressing for Tree Growth

Tree growth is stimulated by subjecting the specimen to a sinusoidal 50 Hz voltage with peak amplitudes between 20 and 31 kV (see Figure

6.14). The high-voltage stressing is done in a standard air atmosphere (25 °C, (50 ± 5)% relative humidity, 1 bar).

Instruments & Measurements

The dielectric spectrometer described in Chapter 6, which is optimized for low-capacitance specimens (<1 pF), is used for recording impedance spectra from 20 mHz to 10 kHz and temperatures from 25 °C to 125 °C.

The specimen is periodically removed from the high-voltage test bench to perform the offline dielectric response analysis. To this end it is placed in a grounded measurement cell ③ that acts as a guard electrode and provides a well-defined electric field distribution. A sinusoidal excitation voltage with a peak value of 100 V is applied to electrode ①. The measurement electrode ② is a virtual ground and collects the (displacement and conduction) current flowing through the shaded dielectric volume. The vacuum capacitance between the excitation and the measurement electrode is about 20 fF (0.02 pF). The bulk of the measured polarization and conduction current is a response from (bound and mobile) charge carriers located inside the smaller volume ④ within which tree growth occurs.

6.3.3. Theory

Electric Modulus

The recorded spectra are graphically represented by using the electric modulus, as it highlights best the characteristics of the SiR spectrum and its changes during tree growth. Moreover, it de-emphasizes the impedance values at the lowest measured frequencies (where the magnitude of the complex permittivity is large), for which a suitable model has not yet been implemented.

The response of a dielectric to an external electric field can be described by various different but mathematically equivalent functions. In the frequency domain, the complex dielectric permittivity (Equation (3.83)) $\underline{\varepsilon}(\omega) = \varepsilon'(\omega) - j\varepsilon''(\omega)$ is often used to describe the response of a linear and isotropic dielectric:

$$\underline{J}(\omega) = j\omega\underline{\varepsilon}(\omega)\underline{E}, \quad (6.21)$$

where $\underline{\mathbf{J}}$ and $\underline{\mathbf{E}}$ are complex vectors representing the local spatio-temporal averages of the total current density and the electric field, respectively, in the frequency domain. A possible DC conductivity is included in the imaginary part of the complex permittivity:

$$\kappa_{\text{DC}} \equiv \varepsilon_0 \lim_{\omega \rightarrow 0} \omega \varepsilon''(\omega). \quad (6.22)$$

The *electric modulus* $\underline{M}(\omega) = M'(\omega) + jM''(\omega)$ is given by the inverse of the dielectric permittivity [TO14]:

$$\underline{M}(\omega) = \underline{\varepsilon}(\omega)^{-1} = \frac{\varepsilon'(\omega) + j\varepsilon''(\omega)}{|\underline{\varepsilon}(\omega)|^2}. \quad (6.23)$$

The dielectric loss factor is given by

$$\tan \delta(\omega) = \frac{\varepsilon''(\omega)}{\varepsilon'(\omega)} = \frac{M''(\omega)}{M'(\omega)}. \quad (6.24)$$

Electrode Polarization

Electrode polarization plays an important role in the present study and a short description of its origin and dynamics will thus be provided.

A material containing mobile charge carriers that cannot be discharged or neutralized at the contacting electrodes (e.g. ions), shows the formation of space charge clouds in front of the electrodes if a voltage is applied to the latter (see Figures 6.13a and b). Under an alternating voltage the space charge dynamics associated with this phenomenon called electrode polarization shows up as a (low-frequency) dielectric relaxation. The associated relaxation strength $\Delta\varepsilon$ mainly depends on the concentration of the charge carriers n , the high-frequency permittivity of the host dielectric ε_∞ , as well as the electrode separation d . The relaxation time τ additionally depends on the charge carrier mobility μ .

A simple model taking into account field-driven carrier drift as well as thermally driven diffusion in the Poisson electric field will be used [Mac53] [KPE14]. The presented model assumes the positive and negative charge to have equal mobility. Under a number of simplifying assumptions (e.g. relative variation of charge density $\Delta n/n \ll 1$, for more details the reader is referred to the cited literature), the space charge relaxation approximates a Debye relaxation:

$$\underline{\varepsilon}(\omega) = \varepsilon_\infty + \frac{\Delta\varepsilon}{1 + j\omega\tau}, \quad (6.25)$$

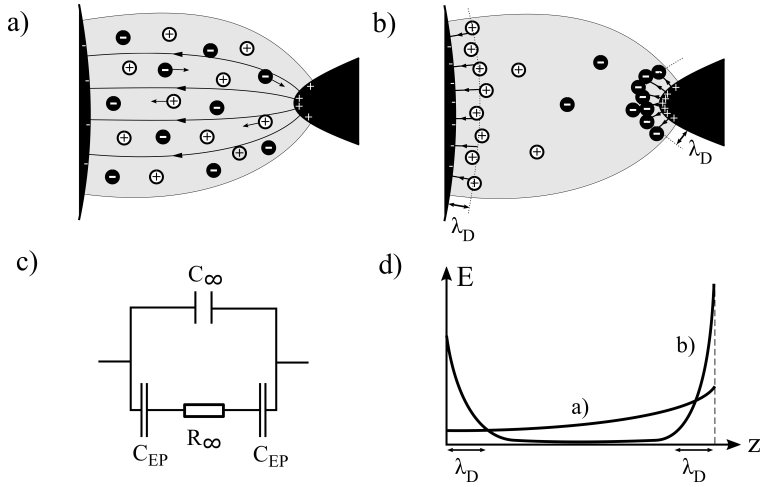


Figure 6.13.: a) Uniformly distributed mobile charge carriers shortly after voltage application b) Buildup of heterocharge cloud in front of blocking electrodes c) Equivalent circuit modelling the associated space charge relaxation (Debye approximation) d) The electric field is screened by mobile charge carriers (screening distance=Debye length λ_D).

where

$$\Delta\varepsilon = \frac{\varepsilon_\infty d}{2\lambda_D} \quad (6.26)$$

and

$$\tau = \frac{d\lambda_D}{2D}. \quad (6.27)$$

The diffusion constant D of the charge carriers (of charge $\pm q$) is related to their mobility μ by the Nernst-Einstein relation:

$$D = \frac{\mu k_B T}{q}. \quad (6.28)$$

The Debye length is related to the density of mobile charge carriers $n = n_\pm$ by

$$\lambda_D = \sqrt{\frac{\varepsilon_0 \varepsilon_\infty k_B T}{2nq^2}}. \quad (6.29)$$

Typical carrier densities in insulating polymers are of the order of 10^{-15} m^3 [DF92], for which λ_D is around $50 \mu\text{m}$.

A simple physical interpretation of the Debye length is obtained by representing the Debye response 6.25 by the equivalent circuit depicted in Figure 6.13c. The lumped circuit elements are given by

$$C_\infty = \varepsilon_\infty C_0 \quad (6.30)$$

$$C_{\text{EP}} = \varepsilon_\infty C_0 \frac{d}{\lambda_D} \quad (6.31)$$

$$R_\infty = \frac{\lambda_D^2}{\varepsilon_\infty C_0 D} \quad (6.32)$$

where C_0 is the vacuum capacitance of the considered electrode configuration and C_{EP} is the additional capacitance due to electrode polarization (capacitance of electrical double layer). Apparently, the response of the dielectric is the same as if two metallic plates are placed a distance λ_D from each electrode and connected through a resistor R_∞ . The initial Laplacian electric field distribution is significantly altered for times $t \gg \tau = R_\infty C_{\text{EP}}/2$ after applying a voltage to the system: the external voltage almost exclusively drops over the two space charge layers of extension λ_D in front of the two electrode surfaces (Figures 6.13b and d). The mobile charges screen the electrode charges such that the electric field is practically zero beyond the Debye length λ_D , that is, in the bulk of the dielectric. The previous arguments can be made more rigorous by using the actual continuous charge distribution: it can be shown that the capacitor plate position λ_D corresponds to the charge center of gravity of the carrier cloud in the continuum description.

To conclude this section we note that if the dielectric response stems from a number of parallel Debye systems, the resultant complex permittivity can be expressed by means of a distribution function $F(\tau/\tau_D)$:¹³

$$\underline{\varepsilon}(\omega) = \varepsilon_\infty + \int_{-\infty}^{+\infty} F(\tau/\tau_D) \frac{\Delta\varepsilon}{1 + j\omega\tau} d \ln(\tau/\tau_D). \quad (6.33)$$

A simple closed form of the resulting complex permittivity,

$$\underline{\varepsilon}(\omega) = \varepsilon_\infty + \frac{\Delta\varepsilon}{1 + (j\omega\tau)^{1-\alpha}}, \quad (6.34)$$

¹³ τ_D is a chosen normalization time constant.

is obtained by using the following one-parameter distribution [HN67]:

$$F(y) = \frac{\sin(\alpha\pi)}{\cosh[(1-\alpha)\ln(y) - \cos(\alpha\pi)]}. \quad (6.35)$$

Values of $\alpha > 0$ induce a broadening of the Debye loss peak while preserving its symmetry (on a logarithmic axis).¹⁴

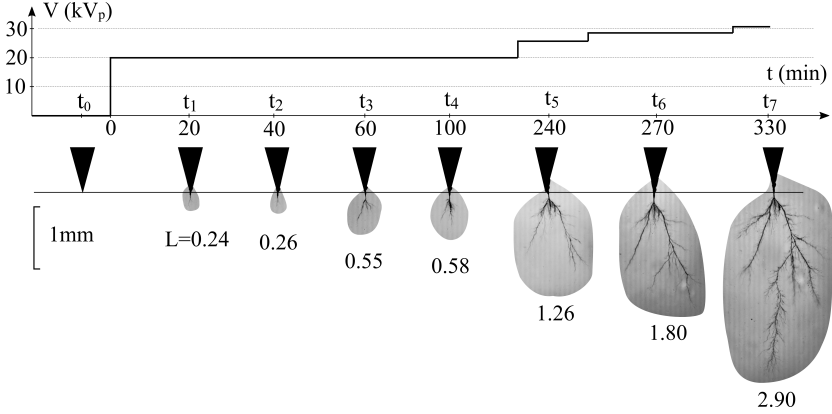


Figure 6.14.: Stressing voltage (AC 50Hz peak value) as a function of time (top) as well as microscope images of the electrical tree at the instants of time for which the impedance spectra have been recorded (bottom, tree length given in mm).

6.3.4. Results

This section first compares the impedance spectra of the unaged material in both quasi-homogeneous and strongly inhomogeneous electrode configurations, and then briefly discusses the observation of an unexpected resistive-inductive impedance regime at low frequencies. Finally, the effect

¹⁴A more general (asymmetric) peak broadening is obtained by the two-parameter distribution given by Equation (9) in [HN67], yielding the famous Havriliak-Negami relaxation function:

$$\underline{\varepsilon}(\omega) = \varepsilon_{\infty} + \frac{\Delta\varepsilon}{[1 + (j\omega\tau)^{1-\alpha}]^{1-\beta}}. \quad (6.36)$$

of tree growth on the impedance spectra in the strongly inhomogeneous configuration is presented and physically interpreted.

Quasi-Homogeneous vs. Strongly Inhomogeneous Electrode Configuration

The real and imaginary part of the electric modulus of the unaged SiR as a function of frequency in a quasi-homogeneous plane-plane geometry (electrode separation $d=5$ mm) is given in Figure 6.15, while Figure 6.16 shows the same quantities for the inhomogeneous needle-plane geometry ($d=8$ mm). The continuous lines between the measured data points are least-square fits based on the Debye relaxation model of electrode polarization (Equations (6.25) to (6.27)).

There are four independent fitting parameters, e.g. the high-frequency permittivity ε_∞ , the relaxation strength $\Delta\varepsilon$, the relaxation time τ , and the distribution parameter α . The spectrum of the unaged samples agree well with a Debye relaxation with a single relaxation time, i.e. $\alpha < 0.005$. While ε_∞ is determined in a robust manner from the high-frequency plateau value of the (real part of the) permittivity, there is an ambiguity in the determination of the parameter pair $(\Delta\varepsilon, \tau)$. It arises because the saturation of the permittivity magnitude towards the low-frequency plateau value, i.e. $\varepsilon_\infty + \Delta\varepsilon$, is not observable within the measured frequency range. Moreover, the low-frequency values are perturbed by an additional process (discussed in the following Section), which is not considered in the used model to fit the data. In this case, only the *ratio* $\Delta\varepsilon/\tau$ can be determined unambiguously. Consequently, other physical model parameters such as the carrier density/mobility and the Debye length are not accessible. An exception is the electrical conductivity, which only depends on the said ratio:

$$\kappa_0 = 2n\mu e = \varepsilon_0 \frac{\Delta\varepsilon}{\tau} = \frac{\varepsilon_0 \varepsilon_\infty D}{\lambda_D^2} \quad (6.37)$$

An overview of the fitting parameters for a selection of temperatures is given Table 6.4. The upper value corresponds to the quasi-homogeneous, the lower value to the needle-plane configuration. Note that ε_∞ is not corrected for thermal expansion of the polymer.

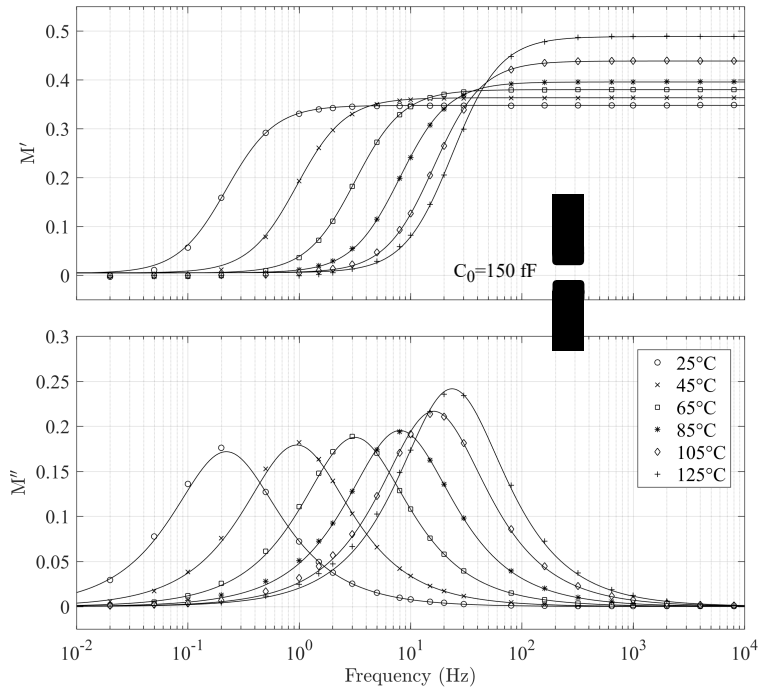


Figure 6.15.: Real and imaginary part of the electric modulus of the unaged SiR as a function of frequency and temperature in a quasi-homogeneous electrode configuration.

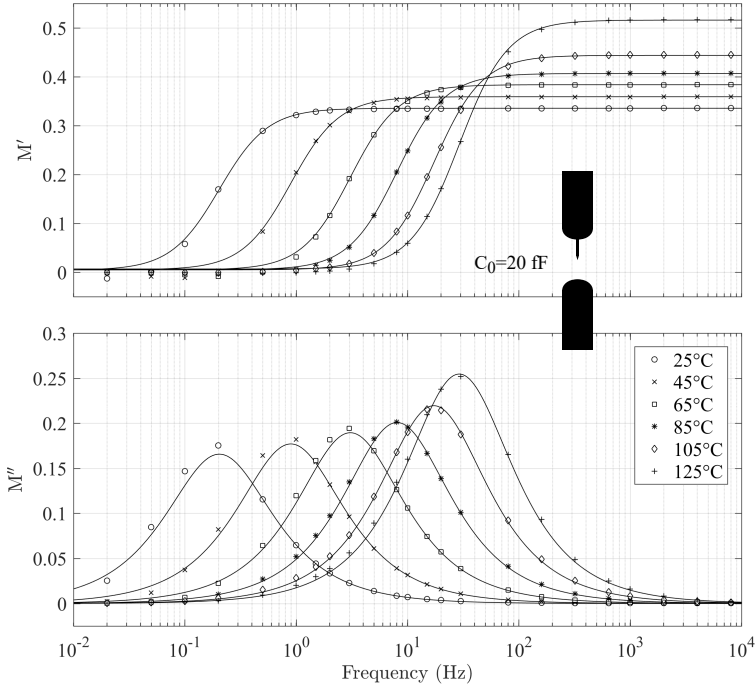


Figure 6.16.: Real and imaginary part of the electric modulus of the unaged SiR as a function of frequency and temperature in a strongly inhomogeneous electrode configuration.

Table 6.4.: Debye fitting parameters of impedance spectra of unaged samples for quasi-homogeneous (upper values) and strongly inhomogeneous (lower values) electrode configuration.

Parameter	Unit	25 °C	65 °C	105 °C
ε_∞	–	2.88	2.64	2.28
		2.98	2.61	2.25
$\Delta\varepsilon/\tau$	s^{-1}	3.95	51.6	228
		3.76	49.4	240
α	–	< 0.005		

Impedance Regimes

At high frequencies (>10 kHz) the sample behaves as a low-loss capacitor with a loss angle on the order of 10^{-3} rad. As shown in Figure 6.17, the loss angle increases with decreasing frequency and levels off towards $\delta = \pi/2$. Such an asymptotic approach to a purely resistive regime around the relaxation frequency is consistent with the space charge relaxation model used in the previous sections. The measured loss angle, however, *crosses* the $\delta = \pi/2$ line (i.e. becomes purely resistive) at a certain frequency and peaks inside the resistive-inductive regime ($\pi/2 < \delta < \pi$). This behavior was observed in both the needle-plane and the quasi-homogeneous electrode configuration, but with much less pronounced excursions into the resistive-inductive regime in the homogeneous case. In order to exclude the possibility of a measurement artefact, additional reference measurements on a (variable) air capacitor in the test cell with the same impedance magnitude as the specimen were carried out, which yielded the expected $\delta = 0$ within the instrument accuracy (10^{-4} rad).

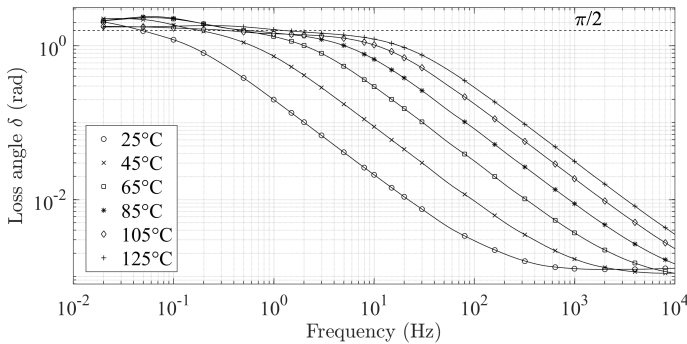


Figure 6.17.: Loss angle as a function of frequency for the unaged needle-plane specimen. The $\delta \geq \pi/2$ regime is not explained within the space charge relaxation model (the continuous lines are spline interpolations here).

Reflections on this peculiar phenomenon (which is not included in the applied model – see negative values of M' in Figures 6.15 and 6.16) point in the direction of a charge injection process occurring at the electrodes when the ion cloud building up over time leads to a sufficient electric field enhancement. The maximal electric field indeed occurs at

the electrode surfaces and reaches values on the order of $E_{\max} = V_0/2\lambda_D$ ($V_0 = 100$ V, electrode voltage), which can be a few kV/mm even in the quasi-homogeneous configuration. In the needle-plane geometry the electrode field itself peaks around 20 kV/mm when $V_0 = 100$ V, hence the effect of the postulated injection process is expected – and observed – to be enhanced.

This scenario is described in [Kao04] in Chapter 7.2.3 (“Effects of Ionic Conduction”): “The positively charged cations moving toward the cathode and the negatively charged anions moving toward the anode under an applied field will create hetero-space charges near the electrodes. If the space charges of the ions are not neutralized at the electrodes, they will accumulate there. These hetero-space charges may trigger the injection of electrons from the cathode and holes from the anode when the accumulated amount of these charges reaches a certain critical value” [Kao04] (p. 385).

Spectroscopic Footprint of the Electrical Tree During its Growth

The time evolution of the electric modulus spectrum during tree growth is illustrated in Figure 6.18. The spectra are recorded at the instants of time t_0 to t_7 for which the microscope images of the tree are shown in Figure 6.14. The tree is invisible at frequencies above about 10 Hz. This indicates that the tree channel walls in SiR are not significantly more conductive than the bulk dielectric. Indeed, conductive tree tubules should increase the capacitance of the arrangement with a 2 mm long tree by at least 10 % (estimation based on numerical simulation). No significant variation is however detectable, i.e. ε_∞ is unaffected by tree growth.

The measurements show instead that it is the space charge relaxation that is altered by incipient tree growth. The fit parameter ratio $\Delta\varepsilon/\tau$ decreases with progressing tree growth, with a particular sensitivity for tree inception (see Figure 6.19).

The structural degradation of the silicone (e.g. PD erosion) near the electrode surface effectively increases the screening distance of the electrode charges, which is consistent with the observed decrease of the ratio $\Delta\varepsilon/\tau$. Moreover, the creation of low-density regions/microvoids in front of the electrode is expected to be non-uniform across the probed surface. This is consistent with the observed evolution from a single Debye relaxation to a superposition of parallel Debye systems with a distribution of relaxation

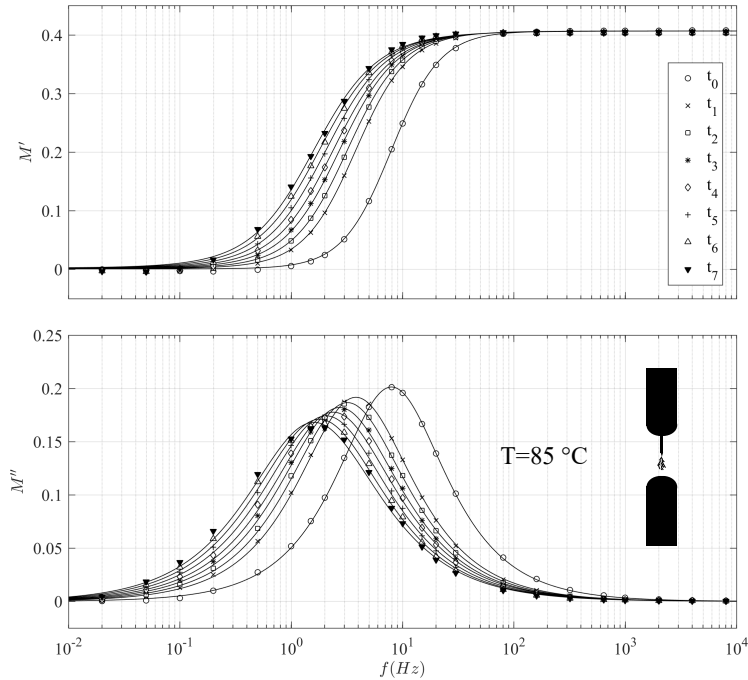


Figure 6.18.: Real and imaginary part of the electric modulus of the SiR as a function of frequency at successive stages of tree growth (see figure 6.14).

times, where the broadness of the distribution is determined by α (see Equation (6.34)).

The results thus suggest that it is the perturbation of the electrode polarization by the electrical tree that generates its footprint in the relaxation spectra. It is especially sensitive to erosive processes within a few Debye lengths of the electrode surface. This makes low-frequency impedance spectroscopy and, by extension, polarization/depolarization current measurements interesting tools for studying tree growth in SiR, with a particular sensitivity for the inception stage, that is, the formation of the first low-density regions/microvoids in front of the high-field electrode.

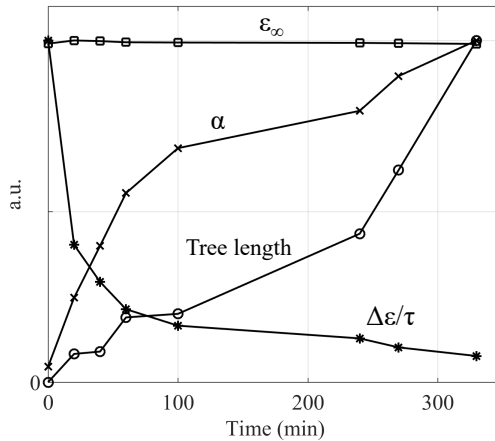


Figure 6.19.: Relative evolution of dielectric system parameters with increasing tree length / aging time. The shown parameters were determined at a temperature of 85 °C.

6.3.5. Discussion

The dielectric response of the unaged material measured in the two electrode configurations (quasi-homogeneous vs. strongly inhomogeneous) agree remarkably well. Although this is the expected result for a linear dielectric, it is not self-evident that this ideal behavior would indeed be observed, as the electric field norm in the needle-plane geometry varies by a factor $s \approx r/d$ inside the dielectric [CD02]. In the used configuration with a needle tip radius of $r \approx 1 \mu\text{m}$ and an electrode distance of $d=8 \text{ mm}$ the field norm spans almost four orders of magnitude ($s \approx 8000$).

The determined conductivity, $\kappa_0 = 3.6 \times 10^{-11} \text{ S m}^{-1}$ at 25 °C, is relatively high when compared to other insulating polymers (typically between $10^{-10} \text{ S m}^{-1}$ and $10^{-18} \text{ S m}^{-1}$ [DF92]). While it is physically reasonable that ionic conduction is strongly enhanced in an elastomer (in which cross-link density is low and chain segments between crosslinks are flexible and subject to thermal fluctuations even at room temperature), it should also be noted that the conductivity κ_0 is derived from a transient model. This is to be contrasted with calculations based on “steady-state” conduction current measurements, which yield an effective (“apparent”) specimen conductivity that ignores possible space charge accumulation

and an associated electric field distortion inside the dielectric:

$$\kappa_{\text{eff}} = \frac{\varepsilon_0}{C_0} \cdot \frac{I(t \rightarrow \infty)}{V_0} \quad (6.38)$$

By using the measured value of $I(80 \text{ h}) = 1.54 \text{ pA}$ at $V_0 = 100 \text{ V}$ and 25°C in the homogeneous configuration one obtains

$$\kappa_{\text{eff}} = 9 \times 10^{-13} \text{ S m}^{-1}, \quad (6.39)$$

which is 40 times smaller than the value

$$\kappa_0 = 2n\mu e = 3.6 \times 10^{-11} \text{ S m}^{-1} \quad (6.40)$$

obtained within the transient model. The latter value compares well with the low-frequency plateau value

$$\kappa_{\text{DC}} = 3.3 \times 10^{-11} \text{ S m}^{-1} \quad (6.41)$$

obtained from the model-independent definition given by Equation (6.22). The associated frequency range (i.e. where $\omega\varepsilon_0\varepsilon''(\omega)$ is approximately constant) is about 0.05 Hz to 5 Hz. This is very different from the equivalent frequency probed with a time-domain measurement at $t = 40 \text{ h}$ (approximately 1 μHz according to the Hamon approximation [Kao04] p. 107), and hence it is not unexpected that two significantly different (apparent) conductivity values are determined within the different frameworks.

6.3.6. Conclusion

The work presented in this chapter was motivated by the question of how the inception and growth of an electrical tree alters the dielectric response of silicone rubber, in order to assess its potential as a diagnostic tool for this degradation mechanism. These are the key findings:

- The electrical tree does not affect the high-frequency dielectric response of the specimen ($\geq 10 \text{ Hz}$).
- The tree tubules are not electrically conductive.
- Electrode polarization is observed and can be quantified within the framework of a simplified space charge relaxation model.

- The space charge polarization is particularly sensitive to tree inception. Within the applied model, the incepting tree leads to an increase of the effective electrode charge screening distance and a progressive broadening of the distribution of relaxation times.
- At low frequencies (<1 Hz) a peculiar resistive-inductive dielectric response is observed, and hypothesized to be related to charge injection due to the strong electric field created by the ionic heterocharge accumulation during the observed electrode polarization.

6.3.7. Limitations and Outlook

The study has shown a good sensitivity of the (low-frequency) dielectric response to tree initiation in an unfilled SiR material. The question arises of whether this method could be used to detect electrical tree initiation in actual insulation systems (e.g. transformer winding insulation). Due to the localized nature of a treeing defect, it seems rather unlikely that the resulting change in the *overall* displacement current would be detectable (because the current probing the defect volume typically represents a negligible fraction of the total probed insulation volume in practical settings). On the other hand, it seems likely that larger area defects such as delamination of the insulator from the electrode surface would be detectable by this test method.

While this diagnostic method is probably not practical for real insulation systems (due to the reasons mentioned above), it seems promising for studying electrical tree inception and growth in the presented laboratory-type specimens. The next step would consist in comparing the response obtained on the unfilled SiR material used in this study with a filled SiR system (which are the ones used in actual insulation systems, in particular when a high thermal conductivity is of importance).

Then one could proceed to investigating tree growth in filled SiR specimens as a function of inverter-type medium voltage parameters (switching frequency, rise time,...). Given the enhanced PD intensity under this voltage profiles, characterizing the susceptibility of an insulation system/material to tree *inception* seems of particular relevance. Resistance to treeing-induced insulation breakdown is an important factor to ensure long-term voltage endurance in potted/encapsulated insulation systems, where (homogeneous) design field strengths are relatively low (typically $\leq 5 \text{ kV mm}^{-1}$) such that a “direct” insulation failure (i.e. not preceded by a slow, progressive erosion of the insulation material) is unlikely.

A few studies on silicone gels (as employed in semiconductor packaging) are already available. They report interesting results, e.g., a decreasing tree inception voltage with increasing fundamental frequency (for both sinusoidal and rectangular waveforms) and increasing switching speed (for rectangular voltages) [MCD⁺17].

7. Inverter-Stress Simulator

“Electric breakdown is a subject to which it is difficult to apply our usual scientific rigour.”

L. Walsh and D. Solymar
in *Lectures on the Electrical Properties of Materials*
(1988)

“The dielectric breakdown test may be used as a material inspection or quality control test, as a means of inferring other conditions such as variability, or to indicate deteriorating processes such as thermal aging. In these uses of the test it is the relative value of the breakdown voltage that is important rather than the absolute value.”

Standard ASTM D149 [AST13] (p. 11)

This chapter describes the design and setup of a test bench (“Inverter Stress Simulator”) for insulation testing under inverter-type medium voltages and controlled environmental conditions (relative humidity and temperature) (Section 7.1), as well as a use case in the form of a study investigating the endurance of polymeric insulation foil exposed to a mixed medium voltage (DC + repetitive pulse) in the presence (Chapter 7.3) and absence (Chapter 7.2) of PD.

7.1. Design and Setup

7.1.1. Layout and Components

The simplified schematic of the MF pulse voltage generator (with variable LF-bias) constructed for the tests reported in Sections 7.3 and 7.2 is shown in Figure 7.1. The pulse voltage is generated by a MOSFET half-bridge S_1/S_2 connected to the DC-bus capacitor $C_1 = 1 \mu\text{F}$ and superimposed onto the LF voltage by capacitive coupling through $C_2 = 2.7 \text{ nF}$. The half-bridge module is a Behlke MOSFET Push-Pull Switch HTS 41-06-GSM with options CCF (Ceramic Cooling Flange), I-FWDN (Integrated Free-Wheeling Diode Network) and HFS (High Frequency Switching).¹The LF voltage is applied to the sample through the $R_4=1 \text{ M}\Omega$ resistor, which provides the necessary decoupling of the LF voltage source.

Due to the AC-coupling, the DC component of the voltage U_{DUT} is still given by the mean value of the LF voltage (which is DC coupled to the sample). Choosing $C_2 \gg C_{\text{DUT}}$ ensures that most of the pulse voltage U_p drops across the specimen capacitance C_{DUT} (test cell and voltage probe capacitance are understood to be included in the latter). The resistors $R_2=220 \Omega$ and $R_3 \geq 50 \Omega$ along with the diodes D_1 and D_2 serve to protect the half-bridge in case of specimen breakdown ($U_{\text{DUT}} \rightarrow 0$). The value of R_3 can be increased to decrease the slew rate of the pulse voltage fronts. The maximal slew rate (at $R_3 = 50 \Omega$) is about $15 \text{ kV}/\mu\text{s}$.

In operation, the LF voltage U_{LF} drops across C_2 , and thus the output node of the half-bridge is pulled towards $\mp U_{\text{LF}}(t_{\text{BD}})$ when the sample breaks down (t_{BD} is the time of breakdown). The fast SiC diodes clamp this voltage rise by providing a discharge path for C_2 through $C_2 - R_3 - D_2 - R_{\text{BD}}$ (for $U_{\text{LF}}(t_{\text{BD}}) > 0$) or $C_2 - R_3 - D_1 - C_1 - R_{\text{BD}}$ (for $U_{\text{LF}}(t_{\text{BD}}) < 0$), where R_{BD} is the breakdown impedance of the specimen. R_2 reduces the share of the breakdown current carried by the MOSFET body diodes.² A current monitor (CT) detects this discharge current, blocks S_1 and S_2 , and shuts down both voltage sources.

¹In the first version of the test bench (used for the studies in this thesis), the switch HTS 21-07-HB-C was used, which limited the pulse peak/peak voltage to max. 2 kV and the switching frequency to $< 10 \text{ kHz}$. The results revealed that higher switching frequencies and higher pulse voltages are desirable for further studies, which is why an upgrade of the test bench has been initiated towards the end of this project.

²Another robust method (also used here), is to block the current through the MOSFET body diode by an anti-serial diode and use a dedicated (integrated) free-wheeling diode network (Behlke Option I-FWDN).

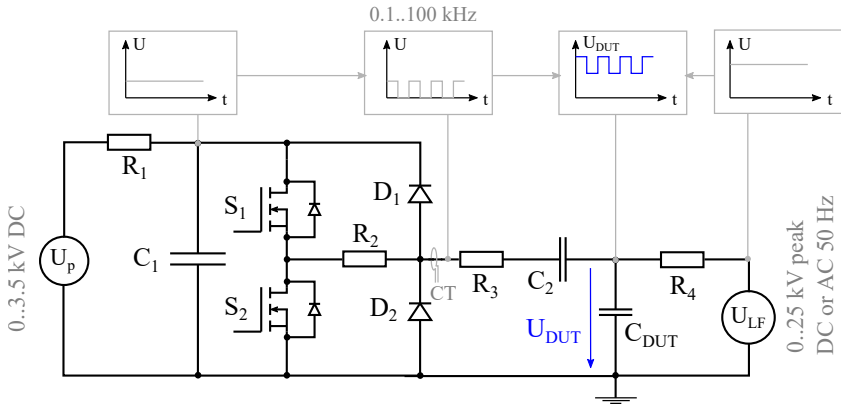


Figure 7.1.: Simplified schematic of the Inverter Stress Simulator. The high-frequency rectangular pulse train generated by the MOSFET half-bridge is superimposed onto the low-frequency voltage by capacitive coupling through C_2 .

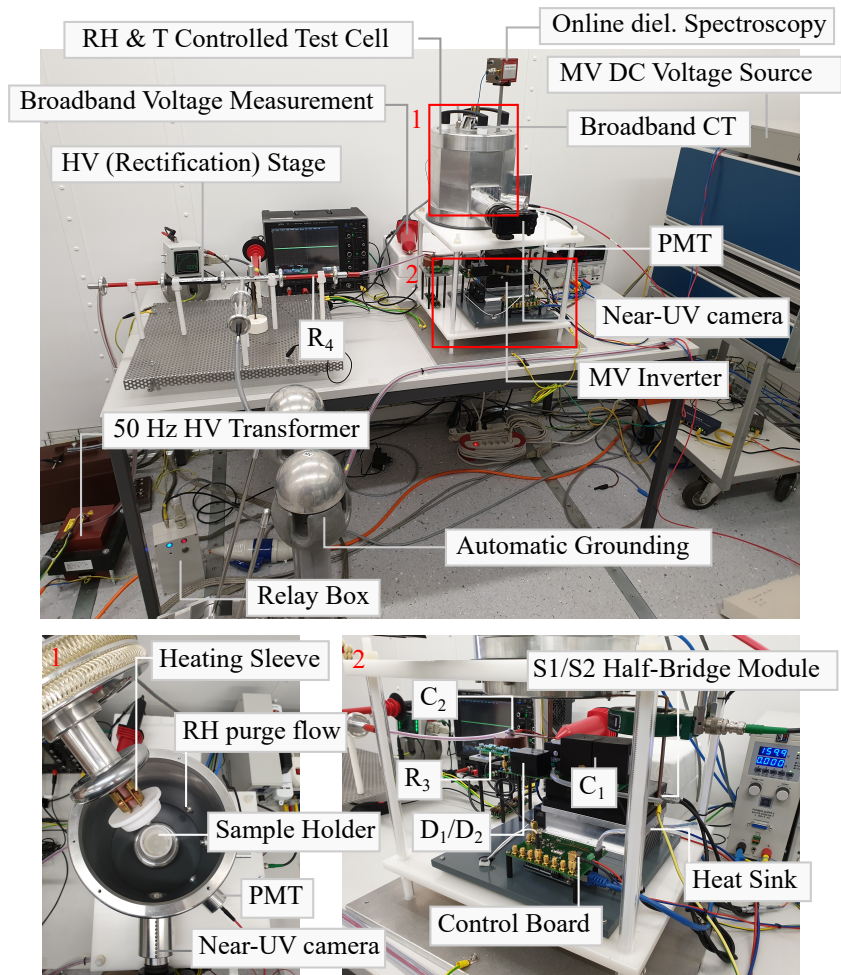


Figure 7.2.: Fully assembled Inverter Stress Simulator.

7.1.2. Diagnostics

Voltage Measurement

The composite voltage U_{DUT} is measured by means of a broadband (220 MHz) high-voltage probe (1000:1), Type CT4028 (Cal Test Electronics).

Current Measurement

The sample current is measured by means of a broadband (20 MHz) current transformer (Pearson Electronics, model 110A) and mainly used to trigger the oscilloscope on sample breakdown. The current measurement for the online dielectric spectroscopy is performed by an in-house current transformer/voltage integrator assembly, and is detailed in Chapter 8.2.3.

Near-UV Camera

A low-cost ($\sim 1000\$$) near-UV camera setup (~ 350 nm to ~ 380 nm) was assembled in order to have access to a spatially resolved monitoring of PD activity within the sample cell. The assembly consists of

- Camera: Full Spectrum Converted Sony NEX 5R
- UV Bandpass Filter: Baader U Filter
- Lens: Nikon EL-Nikkor 63mm/f2.8 (used)³

The camera is directly mounted onto the test cell (see Figure 7.2) and used in a 2f-2f configuration, that is, with a 1:1 magnification of the object onto the imaging sensor (23.5 mm \times 15.6 mm). The camera assembly as well as a test shot on a wet coronating high-voltage transmission line (laboratory setting) are shown in Figures 7.3a and 7.3b, respectively.

Photomultiplier Tube (PMT)

In order to resolve individual PDs, a PMT is used. A collimator is directly mounted onto the test cell (see Figure 7.2) and couples (part of

³A number of lenses not specifically designed for UV operation (hence affordable), but with above-average near-UV transmission are available. See e.g. www.savazzi.net (accessed: 27.07.2019), keyword “lenses for UV photography”.

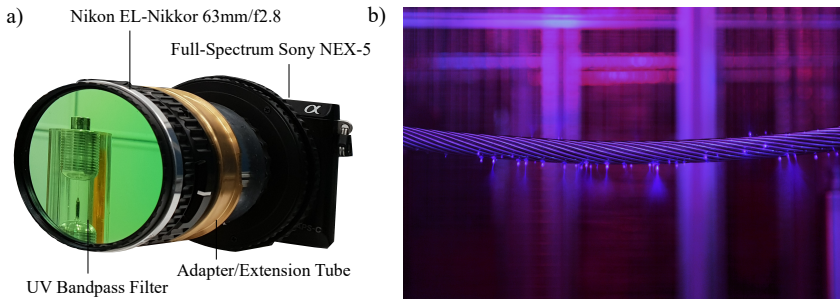


Figure 7.3.: a) Low-cost near-UV camera assembly and b) test shot on coronating high-voltage transmission line. A low-level UV back-lighting is used in order to make the metal surface visible.

the) the emitted light into an optical fiber. In front of the collimator, a UV passband filter (Baader U, 320 nm to 380 nm) can be used to prevent visible light from triggering the PMT. The passband of the collimator, fiber and PMT has a lower cutoff wavelength of about 200 nm.

Online Dielectric Spectrometer

An online dielectric spectrometer using the inverter voltage as its excitation source has been implemented to complement future endurance testing on insulation materials with a simultaneous monitoring of its dielectric properties. It is described in detail in Chapter 8.

7.1.3. Humidity and Temperature Control System

The sample temperature can be regulated by a heating sleeve with integrated temperature sensor and PID control, which is mounted onto the ground electrode (see Figure 7.2). The ground electrode temperature is variable from room temperature to about 150 °C. In the present configuration, the high-voltage electrode is not actively heated, and thus a certain temperature gradient across the sample will occur.

The control of the RH of the ambient air atmosphere inside the test cell is realized according to the flow schematic shown in 7.4. The target relative humidity in the mixing chamber is obtained by adjusting the

flow rates through the two flow paths providing dry (RH $\sim 0\%$) and humidity-saturated (RH $\sim 100\%$) air.⁴ The room temperature RH of the resulting purge flow $Q_{\text{tot}} = Q_{\text{RH},0\%} + Q_{\text{RH},100\%}$ (L min^{-1}) is given by

$$\text{RH}_{25^\circ\text{C}} = \frac{Q_{\text{RH},100\%}}{Q_{\text{tot}}}. \quad (7.1)$$

It turned out that if only relative humidities below about 75% are needed, a heated saturator is not needed. The partial flows are simply regulated by manual flow meters ($0..10 \text{ L min}^{-1}$) until the desired RH is obtained in the mixing chamber. Another RH sensor is mounted inside the test cell in order to monitor the evolution of RH after the test cell has been opened for test sample replacement.

Another branch of the RH-conditioned air flow is passed through a sample storage box, which allows to condition the samples to a specified RH prior to testing.

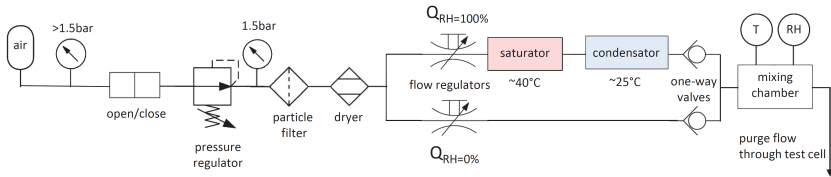


Figure 7.4.: Schematic of the used RH control system.

⁴Saturation with respect to the condenser temperature.

7.2. Time-to-Failure Testing under DC-biased Repetitive Impulse Voltages Below PD Inception

“The difficulties inherent in accelerated-aging procedures are nicely represented by the egg. Age it at one temperature, and you get a rotten egg; at a much higher temperature, a fried one; and in between, a chicken.”

R.L. Feller
in *Accelerated Aging*
– *Photochemical and Thermal Aspects* (1994)

“For many materials the moisture content has more effect on dielectric strength than does temperature.”

Standard ASTM D149 [AST13] (p. 6)

This chapter is based on the publication [FGK⁺19], supplemented with full details on the derivation of the estimation of the maximal sample temperature as well as the indentation depth. The addressed research gap has been formulated in Chapter 2.3.6, and is restated here in the Introduction section 7.2.1.

Abstract

The aim of the study presented in this chapter is to investigate the endurance (characteristic time to failure) of polymeric insulation under a mixed (DC + medium-frequency rectangular pulse) medium-voltage stress below partial discharge (PD) inception. To this end, a dedicated setup is used that deliberately eliminates all known aging factors relating to medium-frequency rectangular pulse voltages. Based on the results obtained from lifetime testing on PET insulation foil, the main conclusion drawn in this chapter is that the adequate consideration of these factors is not only necessary but sufficient for eliminating the adverse effects of these voltages within the investigated parameter ranges. Indeed, it is observed that the physical processes leading to failure under a pure DC voltage are merely modulated by the addition of a medium-frequency rectangular pulse train. In particular, there is no indication of

an additional detrimental “per pulse” degradation/aging process. This constitutes empirical evidence for the completeness of the known list of risk factors for premature insulation failure specifically related to inverter-type voltage stress (high slew rates, high-frequency switching), including inverter voltages with a significant DC bias.

7.2.1. Introduction

The maturing of wide band gap semiconductor technologies for power switching applications (SiC and GaN) considerably enlarges the design space for MF MV converters. In particular, switching losses can be reduced significantly by employing increased switching speeds (>10 kV/ μ s) [OAMS13], and/or a further increase in conversion power density is possible by increasing the switching frequency (up to and beyond 100 kHz).

Increased switching speeds and/or frequencies, however, raise issues concerning the long-term endurance of organic insulation materials employed in MV converter systems [BDM⁺09] [Cig17]. The accelerated degradation and premature failure of insulation systems exposed to inverter-type medium voltages in the presence of PD is a largely investigated topic [IECb] [WCM14] [MJC15] [Yin97] [Kau95], and PD is recognized as one of the main risk factors associated with this type of voltage stress:

- a. *Enhanced partial discharge (PD) intensity.* The number of PDs per unit time is proportional to the switching frequency. In addition, PD amplitudes are observed to increase with switching speed [HBBG14]. Thus, if PD is incepted, the total PD charge and its erosive effect on the insulation material is greatly enhanced when switching frequency and speed are increased.

Moreover, it has been recognized early on [DW91] that the waveform and fundamental frequency of the voltage influence the (local) electric field stress to which the insulation materials are subjected. This thus constitutes another risk factor that must be considered when dealing with inverter-type voltages:

- b. *Systemic overvoltages.* The broad spectral content of the terminal voltage can excite system resonances, generate standing wave phenomena on electrically long conductors (cable/load impedance mismatch), and lead to strongly nonlinear voltage drops along windings or field-grading layers due to parasitic capacitive couplings [BDM⁺09]. As a result, the electric field stress on certain

parts of the insulation can be increased significantly.

While premature failure under inverter-type voltages in the absence of PD is also documented in literature [FM01] [KCD⁺11], the investigation of the associated (accelerated) aging mechanism(s) has not received as much attention as PD degradation under these voltage profiles. The negative impact of increased insulation temperature due to enhanced dielectric losses [SBBG09] is often cited as a possible cause for premature insulation failure under repetitive pulse stress in the absence of PD [WCM14] [Yin97] [Kau95] [NG14], and is certainly a risk factor to be considered in the insulation design:

- c. *Excessive insulation temperature.* Increased switching speeds broaden the spectral content of the terminal voltage, while a higher switching frequency shifts its frequency spectrum as a whole. Both effects typically entail enhanced dielectric losses. Losses associated with charge migration or the dielectric α -relaxation have positive temperature coefficients and can lead to thermal runaway. Moreover, increased capacitive currents can lead to significant heating of (field-grading) semiconductive layers [BDM⁺09]. Even in the absence of thermal runaway, a higher insulation temperature enhances thermally activated degradation processes and – especially for organic materials – compromised (di)electric properties. Moreover, the problem of stress cracking and delamination is accentuated.

It has been shown [FMCM04] that (bulk) space charge evolves under inverter-type voltages that possess a DC offset (e.g. unipolar rectangular voltages). Thus, in addition to increased dielectric heating, several investigators also mention the possibility of space charge playing a role in premature failure, in particular under DC-biased repetitive pulse voltages [HAL⁺00] [GWHL07]. While it is well known that the distortion of the electrode field by space charges in the insulation bulk plays a key role under DC voltage stress, it remains unclear if/how the interaction of the highly dynamic electrode field with bulk space charge influences insulation aging, because the available studies do not allow to clearly separate the influence of dielectric losses from the potential influence of space charge:

- (d.) *Space charge.* Structural aging due to electromechanical stress from the Coulombic interaction between the highly dynamic electrode field (due to repetitive impulse voltages of high slew rate) with space charge evolving under the DC-component of the applied voltage?

The concept that the interaction of space charge with the electrode field and the associated electromechanical stress can lead to the aging of polymeric (especially semicrystalline) insulation materials is not new. The electromechanical force density $\mathbf{f} = \rho\mathbf{E}$ (electrostriction omitted) acting on space charge is indeed a fundamental ingredient in several well-established microphysical models of dielectric aging, see e.g. [JLL05]. While initially developed for DC voltage stress, the operant microphysical aging process (morphological changes such as the opening of sub-microvoids and crack propagation) can also be considered under AC or mixed (DC+AC) voltages. In this case the deformation of the polymer structure (e.g. straining of polymer ties in the amorphous regions) will be modulated by the dynamics of the AC component of the electric field. It is argued in [BB05] (Chapter 6.6) that cyclic mechanical stress is expected to accelerate these processes because it causes the polymer chains to occupy conformational states that are more varied relative to the quasi-equilibrium states occupied under a constant electric field stress. Moreover, there is an additional mechanical energy dissipation (proportional to the excitation frequency) associated with the cyclic conformational changes.

It is thus expected that this mode of dielectric aging – if active at all – should be particularly pronounced when a DC voltage (promoting the creation of space charge) is superimposed with a highly dynamic (i.e. with steep voltage fronts) medium-frequency voltage. In order to test this hypothesis, electrical endurance testing of PET insulation foils is performed under a DC medium-voltage stress superimposed by medium-frequency rectangular voltage impulses (Figure 7.5a). A dedicated setup is used in order to deliberately eliminate the known risk factors a. to c. (i.e. erosion due to repetitive PD, overstressing due to voltage overshoot and excessive heating of the sample). If the lifetime then still shows a dependency on impulse repetition frequency (i.e. a sign of a “per pulse” degradation), this would be strong empirical evidence for an additional degradation mechanism (such as d.) specifically related to repetitive impulse aging. If, on the other hand, the lifetime shows no dependence on the impulse switching frequency, this is strong empirical evidence for the completeness of the risk factors a. to c. The aim of this investigation is thus to provide empirical evidence which helps to decide on the question of completeness of the listed risk factors a. to c. for arbitrary inverter-type voltages.

7.2.2. Methods

Test Bench

The inverter stress simulator test bench described in Chapter 7.1 is used to perform the time-to-failure testing. A dedicated holder for the foil samples (Figure 7.5b) is used here. The parameters for the employed mixed voltage waveform are specified in Figure 7.5a.

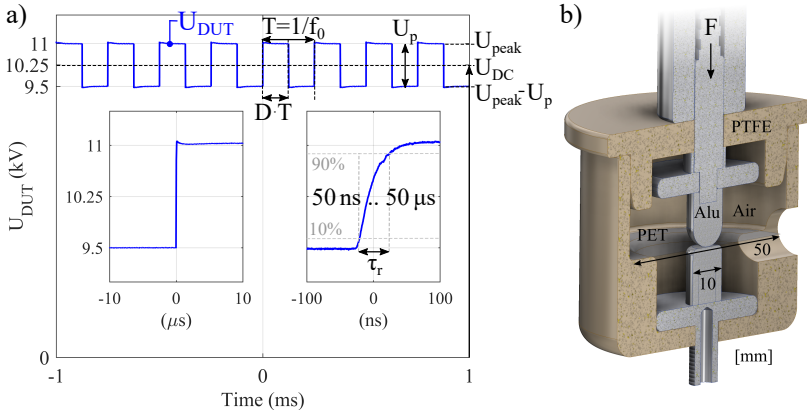


Figure 7.5.: a) Exemplary pulse voltage waveform and b) Electrode-specimen geometry used for time-to-failure testing of PET foil in this study.

Sample Preparation and Electrode Geometry

Polyethylenterephthalat (PET) insulation foil (DuPont Melinex[®] S) is used for the voltage endurance tests. It is a semicrystalline polymer foil, commonly used in electrical applications as a capacitor dielectric or as a layer insulation in high-voltage transformers. The idea was to use a “typical, widely used” insulation material such that the obtained results are more likely to be representative for a larger group of polymeric insulation materials. The nominal thickness of the used foil is $d = 23 \mu\text{m}$, and measured to be within $22.5 \mu\text{m}$ and $23.5 \mu\text{m}$ for all samples (all from same reel). The foil is cut into circles of 50 mm diameter and stored

in an air atmosphere with $(33 \pm 2)\%$ RH and a temperature of 22 ± 2 °C for at least 12 h prior to testing. Before the sample is placed in the sample holder shown in Figure 7.5b, its surface is cleaned with ethanol and possible static charges are removed by contacting both sides with a conductive foil. The sample holder is then placed inside the test cell, which is at room temperature 24 ± 2 °C. A strong dependence of the time to failure on the air RH was observed (not further investigated in this study). The RH inside the test chamber was thus held constant at $(33 \pm 2)\%$ by a conditioned purge flow ($\sim 10 \text{ L min}^{-1}$). At room temperature, the ingress of water molecules into a PET foil of $23 \mu\text{m}$ thickness is expected to reach the equilibrium concentration after a few minutes (estimation based on the diffusion length $2\sqrt{D \cdot t}$ and the diffusion constant $D = 4 \times 10^{-9} \text{ cm}^2 \text{ s}^{-1}$ [YS62]). Controlling the RH *inside* the test cell is thus especially important when testing thin foil samples.

The high-voltage electrode (lower electrode in Figure 7.5b) is planar (diameter 10 mm with 1.5 mm fillet radius) while the ground electrode is a half-sphere of radius 5 mm. A spring mechanism generates a mechanical contact force $F_c \approx 3 \text{ N}$ to ensure a reliable and reproducible electrode contact. The electrostatic force between the electrode charges leads to an additional, voltage-dependent contribution to the contact force. From the Hertzian theory of elastic contact [TG82] with the extension proposed in [Wat65] to include thin sheets of elastic materials on a rigid substrate (see Appendix B), the foil indentation depth is calculated to be $\delta \approx 1.2 \mu\text{m}$ at 11 kV ($\delta \approx 0.9 \mu\text{m}$ at 0 kV), which corresponds to about 5% of the foil thickness. The target insulation volume is thus localized underneath the indent of diameter $2r_c = 2\sqrt{R\delta} \approx 0.16 \text{ mm}$.

Outside of the indented region (i.e. near the triple point) the electrode potential is transferred to the polymer surface by means of partial discharges (PDs). If the repetitive pulses do not incept PDs (the case investigated in this study), it is only the time-averaged voltage (i.e. the DC component) which is transferred. In summary, the foil is stressed with a quasi-homogeneous electrical field whose maximum is at the point of maximal indentation. Since all breakdown channels were located within the indented area, no attempt was made to quantify the lateral extent of the deposited surface charge layer.

The aluminum electrodes are removed and polished to a surface roughness of about $R_a \approx 0.44 \mu\text{m}$ ($R_q \approx 0.58 \mu\text{m}$) after each breakdown in order to eliminate the influence of metal protrusions generated by the breakdown channel. Figure 7.6 shows an image of the electrode surface after

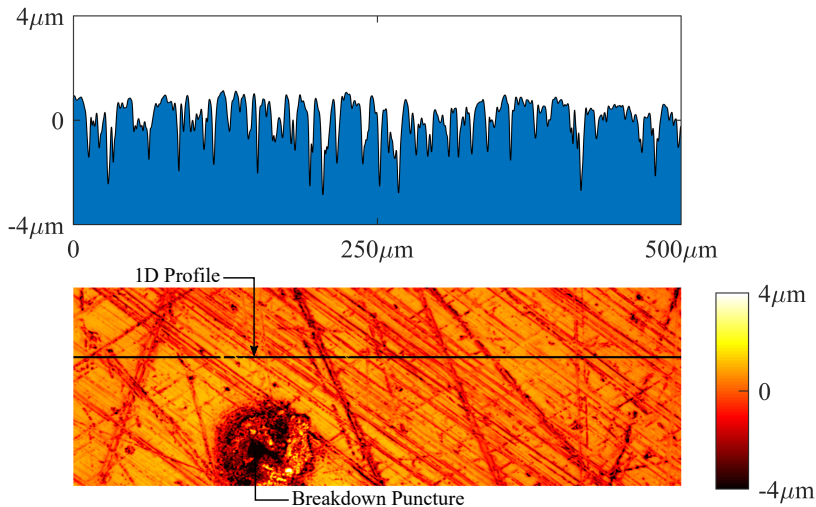


Figure 7.6.: Surface topology of the aluminum electrode surface.

breakdown, based on confocal microscopy data. A Gauss-filter with a cutoff wavelength of $2.5 \mu\text{m}$ is applied for the determination of the surface roughness (following DIN ISO 4287).

The PD inception voltage of the used electrode-specimen configuration is experimentally determined to lie between 1.0 and 1.1 kV. The sharp transition between the PD and non-PD regime can be well distinguished by means of an installed near-UV camera ($\sim 350 \text{ nm}$ to $\sim 380 \text{ nm}$) and a photomultiplier tube ($\sim 200 \text{ nm}$ to $\sim 380 \text{ nm}$). In this study, the focus is on pulse voltages below 1 kV (peak-peak), i.e. a regime where the pulse voltage does not incept PDs, and hence no PD-induced erosion of the polymer foil surface takes place (also validated by microscopic inspection of the foil surface after stressing). The inception voltage for repetitive PDs is determined only by the peak-to-peak value of the pulse voltage, but not the DC-bias. Indeed, the latter is eliminated within the air gap by an initial deposition of surface charges near the electrode contact area on the foil. The repetition rate of DC PDs is measured to be below 1 s^{-1} and its effect on insulation deterioration can thus be neglected. The PD regime is investigated in Chapter 7.3.

The presented electrode-specimen configuration was chosen for the fol-

lowing reasons:

- The stressed volume is small, which allows to avoid a significant heating of the insulation volume even at high pulse frequencies (quantitative analysis given in Section 7.2.2), and thus to investigate insulation failure outside the thermal aging/thermal breakdown regime.
- The configuration has a high degree of (macroscopic) symmetry, and thus is more easily amenable to numerical estimations of system properties (thermal, electric field, etc.) than more complicated systems (such as twisted wires).
- The arrangement can be used to investigate the breakdown of polymeric insulation in the presence or absence of PDs without the need for replacing the surrounding air with insulating oil. This is a consequence of b) and the associated existence of a stable, well-defined PD inception voltage for this configuration.
- Foil samples are easily prepared in the large quantities (several hundred) needed for the presented multiparameter study, and exhibit uniform physico-chemical and geometrical characteristics (all from same reel).
- Using an electrode contact point (or, more accurately, a small plastically deformed contact area) allows using thin foil insulation without the need for a metallic contact coating.

The time to failure is always a system property (electrodes + sample material + environmental influence), and hence in general different for different setups. Thus, it is quantifying the relative variation of the time to failure as a function of certain parameters that is the most relevant information in the obtained data (the sample and electrode material/geometry are also considered as parameters). Therefore, in essence, a “good” setup for time-to-failure testing restricts the variation of all parameters influencing the time to failure to a degree such that the variation (if present) caused by the target parameter is discernable. In addition, it should either be close enough to actual use conditions (in order to allow inference/scaling from experiment to applications) or answer a specific research question (in order to extend the understanding of the fundamental processes leading to electrical breakdown under the investigated conditions).

Test Procedure

The investigated voltage waveforms consist of a rectangular pulse train with a DC offset, as exemplified in Figure 7.5. The investigated variables are the pulse amplitude U_p , the pulse fundamental frequency f_0 , the pulse rise time τ_r and the pulse duty cycle D . The variation of the time to failure under pure DC voltage is also examined for the interpretation of the results. The investigated subset of the parameter space is shown in Table 7.1.

Table 7.1.: Voltage parameter values. The default values are indicated in bold. Environmental conditions: held constant at $T = 24 \pm 1^\circ\text{C}$, $\text{RH} = 33 \pm 2^\circ\text{C}$.

Parameter	Unit	Values
U_p	kV	0.00 0.50 0.75 1.00 1.25 1.50
f_0	kHz	0.0 0.5 1.0 2.0 4.0 6.0 8.0
τ_r	μs	0.04 0.3 1.0 2.0 10 20
D	%	0 1 5 10 50 100
U_{DC}	kV	9.5 10.25 10.625 11.0

For all pulse-modulated waveforms the DC offset voltage is adjusted to keep the nominal peak voltage at 11 kV for all tests (transient overvoltages are discussed in Section 7.2.4). The nominal peak voltage is given by

$$U_{\text{peak}} = U_{\text{DC}} + U_p \frac{1 - D}{2} \stackrel{!}{=} 11 \text{ kV} \quad \text{for all } U_p \text{ and } D. \quad (7.2)$$

As mentioned at the end of the Introduction, the prime motivation for choosing this type of mixed-voltage stress (DC+repetitive pulse) in combination with the shown electrode-specimen configuration is to...

- ...eliminate the known risk factors a. to c.
- ...promote favorable conditions for the occurrence of the additional potential aging mechanism (d.)

In addition, lifetime data on insulation aging under this voltage profile may be of direct practical interest for the high-voltage insulation design of e.g. Input Series Output Parallel (ISOP) DC-DC converters [FL11], gate drive transformers of MV solid-state switches etc.

At the beginning of a test, the pulse voltage is applied and the DC bias is ramped up to its final value within five seconds. This stress is then left unchanged until breakdown occurs. The time to failure is recorded automatically when the breakdown current detector triggers. All samples are visually inspected to ensure the presence of the breakdown puncture.

Statistical Analysis

The recorded time-to-failure (TTF) values are fitted by a two-parameter Weibull distribution, whose cumulative distribution function is given by

$$F(\text{TTF}) = 1 - e^{-\left(\frac{\text{TTF}}{\alpha}\right)^\beta} \quad (7.3)$$

The fit is obtained by performing a least-square linear regression in the coordinate system within which all Weibull distributions appear as straight lines (see Figure 7.7). It is obtained by plotting $\ln\{-\ln[1 - F(\text{TTF})]\}$ as a function of $\ln(\text{TTF})$.

The scale parameter α is equal to the 0.63 percentile while the shape parameter β is a measure of the scatter of the TTF values around the median, and is given by the slope of the regression line. Instead of the scale parameter, the 0.5 percentile (i.e. the median) will be used for the characteristic TTF values reported in the Results section. The 95% confidence interval for the median is obtained from the corresponding confidence bounds on the linear regression (the curved lines in Figure 7.7).

In some samples (about 1 out of 50) early failure occurred, probably due to accidentally placing the high electric field stress region onto a weak spot in the polymer foil. They could be well separated from “regular” earlier failures with the aid of the Weibull fitting procedure: including/excluding any “regular” failure time in the fit is observed to not decrease the value of the slope β by more than a few percent (always < 10%), while including/excluding early failures leads to a significant decrease of >20%. There is thus a clear gap which allows an algorithmic identification of early failures. The early failures have been excluded in the calculation of the characteristic times to failure.

Maximal Sample Temperature

Although the present study is designed to *not* operate in a regime where the dielectric losses due to the pulse voltage cause a significant insulation

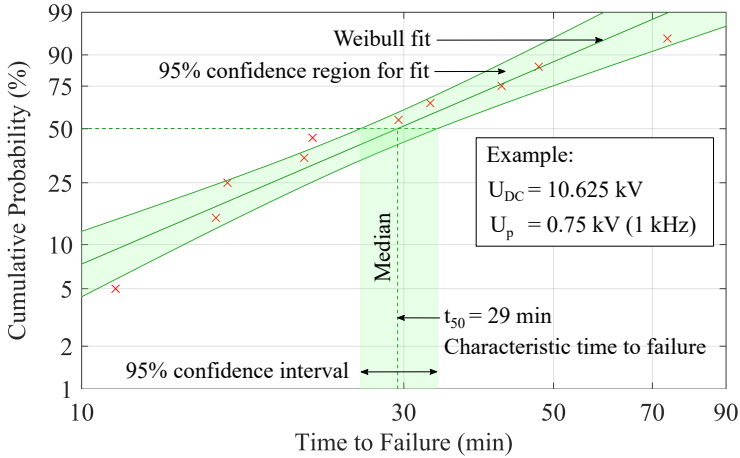


Figure 7.7.: 10 times to failure are recorded for each stress condition (table 7.1) and fitted by a Weibull distribution. The corresponding median value and its 95 % confidence bound are given in the Results section (Figure 7.8).

temperature rise, dielectric heating of the foil was analyzed in detail in order to ensure that this is indeed the case.

The detailed derivation is given in Appendices C, D and E. Given an excitation voltage of period T ,

$$u(t) = \operatorname{Re} \left[\sum_{n=1}^{\infty} \frac{U_n}{-n} e^{j\omega_n t} \right] \quad \text{with } \omega_n = n \frac{2\pi}{T}, \quad (7.4)$$

an upper bound on the maximal insulation temperature is shown to be the solution of the iterative scheme E.15:

$$\vartheta_{i+1} = \vartheta_i + \frac{\dot{q}(\vartheta_i)}{\Gamma} \quad i = 1, 2, \dots \quad (7.5)$$

where the (local) cooling coefficient Γ ($\text{W K}^{-1} \text{m}^{-3}$) is a function of the geometry, the thermal conductivity of the foil and the thermal resistance to the heat bath of temperature ϑ_0 (electrodes). See Figure C.1. The spatial maximum of the dielectric loss density (time-averaged over a

period T) is given by

$$\dot{q}(\vartheta) = \kappa_{\text{DC}}(\vartheta) \left[\frac{U_{\text{DC}}}{d} \right]^2 + \frac{\varepsilon_0}{2} \sum_{n=0}^{\infty} \omega_n \varepsilon''_{\text{eff},n}(\vartheta) \left[\frac{|U_n|}{d} \right]^2. \quad (7.6)$$

where κ_{DC} is the DC conductivity and $\varepsilon''_{\text{eff},n}$ the imaginary part of the effective dielectric permittivity (it includes the DC conductivity for the voltage components $n \geq 1$).

7.2.3. Results

The results section starts out by showing that excessive insulation temperature can be excluded as a cause of insulation failure for the stress profiles and electrode configuration used in this study. Then, the measured characteristic TTF values (median and 95 % confidence interval of the fitted Weibull distribution) are presented for the parameter variations specified in table 7.1, and it is shown that they obey the modulated DC stress hypothesis (defined below) within the investigated parameter ranges.

Thermal Stability

For (mixed) broadband voltages, the dielectric loss density is a convolution of the power spectrum and dielectric parameters, as given by Equation (7.6). For the calculations, the following parametrization of the DC conductivity of PET is used:⁵

$$\kappa_{\text{DC}}(\vartheta) = \kappa_0 e^{-\frac{E_a}{k_B \vartheta}} \quad (7.7)$$

where $\kappa_{\text{DC}} = 1.04 \cdot 10^5 \text{ S m}^{-1}$ and $E_a = 0.97 \text{ eV}$ are derived from the high-field measurement data (up to 50 kV mm^{-1}) provided in [MGMD97], by linear extrapolation to the maximal DC field strengths occurring here ($\sim 400 \text{ kV mm}^{-1}$). The effective dielectric permittivity was determined by dielectric spectroscopy on the actual PET foil samples used in the TTF testing (using the setup described in Chapter 6). Figures 5.5a and

⁵A posteriori, the DC conductivity is observed to not make a significant contribution to the overall dielectric losses *under the investigated conditions*. However, its relative contribution to dielectric losses increases with increasing temperature, and above a certain threshold temperature, it can lead to thermal runaway due to its large temperature feedback coefficient $\partial \kappa_{\text{DC}}(\vartheta) / \partial \vartheta$ (divergence of the iterative scheme 7.5).

5.5b shows the measured real and imaginary part, respectively, of $\underline{\varepsilon}$ as a function of frequency and temperature. The frequency range above 200 kHz was obtained by fitting the β loss peak at 15 °C (where it is inside the measureable frequency range), and then determining its shift to higher frequencies by fitting it to the available data points at higher temperatures (where the peak maximum is outside the accessible region.)

The maximum insulation temperature ϑ_m was determined with the formalism outlined in the Methods section, by using worst case estimates of the involved parameters (e.g. thermal coupling to electrodes). Of all the parameter combinations used in this study, the highest insulation temperature increase $\Delta\vartheta_m = \vartheta_m - \vartheta_0$ is obtained with $U_p = 1.5$ kV, $U_{DC} = 10.25$ kV, $f_0 = 8$ kHz, $\tau_r = 40$ ns, and equals about 3 °C. The conduction losses (first term in Equation 7.6) are negligible at room temperature and cannot be activated by the temperature rise provoked by the AC dielectric losses. Based on this analysis it is thus justified to exclude risk factor *c*. (Excessive insulation temperature) as a possible cause of insulation failure in this study.

With a view to the typically more bulky insulation encountered in actual MV insulation systems, it is useful to keep in mind that the risk of a thermal instability (at fixed electric field stress) increases rapidly with insulation thickness d , because the cooling coefficient Γ scales approximately as d^{-2} (see Appendix E).

Times to Failure

The main goal of this study was to find out if there is experimental evidence of an additional degradation/aging mechanism (d.) that is activated by superimposing a repetitive pulse voltage onto a DC bias voltage. We take the (non-)existence of such an additional degradation as equivalent to the (non-)applicability of the *modulated DC-stress hypothesis*. The latter assumes that the failure mechanism active under pure DC voltage is just “modulated” by the changing voltage levels U_{peak} and $U_{\text{peak}} - U_p$. This assumes in particular that the transition between these levels does not lead to an acceleration of the failure mechanism operant under “pure” DC stress. More specifically, let $\text{TTF}_{DC}(U)$ be the median time to failure under a pure DC stress of amplitude U (see Figure 7.8e). Then, the chosen formulation of the modulated DC-stress hypothesis reads

Modulated DC Stress Hypothesis

$$\text{TTF}_{\text{DC}}(U_{\text{peak}}) \leq \text{TTF}_{\text{p}}(U_{\text{peak}}, U_{\text{p}}, D) \leq \text{TTF}_{\text{DC}}(U_{\text{peak}} - U_{\text{p}}), \quad (7.8)$$

where $\text{TTF}_{\text{p}}(U_{\text{peak}}, U_{\text{p}}, D)$ is the median time to failure under the (DC-biased) rectangular pulse voltage of duty cycle D with levels U_{peak} and $U_{\text{peak}} - U_{\text{p}} > 0$. Note that TTF_{p} (by definition of the hypothesis) is not an implicit function of pulse frequency and rise time. In contrast, it necessarily depends on the duty cycle D , because otherwise the limiting cases

$$\text{TTF}_{\text{p}}(U_{\text{peak}}, U_{\text{p}}) \stackrel{!}{=} \text{TTF}_{\text{DC}}(U_{\text{peak}}) \quad \text{for } D = 1, \quad (7.9)$$

$$\text{TTF}_{\text{p}}(U_{\text{peak}}, U_{\text{p}}) \stackrel{!}{=} \text{TTF}_{\text{DC}}(U_{\text{peak}} - U_{\text{p}}) \quad \text{for } D = 0, \quad (7.10)$$

would lead to the absurd conclusion that $\text{TTF}_{\text{DC}} = \text{const.}$

It can now be shown that the experimental results respect the modulated DC-stress hypothesis, except for the cases where one of the mechanisms a. or b. from Section 7.2.1 is active (mechanism c. is excluded according to the previous section). Figure 7.8b shows – and this is the main result of this study – that TTF_{p} is indeed independent of the pulse frequency (within the experimental uncertainty). Moreover, the times to failure $\text{TTF}_{\text{p}}(11 \text{ kV}, 0.75 \text{ kV}, 0.5)$ lie between $\text{TTF}_{\text{DC}}(11 \text{ kV})$ and $\text{TTF}_{\text{DC}}(10.25 \text{ kV})$ for all tested frequencies, and thus satisfy inequality 7.8 required by the modulated DC-stress hypothesis.

Similarly, Figure 7.8a also shows that the TTF increases when U_{p} is increased (for a fixed peak voltage $U_{\text{peak}} = 11 \text{ kV}$). For $U_{\text{p}} = 1 \text{ kV}$ the further increase only applies to samples which do not yet incept PDs. The ones with (intermittent) PDs show a marked decrease in TTF. This also explains the unusually large scatter, as compared to the cases $U_{\text{p}} < 1 \text{ kV}$ and $U_{\text{p}} > 1.1 \text{ kV}$ where none/all of the samples incept PDs, respectively.

In Equations (7.9) and (7.10) the limits of TTF_{p} for $D \rightarrow 0$ and $D \rightarrow 1$ are related to the corresponding values of TTF_{DC} . The results in Figure 7.8c are interesting in this respect, because they show *how* these limits are approached. Surprisingly, $\text{TTF}_{\text{p}}(U_{\text{peak}}, U_{\text{p}}, D)$ remains close to $\text{TTF}_{\text{DC}}(U_{\text{peak}})$ for values of D down to 0.01. It is only in the interval

$D \in (0, 0.01]$ that TTF_p makes the large jump to $\text{TTF}_{\text{DC}}(U_{\text{peak}} - U_p)$.

Finally, from 7.8d $\text{TTF}_p(11 \text{ kV}, 0.75 \text{ kV}, 0.5)$ is seen to be independent of rise time, except for values lower than about $0.5 \mu\text{s}$ ($> 1.2 \text{ kV } \mu\text{s}^{-1}$), where a small but statistically significant decrease of TTF_p is observed. This observed dependence of TTF_p on rise time below $\tau_r = 0.5 \mu\text{s}$ is the only violation of the modulated DC stress hypothesis as formulated above, and its practical implications are further discussed in Section 7.2.4.

Another result of this study that is in line with the modulated DC stress hypothesis is the observation that the functional dependence of TTF_{DC} and TTF_p on relative humidity is the same (namely $\propto e^{-a \cdot \text{RH}}$, with $a > 0$ a constant).

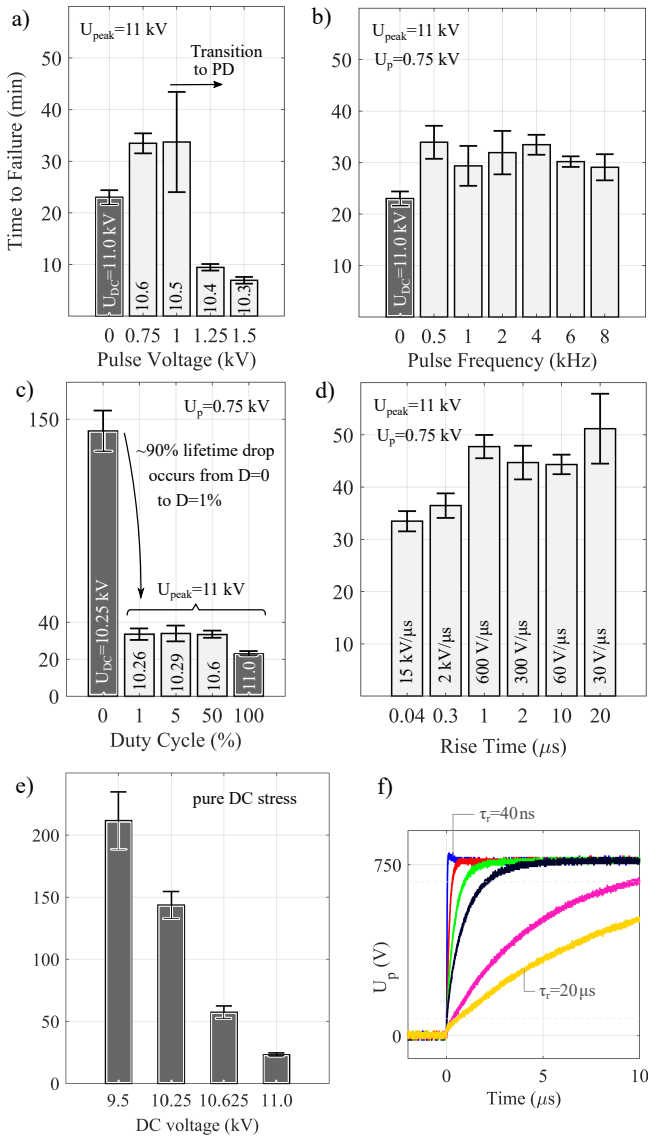


Figure 7.8.: Characteristic TTF values as a function of a) pulse voltage b) pulse frequency c) pulse duty cycle and d) pulse rise time e) pure DC voltage. Default parameter values are $U_p = 0.75$ kV, $f_0 = 4$ kHz, $D = 50\%$, $\tau_r = 40$ ns and $U_{DC} = 10.625$ kV (the dark bars correspond to pure DC voltage stress tests). Repetitive PD is absent, except for the cases $U_p \geq 1$ kV in figure a. Figure f) shows the measured voltage fronts for the investigated rise times.

7.2.4. Discussion

Before entering into the discussion of the results, it seems appropriate to stress that the conclusions drawn from the empirical data of this study (covering a small part of the full parameter space of mixed inverter-type voltages) should not be transferred – unless there is a physical reason to do so – to other types of mixed-voltage stresses and/or other insulation materials. Moreover, it is important to be aware of the inherent limitations of accelerated aging tests. Although the core result of this study is mostly based on the observed absence of differences in TTF values (Figure 7.8b), extrapolating this result to use conditions still needs further experimental corroboration.

With these reservations in mind, the observed results suggest that there is no premature failure observable when modulating a DC voltage with a MF pulse voltage (keeping the same peak voltage). In fact, the results indicate that the physical processes leading to insulation failure under a pure DC voltage are merely modulated by the varying voltage levels. There is thus no empirical evidence for an additional “per pulse” degradation mechanism beyond those considered in points a. to c. of the Introduction. In particular, within the time scales investigated in this study, there is no evidence of the potential aging mechanism (d.) based on the cyclic electromechanical force exerted (by the repetitive voltage pulses) on space charge evolving under the DC field component of the applied stress. Although space charge was not quantified within this study, its presence under the applied level of DC field stress (in excess of 400 kV/mm) is extremely likely, since space charge in PET foil has been measured at field strengths as low as 0.5 kV/mm [ND09].

Although limited data is available on this point, the results show a small but significant dependence of TTF_p on rise time below about 0.5 μs . Inequality 7.8 still holds for the investigated range of rise times, but the possible dependence $\text{TTF}_p(U_{\text{peak}}, U_p, D, \tau_r)$ must be accommodated. However, the observed independence of TTF_p on pulse frequency f_0 for $\tau_r = 40$ ns (Figure 7.8b) suggests that there is no additional “per pulse” degradation occurring even at these short rise times (otherwise TTF_p would be expected to decrease with increasing f_0), but rather that the final cascade of processes leading to breakdown is triggered somewhat earlier in the presence of fast voltage flanks ($> 1 \text{ kV } \mu\text{s}^{-1}$).

Our first hypothesis for explaining the observed dependence of TTF_p on rise time (for $\tau_r < 0.5 \mu\text{s}$) as a consequence of risk factor b., that is, the

excitation of overvoltages (sample/cell capacitance and series inductance) could not be confirmed. Indeed, the measured waveforms displayed in Figure 7.8f do not show a significant overshoot ($< 5\%$) even at the shortest rise time (measured with LeCroy PPE 20 kV/100 MHz).

One rather surprising result is the observed functional dependence of TTF_p on pulse duty cycle D . For a given peak voltage, the insulation lifetime is largely independent of the duty cycle in the range $D \in [0.01, 0.5]$. It thus seems that the mere presence – and not primarily the duration – of the (repetitive) peak voltage is decisive for insulation lifetime. Here, further investigations would be interesting to gain more insight into the dynamics of the operant (DC stress) failure mechanism (e.g. determining the *necessary* repetition rate for keeping the peak voltage as determinant of insulation lifetime, or determining the value of the duty cycle below which TTF_p begins to increase significantly from $TTF_{DC}(U_{peak})$ towards $TTF_{DC}(U_{peak} - U_p)$). This exemplifies that the unconventional nature of synthesized waveforms can constitute an active tool for gaining insight into the fundamental processes leading to insulation aging and failure.

7.2.5. Conclusion

By drawing on the existing research literature, three established risk factors promoting insulation failure under inverter-type voltage stress were identified:

- a. Enhanced partial discharge intensity
- b. Systemic overvoltages
- c. Excessive insulation temperature

This study's aim was to provide empirical data that helps to answer the open question of whether or not this list is complete. If so, the elimination of the above risk factors would provide a sufficient criterion for ensuring insulation reliability under this type of insulation stress.

To this end, a sphere-plane electrode configuration on PET insulation foil was employed, which deliberately eliminates all established risk factors for inverter-type voltages, that is, PD erosion, systemic overvoltages and significant heating of the dielectric volume by dielectric losses. The chosen voltage stress consists of a unipolar mixed voltage (DC-biased medium-frequency rectangular pulse voltage).

For the investigated material, parameter ranges and stress levels, the main

result of this study is that no experimental evidence of a hypothesized “per pulse” aging mechanism (e.g. due to the cyclic electromechanical force acting on space charge in the insulation bulk) could be found. The empirical data of this study thus suggests that the proper consideration of the known risk factors a. to c. is sufficient to eliminate any detrimental impact associated with the switching transitions, even in the presence of a significant DC bias voltage.

An auxiliary result – possibly of interest for practical applications – is the observation that the TTF depends strongly non-linearly on the duty cycle D of the pulses. For the investigated case of a 4 kHz rectangular pulse train superimposed onto a DC voltage (to give 11 kV peak), most of the drop in TTF is observed to occur in the interval $0 < D < 1\%$.

7.2.6. Limitations and Outlook

For the estimation of the temperature increase due to dielectric losses it would be preferable to use *measured* conduction currents under the applied field stress instead of extrapolated literature values for (apparent) DC conductivities of PET. This would reduce the uncertainty in assessing the role of DC conduction losses in specimen breakdown under the investigated stress profile (in particular for the estimation of the threshold voltage/temperature for thermal runaway).

One of the main limitations of this study (already mentioned in the Discussion section) concerns the high electric field stress applied to the samples (as compared to typical operating field stresses) and the associated short duration of the time to failure. It cannot be excluded (is even expected) that the relative strength of different failure mechanisms changes as a function of the applied field stress. Hence, it is possible that a failure mechanism that was negligible under the stress conditions employed in this study will begin to dominate as the stress profile is altered.

The following alternative approaches are suggested for future investigations:

- Generate life curves, i.e. TTF as a function of applied stress levels. The slope of the obtained life curve provides information about the active aging mechanism(s). On the basis of a suitable life model for the considered system/stress, an estimation of TTF by extrapolation to use conditions is possible, even though typically associated with

relatively large uncertainties (unless time-consuming tests for stress amplitudes close to the operating stresses are included).

- Exposing a number of samples *simultaneously* to actual use conditions (electric field, temperature, humidity, etc.) and assess their dielectric strength (i.e. short-term voltage withstand) with voltage ramp testing after certain stressing intervals. Dielectric strength testing is much less time-consuming than constant-stress testing. However, when used without a prior realistic pre-stressing scenario, its results are of very limited informative value, because the operation-relevant aging mechanisms are never activated. It may however be used for quality control and related purposes (see citation from ASTM-D149 on p. 145).
- Instead of (or in addition to) destructive dielectric strength testing, dielectric spectroscopy may be used to quantify the stress-induced changes in the insulation material/system. In a sense this also generates “life curves”⁶ that may be used to infer information about the active aging mechanism, but with the big advantage that the procedure is non-destructive and can be used repetitively under *operating* (realistic) stress conditions (for which time-to-failure testing is not applicable/feasible). Here in particular, the online dielectric spectrometer presented in chapter 8 is an interesting tool, because it allows a non-invasive, continuous monitoring of the dielectric response while the stress is applied.

Finally, given the observed drop in lifetime for rise times below about $\tau_r < 0.5 \mu\text{s}$ (corresponding to switching speeds $> 1 \text{ kV } \mu\text{s}^{-1}$), it seems relevant from a practical perspective to investigate the trend of this decrease for switching speeds above $15 \text{ kV } \mu\text{s}^{-1}$ (is TTF levelling off, or decreasing even more?). Moreover, the reason for the observed decrease in lifetime is still unclear – the only observation being that it is not a “per pulse” degradation (because there is no dependence of TTF on switching frequency even at $15 \text{ kV } \mu\text{s}^{-1}$), but rather an earlier initiation of the final cascade of processes leading to breakdown.

⁶The time series of the value of some functional acting on the complex permittivity spectrum $\underline{\epsilon}(\omega, t)$ recorded at time t .

7.3. Time-to-Failure Testing under DC-biased Repetitive Impulse Voltages Above PD Inception

“The breakdown field of a dielectric is as notoriously irreproducible as the d.c. conductivity unless great care is taken.”

P.J. Harrop
in *Dielectrics* (1972)

“The electric breakdown of plastic cannot be defined by a single value. Tables of values may be useful for comparison and initial screening, but may also be misleading and should not be used for design. For each application it is necessary to evaluate properties under the conditions of use because service factors may affect the voltage performance of plastics.”

K.N. Mathes
in *Encyclopedia of Polymer Science and Technology – Electrical Properties* (2010)

7.3.1. Introduction

Premature insulation failure due to the inception of PD under repetitive MF pulse voltage stress is well-documented in literature (see Section 2.3.1). This chapter will complement the available research literature by providing lifetime data on polymeric insulation foil exposed to a strictly unipolar inverter voltage stress (a DC-biased rectangular MF pulse voltage). The dependence of insulation lifetime on waveform parameters (fundamental frequency f_0 , duty cycle D , rise time τ_r , DC bias U_{DC}) is investigated. Moreover, a quantification of the observed PD erosion by means of confocal microscopy is provided.

7.3.2. Methods

Instrumentation & Materials

The same test bench, samples, electrode configuration, sample preparation and environmental conditions as described in the study below PD inception (see Chapter 7.2.2) were used here. The same type of mixed voltage (DC-biased rectangular MF pulse voltage) is used, the only difference residing in the employed amplitude U_p of the repetitive pulse voltage. While the study presented in Chapter 7.2 focused on the non-PD regime $U_p < 1$ kV, the PD regime $U_p > 1.1$ kV is investigated here (see transition in Figure 7.8a). The used parameter values are summarized in table 7.2.

Table 7.2.: Varied voltage waveform parameter values for lifetime testing. The default values are indicated in bold. Environmental conditions: held constant at $T = 24 \pm 1^\circ\text{C}$, $\text{RH} = 33 \pm 2^\circ\text{C}$.

Parameter	Unit	Values
U_p	kV	0.00 1.5
f_0	kHz	0.0 0.5 1.0 2.0 4.0 8.0
τ_r	μs	0.05 0.5 1.0 2.0
D	%	0 0.5 1 5 20 50 80 95 99 100
U_{DC}	kV	8.75 9.25 9.75 10.25 11.0

The presence of PDs can be detected by the installed PMT and the near-UV camera (Section 7.1.2). Moreover, the near-UV camera provides information about the spatial extent of the corona discharge and the (time-averaged) radiant intensity within the optical setup's transmission band.⁷

The confocal microscope images were recorded on a *Zeiss LSM 880*⁸, while a *Wild M5* microscope was used for conventional light microscopy. For the images shown in Figure 7.11, the foil surface was sputter coated

⁷The UV-light intensity analysis is used merely as a semi-quantitative tool, because no attempt to linearize the detection sensitivity (transmission spectrum of the collimator/lens/fiber system, quantum efficiency of the CCD detector, etc.) has been made.

⁸Scientific Center for Optical and Electron Microscopy (ScopeM) at ETH Zürich.

with a 50 nm layer of a Platinum-Palladium alloy in order to enhance surface contrast.

PD Inception Criterion

In order to obtain an understanding of the spatial extension and the inception of repetitive PDs in the chosen electrode configuration, the streamer criterion is used. The electric field close to the triple point is approximately equal to⁹

$$E_{\max} \approx \frac{\varepsilon_{\text{PET}} \cdot U}{d}, \quad (7.11)$$

and the critical field of air at atmospheric pressure ($E_{\text{crit}} = 24.4 \text{ kV cm}^{-1}$) near the triple point is reached already at about 20 V of potential difference between the electrodes (see Figure 7.9a, left axis).¹⁰ However, in order for an electron avalanche to develop and generate a sufficient number of electrons $N_c = 10^6 \dots 10^8$ for streamer inception, the discharge path within the critical field region must be sufficiently long (see 7.9a, right axis). This is expressed by the streamer criterion [BBMZ83]:

$$\int_0^{x_{\text{crit}}} \alpha_{\text{eff}}(x) dx \stackrel{!}{=} K_{\text{St}} \stackrel{?}{=} \ln(N_c) \approx 14.18, \quad (7.12)$$

where α_{eff} is the effective ionization coefficient [BBMZ83]. The integration path follows the electric field lines within the critical volume, that is, where $\alpha_{\text{eff}} > 0$. The applicability of the relation $K_{\text{St}} = \ln(N_c)$ will be discussed in Section 7.3.4.

A numerical evaluation of the streamer integral 7.12 for an electrode potential difference of 500 V to 550 V as a function of the radius (electric field base point) is shown in Figure 7.9b. The effective ionization coefficient

⁹An idealized geometry is considered here: a single contact *point* of a perfectly smooth half-sphere on a non-indented insulation foil. See Appendix B for the expected deviations from this geometry.

¹⁰The x-axis radius value is the base point location (on the foil surface) of the considered field line.

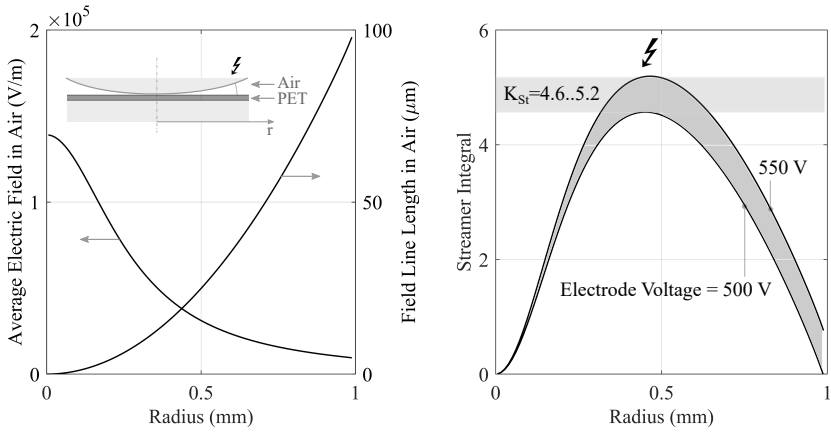


Figure 7.9.: a) Average electric field in air along field line (left axis) and its length (right axis). The radius corresponds to the base point location of the field line on the PET surface. b) Evaluation of the streamer integral 7.12.

(in $\text{mm}^{-1} \text{bar}^{-1}$) is parametrized by [ZP94]

$$\frac{\alpha_{\text{eff}}}{p} = 27.9 \cdot \left[\frac{E}{p} - 8.9246 \right] \quad \text{for } \frac{E}{p} \leq 12.36 \text{ kV mm}^{-1} \text{bar}^{-1} \quad (7.13)$$

$$\frac{\alpha_{\text{eff}}}{p} = 22.3595 \cdot \frac{E}{p} - 180.1709 \quad \text{for } \frac{E}{p} > 12.36 \text{ kV mm}^{-1} \text{bar}^{-1}, \quad (7.14)$$

where p is the gas pressure (here $p = 1 \text{ bar}$)¹¹ and E/p is the value of the reduced electric field in units of $\text{kV mm}^{-1} \text{bar}^{-1}$.

¹¹For open systems, the pressure must be replaced by the particle number density N (e.g. by using the ideal gas law $p = Nk_B T$) in order to correctly account for the influence of temperature on the ionization coefficient (because increasing the temperature in an open system decreases the particle number density while leaving the pressure unchanged). See e.g. [LCd⁺19].

7.3.3. Results

This section first presents optical inspections of the polymer surface after its exposure to PD attack. In the second part, the dependence of sample lifetime on a number of parameters of the applied mixed voltage (DC-bias, pulse frequency, rise time and duty cycle) is illustrated.

PD Erosion of Insulation Foil: Optical Characterization

A corona discharge (repetitive, visible PDs) occurs in the air near the triple point of the electrode configuration when the peak/peak value of the pulse voltage exceeds $U_p \approx 1.1$ kV (see Figures 7.10a and b). The DC component (DC bias voltage U_{DC}) is found to not significantly influence the (repetitive) PD inception voltage. For 1.0 kV $\lesssim U_p \lesssim 1.1$ kV, intermittent corona (i.e. of varying intensity, even to the point of extinction/re-inception) is observed.

The erosive effect of the corona discharge on the foil surface is visible with the naked eye: a diffuse white ring of inner diameter ~ 0.6 mm and outer diameter ~ 2.5 mm is formed around the electrode contact point. Figures 7.10d and e show optical microscope images of the eroded area. The breakdown puncture is observed to lie within the eroded area. The aluminum surface of the half-sphere electrode is also eroded by the corona discharge (Figure 7.10c).

An image of the eroded area based on confocal microscopy is shown in Figure 7.11a. Although a fully quantitative analysis is difficult due to a curvature of the foil surface, it clearly reveals that where the corona discharge occurs, the polymer is eroded to a substantial fraction of the foil thickness. Figure 7.11b depicts the same surface as seen through a conventional light microscope with side lighting (which accentuates the three-dimensional structure of the surface topology). In this plan view, a peculiar pattern of polygonal “craters” is visible just outside the electrode contact area (i.e. where the innermost streamer channels occur).

Dielectric spectroscopy on the eroded samples ($\varnothing 2$ mm Pt-Pd sputter coated electrode on eroded area) revealed a noticeable capacitance increase which agrees well with the expected increase due to the change in the sample’s vacuum capacitance. No significant changes in $\tan \delta$ were observed in these short stress exposures (5 to 20 minutes).

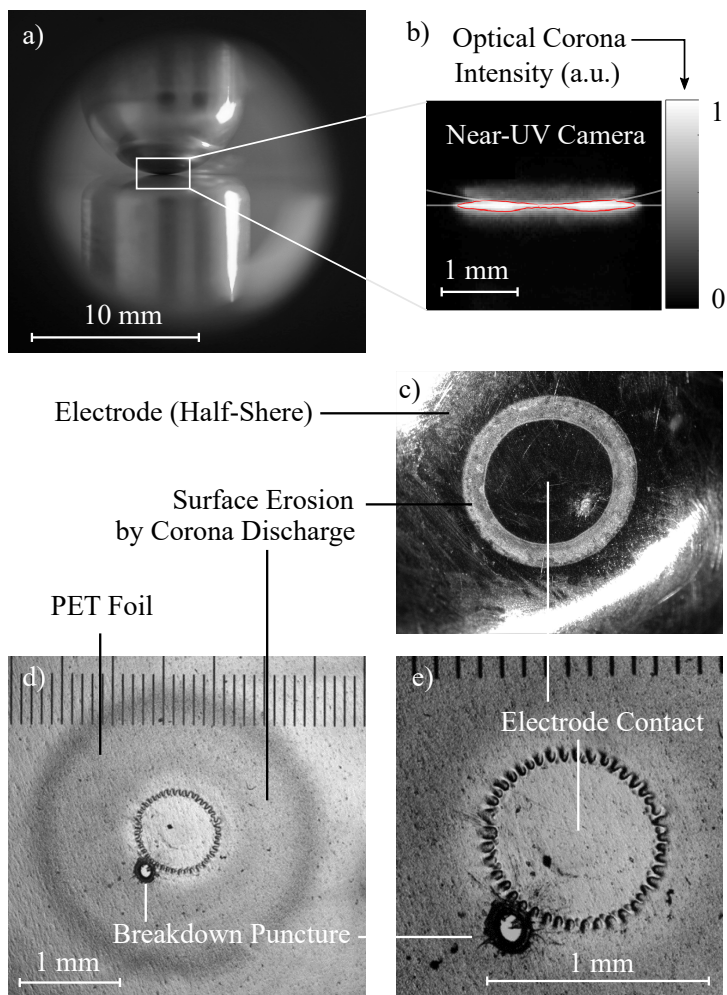


Figure 7.10.: a) Electrode configuration as seen through the near-UV camera b) Corona discharge imaged by near-UV camera c) Electrode surface erosion caused by corona discharge d) and e) Erosion of PET foil surface and breakdown puncture seen through optical microscope.

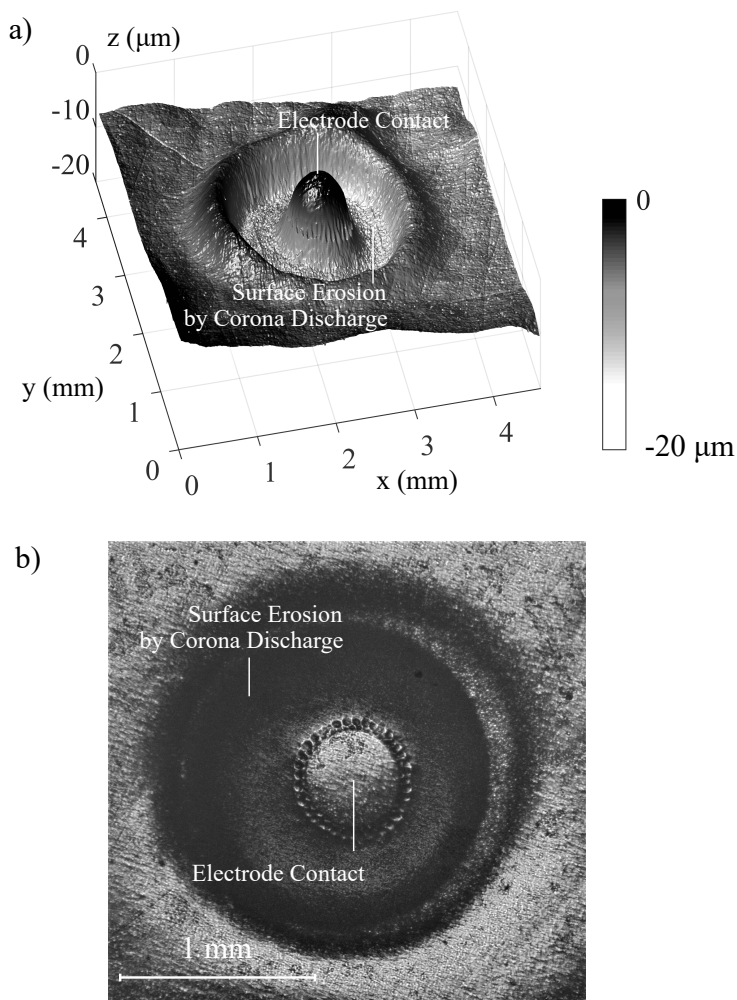


Figure 7.11.: Erosion of the PET foil by surface PD imaged by a) a confocal microscope and b) a conventional microscope with side lighting. The shown sample foil was exposed to 5 min of voltage stressing ($U_p = 1.3 \text{ kV}$, $U_{\text{DC}} = 0$, $f_0 = 8 \text{ kHz}$, $\tau_r = 50 \text{ ns}$, $D = 50 \%$).

Times to Failure

The characteristic times to failure of the insulation foil under the waveform parameter variations mentioned in Table 7.2 are shown in Figure 7.12.

A decreasing DC bias voltage increases the TTF, see Figure 7.12a. When compared to the lifetime under pure DC stress (Figure 7.8e) of the same peak voltage value, the TTF is seen to be significantly shorter (e.g. at $U_{\text{peak}} = 11 \text{ kV}$: 7 minutes under DC+pulse vs. 23 minutes under pure DC). This contrasts the result below PD inception, where the addition of a rectangular pulse train (while keeping the peak value fixed) *increases* the TTF. The modulated DC stress hypothesis (Equation (7.8)) is thus generally not valid above PD inception.

The pulse frequency is seen to have a strong impact on the TTF (Figure 7.12b). A power function fit, $\text{TTF} \propto f_0^{-k}$, leads to a value of $k = 0.65$.

Increasing the rise/fall time (i.e. reducing switching speed) of the pulse flanks is observed to significantly prolong the measured lifetime (Figure 7.12c). Most of the change occurs around $\tau_r \approx 1 \mu\text{s}$, with TTF values leveling off below $0.1 \mu\text{s}$ and above $10 \mu\text{s}$, respectively.

Finally, a minimum of TTF as a function of the pulse duty cycle is measured around $D = 80\%$. Most of the lifetime drop occurs in the interval $D \in [0, 0.005]$, continues to decrease in $D \in [0.005, 0.8]$ and finally recovers to the pure DC breakdown ($D = 1$) within the interval $D \in [0.8, 1]$.

The times to failure correlate well with the inverse of the radiant intensity determined by means of the near-UV camera. In quantitative terms, the latter was determined by averaging the gray-scale value $I(n, m)$ of all pixels satisfying $I(n, m) > 0.75 \cdot \max_{(n, m)} I(n, m)$ (area inside red contour in Figure 7.10b).¹² For example, the values thus established for the cases $f_0 = [1, 4, 8] \text{ kHz}$ (at $U_p = 1.5 \text{ kV}$, $U_{\text{DC}} = 10.25 \text{ kV}$, $\tau_r = 50 \text{ ns}$, $D = 50\%$) yield products of $\text{TTF} \times \text{average near-UV intensity}$ of $[1, 0.96, 0.94]$ (arbitrary units).

¹²This procedure excludes the low-level contributions from reflected UV light (on the electrode and foil surface).

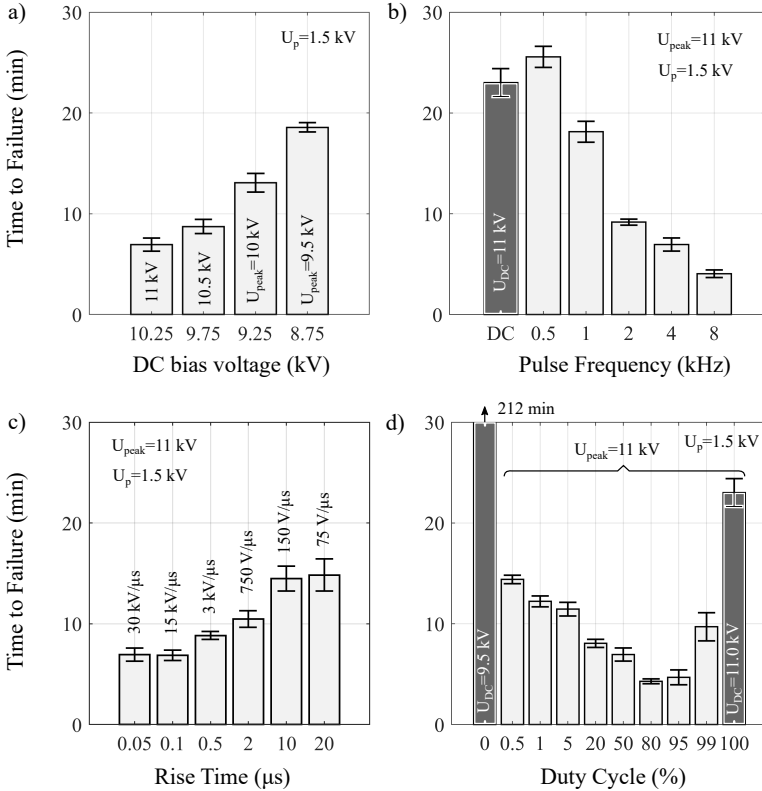


Figure 7.12.: Characteristic TTF values as a function of a) DC bias voltage b) pulse frequency c) pulse rise time and d) pulse duty cycle. Default parameter values are $U_p = 1.5$ kV, $f_0 = 4$ kHz, $D = 50$ %, $\tau_r = 50$ ns and $U_{DC} = 10.25$ kV (the dark bars correspond to pure DC voltage stress tests). Repetitive PD is present in all cases (except for pure DC stress).

Partial Discharge Inception Voltage

PD inception in the present setup (under a bipolar rectangular pulse train with $f_0 = 4$ kHz, $D = 50\%$, $\tau_r = 50$ ns and $U_{DC} = 0$) is determined to occur when U_p is between 1 kV and 1.1 kV, which corresponds to a potential difference between 500 V and 550 V between the electrodes (alternating in sign because of the assumed bipolar waveform). The corresponding streamer integral values K_{St} lie between 4.6 and 5.2.

7.3.4. Discussion

PD Erosion

The optical investigations clearly reveal that in the presence of PDs (corona), the polymer foil is thinned-out in a circular region around the electrode contact area. The circular form of the eroded region is explained by basic air discharge theory. Indeed, the high-field air volume immediately outside the indented region ($r > r_c$ in Figure C.1) cannot generate streamer discharges because the discharge paths are too short. On the other hand, the electric field decreases with increasing radius, and thus streamers cannot develop beyond a certain radius. There is thus a certain radial *range* in which streamer development occurs. Formally, the aforementioned hand-waving argumentation can be put on a more rigorous mathematical basis by using the streamer criterion (Equation (7.12)).

The observed corona discharge is expected to be a cold plasma discharge (i.e. with an electron temperature significantly above the temperature of the heavy particles), as described in the theory of Dielectric Barrier Discharges (DBDs) [Kog03] [Bra17]. The observed erosion of the polymer surface is thus a type of plasma etching, as employed e.g. in integrated circuit manufacture. Consequently, the wealth of knowledge on the interaction between isolating substrate layers (e.g. polymers, ceramics) and the DBD plasma can be used for a better understanding of the physico-chemical processes leading to insulation degradation. For example, [MF89] (p. 18) describe the following three basic mechanisms active in plasma edging:¹³

1. *Sputtering (ion-bombardment with energies > surface binding energy)*. Removal of substrate material by purely physical processes:

¹³Mechanisms 3. and 4. in [MF89] are condensed into a single point 3. here.

energetic ions crossing the plasma sheath act as projectiles ejecting substrate material into the gaseous half space upon impact. Net removal of material only occurs if the sputtered material is not back-scattered onto the substrate surface, that is, if the gas pressure is low enough (mean free path comparable to vessel dimensions). Sputtering is thus most efficient in low-pressure plasmas (<1 mbar), where ion energies are high and the mean free paths long. Sputtering is characterized by its lack of selectivity to the substrate material: the magnitude of the bonding energies rather than their chemical nature is relevant.

2. *Chemical gasification.* The plasma acts as a “chemical reactor” providing reactive molecules or atoms (the etchant species) through the collisions of the high-energy free electrons with gas molecules (e.g. the generation of atomic oxygen or ozone molecules in air). Etching occurs when these etchant species react with the substrate *and* form volatile reaction products (which are transferred to and remain in the gas phase and do not condense on the substrate). It is characterized by its high selectivity to the substrate’s chemical nature. Purely chemical plasma etching is typically non-directional (i.e. proceeding vertically and horizontally at the same rate).
3. *Ion-enhanced chemical gasification.* Mechanisms 1. and 2. may act together to produce directional chemical etching. In this case, the plasma forms reactive species that are unable to attack the substrate without further assistance. Only in concurrence with energetic ion bombardment of the substrate surface (leading to surface defects that increase its reactivity to the etchant species) is a transformation to volatile reaction products possible. Since the creation of surface defect sites (lattice dislocations, dangling bonds, partial dissociation of surface compounds) by ion bombardment occurs preferentially in the vertical direction (preferential direction of impact of ions), the resulting etching rate is much faster in the vertical than horizontal direction.

The discharge (ionized gas volume) in DBDs is typically restricted to a (large) number of discrete microdischarge channels, with neutral gas in-between [Kog03]. Maybe the observed pattern in the eroded polymer surface close to the electrode contact area corresponds to stable base points of the tightly packed microdischarges in this area. Indeed, hexagonal configurations of discharge filaments have been observed in corresponding research on the self-organizing behavior of interacting dielectric barrier

discharge channels. Figure 2b in [Sto10] shows a hexagonal pattern of “closely packed” discharge filaments, while Figure 2c displays a loose arrangement of filaments with no particular order.

PD Inception

From experiments on cm-sized air gaps at atmospheric pressure [BBMZ83], the streamer constant is found to lie in the range of $K_{St} = 14..18$, corresponding to a critical number of electrons N_c (for the emergence of the streamer mechanism for discharge propagation) of about 10^6 to 10^8 . The value $K_{St} = 4.6..5.2$ determined here to match the observed PDIV is considerably lower. The predicted value of the PDIV is 1200 V and 1400 V for $K_{St} = 14$ and $K_{St} = 18$, respectively. This significantly deviates from the observed value of ~ 550 V, and is thus inappropriate for design purposes.

Similar low values ($K_{St} \approx 6$) of the streamer constant are reported in the recent literature [LCd⁺19] on the investigation of PDIV for twisted pairs of enamelled wire, where the electrode configuration and dimensions of the discharging air gap are similar to those occurring in the present study. The authors in [LCd⁺19] refer to literature that scrutinizes the value of the streamer constant, in particular the relation $K_{St} = \ln(N_c)$: “[T]here is no reason apart from tradition for retaining K equal to 18” [Ped89] (p. 729). There thus seems to be a need for better understanding the inception criteria of PD in dielectric-barrier type electrode configurations such as the one studied here.

Times to Failure

Based on the observed erosion of the insulation foil by the corona surface discharge, insulation failure under the employed mixed voltage seems to occur by the mechanism active under pure DC voltage, but operating on a thinner (PD-eroded) insulation layer. Indeed, the surface charges generated by the PDs transfer the electrode potential onto the foil surface, which leads to higher electric field strengths in the eroded regions.

The higher the PD intensity (as characterized by the near-UV cam), the faster the minimal insulation thickness decreases, and hence the faster breakdown occurs. Higher fundamental frequencies, shorter rise times and duty cycles close to $D = 0.8$ correlate with higher PD intensity, and thus lead to shorter times to failure.

The data point measured at $f_0 = 0.5$ kHz (Figure 7.12b) illustrates the presence of the two operant aging/degradation mechanisms: while at higher frequencies ($f_0 \geq 1$ kHz) it is the PD erosion that dominates the time to failure ($\text{TTF}_p(U_{\text{peak}} = 11 \text{ kV}) < \text{TTF}_{\text{DC}}(11 \text{ kV})$), it is comparatively weak at $f_0 = 0.5$ kHz, which leads to $\text{TTF}_p(U_{\text{peak}} = 11 \text{ kV}) > \text{TTF}_{\text{DC}}(11 \text{ kV})$. Thus, lowering the DC component of the applied voltage stress at the cost of some PD leads to an overall *increase* of the time to failure for $f_0 \lesssim 0.5$ kHz.

Finally, the observed scaling $\text{TTF} \propto f_0^{-k}$ with $k = 0.65$ indicates that the per pulse degradation incurred by the associated corona discharge (as quantified by the observed TTF) decreases with increases switching frequency ($k = 1$ would correspond to a per pulse degradation independent of switching frequency).

7.3.5. Conclusion

The following conclusions are drawn from the study of electrical endurance of polymer insulation foil under DC-biased MF MV stress above PD inception:

- PD erosion leads to a thinning of the polymer foil. When the applied DC-bias voltage divided by the residual thickness of the foil reaches the DC-breakdown strength of the insulation, breakdown occurs.
- Time to failure is inversely proportional to optical intensity of corona discharge (as quantified by near-UV camera).
- Time to failure is observed to decrease as $f_0^{-0.65}$ with increasing switching frequency. This indicates that the “per pulse” degradation decreases with increasing switching frequency.
- The discharge is as a dielectric barrier discharge (a non-equilibrium “cold” plasma at atmospheric pressure), leading to plasma etching of the polymeric (and electrode) surface by means of ion bombardment and/or chemical gasification.
- The spatial extent of the eroded region can be quantitatively explained by application of the streamer criterion. However, the range of values 14..18 commonly used for the streamer constant does not predict the experimentally observed PDIV (the latter is a factor ~ 2.5 smaller than the predicted value).

7.3.6. Limitations and Outlook

Given the disagreement between the result of the streamer criterion for discharge inception and the measured PDIV, a closer look at the theoretical foundation for the prediction of PDIVs in DBD arrangements is required. Predicting inception voltages accurately based on gas parameters (pressure, temperature, gas species) and electrode/solid insulator geometry is of great practical importance for the design process of Type I insulation systems. A comprehensive review on what is already available in the published literature on this topic could – for time reasons – not be included in this work.

Moreover, the influence of humidity on PDIV should be studied in order to ensure the usability of “dry air” data for the effective ionization coefficient. This is easily done in the present setup, as relative humidity control is available.

Furthermore, a study of the dependence of the PDIV on various waveform parameters (especially slew rate) should be done, as there is disagreement on this specific point in literature (see Section 2.3.1). While constituting a fundamental ingredient in any model aiming at the prediction of PDIVs (including inverter-type voltages), the streamer criterion does not incorporate any information about the voltage dynamics. A clear experimental corroboration on the existence (or non-existence) of such an influence is thus interesting from both a very practical but also theoretical perspective.

8. Online Dielectric Spectrometer for Inverter-Type Medium Voltages

“Dielectric spectroscopy is an ideal tool to study molecular dynamics and charge transport.”

F. Kremer and M. Arndt
in *Dielectric Spectroscopy of Polymeric Materials*
(1997)

This chapter is based on the publication [FNF19].

Abstract

A custom-made dielectric spectrometer using the broadband excitation of pulse-width-modulated medium-voltages is presented and its performance assessed. A simple technique is suggested and validated for eliminating the problem associated with the digitization of capacitive currents with large crest factors, which arise with rectangular excitation voltages. The developed system allows a quasi-continuous monitoring of the dielectric spectrum (time resolution ~ 1 s, frequency range ~ 1 kHz to 100 kHz) of insulation specimens exposed to mixed voltages (DC-biased MF rectangular pulse), and thus represents a promising tool for insulation aging studies under these non-conventional high-voltage stress profiles.

8.1. Introduction

The dielectric spectrum of an insulating material provides a rich source of information about the dynamics of its constituent (bound and mobile) electrical charge carriers. Thus, it is potentially susceptible to

stress-induced changes of a specimen's molecular structure. Consequently, dielectric spectroscopy has found widespread application in insulation aging studies [Zae03b] [NG14]. Under high-voltage stress (>1 kV), however, the excitation voltage is typically limited to a sinusoidal waveform [PT14] [SL17]. While non-sinusoidal excitations are widely used in impedance spectroscopy, these systems do not operate in the high-voltage regime, or suffer from other constraints such as limited excitation voltage bandwidth, the inability to survive test object breakdown or the need for elaborate measurement circuit modelling [SBBG08].

In this chapter, an online dielectric spectrometer setup for mixed-frequency voltages up to 30 kV is presented. It is immune against test object breakdown, employs analog signal processing to remove the limitation on the rate of rise of voltage, and uses a referencing technique to avoid the need for modelling. It is therefore suitable to complement time-to-failure testing of insulation materials under medium-voltage inverter waveforms, providing in-situ measurements of the pre-breakdown dynamics of the dielectric spectrum. As such, it constitutes a promising tool for further illumination of the active degradation mechanisms in insulation systems exposed to mixed-frequency medium-voltages (e.g. DC-biased rectangular voltages), both above and – in particular – below partial discharge inception.

The chapter is organized as follows. First, detailed information about the excitation voltage used in this study, as well as the analog and digital signal processing employed for determining the dielectric permittivity is provided. Then, the dielectric spectrometer is characterized based on its precision, accuracy and stability. Finally, a proof of concept measurement is shown and discussed.

8.2. Design and Setup

The measurement setup as well as parameter definitions and theoretical concepts used in the result section are detailed in the following subsections.

8.2.1. Voltage Source

The online dielectric spectrometer is designed to operate on a mixed-frequency test bench, whose schematic is shown in Figure 8.1a. The sample inside the test cell can be stressed by a DC voltage U_{DC} (0 to

30 kV) and a superimposed medium-frequency rectangular pulse voltage U_p (0 to 1.5 kV peak-peak, with a fundamental frequency between 500 Hz and 10 kHz).

A more detailed description of the test bench as well as results on time-to-failure testing under this stress profile can be found in Chapter 7.

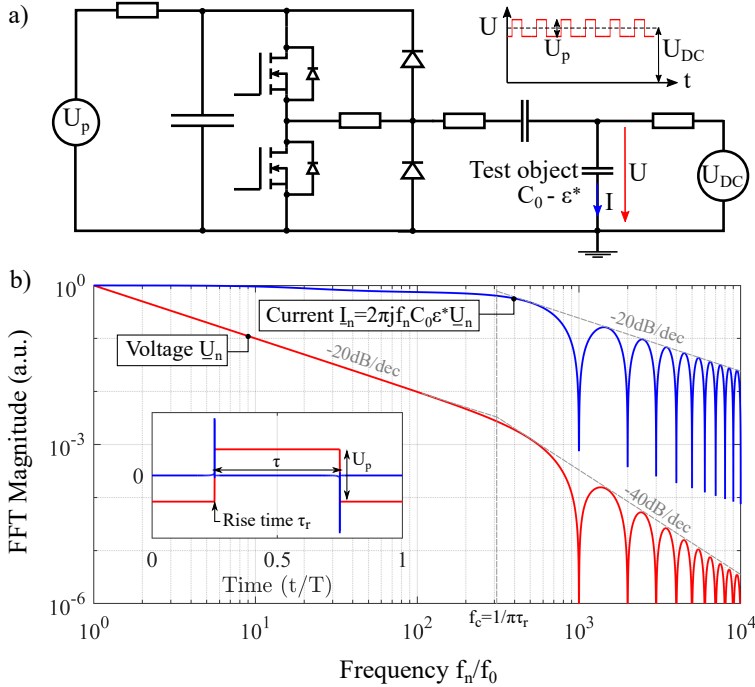


Figure 8.1.: Spectrum of the applied trapezoidal pulse voltage and the corresponding response current through the dielectric test object. The simple Debye response (8.4) is used to model a dielectric relaxation.

8.2.2. Excitation Voltage and Response Current

The Fourier components of a trapezoidal pulse of fundamental period T , pulse length τ (full width at half maximum), rise time τ_r and peak-to-peak

amplitude U_p can be calculated to be (see Section 3.1.4)

$$\underline{U}_n = 2U_p \frac{\tau}{T} \operatorname{sinc}(\pi f_n \tau_r) \operatorname{sinc}(\pi f_n \tau), \quad (8.1)$$

with $f_n = n/T$ and $n = 1, 2, 3, \dots$ (DC component not considered). The associated time-domain waveform reads

$$U(t) = \operatorname{Re} \left[\sum_{n=1}^{\infty} \underline{U}_n e^{2\pi j f_n t} \right]. \quad (8.2)$$

The summation becomes finite for bandwidth-limited signals, e.g. digitized voltages $U_m = U(t_m)$ with $t_m = m/f_s$ ($m = 0, 1, 2, \dots$), for which the highest frequency is half the sampling frequency, $f_s/2$ (= Nyquist frequency). The spectral components of a pulse train with duty cycle $D = \tau/T = 0.5$ and $\tau_r = 10^{-3}T$ is shown in Figure 8.1b (note that a significant constant regime is only present if $D \ll 1$). The frequency range $[f_0, f_c]$ contains 99.97% of the spectral power, and hence the spectral contribution above f_c can usually be neglected for, e.g., dielectric loss calculations.

The current flowing through a capacitor with a linear and isotropic dielectric characterized by the complex dielectric permittivity $\underline{\varepsilon}_n = \underline{\varepsilon}(f_n)$ is given by

$$I(t) = C_0 \operatorname{Re} \left[\sum_{n=1}^{\infty} 2\pi j f_n \underline{\varepsilon}_n U_n e^{2\pi j f_n t} \right] \quad (8.3)$$

The corresponding Fourier amplitudes are also shown in Figure 8.1b. The complex permittivity in the given example is modelled by a Debye relaxation

$$\underline{\varepsilon}(f) = \varepsilon_{\infty} + \frac{\Delta\varepsilon}{1 + 2\pi j \frac{f}{f_{\text{rel}}}} = 3 + \frac{1}{1 + 2\pi j \frac{f}{20 \cdot f_0}}. \quad (8.4)$$

It causes the current components to decrease by a factor $1 + \Delta\varepsilon/\varepsilon_{\infty} \approx 1.3$ when the frequency changes from $f \ll f_{\text{rel}}$ to $f_{\text{rel}} \gg f \lesssim f_c$. For a given excitation voltage, the current response contains – in principle – all the information about the dielectric permittivity as defined above. If the vacuum capacitance C_0 is known, $\underline{\varepsilon}$ can be evaluated at all “measurable” harmonics of the excitation voltage by using

$$\underline{\varepsilon}_n = \left[2\pi j f_n C_0 \frac{U_n}{I_n} \right]^{-1}. \quad (8.5)$$

The crux of the matter lies in the limited ability to experimentally determine the Fourier coefficients with sufficient precision and accuracy.

8.2.3. Signal Conditioning and Measurement

Dielectric spectroscopy relies on a precise measurement of the applied excitation voltage and the associated sample current. A signal processing procedure optimized for rectangular voltage excitation is presented in the following subsections.

Voltage Measurement

In order to increase the signal-to-noise ratio (SNR), a custom-made voltage divider with a band-pass characteristic as shown in Figure 8.2 is employed to measure the AC voltage applied to the specimen. The pass band corner frequencies are set to 500 Hz and 100 kHz, which is deemed a suitable compromise between system bandwidth and noise performance for the available pulse excitation frequencies. This range can be adjusted to match other excitation spectra by modifying the filter component values. The full transfer from the applied high voltage $\underline{U}_{\text{HV}}$ to the digitized low voltage $\underline{U}_{\text{out}}^{(1)}$ can – under the assumption of system linearity – be written as

$$\underline{U}_{\text{out}}^{(1)} = \frac{C_{\text{HV}}}{C_{\text{LV}}} \underline{T}^{(1)} \underline{U}_{\text{HV}} \equiv \frac{\underline{U}_{\text{HV}}}{\underline{\alpha}^{(1)}}, \quad (8.6)$$

where $\underline{T}^{(1)}$ is the transfer function of the band-pass filter. The mid-band divider ratio is given by

$$r = |\underline{\alpha}^{(1)}| \approx \frac{100 \text{ nF}}{100 \text{ pF}} \cdot \frac{1}{4 \text{ V/V}} = 250. \quad (8.7)$$

Current Measurement

The crest factor (CF) of a periodic signal is defined as the ratio of its peak value to its RMS value. While for the trapezoidal voltage $\text{CF}_U \approx 1$ (assuming $\tau \approx T/2$ and $\tau_r \ll T$, the associated capacitive current features $\text{CF}_I \approx \sqrt{T/2\tau_r} \gg 1$). For a given spectral content of a signal (i.e. given Fourier magnitudes), a higher crest factor leads to a higher quantization

noise during analog-to-digital conversion and hence a smaller SNR for the spectral components. Indeed, for a given set of magnitudes

$$\{\hat{A}_n \geq 0, n = 1, 2, \dots\} \quad \text{with} \quad \sum_{n=1}^{\infty} \frac{\hat{A}_n^2}{2} = A_{\text{RMS}} \stackrel{!}{=} 1, \quad (8.8)$$

consider the (infinite) set of signals

$$\{\underline{A}_n^{(i)} = \hat{A}_n e^{j\phi_n^{(i)}}, \phi_n^{(i)} \in [0, 2\pi)\}. \quad (8.9)$$

While the RMS value of all these signals is the same (=1), the peak values $A_{\text{peak}}^{(i)}$ are functions of the phases $\phi_n^{(i)}$. Let $A_{\text{peak,min}} = \text{CF}_{A,\text{min}}$ be the infimum of all peak values, and $A_{\text{peak,max}} = \sum \hat{A}_n = \text{CF}_{A,\text{max}}$ their maximum. Hence, when digitizing with N_b bits, the largest and smallest digitization quanta are given by

$$\Delta A_{\text{max}} \geq \frac{\text{CF}_{A,\text{max}}}{2^{N_b}} \quad \text{and} \quad (8.10)$$

$$\Delta A_{\text{min}} \geq \frac{\text{CF}_{A,\text{min}}}{2^{N_b}}, \quad (8.11)$$

respectively.¹ It thus follows that in order to utilize best the available vertical resolution of the ADC, one should avoid large crest factors of the analog input signals.

In order to reduce the current signal's large crest factor $\text{CF}_I \approx \sqrt{T/2\tau_r}$ (e.g. equal to 71 for $T = 1$ ms and $\tau_r = 100$ ns), an analog integration of the signal is performed before digitization. The resulting crest factors are much smaller ($\lesssim 2$) and thus the signal can be digitized without sacrificing more than one bit of the ADC's dynamic range (instead of sacrificing more than six bits with a crest factor of 71). Numerical simulation shows the instrument precision Δ (definition given in Section 8.2.4) for both magnitude and phase to scale strongly with the number of digitization bits:

$$\Delta \propto e^{-a \cdot N_b} \quad \text{with} \quad a \approx 0.6. \quad (8.12)$$

(this of course only applies if the noise level at the ADC inputs is lower than the quantization noise associated with N_b). Saving 5 bits of resolution thus amounts to an order of magnitude improvement on precision.

¹Equality applies when the reference value for the quantization is optimal, i.e. equal to the peak value of the signal.

Figure 8.3 shows the constructed current measurement system with its simplified schematic and its transfer function. The latter features the integrating behaviour $\propto [jf]^{-1}$ within the target frequency range between about 500 Hz and 100 kHz. The full transfer from the sample current \underline{I}_S to the digitized voltage $uU_{\text{out}}^{(2)}$ reads

$$\underline{U}_{\text{out}}^{(2)} = \underline{T}^{(\text{CT})} \underline{T}^{(2)} \underline{I}_S \equiv \frac{\underline{I}_S}{\underline{\alpha}^{(2)}}, \quad (8.13)$$

where $\underline{T}^{(\text{CT})}$ and $\underline{T}^{(2)}$ are the transfer functions of the current transformer and the integrator-amplifier, respectively. The current transformer used for this application is described in the following subsection.

In addition to ensuring good utilization of the ADC's dynamic range, using an integrator also matches the SNR of the current harmonics to those of the voltage signal. Specifically, prior to implementing integration, the SNRs of the current harmonics are approximately constant (assuming a constant noise floor), while after integration they decrease with the inverse of the frequency (as they do for the voltage harmonics).

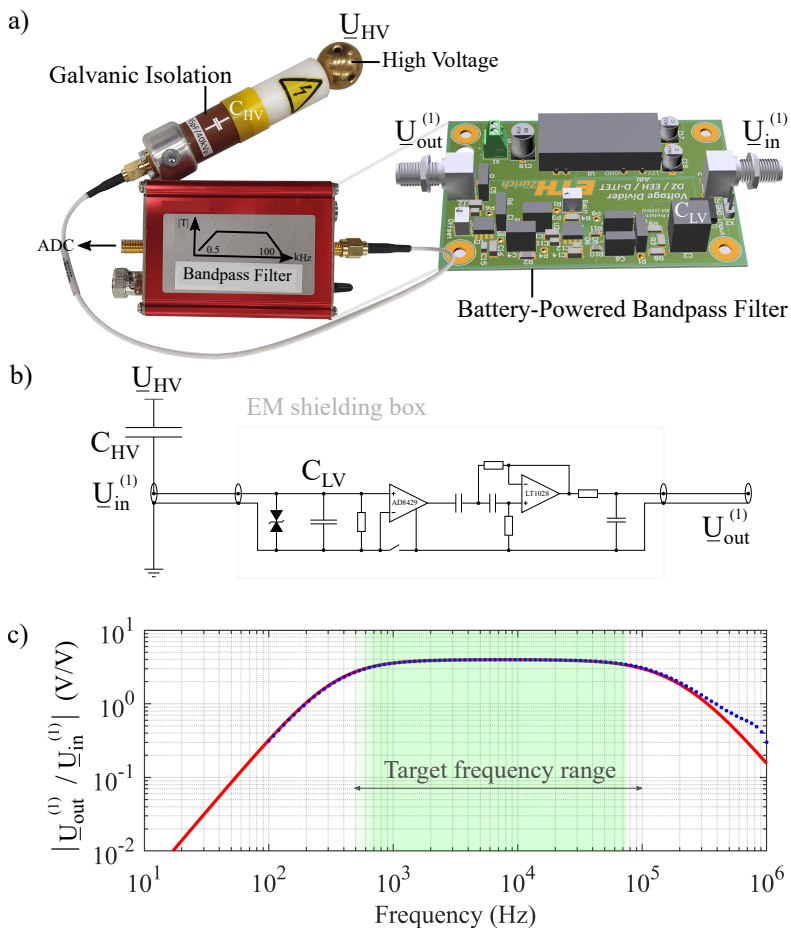


Figure 8.2.: a) Voltage probe (capacitive coupling) and bandpass filter b) Simplified schematic c) Simulated (—) and measured (···) transfer function.

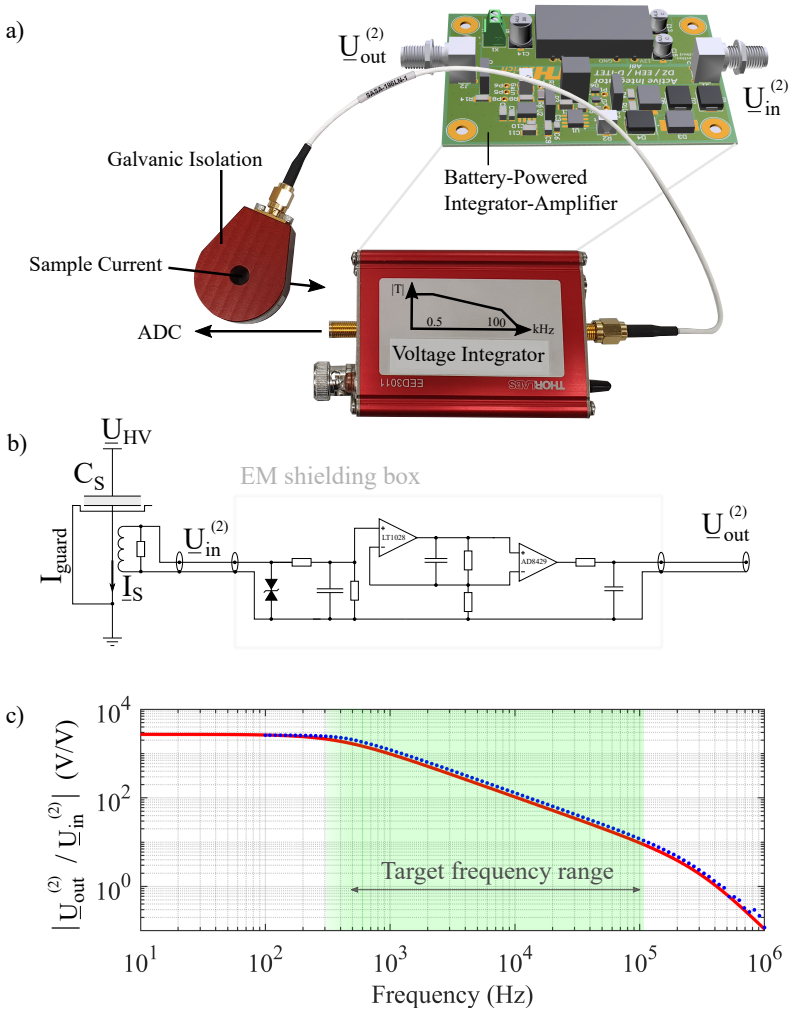


Figure 8.3.: Current monitor (inductive coupling) and analog signal integrator b) Simplified schematic c) Simulated (—) and measured (···) transfer function.

Current Transformer

In the first version of the setup, a commercial current transformer was used. Since the requirements in terms of bandwidth are not significant (flat response from about 1 kHz to a few hundred kHz is sufficient), a custom-made CT was constructed. It uses $N = 40$ turns of enamelled wire ($\varnothing 0.5$ mm) on a N30 ferrite core ($\mu_i = 4300$). The resulting winding inductance is estimated to [HM89]

$$L_s \approx \frac{\mu_0 \mu_i N^2 h}{2\pi} \ln\left(\frac{b}{a}\right) = 7.3 \text{ mH}, \quad (8.14)$$

where $b = 13$ mm, $a = 8$ mm and $h = 11$ mm are the outer/inner winding diameter and its height, respectively.

The high-pass cutoff frequency reads

$$f_{\text{HP}} = \frac{R_s}{2\pi L_s} = 1.1 \text{ kHz}, \quad (8.15)$$

where $R_s = 50 \Omega$ is the chosen burden resistor. The mid-band transimpedance gain (sensitivity) is given by²

$$S = \frac{R_s}{N} = 1.25 \text{ V A}^{-1}. \quad (8.16)$$

It follows that

$$f_{\text{HP}} = \frac{S}{\mu_0 \mu_i N h \ln\left(\frac{b}{a}\right)}. \quad (8.17)$$

There is thus a tradeoff between sensitivity and the lower cut-off frequency. A larger core, a higher relative permeability of the core material and a higher number of turns will decrease f_{HP} for a given sensitivity.

The high-frequency performance is mainly determined by the parasitic capacitances between winding turns, between the winding and the grounded case and the parasitic (parallel) capacitance of the burden resistor. Choosing large core dimensions and/or a large number of turns will thus compromise the high-frequency performance.

An anodized aluminum case consisting of two (electrically isolated) parts provides EMI shielding and mechanical protection. Relative immunity against external magnetic fields is obtained by using a wire return path

²Into a high-impedance input. Into a 50Ω input, the gain is reduced by a factor of 2.

along the winding, such that external magnetic fields do not generate a significant magnetic flux.

The performance of the constructed CT is compared to the commercial CT in Figure 8.4. There seems to be a system resonance around 40 MHz in the custom-made transformer, but the usable bandwidth (up to about 35 MHz) is more than enough for its application in dielectric spectroscopy.

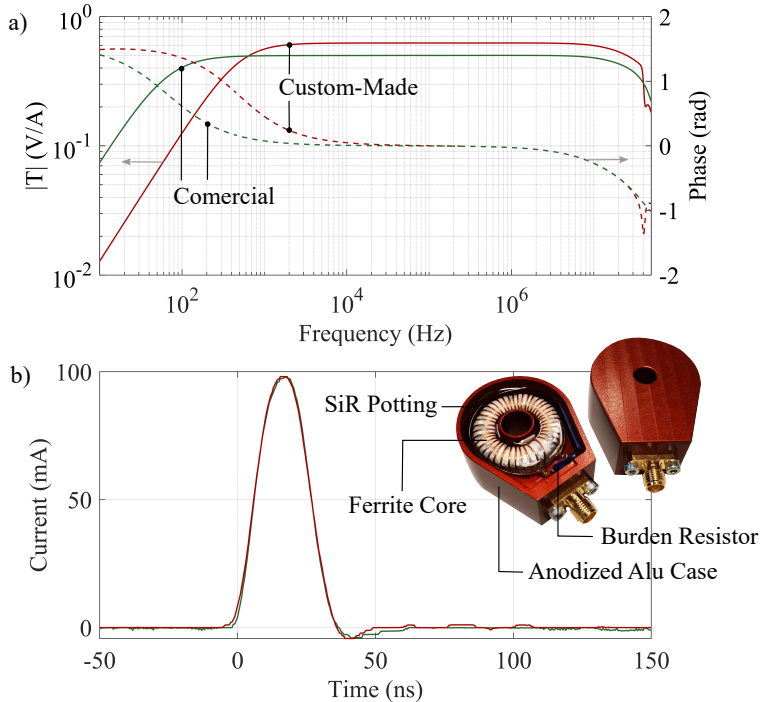


Figure 8.4.: Performance assessment of custom-made current transformer in a) frequency and b) time domain.

Digitization and Fourier Transform

The voltages $U_{\text{out}}^{(1,2)}(t)$ are digitized by using a 16-bit ADC with a maximum sampling frequency f_s of 6.25 MHz. Frequencies that could be aliased onto a frequency in the target range are suppressed by the transfer functions with -60 dB or more with respect to the target frequency. A

Fast Fourier Transform is performed on a pulse train containing 100 fundamental cycles in order to determine the spectral components $\underline{U}_{\text{out}}^{(1,2)}(t)$. Spectral leakage is reduced by applying a Hanning window.

8.2.4. A Definition of Instrument Precision

Let $\{x_i, i = 1, \dots, N\}$ be $N > 1$ measured values of a physical parameter (e.g. the magnitude or phase of the dielectric permittivity at a certain frequency). Assume that it is a sample of a random variable X distributed according to a probability distribution function (PDF) f , whose mean value and standard deviation are denoted by μ and σ , respectively. For a given confidence level α , let the quantity Δ be the smallest real number satisfying

$$P\left(|X - \mu| \geq \frac{\Delta}{2}\right) \leq 1 - \alpha. \quad (8.18)$$

For example, for $\alpha = 95\%$, Equation (8.18) asserts that the probability of a measured value lying outside $\mu \pm \frac{\Delta}{2}$ is $\leq 1 - \alpha = 5\%$. In the present context, for given instrument settings, we thus call Δ the α -precision of the instrument with respect to the measured parameter. Unless stated otherwise, a confidence level of $\alpha = 95\%$ is assumed in the following.

Δ is conveniently expressed in units of standard deviations:

$$\Delta = k_{\Delta} \cdot \sigma. \quad (8.19)$$

Chebyshev's inequality [Ion01] then provides the distribution-independent precision

$$k_{\Delta} = \frac{2}{\sqrt{1 - \alpha}} \approx 9. \quad (8.20)$$

Making the assumption that the distribution of X is symmetrical and unimodal [Ion01] leads to a precision

$$k_{\Delta} = \frac{4}{3\sqrt{1 - \alpha}} \approx 6 \quad (8.21)$$

The familiar stronger bound $k_{\Delta} \approx 4$ ("95% of the measurements lie within two standard deviations of the mean") requires X to be normally distributed.

Since the standard deviation σ is unknown, it must be estimated from the measured sample values:

$$\sigma_N = \sqrt{\frac{\sum_{i=1}^N (x_i - \mu)^2}{N - 1}}. \quad (8.22)$$

This estimate is itself subject to statistical fluctuations. Its upper α -confidence bound in units of the estimator σ_N is given by [She00]

$$u_N = \sqrt{\frac{N - 1}{\chi_{\frac{1-\alpha}{2}, N-1}^2}}, \quad (8.23)$$

where $\chi_{\frac{1-\alpha}{2}, N-1}^2$ is the $\frac{1-\alpha}{2}$ -percentile of the Chi-Squared distribution.³ An instrument precision, based on a number N of measured values $\{x_i, i = 1, 2, \dots, N\}$, can thus be defined in terms of the standard deviation σ_N by

Instrument Precision

$$\Delta = k_\Delta \cdot u_N \cdot \sigma_N \quad (8.24)$$

The instrument precision (quantifying the scatter on the outcome of a *single* measurement) is different from the confidence interval on the mean value $\mu_N = N^{-1} \sum_{i=1}^N x_i$ of N measurements. The α -confidence range of the mean value μ_N is given by [She00]

Confidence Range for the Arithmetic Mean

$$\mu_N \pm \frac{t_{\frac{1-\alpha}{2}, N-1}}{\sqrt{N}} \sigma_N, \quad (8.25)$$

where $t_{\frac{1-\alpha}{2}, N-1}$ is the $\frac{1-\alpha}{2}$ -percentile of Student's t distribution.⁴ The

³Given in MATLAB® by `chi2inv((1-alpha)/2, N-1)`.

E.g. $u_5 = 2.87$, $u_{20} = 1.46$ and $u_{100} = 1.16$ ($\alpha = 0.95$).

⁴Given in MATLAB® by `tinv((1-alpha)/2, N-1)`.

For example, Student's t coefficient equals 2.57, 2.09 and 1.98 for $N = 5$, 20 and 100, respectively ($\alpha = 0.95$).

validity of 8.25 depends on $N^{-1} \sum_i X_i$ being normal (where all X_i are distributed according to f , i.e. the PDF of the measured quantity). According to the Central Limit Theorem [She00], the PDF of $N^{-1} \sum_i X_i$ converges towards a normal distribution as $N \rightarrow \infty$. In practice the approximation is good already for $N \gtrsim 10$, even if the PDF for a single measurement is very far from normal.

8.2.5. Calculating the Dielectric Permittivity

For an electrode configuration of vacuum capacitance C_0 the (effective) complex dielectric permittivity of the sample is – by definition – related to the measured impedance by

$$\underline{\varepsilon} = \varepsilon' - j\varepsilon'' = |\underline{\varepsilon}|e^{-j\delta} = [2\pi j f C_0 \underline{Z}_S]^{-1} \quad (8.26)$$

Equations (8.6) and (8.13) yield

$$\underline{Z}_S = \frac{U_{\text{HV},S}}{I_S} = \frac{\underline{\alpha}_S^{(1)} U_{\text{out},S}^{(1)}}{\underline{\alpha}_S^{(2)} U_{\text{out},S}^{(2)}}, \quad (8.27)$$

where $\underline{\alpha}_S^{(1,2)}$ are the transfer functions (described in Section 8.2.3) applying at the instant of the measurement (S=sample). Performing a “reference measurement” is a practical way for eliminating the unknown transfer functions (compare to Chapter 6.1.1). Let \underline{Z}_R be the impedance of a “reference sample”:

$$\underline{Z}_R = \frac{U_{\text{HV},R}}{I_R} = \frac{\underline{\alpha}_R^{(1)} U_{\text{out},R}^{(1)}}{\underline{\alpha}_R^{(2)} U_{\text{out},R}^{(2)}}. \quad (8.28)$$

Under the assumption of equal transfer at the moment of the sample (S) and reference (R) measurements (the validity of this assumption will be discussed in Section 8.4),

$$\underline{\alpha}_S^{(i)} = \underline{\alpha}_R^{(i)} \quad (i=1,2), \quad (8.29)$$

one obtains

$$\frac{\underline{\varepsilon}_S}{\underline{\varepsilon}_R} = \frac{C_{0,R}}{C_{0,S}} \cdot \frac{\underline{Z}_R}{\underline{Z}_S} = \frac{C_{0,R}}{C_{0,S}} \cdot \frac{U_{\text{out},S}^{(2)} U_{\text{out},R}^{(1)}}{U_{\text{out},S}^{(1)} U_{\text{out},R}^{(2)}} \quad (8.30)$$

The reference sample may be an air capacitor, in which case $\underline{\varepsilon}_R = 1$, and thus Equation (8.30) provides the complex permittivity of the sample in terms of measured voltages and vacuum capacitances.

Alternatively, using the sample itself as a reference is an interesting choice for aging experiments. Equation (8.30) then reads

$$\frac{\underline{\varepsilon}(t)}{\underline{\varepsilon}(t_0)} = \frac{U_{\text{out}}^{(2)}(t) U_{\text{out}}^{(1)}(t_0)}{U_{\text{out}}^{(1)}(t) U_{\text{out}}^{(2)}(t_0)} \quad (8.31)$$

and provides the time evolution of the complex permittivity as compared to its value at some time t_0 (e.g. the permittivity of the unaged material).

8.3. Results

The results section presents data characterizing the measurement setup (accuracy / precision / stability) as well as a proof-of-concept measurement assessing its applicability on actual dielectric samples subject to electrical field stressing.

8.3.1. Instrument Accuracy – Debye Sample

In order to validate the basic operating principle of the setup and to assess its accuracy, the frequency-dependent permittivity of a Debye network (Figure 8.5),

$$\underline{\varepsilon}_{\text{Debye}} = \frac{\underline{Z}_{\text{Debye}}(C_1 = 0)}{\underline{Z}_{\text{Debye}}} = 1 + \frac{C_1/C_0}{1 + 2\pi j f R_1 C_1}, \quad (8.32)$$

is measured by using the reference principle (see Equation (8.30)). The nominal component values are $C_0 = 700$ pF, $C_1 = 220$ pF and $R_1 = 60$ k Ω . A relatively low excitation voltage of 150 V (peak) is chosen for this sample in order to match the current amplitude to those expected for “real” material samples (for which the typical capacitance is in the range of only 5 to 100 pF). A rectangular pulse train voltage excitation with a fundamental frequency of 1 kHz and a rise time of 100 ns is used. The magnitude and phase of the permittivity are determined from 1 kHz to 100 kHz and compared to the expected frequency response given by Equation (8.32), as shown in Figure 8.5). A linear frequency axis is chosen because the square wave harmonics $(2n + 1)f_0$ are equidistant on this scale.

The lumped circuit components are treated as ideal, which is a valid approximation in the considered frequency range. For example, the loss factor of the used film capacitors is $\leq 10^{-4}$, which is much smaller than the maximum value (0.14) of the constructed Debye sample.

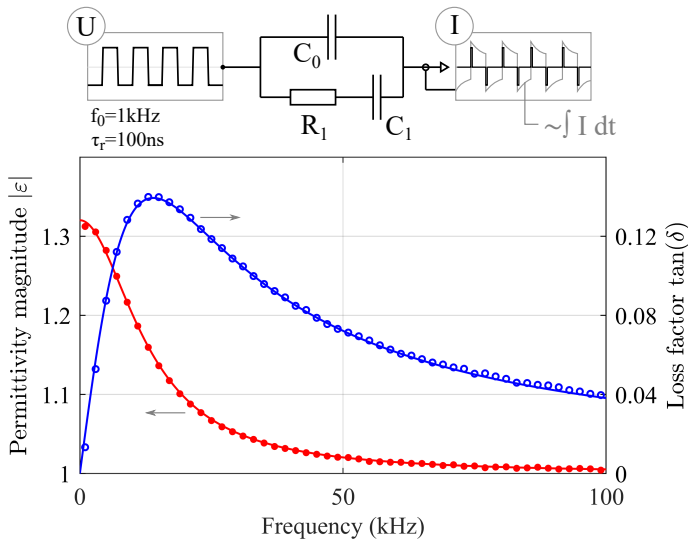


Figure 8.5.: Validation of the measurement principle on a Debye network of known frequency response. Continuous lines are theoretical predictions based on Equation (8.32). Measured values (circles) are extracted from the harmonics of the square wave excitation and the corresponding current response.

8.3.2. Instrument Precision and Stability

The instrument precision Δ is calculated according to Equation (8.24), using $\alpha = 0.95$, $N = 100$, $k_\Delta = 6$ and $u_{100} = 1.16$, which yields $\Delta \approx 7 \cdot \sigma_{100}$. Figure 8.6 shows the instrument precision on the permittivity magnitude $|\underline{\varepsilon}|$ and phase angle δ as a function of the harmonic frequency. As illustrated, averaging the outcome of N consecutive measurements reduces the scatter of the average value (at the expense of temporal resolution) as described by Equation (8.25).

The long-term stability of the output readings was evaluated by measurements on a commercial 50 kV ceramic capacitor for which no significant changes of the dielectric are expected. The DC voltage was increased stepwise up to 10 kV (1 kV every 2 minutes) with a superimposed $U_p = 0.75$ kV (peak-peak) / $f_0 = 1$ kHz / $\tau_r = 100$ ns rectangular pulse train. Over a period of one hour (the maximal measurement time for the tests presented in this investigation), the measured values of the magnitude and the phase of the permittivity are observed to fluctuate within a band of $\leq 10^{-3}$ and $\leq 2 \cdot 10^{-4}$ rad, respectively. These values are thus taken as thresholds below which measured changes are not attributed to the test object.

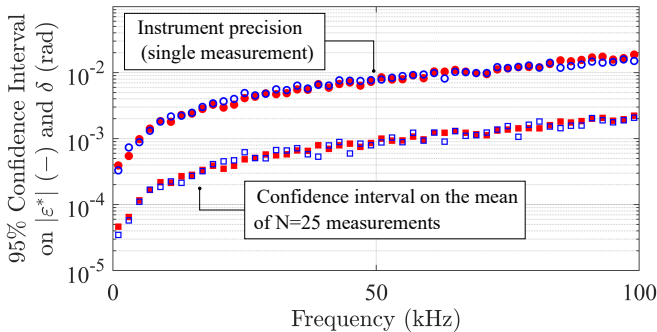


Figure 8.6.: 95 % confidence intervals on single measurements (instrument precision) and the mean of 25 measurements. Filled markers: permittivity magnitude, unfilled markers: phase angle (in rad).

8.3.3. Pre-Breakdown Evolution of Dielectric Response

A sample made of biaxially oriented PET foil (DuPont Melinex[®] S, 23 μm thickness) is subject to a DC-biased rectangular pulse voltage. The electrodes ($D = 10\text{ mm}$) consist of silver paint (Electrolube SCP). The sample is conditioned and tested at $T = 25 \pm 1^\circ\text{C}$ and $\text{RH} = 33 \pm 2\%$.

Figure 8.7 represents the time evolution of the normalized permittivity (Equation (8.31)) when the sample is stressed with a step-wise increasing DC voltage U_{DC} , superimposed by a $U_{\text{p}} = 0.75\text{ kV}$ (peak-peak) / $f_0 = 1\text{ kHz}$ / $\tau_{\text{r}} = 100\text{ ns}$ rectangular pulse train. A full spectrum is acquired every 6 seconds. For $t > 22$ minutes the DC voltage is kept constant at 10 kV until breakdown occurs. While both the measured magnitude and phase change as a function of U_{DC} , sample breakdown is not preceded by any detectable “abnormality” in the dielectric response (in the measured frequency range). While the magnitude shows no significant change at all ($< 10^{-3}$) prior to breakdown, the phase increases only slightly (and gradually) by at most 10^{-3} rad across all frequencies.

8.4. Discussion

The observation that the dielectric spectrum of the tested PET foil does not show any peculiarities prior to breakdown was surprising at first. However, on the one-hour time scale used here, electric field-induced changes to the molecular structure are not expected to occur in a significant fraction of the sample’s volume, i.e. properly speaking there is no electrical aging of the bulk material. The measurement suggests that during the time prior to breakdown, the processes occurring at a potential breakdown site are so localized that they do not alter the dielectric response of the sample. It is however important to note that some internal change (albeit local) must occur, since the sample suddenly breaks down after having been exposed to a constant external stress level for 25 minutes. The injection and accumulation of space charge with the associated distortion of the electrode electric field is likely to be a factor contributing to breakdown under the employed voltage stress [HAL⁺00] [ND09].

At this point, a full explanation of the permittivity’s variation with DC bias voltage has not been realized. However, a significant fraction of the apparent magnitude increase can be explained by an actual increase in

the vacuum capacitance of the foil electrodes, caused by the increased mechanical stress (and associated strain) on the dielectric foil,

$$\frac{|\Delta C_0|}{C_0} \approx \frac{\Delta d}{d} \approx \frac{\varepsilon_0}{E_{\text{PET}}} \left(\frac{\varepsilon_\infty U_{\text{DC}}}{d} \right)^2 \approx 0.5\% \quad (8.33)$$

where E_{PET} is the elastic modulus of the foil (4 GPa).⁵ While the numerical value obtained is already in the right ballpark for explaining the observed increase in magnitude ($\sim 2.2\%$), there seems to be (at least) one additional mechanism at work, as the increase of C_0 does not explain the change in the loss angle, as well as the frequency-dependence of the (additional) changes in $|\varepsilon|$.

⁵The static bound surface charge density at the dielectric surface is given by

$$\sigma_b = \varepsilon_0 \varepsilon_\infty \frac{U_{\text{DC}}}{d}, \quad (8.34)$$

and the electric field acting on this surface charge is $E = \varepsilon_\infty \frac{U}{d}$. Hence the surface force density (N m^{-2}) is equal to

$$f_s = \sigma_b E = \varepsilon_0 \left(\frac{\varepsilon_\infty U_{\text{DC}}}{d} \right)^2. \quad (8.35)$$

Moreover, the first-order variation of the vacuum capacitance with the electrode separation is

$$\Delta C_0 \approx \frac{\partial C_0}{\partial d} \Delta d = -\frac{\varepsilon_0 A}{d^2} = -C_0 \frac{\Delta d}{d}. \quad (8.36)$$

Hence

$$\frac{|\Delta C_0|}{C_0} = \frac{\Delta d}{d} = \frac{f_s}{E_{\text{PET}}}, \quad (8.37)$$

from which Equation (8.33) follows.

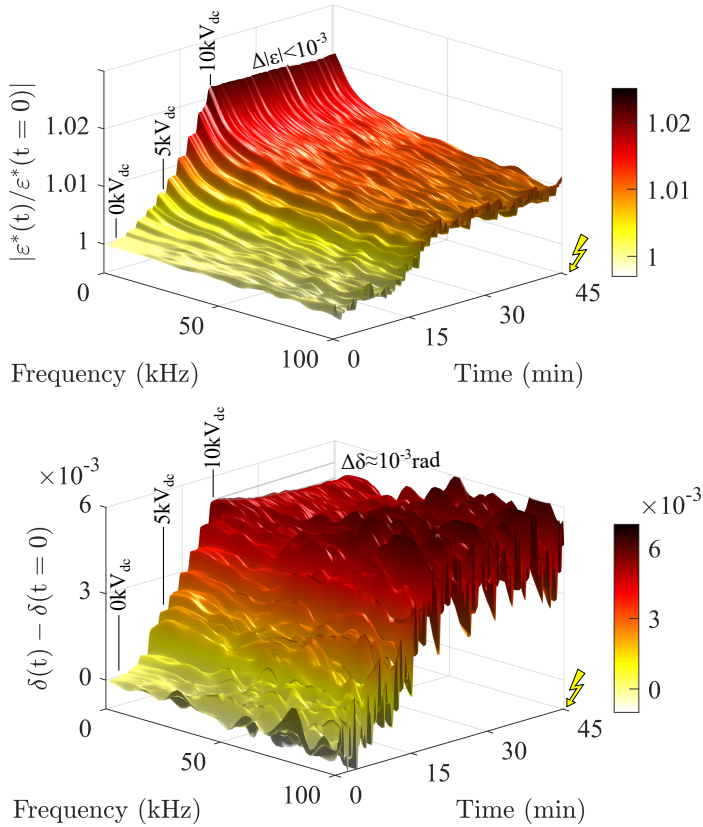


Figure 8.7.: Time evolution of the absolute value (top) and the phase angle (bottom) of the normalized dielectric permittivity when the DC-bias voltage is increased in 1 kV steps from 0 to 10 kV (within 22 minutes) and then left constant unchanged breakdown occurs at $t=47$ minutes.

It was shown in Chapter 5.1 that static space charge in the insulation volume does not influence the AC steady-state dielectric response. It may be possible, however, that the periodic electromechanical force exerted on the space charges by the AC component of the electric field leads to a large enough periodic displacement of the space charges (with associated induced electrode currents) that could influence the measured AC dielectric response. The dielectric response would then be influenced by the (micro)mechanical stress-strain relationship of the material. A more detailed analysis is needed to assess the magnitude (and hence the practical relevance) of this effect.

On the methodological side, the presented setup demonstrates the possibility of broadband high-voltage dielectric online monitoring down to a precision that is ultimately limited by the drift of the transfer functions over time (rather than the achievable instrument precision). This drift could however be taken into account by trading some of the current setup's simplicity. Indeed, by using a second, identically constructed current transformer that measures the current flowing through the capacitive divider (with the same settings of the prior sample measurement) one could limit the overall drift of the system to the drift of the divider capacitor and the differential drift of the two current transformers. The capacitance of the voltage divider is mainly determined by the high-voltage capacitor, for which a vacuum or gas type construction would be the preferred choice for lowest drift. Moreover, the measurement of absolute values of permittivity would then be possible (Equation (8.30)).

The applied signal processing (analog integration of the current signal) is shown to be a simple solution for dealing with the challenge associated with the precise digitization of signals with large crest factors. Another – arguably even simpler approach – was tested and consists of using a commercial low-noise linear amplifier in conjunction with a high-order low-pass filter with a cutoff frequency f_{LP} above the target frequency range. Then, only the harmonics in the target range contribute to the current peak and the crest factor is reduced by a factor of about f_c/f_{LP} , that is, to $CF_{I,LP} \approx 2f_{LP}\sqrt{T} \cdot \tau_T$. For example, using $f_{LP} = 200$ kHz reduces the crest factor of the current (for $\tau_T = 100$ ns and $T = 1$ ms) from 71 to about 4, which is close to the crest factor obtained with the integrator ($\lesssim 2$). Either case is a variation on the theme of low-pass filtering, thus yielding comparable performance.

While in this study only rectangular waveforms with a fixed frequency (1 kHz) and duty cycle (50%) have been used, it is possible to synthesize

and apply pulse-width-modulated binary signals with tailored frequency spectra [MOM⁺12]. The voltage excitation would then be switched (e.g. for a second every minute) from the stressing waveform to the scanning waveform, which covers the frequency range desired for the dielectric response analysis.

8.5. Summary

The work presented in this chapter merges and improves existing technologies to design a dielectric spectrometer that allows the quasi-continuous online monitoring of a specimen's dielectric spectrum under repetitive medium-voltage pulse stress. Limitations on switching speeds are removed by using analog integration of the current signal. Furthermore, a reference technique that eliminates the need for modelling transfer functions is proposed. It allows monitoring the time evolution of relative changes in the specimen's dielectric spectrum. This is useful information for dielectric aging studies, because the dielectric spectrum mirrors changes in the molecular structure.

8.6. Limitations and Outlook

It is clear that the developed system is still a work in progress, and a number of points that could not be addressed in the present investigation should be considered in future adaptations of the setup.

First and foremost, the system needs further calibrations measurements in order to make sure that the observed changes have their origin in the test sample and not the acquisition system. For example, the stability test described in Section 8.3.2 should be repeated on an air or vacuum capacitor (instead of a ceramic capacitor). A potential problem in the present configuration is that the voltage divider uses an identical ceramic capacitor (see C_{HV} in Figure 8.2a), and these are known to show voltage-dependent characteristics (e.g. capacitance values). This voltage dependence might not show up in the calibration measurement on the identical ceramic capacitor, but might be present in the PET foil measurement. The proposed upgrade (using a reference signal through the the vacuum capacitance of the voltage divider) is expected to provide remedy in this respect.

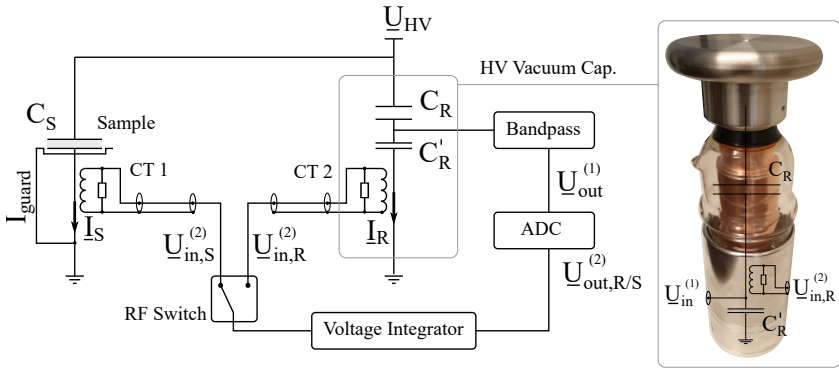


Figure 8.8.: Suggested extension of the online spectroscopy setup to allow determining absolute values of dielectric permittivity magnitude and phase (not just relative variation as a function of time). The vacuum capacitor on the right serves both as part of the divider for the voltage measurement as well as a quasi-lossless reference for calibration ($\tan \delta = 0$).

Moreover, a larger number of measurements are required to fully assess the utility of online dielectric spectroscopy for inverter-type applications. In particular, more realistic long-term measurements should be done, for which structural changes of the polymer insulation can realistically be expected to occur and thus generate more relevant results/insights with respect to their long-term behavior under these stresses.

Finally, the stress profile should ultimately include a more realistic combination of stresses (not just electrical stress). Having MF MV transformer insulation in mind, these could/should include thermal stress (including thermal cycling), “chemical” stress (e.g. high humidity) and mechanical stress (especially for mobile applications), to name a few (see Table 9.1).

9. Design Process of MF MV Transformer Insulation

“The study of electrical breakdown is not a trivial pursuit.”

L.A. Dissado and J.C. Fothergill
in *Electrical Degradation and Breakdown in Polymers* (1992)

This chapter is based on the coauthored publication [GFR⁺19].

This chapter describes the rationale behind the selection process of a dry-type insulation material, as well as the employed vacuum potting setup and process used for the MF MV transformer prototype characterized in [GFR⁺19]. The followed recipe draws on the insights gained from the investigations presented in the previous chapters.

9.1. MF MV Transformer Insulation Design Guidelines

The electric strength of the pristine solid insulation material per se is not the limiting factor in its application in the MF MV transformer. Indeed, nominal design field strengths are on the order of 5 kV mm^{-1} [GFK⁺16], which is below the (short-term) electric strength of virtually all solid insulation materials. Rather, it is the slow changes occurring on time scales of months or years of service (i.e. with the insulation system being exposed to long-term external stresses such as high electric fields, elevated temperatures, vibrations and mechanical strain, water ingress etc.) that are critical: the insulation system must not loose its electric strength *after these long-term stresses have left their mark*. In this respect, the requirements of the insulation system for a MF MV transformer are not different than for a LF MV transformer. There are, however, the following

issues that are accentuated specifically in MF applications:¹

- If PDs are incepted, their intensity is significantly enhanced. This increases the rate at which (non-PD-resistant) insulation materials are eroded.
- Dielectric losses are increased.

Thus, the knowledge from the presented investigations (in particular: no indication of a “per pulse” degradation below PD inception) suggests that the design of MF MV insulation systems can be linked to the design of LF MV and DC MV systems, with the only difference being that it needs to be designed for the actual (higher) insulation temperature profile brought about by the MF operation.

9.2. Material Properties: Requirements

A compilation of requirements for insulation materials specifically for MF applications is compiled in Table 9.1. Many of the stated issues (e.g. thermal conductivity/runaway, cracking/delamination due to thermo-mechanical stress and shrinkage upon cure) are accentuated in resin-rich insulation systems (i.e. using potting/encapsulation as opposed to mere impregnation).

The stated requirements are often in conflict with each other (e.g. a material featuring a high thermal conductivity may not possess good dielectric properties), and therefore tradeoffs are necessary in the material selection.

The electrical property that requires careful consideration in MF applications is the imaginary part of the (effective) dielectric permittivity of the employed materials across the whole range of operating temperatures and frequencies. A large real part (magnitude) increases parasitic capacitive currents and associated EMI issues and is thus not desirable.

The insulation temperature is expected to be higher in MF than in LF transformers (see Appendix A). The associated thermal aging of materials must not compromise their (di)electric properties beyond a certain tolerable margin. Moreover, different thermal expansion coefficients of materials lead to mechanical stresses and strains, which pose a risk of

¹See risk factors in Chapter 7.2.1. It is assumed here that the possible (local) enhancement of electric stress (risk factor b.) has been properly considered in the system design process.

generating cracks in brittle materials and delamination at interfaces (both paving the way for PD erosion).

Table 9.1.: Desired material properties of dry-type insulation materials with specific emphasis on MF MV applications.

Property/ Stress	Desired Behavior	Purpose
Electrical field	Long voltage endurance Low dielectric losses Low diel. permittivity	Avoid insulation failure Avoid thermal runaway or local hotspots Minimize parasitic capacitive coupling (EMI)
Thermal	High temperature stability High thermal conductivity	Reduce thermal degradation rate Reduce insulation temperature
Thermal cycling	Some elasticity Good adhesion to substrates Small thermomechanical stress	Avoid cracks/delamination Avoid delamination
Mechanical	Sufficient mechanical support Good surface adhesion	Avoid deformations/ruptures Avoid delamination
Processability	Low viscosity/surface tension Avoid voids/inhomogeneities during curing Low shrinkage	Good impregnation Reduce internal mechanical stress
Chemical	Compatibility Oxidation/hydrolysis	Avoid inhibition of curing agent Slow down chemical aging (chain scission/depolymerization)
(Safety)	Low flammability Low toxicity Low environmental impact	Operating safety Processing/operating safety
(Cost)	Free of charge	Save money

9.3. Material Characterization and Selection

Based on the property profile established in Table 9.1, silicone elastomers (with aluminum oxide micro-fillers) were identified as promising potting materials for MF MV applications.

Due to the relatively strong covalent bond energy of the $(\text{Si}-\text{O})_n$ backbone (as compared to carbon-based backbones), silicone polymers exhibit excellent thermal stability (long-term operating temperatures up to 200 °C).² Moreover, they have glass transition temperatures that are below room temperature (as opposed to most epoxy polymers). Depending on the degree of cross-linking, this produces network polymers with relatively high elasticity (hence its name). This implies that the polymer can relieve thermo-mechanical stresses by a corresponding strain, thus greatly reducing the risk of crack formation.

Another consequence of the low glass transition temperature is that the dielectric α -relaxation loss peak associated with segmental motion of the polymer backbone is far above the operation frequency at all operating temperatures, and the overall dielectric losses and the risk of thermal runaway is thus reduced as compared to polymers that are in a glassy state at room temperature [GFR⁺19].

The uncured silicone liquids are available in low-viscosity formulations and exhibit a low surface tension, which provides excellent impregnation of fine structures (e.g. Litz wire surface). A low mixed viscosity ($\lesssim 3000$ mPa·s) and the associated good flowability was an important selection criterion to enable the use of the employed vacuum potting system.

Typically, thermal conductivities up to about $1 \text{ W m}^{-1} \text{ K}^{-1}$ are obtained due to the added inorganic filler particles to the silicone components (typically consisting of silicon oxide or aluminum oxide). This is roughly a five-fold increase compared to the thermal conductivity of unfilled polymers [MP09].

The adhesion (chemical bonding) to surfaces is typically much weaker than e.g. for epoxy polymers. In order to obtain sufficient adhesion, it is thus often necessary to use a bonding agent (“primer”) on the target surface. Here, it is advised to use so-called *self-priming* formulations (especially when dealing with intricate geometries), which contain a primer compound in the provided 2-component system. The primer is activated upon curing at elevated temperatures (typical curing temperatures are around 120 °C).

²See manufacturer data sheets.

Applying a dedicated primer to the complex geometry (especially the litz wire) is difficult and promotes the risk of introducing weak points into the system. This was e.g. one of the major disqualifying factors for the more closely investigated systems “SE-3000” (ACC Silicones[®]) and “Q3-3600” (Dow Corning[®]), as compared to the self-priming system “TC-4605 HLW” (Dow Corning[®]).

Silicone formulations whose cure is platinum-catalyzed (addition-curing) are sensitive to certain chemical compounds that can act as cure inhibitors. Superglues based on cyanoacrylate (first used in the fabrication of the coil former) were for example found to inhibit the cure in the silicone system used for the transformer prototype (Dow Corning[®] TC-4605 HLW).

A disadvantage of silicones is their comparatively high cost (as compared e.g. to epoxies). This, however, is not disqualifying in MF applications where the power densities are large, and consequently, the cost per volume of insulation material can be relatively high until it would carry weight with respect to the overall converter cost.

The dielectric permittivity and $\tan \delta$ values of three silicone systems are shown in Figure 9.1.³ The observed significant differences emphasize the importance of assessing the dielectric spectra by dedicated measurements (the data sheets typically only provide dielectric characterization at one or two frequencies and room temperature, if at all). For the MF MV transformer prototype, the uppermost silicone (Dow Corning[®] TC-4605 HLW) was chosen. Although it does not feature the lowest dielectric loss ($\tan \delta \approx 1\%$ at the operating frequency of 50 kHz), it features a convincing overall property profile (see Table 9.2): it has a relatively low dielectric permittivity magnitude ($\lesssim 4$), good thermal conductivity, low viscosity and low flammability (UL94 V-0). It is self-priming with good adhesion to a large range of substrates. The option “HLW” stands for “hard – low viscosity”, i.e. higher hardness of the cured polymer (Shore A 60) and a lower viscosity of the uncured mixture. Its room temperature pot life of 130 minutes allows for sufficient processing time.

³The extension of the shown data to the range above 150 kHz to 2 MHz was obtained with a precision impedance analyzer (Agilent 4294A).

Table 9.2.: Properties of the employed silicone system TC-4605 HVL (Dow Corning[®]).

Property	Value
Mixed viscosity	1900 mPa s
Hardness	60 (Shore A)
Adhesion to aluminum	150 N cm ⁻²
Thermal conductivity	1 W m ⁻¹ K ⁻¹
Max. operating temperature	200 °C
Electrical conductivity	10 ⁻¹³ S m ⁻¹
Dielectric strength	24 kV mm ⁻¹
Diel. Permittivity: magnitude	< 4.1 (for $f_0 > 50$ kHz and $T < 120$ °C)
Diel. Permittivity: $\tan \delta$	< 1 % (for $f_0 > 50$ kHz and $T < 120$ °C)

Its dielectric spectrum hints at a relatively large contribution from migrating charge carriers, with an associated low-frequency dispersion (large increase in both $|\underline{\epsilon}|$ and $\tan \delta$). This was not critical in the present application, where the voltage stress (both CM and DM) does not contain a DC bias. If a DC bias voltage was present, the choice of material would need to be reconsidered (although the transformer prototype endured the short-term ± 15 kV DC stressing).

9.4. Vacuum Potting

Figure 9.2 depicts the schematic and the actual realization of the vacuum potting setup. The procedure is as follows. The silicone components are thoroughly mixed⁴, degassed in partial vacuum (~ 30 mbar) for a few minutes, and then placed inside the left vessel (reservoir). After the tubes are installed, both vacuum chambers are evacuated to a residual pressure of about 30 mbar (valves ③ ④ ⑤ open, ① ② closed). Then valves ④ ⑤ are closed, and subsequently valve ① is carefully opened for a short time to generate a slight overpressure Δp in the reservoir chamber. The still liquid silicone will begin to flow through the connecting tube (this

⁴The filler particles sediment into a hard clay during storage and need to be homogeneously re-dispersed before mixing the components. This is a disadvantage of low-viscosity systems.

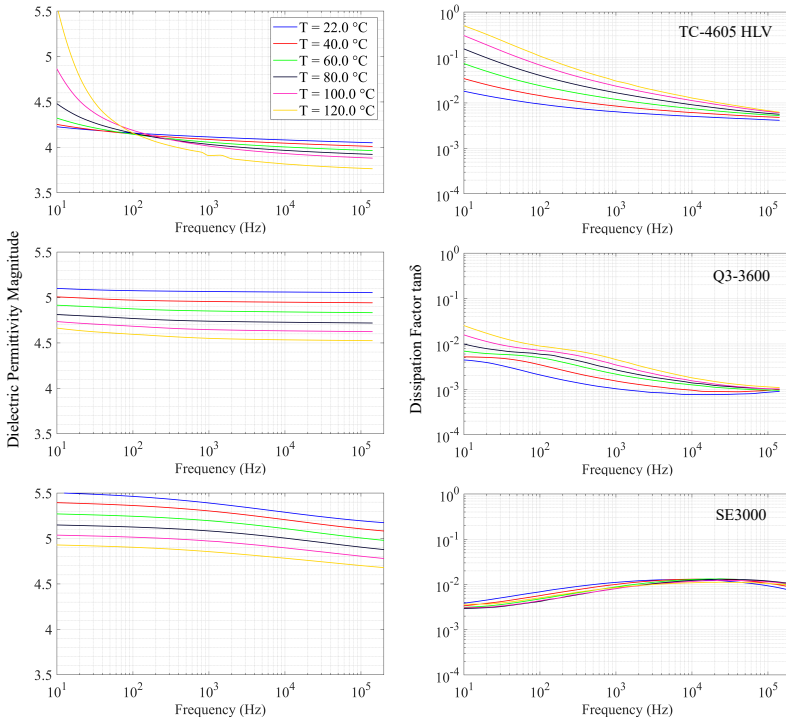


Figure 9.1.: Dielectric spectra of three commercial silicone rubber systems (all containing inorganic micro-fillers to enhance thermal conductivity).

takes some time depending on the viscosity of the mixture), and begin to fill the evacuated transformer casting mold. The potting process is complete when the collecting container begins to fill. Valve ① can then be fully opened and shortly thereafter also valve ②, which brings the whole setup back to ambient pressure. The transformer is removed and, in the final step, cured according to the schedule prescribed in the data sheet of the employed potting material.

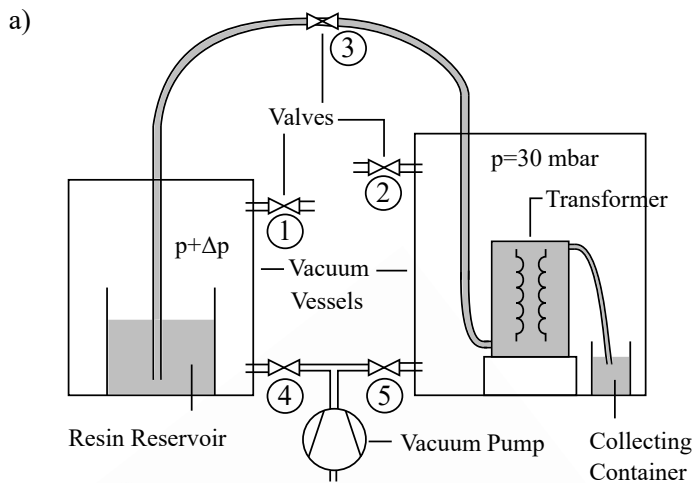


Figure 9.2.: a) Schematic and b) realization of the vacuum potting setup.

9.5. Simulation and Measurements

The voltage endurance of the transformer insulation was tested under nominal and overvoltage operating conditions (see Table 9.3), and no insulation-related problems have been identified. No assessment of the long-term endurance is possible at this point, as the transformer has not yet undergone endurance testing (at present, the overall operation time under nominal conditions adds up to about 40 hours).

Table 9.3.: Applied common-mode (CM) and differential-mode (DM) voltages for MF MV transformer prototype insulation testing (stressing time at least 5 min).

Type	Waveform	Amplitude	Frequency
CM	DC	± 15 kV	–
CM	AC	± 15 kV peak	50 Hz
CM	AC	± 3.8 kV peak	50 kHz
CM	AC	± 3.8 kV peak	100 kHz
CM	PWM	± 3.5 kV	50 kHz
DM	AC	± 3.8 kV peak	50 kHz
DM	AC	± 3.8 kV peak	100 kHz
DM	AC	± 3.5 kV	50 kHz

The applied simulation model uses frequency-domain FEM [GFR⁺19] in order to determine the electric and magnetic fields under specified converter operation conditions. These in turn are then used to calculate the magnetic core, winding and dielectric losses and the corresponding (stationary) temperature distribution. An important step consists in updating the initially assumed material data values to this new temperature profile. The calculation is then iterated until the observed change in the temperature profile falls below a certain threshold. A divergence of this iterative scheme corresponds to a thermal runaway (see [GFR⁺19], Figure 14).

Good agreement (<10% relative error) between the dielectric loss predictions based on low-voltage (< 150 V peak) dielectric spectroscopy data and calorimetric measurements under nominal voltage (± 3.5 kV, 50 kHz, $D = 50\%$, $\tau_r = 0.48$ and 0.96 μ s) is obtained. Although this result needs

further corroboration for other materials and (especially DC-biased) waveforms (see Section 2.4.2), it is a promising outcome because low-voltage dielectric spectroscopy in combination with FEM analysis is a powerful prototyping tool.

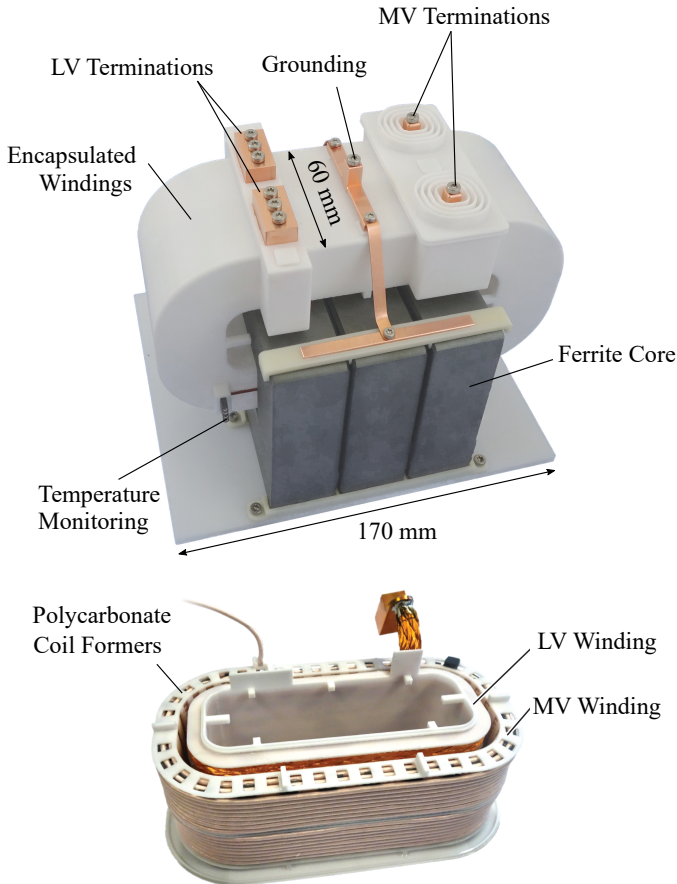


Figure 9.3.: Finalized MF MV transformer prototype (top) and unpotted winding package (bottom).

9.6. Summary

The insights gained from the investigations of the previous chapters are used to suggest design rules for a MF MV transformer insulation system. A desired property profile for insulation materials specifically tailored to the requirements for operation in MF MV applications is compiled. A large number of commercially available potting compounds were subsequently screened and assessed based on their data sheet profiles. Given the importance of the dielectric properties in MF applications, the dielectric properties of the most promising candidate materials were then determined by using the dielectric spectrometer described in Chapter 6. Finally, a suitable potting material was identified and applied to a MF MV transformer prototype in a vacuum potting process. The transformer prototype successfully passed the applied series of electrical insulation tests.

9.7. Limitations and Outlook

There is as of yet no information on the voltage endurance (i.e. the long-term voltage withstand capability > 40 hours) of the insulation system under multifactor aging conditions. Thus, as part of possible future investigations, endurance testing on transformer mockups should be done, including all stresses (electrical, thermal (cycling), mechanical, environmental) that the insulation system is expected to endure during its operation. Therefore, the suggested insulation design and material choice will probably evolve as new insights about the long-term performance are included.

A similar limitation applies to the design rules: the absence of experimental evidence for a “per pulse” degradation was obtained from time-to-failure testing with stresses above the expected operation field strengths, and accordingly short times to failure. Endurance testing on a small number of transformer mockups with two significantly different switching frequencies (e.g. 5 kHz vs. 50 kHz) and electric fields closer to operation field strengths could help to remove this uncertainty.

10. Conclusion and Outlook

Note: detailed conclusions and outlooks on the various subtopics of this thesis are given at the end of the respective chapters.

The following test facilities / measurement setups have been implemented:

- *Inverter Stress Simulator.* Enables the exposure of insulation materials/systems to inverter-type voltages under controlled environmental conditions (relative humidity, temperature).
- *Modular low-voltage (offline) dielectric spectrometer.* Provides high-precision measurements of dielectric spectra across the frequency range from 10 mHz to 200 kHz and temperatures from 15 °C to 125 °C.
- *High-voltage (online) dielectric spectrometer.* Employs capacitive and inductive coupling to the inverter stress simulator test bench to determine the relative temporal evolution of the complex dielectric permittivity. It uses the broadband excitation provided by the inverter-type stressing voltage, and thus is able to provide a full dielectric spectrum (fundamental frequency up to 100 kHz) of the stressed material every few seconds.

They have been successfully tested, thoroughly characterized and subsequently employed in the following experimental investigations:

- *Complex dielectric permittivity as an aging marker.* The low-voltage (offline) dielectric spectrometer allows to identify aging-induced changes in insulation specimens with high precision. In proof-of-concept measurements, it is applied to study the impact on the dielectric response of large-area structural aging (thermal, hygrothermal, UV) as well as localized insulation deterioration (electrical treeing). The high-voltage (online) dielectric spectrometer is applied to study the evolution of the dielectric permittivity of PET insulation foil under a DC-biased rectangular MV MF pulse voltage up to breakdown. While the value of the DC bias voltage is found to influence both the magnitude and the phase of the dielectric per-

mittivity, there is no significant aging (as quantified by the dielectric response in the range from 1 kHz to 100 kHz) due to the influence of the dielectric field. It is likely that this is due to the relatively short (~ 1 hour) time to failure, which prevents large-scale electric-field-induced structural changes in the material from (rather, the breakdown occurs along local weak spots in an otherwise “healthy” structure). It is thus advisable to use the dielectric permittivity as an aging marker in more long-term endurance testing (see below).

- *Insulation aging and degradation under inverter-type medium voltages.* Time-to-failure testing on PET insulation foil in a dedicated electrode arrangement (providing low dielectric heating and a well-defined PD inception voltage) under a DC-biased rectangular pulse voltage revealed no evidence of a “per pulse” degradation if care is taken to eliminate PD and excessive dielectric heating. On the contrary, a clear “per pulse” degradation (erosion of the foil surface) is active above PD inception and leads to a drastic reduction of the mean time to failure.
- *Determination of dielectric spectra of candidate potting materials.* Silicone elastomers are identified as a suitable alternative to glassy polymers (e.g. epoxies) for MV MF potting applications. The obtained dielectric spectra allowed an accurate thermal design (coupled thermo-electric numerical simulation), which was found to agree well with calorimetric measurements of dielectric losses. Moreover, the dielectric spectra of the measured silicone systems are found to differ significantly, which underlines the necessity for a thorough dielectric characterization prior to its use in a specific application.

All in all, the results of both the theoretical and the experimental investigations suggest that if PD and excessive insulation temperatures are avoided by a proper design, there is no indication of an accelerated aging of insulation materials under inverter-type medium voltages (as compared to LF sinusoidal voltages). On the system level, it is important to include a proper evaluation of the local electric field stress *under the applied voltage waveform*.

A limitation of the employed accelerated aging studies are the relatively short times to failure and the related high electric field stress (far above the typical operating field stress). As the relative strength of aging mechanisms is typically dependent on the applied electric field amplitude, this leaves some uncertainty about the possible “activation” of a “per pulse”

degradation even below PD inception. For this reason, it is suggested to complement the results obtained so far by long-time endurance testing on small transformer mockups (potted litz wire). Moreover, employing online dielectric spectroscopy under long-time endurance testing could prove useful, as it can provide “life curves” (the value of a dielectric-permittivity-based aging marker as a function of time) without the need for reaching insulation breakdown (hence allowing endurance testing even at operating conditions).

Appendices

A. Dimensional Scaling of Maximal Device Temperature for a Given Total Loss Power

For the sake of the argument, consider a solid sphere of radius R and thermal conductivity k ($\text{W m}^{-1} \text{K}^{-1}$), uniformly heated by a total loss power \dot{Q} (W). The surface of the sphere is coupled to a heat bath of temperature ϑ_0 by a thermal interface of conductance h ($\text{W m}^{-2} \text{K}^{-1}$). The solution of the thermal boundary value problem (Equations (E.1) and (E.2)) leads to the maximal temperature of

$$\vartheta_{\text{m}} = \vartheta(r=0) = \vartheta_0 + \frac{\dot{Q}}{4\pi R} \left[\frac{1}{2k} + \frac{1}{Rh} \right]. \quad (\text{A.1})$$

For $R \gg 2k/h$, most of the temperature drop occurs inside the sphere and the maximum temperature scales as R^{-1} . For $R \ll 2k/h$, the temperature drops predominantly across the interface, and the maximum temperature scales as R^{-2} .

In the case of a transformer, its volume V scales approximately as $V \propto f^{-\frac{3}{4}}$, where f is its operating frequency [HK16]. Hence, the insulation temperature rise scales between

$$\vartheta_{\text{m}} - \vartheta_0 \propto V^{-\frac{1}{3}} \propto f^{\frac{1}{4}} \quad \text{for } V \gg \left(\frac{2k}{h} \right)^3 \quad \text{and} \quad (\text{A.2})$$

$$\vartheta_{\text{m}} - \vartheta_0 \propto V^{-\frac{2}{3}} \propto f^{\frac{1}{2}} \quad \text{for } V \ll \left(\frac{2k}{h} \right)^3. \quad (\text{A.3})$$

Although this represents a very simplified analysis, it nonetheless illustrates the importance of a carefully considered thermal design for power transformers operating at higher frequencies.

B. Indentation of an Elastic Insulation Foil in a Sphere-Plane Electrode Configuration

Since the elastic modulus of aluminum ($E_{\text{Alu}} \approx 70 \text{ GPa}$) is much larger than that of PET ($E_{\text{Alu}} \approx 4 \text{ GPa}$), it is justified to assume the electrodes to be non-elastic. According to the Hertzian theory of elastic contact [TG82], a rigid sphere of radius R indents a semi-infinite elastic medium (with $E'_{\text{PET}} = E_{\text{PET}}/(1 - \nu_{\text{PET}}^2)$ and Poisson's ratio $\nu_{\text{PET}} \approx 0.38$) by

$$\delta_{\infty} = \left[\frac{3F}{4E'_{\text{PET}}\sqrt{R}} \right]^{\frac{2}{3}}, \quad (\text{B.1})$$

where F is the applied contact force. The radius of the associated area of contact is given by $a_{\infty} = \sqrt{d_{\infty}R}$. Waters [Wat65] proposed a semi-empirical extension of the Hertz model to include thin sheets of elastic materials on a rigid substrate:

$$\delta = \delta_{\infty} \left[1 - e^{-\frac{Ad}{\sqrt{R}\delta}} \right], \quad (\text{B.2})$$

where $A = 0.67$ is an empirical constant. It can be seen that correction factor becomes relevant (< 0.95) when the radius of the contact area approaches 10% of the foil thickness.

The contact force consists of the spring contact force $F_c \approx 3 \text{ N}$ and the voltage-dependent electrostatic attraction F_e of the electrodes:

$$F(\delta) = F_c + F_e(\delta) = F_c + \frac{\pi\epsilon_0 R \epsilon'(0) U_{\text{DC}}^2}{d - \delta}, \quad (\text{B.3})$$

where F_e is estimated on the basis of the formula for the geometric capacitance $C_0(\delta)$ (in the limit $d \ll R$) presented in [Cro08], i.e. using "force = partial derivative of the electrostatic energy with respect to electrode separation":

$$F_e(\delta) = \frac{1}{2} \epsilon'(0) U_{\text{DC}}^2 \frac{\partial C_0(\delta)}{\partial \delta}. \quad (\text{B.4})$$

Thus, the indentation depth δ is the solution of the Equation

$$\left[\frac{3F(\delta)}{4E'_{\text{PET}}\sqrt{R}} \right]^{\frac{2}{3}} \left[1 - e^{-\frac{Ad}{\sqrt{R}\delta}} \right] - \delta = 0. \quad (\text{B.5})$$

For $R = 5 \text{ mm}$, $d = 23 \text{ }\mu\text{m}$, $E'_{\text{PET}} \approx 3.4 \text{ GPa}$ and $\varepsilon'(0)=3.2$ the indentation depth is numerically determined to be:

$$\delta = 0.9 \text{ }\mu\text{m} \quad (\delta_{\infty} = 4.4 \text{ }\mu\text{m}) \quad \text{at } U_{\text{DC}} = 0 \quad (\text{B.6})$$

$$\delta = 1.2 \text{ }\mu\text{m} \quad (\delta_{\infty} = 7.4 \text{ }\mu\text{m}) \quad \text{at } U_{\text{DC}} = 11 \text{ kV}. \quad (\text{B.7})$$

The electrostatic force $F_e(1.2 \text{ }\mu\text{m}, 11 \text{ kV}) = 2.5 \text{ N}$ adds a non-negligible fraction (45%) to the total electrode force, and the associated increase of the indentation depth amounts to about 20%.

Moreover, the difference between δ and δ_{∞} is very substantial, indicating that considering the indentation in a semi-infinite elastic half-space (i.e. without the correction factor introduced in Equation (B.2)) would be inadequate.

C. Thermal Contact Conductance of Aluminum-PET Interface

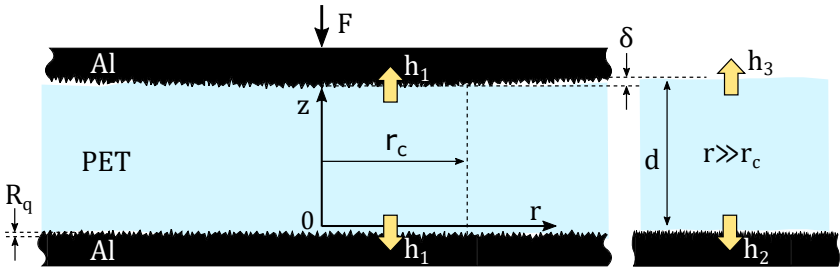


Figure C.1.: Enlarged view of the electrode contact area (PET foil on plane indented by half-sphere). The radius r_c is the radius of the indented area. The coefficients h_1 , h_2 and h_3 are thermal contact conductances at the respective interfaces (unit: $\text{W m}^{-2} \text{K}^{-1}$).

An enlarged view of the electrode contact area is shown in figure C.1. The contact conductance h_j ($\text{W m}^{-2} \text{K}^{-1}$) across the aluminum-PET interface in the indented area is given by [BYC04]

$$h_j^{-1} \approx \left[h_c \frac{A_r}{A_a} \right]^{-1} + \left[h_g \frac{A_g}{A_a} \right]^{-1} \quad (\text{C.1})$$

where h_c and h_g represent the thermal interface conductance through the direct Al-PET contact area A_r and through the interstitial air gaps of area A_g , respectively.¹ $A_a = A_r + A_g$ is the apparent macrocontact area (projected onto contact plane). With the numerical values given in Appendix B, the average contact pressure equals $\bar{p} = F_c/A_a \approx 150$ MPa, with $A_a = \delta R\pi \approx 1.4 \times 10^{-8} \text{ m}^2$ the apparent contact area (at $U_{\text{DC}} = 0$). The contact pressure being of the same order of magnitude as the microhardness of PET (i.e. $\bar{p}/H_{\text{PET}} \sim 1$) implies that the wetting of the Al-surface by plastic deformation of the polymer is very good, i.e. that $1 - A_r/A_a \ll 1$. A rough estimate of the contact conductance is thus given by [BYC04]

$$h_j \approx h_c \approx m \frac{k_s}{R_q} h_p > 1 \text{ kW/mm}^2\text{K}, \quad (\text{C.2})$$

where $m = 0.57$ is the measured absolute mean asperity slope of the aluminum surface, $R_q = 0.7 \mu\text{m}$ is the aluminum RMS surface roughness (measured by confocal microscopy), $h_p \approx 10^{-2}$ the dimensionless thermal contact conductance for Al-polymer interfaces at $\bar{p}/H_{\text{PET}} \sim 1$ [MF96], and $k_s = 2(k_{\text{Al}}k_{\text{PET}})/(k_{\text{Al}} + k_{\text{PET}}) = 0.4 \text{ W m}^{-1} \text{ K}^{-1}$ the harmonic mean of the bulk thermal conductivities. Since k_{PET}/h_j is a negligible fraction of the foil thickness, the limit $h_1 \rightarrow \infty$ can be used within the indented area (i.e. $\vartheta(0) = \vartheta(d) = \vartheta_0$ for $r \leq r_c$).

D. Thermal Interface Conductance of Thin Air Layers

Outside the high-pressure contact spot (region $r > r_c$ in figure C.1), the PET foil is loosely lying on the aluminum surface of the lower electrode. More specifically, let $\phi(y)$ be the probability distribution of the air gap thickness y . The average thermal interface conductance ($\text{W m}^{-2} \text{ K}^{-1}$) then reads [BYC04]

$$h_g = \int_0^\infty \frac{k_g}{y + M} \phi(y) dy, \quad (\text{D.1})$$

where $k_g = 0.024 \text{ W m}^{-1} \text{ K}^{-1}$ is the thermal conductivity of air and $M=0.36 \mu\text{m}$ is a parameter that corrects for the molecular (i.e. non-continuum) nature of the air as y approaches the free mean path of the

¹Index key: j=junction, c=contact, r=real, g=gas, a=apparent.

constituent particles (which is about $0.07 \mu\text{m}$). For a uniformly distributed air gap width between 0 and $d_a = 50 \mu\text{m}$, it follows that

$$h_g = \frac{k_g}{d_a} \ln \left[1 + \frac{d_a}{M} \right] = 2.4 \text{ W m}^{-2} \text{ K}^{-1}. \quad (\text{D.2})$$

The cooling of the upper foil surface by natural convection is negligible in comparison. Also note that h_g saturates to $h_{g,\text{max}} = \frac{k_g}{M} = 67 \text{ W m}^{-2} \text{ K}^{-1}$ as $d_a \rightarrow 0$. Thus, as long there is no pressure on the foil to make direct contact (see C), the thermal resistance of the air gap should be considered irrespective of the value of d_a , because $k_{\text{PET}}/h_{g,\text{max}} \approx 3 \mu\text{m}$ is not a negligible fraction of the foil thickness.

E. Temperature Distribution Inside an Asymmetrically Cooled Dielectric Foil

The goal of this section is to provide an upper bound on the maximum temperature ϑ_m inside the PET foil for a specified excitation voltage $v(t)$ and given material parameters. In order to simplify the mathematical treatment, a number of approximations that overestimate ϑ_m will be used. This will provide a formalism for determining an upper bound on ϑ_m , and hence for deciding under which conditions thermal breakdown does *not* occur.

The temperature distribution $\vartheta(r)$ inside the dielectric volume Ω is determined by the balance of the heat generation and its transfer to the environment (a heat bath of temperature ϑ_0). For the considered system, the steady-state temperature distribution $\vartheta(r)$ is the solution of the boundary value problem

$$-\nabla \cdot [k_{\text{PET}} \nabla \vartheta(\mathbf{r})] = \dot{q}(\mathbf{r}) \quad \forall \mathbf{r} \in \Omega, \quad (\text{E.1})$$

$$-k_{\text{PET}} \nabla \vartheta(\mathbf{r}) \cdot \mathbf{n}(\mathbf{r}) = h(\mathbf{r})[\vartheta(\mathbf{r}) - \vartheta_0] \quad \forall \mathbf{r} \in \partial\Omega \quad (\text{E.2})$$

where $k_{\text{PET}} = 0.2 \text{ W m}^{-1} \text{ K}^{-1}$ is the thermal conductivity of PET, $\mathbf{n}(\mathbf{r})$ are the (outward-facing) surface normals at the insulation boundary $\partial\Omega$, and $h(\mathbf{r})$ the thermal interface conductances. The latter are estimated as follows (see Appendices C and D):

$$h_1 > 1 \text{ kW/mm}^2 \text{ K} \quad (\text{E.3})$$

$$h_2 = 2.4 \text{ W m}^{-2} \text{ K}^{-1} \quad (\text{E.4})$$

$$h_3 = 0. \quad (\text{E.5})$$

The heat source term for $r \ll R$ is given by

$$\dot{q}(r, z) = \kappa_{\text{DC}} \left[\frac{U_{\text{DC}}}{d} \right]^2 + \frac{\varepsilon_0}{2} \sum_{n=1}^{\infty} \left[\frac{|U_n|}{d + |\varepsilon_n| \frac{r^2}{R}} \right]^2 \quad (\text{E.6})$$

where $|\varepsilon_0|$ is set to zero because the DC component of the electric field is assumed to be expelled from the air gap by the deposition of surface charge. The problem can be simplified to a one-dimensional treatment (i.e. no significant lateral thermal coupling), if the spatial variation of the heat source \dot{q} is small on length scales $\iota_{\text{th}} = k_{\text{PET}} \left(\frac{d}{k_{\text{PET}}} + \frac{1}{h_2} \right) = 0.1 \text{ mm}$.² This simplification will be used, as Equation (E.6) satisfies this condition reasonably well, and in any case, the resulting peak temperatures are higher than those derived with a two-dimensional analysis that includes in-plane heat fluxes. Equation (E.1) can thus be solved by considering heat fluxes along the vertical (z) axis only, i.e. as a one-dimensional boundary value problem (no in-plane heat fluxes). The sought-after maximum temperature ϑ_{m} occurs at some position $z = \xi d$ with $0 \leq \xi \leq d$. If the local dielectric loss density $\dot{q}(r = 0, z)$ is approximated by $\dot{q}(\vartheta_{\text{m}})$, the upper (u) and lower (d) foil surface temperatures read

$$\vartheta_{\text{u}} = \vartheta_0 + \frac{\dot{q}(\vartheta_{\text{m}})(1 - \xi)d}{h_{\text{u}}} \quad (\text{E.7})$$

$$\vartheta_{\text{d}} = \vartheta_0 + \frac{\dot{q}(\vartheta_{\text{m}})\xi d}{h_{\text{d}}} \quad (\text{E.8})$$

Equation (E.1) can be integrated to

$$\vartheta(z) - \vartheta_{\text{m}} = -\frac{\dot{q}(\vartheta_{\text{m}})}{2k_{\text{PET}}} (z - \xi d)^2. \quad (\text{E.9})$$

By imposing the boundary conditions E.7 and E.8, one obtains

$$\dot{q}(\vartheta_{\text{m}}) = \kappa_{\text{DC}}(\vartheta) \left[\frac{U_{\text{DC}}}{d} \right]^2 + \frac{\varepsilon_0}{2} \sum_{n=1}^{\infty} \omega_n \varepsilon''_{\text{eff},n}(\vartheta) \left[\frac{|U_n|}{d} \right]^2 \quad (\text{E.10})$$

$$= (\vartheta_{\text{m}} - \vartheta_0) \underbrace{\left[\frac{d}{2} \left\{ \frac{\xi}{h_{\text{u}}} + \frac{1 - \xi}{h_{\text{d}}} + \frac{d}{2k_{\text{PET}}} [\xi^2 + (1 - \xi)^2] \right\} \right]^{-1}}_{\equiv \Gamma} \quad (\text{E.11})$$

$$= (\vartheta_{\text{m}} - \vartheta_0)\Gamma, \quad (\text{E.12})$$

²For volume elements in the foil that are apart by more than ι_{th} the thermal coupling to the heat bath is stronger than the thermal coupling between them.

with

$$\xi = \frac{1 + \frac{h_u d}{2k_{\text{PET}}}}{1 + \frac{h_u}{h_d} + \frac{h_u d}{k_{\text{PET}}}}. \tag{E.13}$$

The Equation for finding ϑ_m thus reads

$$\dot{q}(\vartheta_m) = (\vartheta_m - \vartheta_0)\Gamma, \tag{E.14}$$

and can e.g. be solved iteratively:

$$\vartheta_{i+1} = \vartheta_i + \frac{\dot{q}(\vartheta_i)}{\Gamma} \quad i = 1, 2, \dots \tag{E.15}$$

The convergence of this iterative scheme implies the thermal stability of the sample.³ The higher-order corrections ($i \geq 2$) account for the temperature dependence of the dielectric losses (through κ_{DC} and $\varepsilon''_{\text{eff},n}$).

Once ϑ_m is determined, the associated temperature distribution is found from E.9 and E.14:

$$\vartheta(z) = \vartheta_m - \frac{\vartheta_m - \vartheta_0}{2k_{\text{PET}}\Gamma}(z - \xi d)^2 \tag{E.16}$$

for $0 \leq z \leq d$. Note that $\xi \in [0, 1]$ transforms into $1 - \xi \in [0, 1]$ under the permutation $h_u \leftrightarrow h_d$, and hence Equation (E.13) is – as required on physical grounds – manifestly invariant under this transformation.

³Its divergence does not necessarily imply a thermal runaway because a number of approximations have been used that overestimate the maximal sample temperature.

Bibliography

- [Alm15] L. Almquist. Nonlinear Impedance Spectroscopy - Using Higher Harmonics Response and Differential Impedance for Electrical Characterization of DC Insulation Materials. Master's thesis, Chalmers University, 2015.
- [Art96] J. Artbauer. Electric strength of polymers. *Journal of Physics D: Applied Physics*, 29(2):446–456, 1996.
- [AST13] ASTM D-149-09. *Standard Test Method for Dielectric Breakdown Voltage and Dielectric Strength of Solid Electrical Insulating Materials at Commercial Power Frequencies*. American National Standard (2013)., 2013.
- [AV95] D.W. Auckland and B.R. Varlow. Electrical treeing in solid polymeric insulation. *Engineering Science and Education Journal*, 4(1):11–16, Feb 1995.
- [BB78] C.J.F. Böttcher and P. Bordewijk. *Theory of Polarization (Volume II)*. Elsevier, 1978.
- [BB05] A.R. Blythe and D. Bloor. *Electrical Properties of Polymers*. Cambridge University Press, second edition, 2005.
- [BBMZ83] M. Beyer, W. Boeck, K. Möller, and W. Zaengl. *Hochspannungstechnik*. Springer-Verlag Berlin Heidelberg GmbH, 1983.
- [BCL⁺95] L. Barral, J. Cano, A.J. Lopez, J. Lopez, P. Nogueira, and C. Ramirez. Thermal degradation of a diglycidyl ether of bisphenol a/1,3-bisaminomethylcyclohexane (dgeba/1,3-bac) epoxy resin system. *Thermochimica Acta*, 269-270:253 – 259, 1995. Recent Advances in Thermal Analysis and Calorimetry.
- [BCL99] J.P. Bellomo, P. Castelan, and T. Lebey. The effect of pulsed voltages on dielectric material properties. *IEEE Transactions on Dielectrics and Electrical Insulation*, 6(1):20–26, Feb 1999.
- [BCV71] A. Bradwell, R. Cooper, and B. Varlow. Conduction in poly-

- thene with strong electric fields and the effect of prestressing on the electric strength. *Proceedings of the Institution of Electrical Engineers*, 118(1):247–254, January 1971.
- [BDM⁺09] T. Bengtsson, F. Dijkhuizen, L. Ming, F. Sahlen, L. Liljestrand, D. Bormann, R. Papazyan, and M. Dahlgren. Repetitive fast voltage stresses-causes and effects. *IEEE Electrical Insulation Magazine*, 25(4):26–39, July 2009.
- [BH83] C.F. Bohren and D.R. Huffman. *Absorption and Scattering of Light by Small Particles*. Wiley, 1983.
- [Bin18] A. Bindra. Wide-Bandgap Power Devices: Adoption Gathers Momentum. *IEEE Power Electronics Magazine*, 5(1):22–27, March 2018.
- [BL13] M. Birle and C. Leu. Breakdown of polymer dielectrics at high direct and alternating voltages superimposed by high frequency high voltages. In *2013 IEEE International Conference on Solid Dielectrics (ICSD)*, pages 656–661, June 2013.
- [Bra17] R. Brandenburg. Dielectric barrier discharges: progress on plasma sources and on the understanding of regimes and single filaments. *Plasma Sources Science and Technology*, 26(5):1–29, 2017.
- [BYC04] M. Bahrami, M.M. Yovanovich, and J.R. Culham. Thermal Joint Resistances of Nonconforming Rough Surfaces with Gas-Filled Gaps. *Journal of Thermophysics and Heat Transfer*, 18(3):326–332, 2004.
- [CD02] R. Coelho and J. Debeau. Properties of the tip-plane configuration. *Journal of Physics D: Applied Physics*, 4:1266, 05 2002.
- [CFM10a] A. Cavallini, D. Fabiani, and G.C. Montanari. Power electronics and electrical insulation systems – Part 1: Phenomenology overview. *IEEE Electrical Insulation Magazine*, 26(3):7–15, May 2010.
- [CFM10b] A. Cavallini, D. Fabiani, and G.C. Montanari. Power electronics and electrical insulation systems – part 2: life modeling for insulation design. *IEEE Electrical Insulation Magazine*, 26(4):33–39, July 2010.

-
- [CFM10c] A. Cavallini, D. Fabiani, and G.C. Montanari. Power electronics and electrical insulation systems – Part 3: Diagnostic properties. *IEEE Electrical Insulation Magazine*, 26(5):30–40, Sep. 2010.
- [Cig17] Cigre Working Group D1.43. *Insulation degradation under fast, repetitive voltage pulses*. Technical Brochure 703 (2017)., 2017.
- [CL63] W. Corson and P. Lorrain. *Introduction to Electromagnetic Fields and Waves*. W.H. Freeman and Company, 1963.
- [CMFT11] A. Cavallini, G.C. Montanari, D. Fabiani, and M. Tozzi. The influence of PWM voltage waveforms on induction motor insulation systems: Perspectives for the end user. In *8th IEEE Symposium on Diagnostics for Electrical Machines, Power Electronics Drives*, pages 288–293, Sep. 2011.
- [CNP⁺12] D. Conklin, S. Nanayakkara, T.H. Park, M.F. Lagadec, J.T. Stecher, M.J. Therien, and D.A. Bonnell. Electronic Transport in Porphyrin Supermolecule-Gold Nanoparticle Assemblies. *Nano Letters*, 12(5):2414–2419, 2012.
- [Coe79] R. Coelho. *Physics of Dielectrics for the Engineer*. Elsevier, 1979.
- [CPL89] J.P. Crine, J.L. Parpal, and G. Lessard. A model of aging of dielectric extruded cables. In *Proceedings of the 3rd International Conference on Conduction and Breakdown in Solid Dielectrics*, pages 347–351, July 1989.
- [Cro08] J.M. Crowley. Simple Expressions for Force and Capacitance for a Conductive Sphere near a Conductive Wall. In *Proc. ESA Annual Meeting on Electrostatics*, 2008.
- [CZLZ16] G. Chen, C. Zhou, S. Li, and L. Zhong. Space Charge Modulated Electrical Breakdown. *Nature Scientific Reports*, 6(32588):1–4, September 2016.
- [Dak48] T.W. Dakin. Electrical Insulation Deterioration Treated as a Chemical Rate Phenomenon. *Transactions of the American Institute of Electrical Engineers*, 67(1):113–122, Jan 1948.
- [DF92] L.A. Dissado and J.C. Fothergill. *Electrical Degradation and Breakdown in Polymers*. Peter Peregrinus Ltd., 1992.
- [DMM97] L.A. Dissado, G. Mazzanti, and G.C. Montanari. The role

- of trapped space charges in the electrical aging of insulating materials. *IEEE Transactions on Dielectrics and Electrical Insulation*, 4(5):496–506, Oct 1997.
- [DP11] A. Dimopoulos and A.A. Skordos I.K. Partridge. Cure kinetics, glass transition temperature development, and dielectric spectroscopy of a low temperature cure epoxy/amine system. *Journal of Applied Polymer Science*, 124(3):1899–1905, 2011.
- [DP15] L. Deuschle and A. Philipp. *Feasibility Study on the Use of Current Transformers in Dielectric Spectroscopy*. Semester Thesis, ETH Zürich, 2015.
- [DW91] R.H. Daugherty and C.H. Wennerstrom. Need for industry standards for AC induction motors intended for use with adjustable-frequency controllers. *IEEE Transactions on Industry Applications*, 27(6):1175–1185, Nov 1991.
- [EAB53] P. Ehrlich, L.E. Amborski, and R.L. Burton. Dielectric properties of Teflon from room temperature to 314ÅrC and from frequencies of 10^2 to 10^5 c/s. In *1953 Conference on Electrical Insulation*, pages 28–30, Oct 1953.
- [EC02] A. Elasser and T.P. Chow. Silicon carbide benefits and advantages for power electronics circuits and systems. *Proceedings of the IEEE*, 90(6):969–986, June 2002.
- [EG99] M.W. Evans and V.I. Gaiduk. *Dielectric Relaxation and Dynamics of Polar Molecules*. World Scientific Publishing, 1999.
- [Fab03] D. Fabiani. *Accelerated Degradation of AC-Motor Winding Insulation due to Voltage Waveforms Generated by Adjustable Speed Drives*. PhD thesis, Bologna University, 2003.
- [FF16] R. Färber and C.M. Franck. Modular Arbitrary Waveform Dielectric Spectrometer for Aging Diagnostics of Recessed Specimens. In *2016 IEEE Conference on Electrical Insulation and Dielectric Phenomenon (CEIDP)*, pages 763–767, Oct 2016.
- [FF18a] R. Färber and C.M. Franck. Impedance Spectra of a Silicone Rubber in a Needle-Plane Electrode Arrangement during Electrical Tree Growth. In *VDE High Voltage Technology; ETG-Symposium*, Nov 2018.

- [FF18b] R. Färber and C.M. Franck. Modular high-precision dielectric spectrometer for quantifying the aging dynamics in (Sub-)picofarad polymeric specimens. *IEEE Transactions on Dielectrics and Electrical Insulation*, 25(3):1056–1063, June 2018.
- [FGK⁺19] R. Färber, T. Guillod, F. Krismer, C.M. Franck, and J.W. Kolar. Endurance of Polymeric Insulation Foil Exposed to DC-Biased Repetitive Pulse Voltage Stress below Partial Discharge Inception. *Submitted to IEEE Transactions on Dielectrics and Electrical Insulation*, 2019.
- [FL11] H. Fan and H. Li. High-Frequency Transformer Isolated Bidirectional DC–DC Converter Modules With High Efficiency Over Wide Load Range for 20 kVA Solid-State Transformer. *IEEE Transactions on Power Electronics*, 26(12):3599–3608, Dec 2011.
- [Fla18] L. Flandin. *Physico-Chemical Aging of Polymers*. Thematic School on Dielectrics (Summer School), Porquerolles/France, 2018.
- [FM01] D. Fabiani and G.C. Montanari. The effect of voltage distortion on ageing acceleration of insulation systems under partial discharge activity. *IEEE Electrical Insulation Magazine*, 17(3):24–33, May 2001.
- [FMCM04] D. Fabiani, G.C. Montanari, A. Cavallini, and G. Mazzanti. Relation between space charge accumulation and partial discharge activity in enameled wires under PWM-like voltage waveforms. *IEEE Transactions on Dielectrics and Electrical Insulation*, 11(3):393–405, June 2004.
- [FNF19] R. Färber, A. Nasef, and C.M. Franck. Online Dielectric Response Analysis under Mixed-Frequency Medium-Voltage Stress. In *International Symposium on High Voltage Engineering (ISH)*, Aug 2019.
- [Fro49] H. Froehlich. *Theory of Dielectrics: Dielectric Constant and Dielectric Loss*. Clarendon Press, 1949.
- [GCDDT04] F. Guastavino, G. Coletti, A. Dardano, and E. Torello. Life tests on twisted pairs subjected to PWM-like voltages. In *Proceedings of the 2004 IEEE International Conference on Solid Dielectrics (ICSD)*, volume 2, pages 860–863, July

- 2004.
- [GF97] S. Grzybowski and J. Fan. Electrical breakdown characteristics of the XLPE cables under AC, DC and pulsating voltages. In *Proceedings of 5th International Conference on Properties and Applications of Dielectric Materials*, volume 1, pages 389–393, May 1997.
- [GFH98] C. L. Griffiths, J. Freestone, and R.N. Hampton. Thermo-electric aging of cable grade XLPE. In *Conference Record of the 1998 IEEE International Symposium on Electrical Insulation*, volume 2, pages 578–582, June 1998.
- [GFK99] S. Grzybowski, E.A. Feilat, and P. Knight. Accelerated aging tests on magnet wires under high frequency pulsating voltage and high temperature. In *1999 Annual Report Conference on Electrical Insulation and Dielectric Phenomena (Cat. No.99CH36319)*, volume 2, pages 555–558 vol.2, Oct 1999.
- [GFK⁺16] T. Guillod, R. Färber, F. Krismer, C.M. Franck, and J.W. Kolar. Computation and Analysis of Dielectric Losses in MV Power Electronic Converter Insulation. In *2016 IEEE Energy Conversion Congress and Exposition (ECCE)*, pages 1–8, Sep. 2016.
- [GFR⁺19] T. Guillod, R. Färber, D. Rothmund, F. Krismer, C. M. Franck, and J. W. Kolar. Dielectric Losses in Dry-Type Insulation of Medium-Voltage Power Electronic Converters. *IEEE Journal of Emerging and Selected Topics in Power Electronics*, 2019.
- [GK86] S. Grzybowski and E. Kuffel. Electrical breakdown strength of polypropylene film oil-immersed under combined AC-DC voltage. In *Conference on Electrical Insulation Dielectric Phenomena - Annual Report 1986*, pages 516–521, Nov 1986.
- [Gri21] A.A. Griffith. The phenomena of rupture and flow in solids. *Philosophical Transaction of the Royal Society*, pages 163–198, 1921.
- [GWHL07] B. Gao, G.N. Wu, J.Y. He, and K.G. Lei. Investigation on aging mechanism of winding insulation used in inverter-fed traction motors. In *2007 Annual Report - Conference on Electrical Insulation and Dielectric Phenomena*, pages 107–111, Oct 2007.

-
- [HAL⁺00] C. Hudon, N. Amyot, T. Lebey, P. Castelan, and N. KandeV. Testing of low-voltage motor turn insulation intended for pulse-width modulated applications. *IEEE Transactions on Dielectrics and Electrical Insulation*, 7(6):783–789, Dec 2000.
- [HB05] J. Hedberg and T. Bengtsson. Straight Dielectric Response Measurements with High Precision. June 2005.
- [HBBG14] T. J. Hammarström, T. Bengtsson, J. Blennow, and S.M. Gubanski. Partial discharges in motor wires at PWM voltages of different smoothness. In *Proceedings of 2014 International Symposium on Electrical Insulating Materials*, pages 184–187, June 2014.
- [HBFB03] T.L. Hanley, R.P. Burford, R.J. Fleming, and K.W. Barber. A general review of polymeric insulation for use in HVDC cables. *IEEE Electrical Insulation Magazine*, 19(1):13–24, Jan 2003.
- [HFV⁺17] I.L. Hosier, N.A. Freebody, A.S. Vaughan, S.G. Swingler, and G. Moss. Electrical Treeing in Silicone Rubber. In *17th International Symposium on High Voltage Engineering*, Aug 2017.
- [HJC05] S.U. Haq, S.H. Jayaram, and E.A. Cherney. Evaluation of medium voltage groundwall insulation exposed to high frequency pulse voltages. In *Proceedings Electrical Insulation Conference and Electrical Manufacturing Expo, 2005.*, pages 194–197, Oct 2005.
- [HJCS06] S.U. Haq, S.H. Jayaram, E.A. Cherney, and L.C. Simon. Partial discharge erosion of nano-filled enameled wires subjected to high frequency waveforms. In *Conference Record of the 2006 IEEE International Symposium on Electrical Insulation*, pages 396–399, June 2006.
- [HK16] J.E. Huber and J.W. Kolar. Solid-State Transformers: On the Origins and Evolution of Key Concepts. *IEEE Industrial Electronics Magazine*, 10(3):19–28, Sep. 2016.
- [HM89] H.A. Haus and J.A. Melcher. *Electromagnetic Fields and Energy*. Prentice Hall Inc., 1989.
- [HN67] S. Havriliak and S. Negami. A complex plane representation of dielectric and mechanical relaxation processes in some polymers. *Polymer*, 8:161–210, 1967.

- [Hof17] F. Hoffmann. *Implementation of a Signal Acquisition System for High-Voltage Dielectric Spectroscopy*. Semester Thesis, ETH Zürich, 2017.
- [Hol92] J. Holtz. Pulsewidth Modulation - A Survey. *IEEE Transactions on Industrial Electronics*, 39(5):410–420, Oct 1992.
- [HS16] Y. Huang and L.S. Schadler. On the nature of high field charge transport in reinforced silicone dielectrics: Experiment and simulation. *Journal of Applied Physics*, 120(5), 2016.
- [IECa] IEC 60034-18-41. *Rotating electrical machines – Part 18-41: Partial discharge free electrical insulation systems (Type I) used in rotating electrical machines fed from voltage converters – Qualification and quality control tests*. International Standard, Edition 1.0 (2014).
- [IECb] IEC 60034-18-42. *Rotating electrical machines – Part 18-42: Partial discharge resistant electrical insulation systems (Type II) used in rotating electrical machines fed from voltage converters – Qualification tests*. International Standard, Edition 1.0 (2017).
- [IECc] IEC 60085. *Electrical Insulation – Thermal Evaluation and Designation*. International Standard, Edition 3.0 (2004).
- [Ion01] R.A. Ion. *Nonparametric Statistical Process Control*. PhD thesis, University of Amsterdam, 2001.
- [JLL05] J.P. Jones, J.P. Llewellyn, and T.J. Lewis. The contribution of field-induced morphological change to the electrical aging and breakdown of polyethylene. *IEEE Transactions on Dielectrics and Electrical Insulation*, 12(5):951–966, Oct 2005.
- [Jon78] A.K. Jonscher. Dielectric loss under transient excitation. *Journal of Physics C: Solid State Physics*, 11(14):601–606, 1978.
- [Jon83] A.K. Jonscher. *Dielectric Relaxation in Solids*. Chelsea Dielectrics Press, 1983.
- [KAB⁺00] M. Kaufhold, H. Aninger, M. Berth, J. Speck, and M. Eberhardt. Electrical stress and failure mechanism of the winding insulation in PWM-inverter-fed low-voltage induction motors.

-
- IEEE Transactions on Industrial Electronics*, 47(2):396–402, April 2000.
- [Kao04] K.C. Kao. *Dielectric Phenomena in Solids*. Elsevier Academic Press, 2004.
- [Kau95] M. Kaufhold. Failure mechanism of the interturn insulation of low voltage electric machines fed by pulse controlled inverters. In *Proceedings of 1995 Conference on Electrical Insulation and Dielectric Phenomena*, pages 254–257, Oct 1995.
- [KCD⁺11] T. Koltunowicz, A. Cavallini, D. Djairam, G.C. Montanari, and J. Smit. The influence of square voltage waveforms on transformer insulation break down voltage. In *2011 Annual Report Conference on Electrical Insulation and Dielectric Phenomena*, pages 48–51, Oct 2011.
- [KHS98] D. Konig, N. Hardt, and V. Scherb. Comparative insulation tests with DC and AC at 50 Hz and 50 kHz. In *1998 Annual Report Conference on Electrical Insulation and Dielectric Phenomena (Cat. No.98CH36257)*, volume 2, pages 702–705 vol. 2, Oct 1998.
- [Kir39] J.G. Kirkwood. The Dielectric Polarization of Polar Liquids. *The Journal of Chemical Physics*, 7(10), 1939.
- [KJ17] M. Khanali and S.H. Jayaram. Effect of high-frequency pulse ageing on dielectric response of paper/oil insulation. In *2017 IEEE Conference on Electrical Insulation and Dielectric Phenomenon (CEIDP)*, pages 728–731, Oct 2017.
- [KKB⁺11] T.L. Koltunowicz, R. Kochetov, G. Bajracharya, D. Djairam, and J.J. Smit. Repetitive transient aging, the influence of rise time. In *2011 Electrical Insulation Conference (EIC)*., pages 151–155, June 2011.
- [KMN14] S. Koltzenburg, M. Maskos, and O. Nuyken. *Polymere: Synthese, Eigenschaften und Anwendungen*. Springer Spektrum, 2014.
- [Kog03] U. Kogelschatz. Dielectric-barrier discharges: Their history, discharge physics, and industrial applications. *Plasma Chemistry and Plasma Processing*, 23(1):1–46, March 2003.
- [KPE14] R.J. Kortschot, A.P. Philipse, and B.H. Ern e. Debye Length Dependence of the Anomalous Dynamics of Ionic Double

- Layers in a Parallel Plate Capacitor. *The Journal of Physical Chemistry C*, 118(22):11584–11592, 2014.
- [KS03] F. Kremer and A. Schönhal. *Broadband Dielectric Spectroscopy*. Springer-Verlag Berlin Heidelberg, 2003.
- [LCC⁺18] L. Lusuardi, A. Cavallini, A. Caprara, F. Bardelli, and A. Cattazzo. The Impact of Test Voltage Waveform in Determining the Repetitive Partial Discharge Inception Voltage of Type I Turn/Turn Insulation Used in Inverter-Fed Induction Motors. In *2018 IEEE Electrical Insulation Conference (EIC)*, pages 478–481, June 2018.
- [LCd⁺19] L. Lusuardi, A. Cavallini, M. G. de la Calle, J. M. Mart̃añez-Tarifa, and G. Robles. Insulation design of low voltage electrical motors fed by PWM inverters. *IEEE Electrical Insulation Magazine*, 35(3):7–15, May 2019.
- [Lin09] E. Lindell. *Partial Discharges at Repetitive Rapidly Changing Voltages*. PhD thesis, Chalmers University, 2009.
- [LM83] A. Lustiger and R.L. Markham. Importance of tie molecules in preventing polyethylene fracture under long-term loading conditions. *Polymer*, 24(12):1647–1654, 1983.
- [Lor52] H.A. Lorentz. *Theory of Electrons*. Dover, New York, 1952.
- [Lus18] J. Luszcz. *High Frequency Conducted Emissions in AC Motor Drives Fed by Frequency Converters*. Wiley IEEE Press, 2018.
- [Mac53] J.R. Macdonald. Theory of ac Space-Charge Polarization Effects in Photoconductors, Semiconductors, and Electrolytes. *Phys. Rev.*, 92:4–17, Oct 1953.
- [Max54] J.C. Maxwell. *A Treatise on Electricity and Magnetism*. Dover Publications (reprint of 3rd Edition by Clarendon Press, 1891), 1954.
- [MBL⁺97] A. Mbaye, J.P. Bellomo, T. Lebey, J.M. Oraison, and F. Peltier. Electrical stresses applied to stator insulation in low-voltage induction motors fed by PWM drives. *IEE Proceedings - Electric Power Applications*, 144(3):191–198, May 1997.
- [MCD⁺17] P. Mancinelli, A. Cavallini, S. J. Dodd, N. M. Chalashkanov, and L. A. Dissado. Analysis of electrical tree inception in

- silicone gels. *IEEE Transactions on Dielectrics and Electrical Insulation*, 24(6):3974–3984, Dec 2017.
- [McP13] J.W. McPherson. *Reliability Physics and Engineering*. Springer, 2013.
- [MD79] N.F. Mott and E.A. Davis. *Electronic Processes in Non-Crystalline Solids*. Oxford University Press, second edition, 1979.
- [MF89] D.M. Manos and D.L. Flamm. *Plasma Etching – An Introduction*. Academic Press, Inc., 1989.
- [MF96] E.E. Marotta and L.S. Fletcher. Thermal contact conductance of selected polymeric materials. *Journal of Thermophysics and Heat Transfer*, 10(2):334–342, 1996.
- [MGMD97] G. C. Montanari, I. Ghinello, A. Motori, and D. Das Gupta. An investigation of conduction mechanisms at high-field in PET. In *IEEE 1997 Annual Report Conference on Electrical Insulation and Dielectric Phenomena*, volume 2, pages 451–454 vol.2, Oct 1997.
- [MIT] MIT Open Course Ware (18.03SC). Solutions to Linear First Order ODEs. <https://ocw.mit.edu/courses/mathematics/>. Online; accessed on June 18, 2019.
- [MJC15] M.S. Moonesan, S.H. Jayaram, and E.A. Cherney. Time to failure of medium-voltage form-wound machine turn insulation stressed by unipolar square waves. *IEEE Transactions on Dielectrics and Electrical Insulation*, 22(6):3118–3125, December 2015.
- [MLVB01] A.F. Moreira, T.A. Lipo, G. Venkataramanan, and S. Bernet. High frequency modeling for cable and induction motor overvoltage studies in long cable drives. In *Conference Record of the 2001 IEEE Industry Applications Conference. 36th IAS Annual Meeting (Cat. No.01CH37248)*, volume 3, pages 1787–1794 vol.3, Sep. 2001.
- [MOM⁺12] M. Min, J. Ojarand, O. Märtens, T. Paavle, R. Land, P. Annus, M. Rist, M. Reidla, and T. Parve. Binary Signals in Impedance Spectroscopy. In *Int. Conf. of the IEEE Engineering In Medicine and Biology Society*, pages 134–137, May 2012.

- [MP09] J.D. Menczel and R.B. Prime. *Thermal Analysis of Polymers: Fundamentals and Applications*. John Wiley & Sons, Inc., 2009.
- [MRBA19] A. Mohammed, S.S. Refaat, S. Bayhan, and H. Abu-Rub. AC Microgrid Control and Management Strategies: Evaluation and Review. *IEEE Power Electronics Magazine*, 6(2):18–31, June 2019.
- [MSH⁺04] L. Ming, F. Sahlen, S. Halen, G. Brosig, and L. Palmqvist. Impacts of high-frequency voltage on cable-terminations with resistive stress grading. In *Proceedings of the 2004 IEEE International Conference on Solid Dielectrics (ICSD)*, volume 1, pages 300–303 Vol.1, July 2004.
- [Nas18] A. Nasef. *Online Dielectric Spectroscopy under Medium-Frequency High-Voltage Stress*. Master Thesis, ETH Zürich, 2018.
- [ND09] E. Neagu and C. Dias. Charge injection/extraction at a metal-dielectric interface: Experimental validation. *IEEE Electrical Insulation Magazine*, 25(1):15–22, January 2009.
- [NG14] K. Niayesh and E. Gockenbach. On the aging mechanism of solid insulating materials exposed to repetitive high voltage pulses. *IEEE Transactions on Dielectrics and Electrical Insulation*, 21(1):304–310, February 2014.
- [Nie95] L. Niemeyer. A generalized approach to partial discharge modeling. *IEEE Transactions on Dielectrics and Electrical Insulation*, 2(4):510–528, Aug 1995.
- [OAMS13] N. Oswald, P. Anthony, N. McNeill, and B.H. Star. An Experimental Investigation of the Trade-Off between Switching Losses and EMI Generation with Hard-Switched All-Si, Si-SiC and All-SiC Device Combinations. *IEEE Transactions on Power Electronics*, 1(99):8885–8993, 2013.
- [OB11] G.M. Odegard and A. Bandyopadhyay. Physical aging of epoxy polymers and their composites. *Journal of Applied Polymer Science*, 49(24):1695–1716, 2011.
- [O’D73] J.J. O’Dwyer. *The Theory of Electrical Conduction and Breakdown in Solid Dielectrics*. Clarendon Press, 1973.
- [OHM07] H. Okubo, N. Hayakawa, and G.C. Montanari. Technical

- Development on Partial Discharge Measurement and Electrical Insulation Techniques for Low Voltage Motors Driven by Voltage Inverters. *IEEE Transactions on Dielectrics and Electrical Insulation*, 14(6), December 2007.
- [OLHK17] G. Ortiz, M.G. Leibl, J.E. Huber, and J.W. Kolar. Design and Experimental Testing of a Resonant DC–DC Converter for Solid-State Transformers. *IEEE Transactions on Power Electronics*, 32(10):7534–7542, Oct 2017.
- [Ons36] L. Onsager. Electric moments of molecules in liquids. *Journal of the American Chemical Society*, 58(5), 1936.
- [PCC15] A.K. Pradhan, B. Chatterjee, and S. Chakravorti. Estimation of paper moisture content based on dielectric dissipation factor of oil-paper insulation under non-sinusoidal excitations. *IEEE Transactions on Dielectrics and Electrical Insulation*, 22(2):822–830, April 2015.
- [Ped89] A. Pedersen. On the electrical breakdown of gaseous dielectrics—an engineering approach. In *Conference on Electrical Insulation and Dielectric Phenomena*, pages 21–58, Oct 1989.
- [PEH⁺03] L. Paulsson, B. Ekehov, S. Halen, T. Larsson, L. Palmqvist, A. Edris, D. Kidd, A.J.F. Keri, and B. Mehraban. High-frequency impacts in a converter-based back-to-back tie; the Eagle Pass installation. *IEEE Transactions on Power Delivery*, 18(4):1410–1415, Oct 2003.
- [PM17] P.-A. Pilloud and Q. Monney. *Experimental Investigation on the Voltage Endurance of Polymeric Insulation Materials under Puls-Width-Modulated Medium Voltages*. Bachelor Thesis, HES-SO Fribourg and ETH Zürich, 2017.
- [Pop15] Y.M. Poplavko. *Physics of Active Dielectrics. Volume 1*. Lambert Academic Publishing, 2015.
- [PT14] P. Preetha and M. J. Thomas. Life estimation of electrothermally stressed epoxy nanocomposites. *IEEE Transactions on Dielectrics and Electrical Insulation*, 21(3):1154–1160, June 2014.
- [Rap72] M. Rapos. The electrical properties of insulating materials under the simultaneous action of ac and dc voltage. In *Conference on Electrical Insulation Dielectric Phenomena -*

Annual Report 1972, pages 98–104, Oct 1972.

- [ROAR07] J.A. Rosero, J.A. Ortega, E. Aldabas, and L. Romeral. Moving towards a more electric aircraft. *IEEE Aerospace and Electronic Systems Magazine*, 22(3):3–9, March 2007.
- [Rob73] F.N.H. Robinson. *Macroscopic Electromagnetism*. Pergamon Press, 1973.
- [RPS⁺06] J. Rodriguez, J. Pontt, C. Silva, R. Musalem, P. Newman, R. Vargas, and S. Fuentes. Resonances and overvoltages in a medium-voltage fan motor drive with long cables in an underground mine. *IEEE Transactions on Industry Applications*, 42(3):856–863, May 2006.
- [SBBG08] B. Sonerud, T. Bengtsson, J. Blennow, and S.M. Gubanski. Dielectric response measurements utilizing semi-square voltage waveforms. *IEEE Transactions on Dielectrics and Electrical Insulation*, 15(4):920–926, August 2008.
- [SBBG09] B. Sonerud, T. Bengtsson, J. Blennow, and S.M. Gubanski. Dielectric heating in insulating materials subjected to voltage waveforms with high harmonic content. *IEEE Transactions on Dielectrics and Electrical Insulation*, 16(4):926–933, August 2009.
- [SBBG11] B. Sonerud, T. Bengtsson, J. Blennow, and S.M. Gubanski. Noise and Aliasing Aspects in a Multiharmonic-Dielectric-Response-Measurement System. *IEEE Transactions on Instrumentation and Measurement*, 60(12):3875–3882, Dec 2011.
- [SBG⁺10] B. Sonerud, J. Blennow, S.M. Gubanski, S. Nilsson, and T. Bengtsson. Continuous monitoring of dielectric properties of LDPE samples during electrical treeing. In *2010 10th IEEE International Conference on Solid Dielectrics*, pages 1–4, July 2010.
- [SC14] G.C. Stone and I. Culbert. Review of stator insulation problems in medium voltage motors fed from voltage source PWM drives. In *Proceedings of 2014 International Symposium on Electrical Insulating Materials*, pages 50–53, June 2014.
- [SCL07] G.C. Stone, I.M. Culbert, and B.A. Lloyd. Stator insulation problems associated with low voltage and medium voltage PWM drives. In *2007 IEEE Cement Industry Technical*

- Conference Record*, pages 187–192, April 2007.
- [SCT00] G. Stone, S. Campbell, and S. Tetreault. Inverter-fed drives: which motor stators are at risk? *IEEE Industry Applications Magazine*, 6(5):17–22, Sep. 2000.
- [She00] D.J. Sheskin. *Handbook of Parametric and Nonparametric Statistical Procedures*. Chapman and Hall/CRC, 2nd edition, 2000.
- [SJC10] E. Sharifi, S. Jayaram, and E.A. Cherney. A coupled electro-thermal study of the stress grading system of medium voltage motor coils when energized by repetitive fast pulses. In *2010 IEEE International Symposium on Electrical Insulation*, pages 1–4, June 2010.
- [SKF⁺17] M.P. Souli, P. Klonos, Fragopoulou, A.F., I.V. Mavragani, I.S. Pateras, N. Kostomitsopoulos, and A.G. Georgakilas. Applying Broadband Dielectric Spectroscopy (BDS) for the Biophysical Characterization of Mammalian Tissues under a Variety of Cellular Stresses. *International Journal of Molecular Sciences*, 18(4):838, 2017.
- [SL17] I. Semenov and C. Leu. Loss factor and permittivity measurement at medium-frequency high voltage with an HVDC offset. In *2017 INSUCON - 13th International Electrical Insulation Conference (INSUCON)*, pages 1–4, May 2017.
- [SL19] I. Semenov and C. Leu. Effect of High DC Field on Loss Tangent and Permittivity of Nonimpregnated Transformer-board. August 2019.
- [SMC⁺18] M. Sanduleac, J.F. Martins, I. Ciornei, M. Albu, L. Toma, V.F. Pires, L. Hadjidemetriou, and R. Sauba. Resilient and Immune by Design Microgrids Using Solid State Transformers. *Energies*, 11(12), 2018.
- [SSR⁺14] J. Smajic, T. Steinmetz, M. Rüegg, Z. Tanasic, R. Obrist, J. Tepper, B. Weber, and M. Carlen. Simulation and Measurement of Lightning-Impulse Voltage Distributions Over Transformer Windings. *IEEE Transactions on Magnetics*, 50(2):553–556, Feb 2014.
- [Sti16] T. Stiefel. *Current Sensing for Broad-Band High-Voltage Dielectric Spectroscopy*. Semester Thesis, ETH Zürich, 2016.

- [Sto10] L. Stollenwerk. Interaction of current filaments in a dielectric barrier discharge system. *Plasma Physics and Controlled Fusion*, 52(12):124017, nov 2010.
- [Str41] J.A. Stratton. *Electromagnetic Theory*. McGrawHill Book Company, 1941.
- [SvB92] G.C. Stone, R.G. van Heeswijk, and R. Bartnikas. Investigation of the effect of repetitive voltage surges on epoxy insulation. *IEEE Transactions on Energy Conversion*, 7(4):754–760, Dec 1992.
- [Tan15] D. Tan. Emerging System Applications and Technological Trends in Power Electronics: Power electronics is increasingly cutting across traditional boundaries. *IEEE Power Electronics Magazine*, 2(2):38–47, June 2015.
- [TG82] S.P. Timoshenko and J.N. Goodier. *Theory of Elasticity*. McGraw-Hill, third edition, 1982.
- [TN17] D. Tan and D. Novosel. Towards a (more) electronic transmission and distribution (eT &D). *CES Transactions on Electrical Machines and Systems*, 1(1):15–25, March 2017.
- [TO14] F. Tian and Y. Ohki. Electric modulus powerful tool for analyzing dielectric behavior. *IEEE Transactions on Dielectrics and Electrical Insulation*, 21(3):929–931, June 2014.
- [Wat65] N.E. Waters. The indentation of thin rubber sheets by spherical indentors. *British Journal of Physics*, 16:557–563, 1965.
- [WCM14] P. Wang, A. Cavallini, and G.C. Montanari. The influence of repetitive square wave voltage parameters on enameled wire endurance. *IEEE Transactions on Dielectrics and Electrical Insulation*, 21(3):1276–1284, June 2014.
- [WCR⁺10] N. Wang, I. Cotton, J. Robertson, S. Follmann, K. Evans, and D. Newcombe. Partial discharge control in a power electronic module using high permittivity non-linear dielectrics. *IEEE Transactions on Dielectrics and Electrical Insulation*, 17(4):1319–1326, August 2010.
- [WFA51] S.B. Warder, E. Friedlander, and A.N. Arman. The influence of rectifier harmonics in a railway system on the dielectric stability of 33-kV cables. *Journal of the Institution of Electrical*

Engineers, 1951(7):217–218, July 1951.

- [Whe05] J.C.G. Wheeler. Effects of converter pulses on the electrical insulation in low and medium voltage motors. *IEEE Electrical Insulation Magazine*, 21(2):22–29, March 2005.
- [WLZ⁺12] Y. Wang, J. Li, Y. Zhao, Z. He, S. Wu, and L. Bao. Failure evaluation model of oil-paper insulation under AC-DC combined voltages. *2012 International Conference on High Voltage Engineering and Application*, pages 396–399, 2012.
- [WTE⁺01] P. Werelius, P. Tharning, R. Eriksson, B. Holmgren, and U. Gafvert. Dielectric spectroscopy for diagnosis of water tree deterioration in XLPE cables. *IEEE Transactions on Dielectrics and Electrical Insulation*, 8(1):27–42, Feb 2001.
- [WXWC16] P. Wang, H. Xu, J. Wang, and A. Cavallini. The influence of repetitive square wave voltage duty cycle on partial discharge statistics and insulation endurance. In *2016 International Conference on Condition Monitoring and Diagnosis (CMD)*, pages 274–277, Sep. 2016.
- [YFT87] M. Yashima, H. Fujinami, and T. Takuma. Measurement of Accumulated Charge on Dielectric Surfaces with an Electrostatic Probe. May 1987.
- [Yin97] W. Yin. Failure mechanism of winding insulations in inverter-fed motors. *IEEE Electrical Insulation Magazine*, 13(6):18–23, Nov 1997.
- [YS62] H. Yasuda and V. Stannett. Permeation, solution, and diffusion of water in some high polymers. *Journal of Polymer Science*, 57(165):907–923, 1962.
- [Zae03a] W.S. Zaengl. Applications of dielectric spectroscopy in time and frequency domain for HV power equipment. *IEEE Electrical Insulation Magazine*, 19(6):9–22, Nov 2003.
- [Zae03b] W.S. Zaengl. Dielectric spectroscopy in time and frequency domain for HV power equipment. I. Theoretical considerations. *IEEE Electrical Insulation Magazine*, 19(5):5–19, Sep. 2003.
- [ZP94] W.S. Zaengl and K. Petcharakas. Application of Streamer Breakdown Criterion for Inhomogeneous Fields in Dry Air and SF₆. In *Christophorou L.G., James D.R. (editors)*

Gaseous Dielectrics VII. Springer, Boston, MA, 1994.

[ZS84]

H.R. Zeller and W.R. Schneider. Electrofracture mechanics of dielectric aging. *Journal of Applied Physics*, 56(2):455–459, July 1984.

Acknowledgement

This project was carried out within the frame of the Swiss Centre for Competence in Energy Research on the Future Swiss Electrical Infrastructure (SCCER-FURIES) with the financial support of the Swiss Innovation Agency.

I would like to thank my supervisor Prof. Christian Franck for giving me the trust and possibilities to carry out this project. I very much appreciated the innovative atmosphere within which this project grew and, hopefully, continues to be of service for future research at the High Voltage Laboratory.

I would also like to express my gratitude to Prof. Andrea Cavallini from Bologna University for accepting to be the external examiner of this thesis.

The collaboration with the Power Electronics Systems Laboratory (PES) at ETH Zürich proved to be of great symbiotic value. Thanks in particular to Dr. Thomas Guillod for his continuous support in all questions relating to power electronics (and beyond).

None of the setups designed during this thesis would have materialized without the work and expertise of the workshop staff at our department (D-ITET).

Special thanks to Fabian and Henry for their helpful inputs in all matters concerning mechanical constructions and setups, as well as to Hans-Jürg for his expertise in metrological questions.

I very much appreciated the good atmosphere in our group, which resulted in stimulating inputs and questions from as well as discussions with colleagues. And may those be blessed who had to endure my presence even outside of work.

Last but not least, I would like to thank our secretary Karin for her continuous administrative assistance, as well as just being up for refreshing small chats or the weakly jogging round.

In memory of my father Heinz Färber (1945-1991)

Curriculum Vitae

Name Raphael Färber
Date of Birth 15.09.1986
Citizenship Swiss

Professional Experience

- 2014-2019 Research Assistant at the High Voltage Laboratory at the Swiss Federal Institute of Technology, Zürich (ETHZ)
- 2013 Research Staff at Paul Scherrer Institut (PSI), Villigen, Switzerland
- 2012 Research Intern at ABB Corporate Research Center, Baden-Dättwil, Switzerland
- 2011 Civil Service at the Institute of Radiation Protection (IRA), Lausanne University Hospital (CHUV)
- 2006-2010 Industrial Internships (6 weeks/year) at SwissOptic AG, Heerbrugg, Switzerland

Education

- 2014-2019 Ph.D. Student at the High Voltage Laboratory at the Swiss Federal Institute of Technology, Zürich (ETHZ)
- 2006-2011 M.Sc. in Physics
(École Polytechnique Fédérale de Lausanne, EPFL)
- 2001-2005 Matura (Kantonsschule Heerbrugg SG)